

Metal-organic Framework Mediated Electrode Engineering for Electrochemical CO₂ Reduction

Wang, Riming

DOI

[10.4233/uuid:7de36fae-025d-499a-a726-21657cffce6c](https://doi.org/10.4233/uuid:7de36fae-025d-499a-a726-21657cffce6c)

Publication date

2020

Document Version

Final published version

Citation (APA)

Wang, R. (2020). *Metal-organic Framework Mediated Electrode Engineering for Electrochemical CO₂ Reduction*. [Dissertation (TU Delft), Delft University of Technology]. <https://doi.org/10.4233/uuid:7de36fae-025d-499a-a726-21657cffce6c>

Important note

To cite this publication, please use the final published version (if applicable). Please check the document version above.

Copyright

Other than for strictly personal use, it is not permitted to download, forward or distribute the text or part of it, without the consent of the author(s) and/or copyright holder(s), unless the work is under an open content license such as Creative Commons.

Takedown policy

Please contact us and provide details if you believe this document breaches copyrights. We will remove access to the work immediately and investigate your claim.

**Metal-Organic Framework Mediated
Catalyst Engineering for Electrochemical
CO₂ Reduction**

Riming WANG

Metal-Organic Framework Mediated Electrode Engineering for Electrochemical CO₂ Reduction

Dissertation

for the purpose of obtaining the degree of doctor
at Delft University of Technology,
by the authority of the Rector Magnificus prof. dr. ir. T.H.J.J. van der Hagen,
chair of the Board for Doctorates,
to be defended publicly on
Wednesday, 8th January 2020 at 10 o'clock

by

Riming WANG

Master of Engineering in Material Science and Engineering
at Shandong University, China
born in Qingdao, Shandong Province, China

This dissertation has been approved by the promotor:

Prof. dr. F. Kapteijn and Prof. dr. J. Gascon Sabate

Composition of the doctoral committee:

Rector Magnificus	Chairman
Prof. dr. F. Kapteijn	Delft University of Technology, promotor
Prof. dr. J. Gascon Sabate	Delft University of Technology and King Abdullah University of Science and Technology, promotor

Independent members:

Prof. dr. B. Dam	Delft University of Technology
Prof. dr. A. Urakawa	Delft University of Technology
Prof. dr. ir. W. de Jong	Delft University of Technology
Prof. dr. G. Mul	University of Twente
Prof. dr. J. Pérez-Ramírez	ETH Zürich

The research described in this thesis was conducted in the Catalysis Engineering section of the Chemical Engineering Department, Faculty of Applied Sciences (TNW) of the Delft University of Technology, and co-financed by the China Scholarship Council (CSC).

Dissertation, Delft University of Technology

With summary in Dutch

ISBN: 978-94-028-1858-1

Copyright © 2020 Riming WANG

All rights reserved

Printed by Ipskamp Printing, Enschede

An electronic version of this dissertation is available at <http://repository.tudelft.nl/>.

To my family

CONTENTS

Chapter 1 -

Engineering Metal-Organic Frameworks for the Electrochemical
Reduction of CO₂ 1

1.1. INTRODUCTION 3

1.2. MAIN CHALLENGES FOR CO₂ER 5

1.2.1. Overpotential (voltage efficiency) 6

1.2.2. Faradaic Efficiency (FE) 6

1.2.3. CO₂ Mass Transport 7

1.2.4. Electrode Stability 8

1.3. MOF-RELATED CATALYSTS FOR CO₂ER 8

1.3.1. MOF as Electrocatalysts 11

1.3.2. MOFs as Active Phase Supports 14

1.3.3. MOFs as Electrocatalyst Precursors 18

1.4. CONCLUDING REMARKS 25

1.5. ABBREVIATIONS 27

1.6. REFERENCES 29

OBJECTIVE AND OUTLINE OF THIS THESIS 38

Chapter 2 -

Maximizing Ag Utilization in High Rate CO₂ Electrochemical
Reduction with a Coordination Polymer Mediated Gas Diffusion
Electrode 41

2.1. INTRODUCTION	43
2.2. RESULTS AND DISCUSSION	44
2.3. CONCLUSIONS	55
2.4. REFERENCES	56
2.5. Supporting Information for Chapter 2	62
2.5.1. Optimization of the synthetic conditions for Ag-CP	62
2.5.2. Crystal structure of silver 2,5-pyridinedicarboxylate coordination polymer (Ag-CP): determination and details	64
2.5.3. Experimental details	69
2.5.4. Supplementary experimental results	78
2.5.5. References for supporting information	96

Chapter 3 -

Metal-Organic Framework Mediated Ag-Cu Composite for Enhanced Production of Ethylene in Electrochemical CO ₂ Reduction	100
3.1. INTRODUCTION	102
3.2. EXPERIMENTAL	104
3.2.1. Materials	104
3.2.2. Synthesis of Ag-CP	105
3.2.3. Hydrochloric acid (HCl) etching of Cu foil	105
3.2.4. Spin-coating of Ag-CP onto etched Cu foil.	106
3.2.5. Electroreduction of Ag-CP.	106
3.2.6. Controlled-potential CO ₂ electrolysis.	107
3.2.7. Electrochemical active surface area measurement.	108
3.2.8. Characterization techniques.	109
3.3. RESULTS AND DISCUSSION	110

3.4. CONCLUSIONS	117
3.5. REFERENCES	119
3.6. Supporting Information for Chapter 3	123

Chapter 4 -

Metal-organic Framework Mediated Nitrogen-doped Carbon for Electrochemical CO ₂ Reduction	135
--	-----

4.1. INTRODUCTION	137
4.2. EXPERIMENTAL SECTION	139
4.2.1. Materials	139
4.2.2. Characterization techniques	139
4.2.3. Catalysts synthesis	140
4.2.4. Electrochemical performance	141
4.3. RESULTS AND DISCUSSION	143
4.3.1. Synthesis and Structural Characterization	143
4.3.2. Catalytic Performance	149
4.4. CONCLUSIONS	151
4.5. REFERENCES	152
4.6. Supporting Information for Chapter 4	159

Chapter 5 -

Structure-Activity Relationships in Metal-organic Framework Derived Mesoporous Nitrogen-doped Carbon Containing Atomically Dispersed Iron Sites for Electrochemical CO ₂ Reduction	165
---	-----

5.1. INTRODUCTION	167
5.2. EXPERIMENTAL	169
5.2.1. Materials	169
5.2.2 Catalyst synthesis	170
5.2.3. Characterization	171
5.2.4. Catalyst performance	172
5.3. RESULTS AND DISCUSSION	173
5.3.1. Characterization of mesoNC-Fe catalyst	173
5.3.2. The coordination environment of iron sites in mesoNC-Fe	177
5.3.3. Electrochemical reduction of CO ₂ over the mesoNC-Fe catalyst	188
5.4. CONCLUSIONS	192
5.5. REFERENCES	194
5.6. Supporting Information for Chapter 5	200
5.6.1. Geometry optimization for structural models representing the iron site	200
5.6.2. X-ray absorption and emission spectroscopies (XAS and XES).	201
5.6.4. Supplementary experimental results	206
5.6.5. References for supporting information	220
SUMMARY	227
SAMENVATTING	231
ACKNOWLEDGEMENTS	235
LIST OF ACADEMIC CONTRIBUTIONS	238
ABOUT THE AUTHOR	240

Engineering Metal-Organic
Frameworks for the
Electrochemical Reduction of CO₂

1

This chapter is based on the following publication:

R. Wang, F. Kapteijn, J. Gascon, *Chem. Asian J.* 2019, 14, 3452-3461.

Abstract: Electrochemical CO₂ reduction holds great promise in reducing atmospheric CO₂ concentration. However, several challenges hinder the commercialization of this technology. Energy efficiency, CO₂ solubility in aqueous phase, and electrode stability are among the current issues. In this mini-review, we summarize and highlight the main advantages and limitations that Metal-Organic Frameworks may offer to this field of research, either when used directly as electrocatalysts or when used as catalyst precursors.

1.1. INTRODUCTION

The ever-increasing atmospheric CO₂ concentration is one of the critical issues that require an urgent solution within this century. From a global carbon cycle point of view, industrial activity is the major CO₂ contributor, causing a rapid accumulation of this greenhouse gas in the atmosphere. To counteract this unbalance, CO₂ capture and utilization technologies should be implemented. In this spirit, several technologies have been proposed for CO₂ utilization, based on thermocatalysis, photocatalysis, and electrocatalysis, *etc.* All the above-mentioned catalytic approaches have their economic advantages under certain conditions, and they may all contribute to reducing atmospheric CO₂ [1]. For example, thermocatalysis would already be economically competitive if green H₂ (*e.g.* generated from water splitting using renewable energy) was massively available [2]. Photocatalysis, on the other hand, would be more favourable in remote locations with strong solar irradiation. Electrocatalytic reduction of CO₂ (CO₂ER) is the other technology that holds great promise if efficient electrocatalysts can be developed for the direct transformation of CO₂ into valuable products.

Initially, catalysts used for CO₂ER were pure metal foils directly used as electrodes [3]. With the advancement of nanotechnology, other configurations have been used as catalysts in CO₂ER, significantly enhancing CO₂ER efficiency [4]. In these nanostructured electrocatalysts, the active phase is dispersed within a conductive support, such as carbon cloth, carbon paper or glassy carbon. In the following context, the electrode mainly refers to catalysts dispersed on a conductive support, and catalyst engineering represents the engineering effort to improve CO₂ER efficiencies

(including Faradaic efficiencies towards valuable products, current densities, and energy efficiencies) through the design of catalytic sites and/or the optimization of the catalyst structure.

Metal-organic frameworks (MOFs) have recently emerged in the field of catalysis because of their unique textural and topological properties [5]. On the one hand, when MOFs are used directly as catalysts, not only the atomically dispersed metal nodes can be engineered into active sites, but also the organic linkers hold great potential as catalytic sites [6]. Besides, the porous structure can be tuned to enhance mass transport. On the other hand, MOFs can also be used as catalyst precursors, yielding MOF mediated catalysts [7]. Following this approach, the MOF is decomposed under controlled conditions to lead to the clustering of its metal component into small nanoparticles or to the formation of single atom catalytic sites. At the same time, the organic component (the linker) rearranges into a carbonaceous matrix that may be conductive [8]. Xia *et al.* reviewed the use of MOFs for electrochemical energy storage, including catalytic electrodes [9]. Herein, we summarize the recent works on electrochemical CO₂ reduction using MOF and MOF derived catalysts.

Next to reviewing the work done so far on this interesting topic, we have to realize that the commercialization of CO₂ER will not solely rely on catalyst engineering. Indeed, the design of the electrochemical cell and the optimization of reaction conditions (pressure, temperature, *etc.*) will play a role as important as that of the catalyst itself.

In this mini-review, we first give a brief introduction to the challenges faced by CO₂ER, followed by a summary on MOF-related catalyst

engineering and MOF derived electrocatalysts. We finalize with our personal opinion on future developments.

1.2. MAIN CHALLENGES FOR CO₂ER

CO₂ electrochemical reduction can be seen as a reversed process of fuel cells, and a lot of similarities are shared between these two processes, such as cell configuration, electrolyte, *etc.* CO₂ER with H-cell, one of the most popular cell configurations so far, features cathode and anode compartments filled with aqueous electrolyte and separated by a membrane. MOFs and MOF-derived catalysts are mostly particles, and are used as supported catalysts in CO₂ER cells. CO₂ approaches the catalytic sites through diffusion in aqueous phase, and several valuable products can be generated, such as CO, C₂H₄, HCOOH, oxalic acid, alcohols, *etc.* As proposed by Koper and co-workers [10], the reduction of CO₂ starts with the formation of a •COO⁻ intermediate. Subsequent reaction with a proton-electron pair leads to the formation of HCOO⁻, while the absorption of only a proton results in the formation of •COOH, which will be further reduced to •CO. On the one hand, if the •CO intermediate is strongly bonded by the catalyst, for example Cu, it will be reduced to additional products. On the other hand, if the •CO intermediate is weakly bonded (*i.e.* in case of Ag, Au, or Zn) CO will desorb and become the main product.

The challenges of CO₂ER have been generally summarized and discussed [1, 11], so we will only give a brief introduction to CO₂ER here, with specific emphasis on commercializing considerations.

1.2.1. Overpotential (voltage efficiency)

One of the key drawbacks that hinder the commercialization of CO₂ER is energy efficiency, which is primarily limited by the high overpotential of CO₂ER.

In electrochemistry, overpotential is the potential (voltage) difference between a half-reaction's reduction potential at thermodynamic equilibrium and the potential at which the redox reaction occurs. The existence of overpotential implies that more energy is required than thermodynamically needed to drive a given reaction, and this energy loss, usually in thermal form, directly affects voltage efficiency.

It is widely accepted that the overpotential for CO₂ electrochemical reduction originates from the sluggish kinetics to form a •CO₂⁻ intermediate [11a, 11c]. This step has a standard potential of -1.9 V vs. SHE and is the main reason for high overpotentials. This potential can be improved (lowered) by stabilizing the intermediate, which is one of the primary functions of catalysts.

1.2.2. Faradaic Efficiency (FE)

Faraday efficiency is described as energy losses in the current term. Although all the current in CO₂ER is consumed to form products, the current directed towards undesirable reactions or products is usually considered as energy loss.

One primary undesirable product is H₂, generated by the competing hydrogen evolution reaction (HER) in the aqueous electrolyte. As a consequence, catalysts with high hydrogen overpotentials typically give favourable FE for CO₂ER.

From a commercialization perspective, the potential market of CO₂ER will be fuel and commodity chemicals, where oil derived products are now dominating. Taking the competition between CO₂ER derived chemicals and petrochemicals into consideration, it is clear that some CO₂ER products, for example CH₄, are economically unfavourable. Formation of these products should be avoided since the electricity cost to produce them will not be paid off [1].

A scenario of CO₂ER commercialization would be the direct treatment of post-combustion gas from power plants, avoiding in this case expensive (and highly energy consuming) separation. These streams usually contain a relatively high concentration of unreacted O₂. Thus, CO₂ER catalyst for this specific application should be inactive towards oxygen reduction reaction (ORR) [12]. Moreover, the ORR products are reactive O₂⁻ and H₂O₂ species sometimes, which offer a harmful environment for CO₂ER catalysts [13].

1.2.3. CO₂ Mass Transport

One of the key limiting factors in aqueous-phase CO₂ conversion is the mass transfer of CO₂ to the cathode surface, especially given the low solubility of CO₂ in many electrolytes. In addition to catholyte CO₂ capacity, product bubble formation can disrupt the reaction system as well. Although the low solubility of CO₂ in aqueous phase can be overcome by using gas-diffusion electrodes (GDE), the current density of cathode GDEs may also be limited by the CO₂ flux to the catalyst. The CO₂ transport limit can be seen as the critical issue that hinders the enhancement of current density [14]. Configuration of electrochemical cells may largely influence the CO₂ transportation, and in turn influences the current density, thus it should be

noted that the comparison of current densities should take the cell configuration into consideration [15].

1.2.4. Electrode Stability

Stability is an essential criterion for commercial catalysts. Excellent stability can greatly reduce the operational costs [16]. In CO₂ER, the electrode stability requires not only the resistance to deactivation but also the resistance to impurities [17]. The long-time running of CO₂ER has been reported in several articles [18]. However, the resistance to impurities has not been widely covered. Again, taking the example of using the post-combustion gas from power plant as CO₂ feedstock, the post-combustion gas will contain a relatively high level of impurities, such as SO_x and NO_x, even after a primary treatment, and S has been identified as a harmful component to many electrocatalysts [19]. The electrolyte is another source of impurities [11c, 20]. In this regard, more research into impurity-resistant electrodes will be important. Additionally, electrode stability should be separated from system stability. For instance, electrode clogging because of the formation of bicarbonate crystals during CO₂ER is not related to the electrode itself but to the reactor system and such should be solved through system engineering.

1.3. MOF-RELATED CATALYSTS FOR CO₂ER

Table 1.1. Summary of CO₂ER performance with MOF-related materials.

Electro-catalyst[a]	Main product	Peak FE ^[b] (%)	Peak j_{total} (mA cm ⁻²)	Peak potential ^[c] (V)	Electrolyte
CR-MOF[21]	Formic acid	~100	7.1	-0.78	0.5 M KHCO ₃
Cu-BTC[22]	Oxalic acid	~51	19.22	-2.5 vs. Ag/Ag ⁺	0.01 M TBATFB in DMF
ZIF-8[23]	CO	65	~3	-1.14	0.5 M NaCl
ZIF-8[24]	CO	81	8.5	-1.1	0.25 M K ₂ SO ₄
ZIF-108[24]	CO	52	24.6	-1.3	0.25 M K ₂ SO ₄
Cu-BTC[25]	ethanol	10.3	10	-0.28	0.5 M KHCO ₃
Ligand-doped ZIF-8[26]	CO	90	10.1	-1.2	0.1 M KHCO ₃
Re-MOF[27]	CO	93	>2	-1.6 vs. NHE	0.1 M TBAH in CH ₃ CN+5%TFE
ZIF-BTC[28]	CH ₄	80	3.1	-2.2 vs. Ag/Ag ⁺	BMIMBF ₄
Fe MOF-525[29]	CO	50	~6	-1.3 vs. NHE	1 M TBATF ₆ in DMF
PCN-222(Fe)[30]	CO	91	1.2	-0.6	0.5 M KHCO ₃
Cu ₂ (CuTCPP) nanosheet[31]	HCOO ⁻	68.4	~4.5	-1.55 vs. Ag/Ag ⁺	CH ₃ CN with 1 M H ₂ O and 0.5 M EMIMBF ₄
Al ₂ (OH) ₂ TCP P-Co MOF[32]	CO	76	~1	-0.7	0.5 M KHCO ₃
Ag ₂ O/layered ZIF[33]	CO	~80	32	-1.3	0.25 M K ₂ SO ₄
Cu-SIM NU-1000[34]	HCOO ⁻	28	1.2	-0.82	0.1 M NaClO ₄
Cu ₂ O@Cu-MOF[35]	CH ₄	63.2	-14	-1.71	0.1 M KHCO ₃
OD-Cu/C[36]	CH ₃ OH	~43.2	~8.9	-0.3	0.1 M KHCO ₃

MOF-derived Cu NPs[37]	CH ₄	~50	7.5	-1.3	0.1 M KHCO ₃
ZIF-8 derived Fe-N active sites[38]	CO	93	5.2	-0.43	1 M KHCO ₃
Ni SA/N-C[39]	CO	71.9	10.48	-1.0	0.5 M KHCO ₃
N-coordinated Fe[40]	CO	93	2.8	-0.58	0.1 M KHCO ₃
Low-CN Cu clusters[41]	C ₂ H ₄	45	262	-1.07	1 M KOH
N-coordinated Co[42]	CO	94	18.1	-0.63	0.5 M KHCO ₃
MOF-derived In-Cu bimetallic oxides[43]	CO	92.1	11.2	-0.8	0.5 M KHCO ₃
ZIF-8 derived NC[44]	CO	78	1.1	-0.93	0.1 M KHCO ₃
ZIF-8 derived NC[45]	CO	95.4	1	-0.5	0.5 M KHCO ₃
Pyrolyzed ZIF/MWCNT [46]	CO	100	7.7	-0.86	0.1 M NaHCO ₃

[a] The MOF-related catalysts mentioned in this table were used in a supporting manner. A list of abbreviations is presented at the end of the text.

[b] Peak FE represents the FE of main products.

[c] Peak potential represents the potential where peak FE occurs, and is against RHE unless specifically noted.

1.3.1. MOF as Electrocatalysts

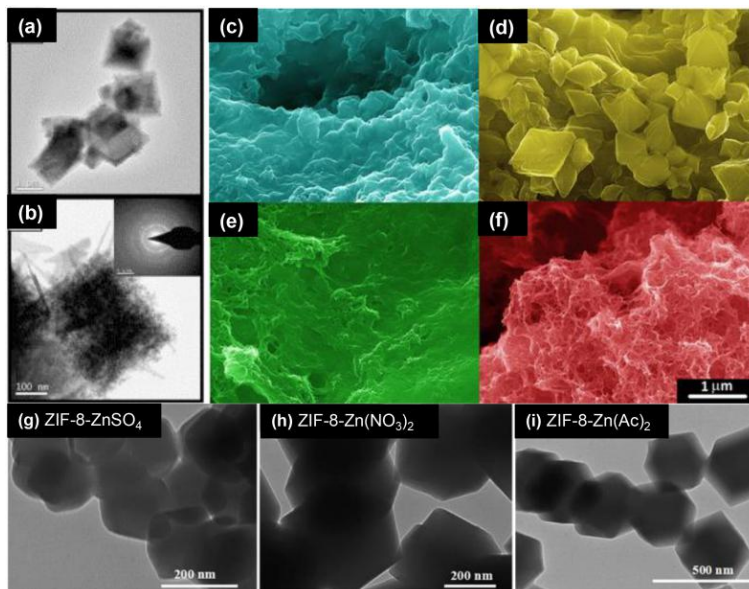


Figure 1.1. Representative electron micrograph of directly using MOF as electrocatalyst. TEM image of (a) lower and (b) higher magnification, SAED pattern (inset) of Cu-BTC;[22] SEM images at 25 000 \times magnification of (a) HKUST-1, (b) CuAdeAce, (c) CuDTA, and (d) CuZnDTA, not real colors;[25] TEM images for ZIF-8-ZnSO₄ (g), ZIF-8-Zn(NO₃)₂ (h), and ZIF-8-Zn(Ac)₂ (i) [23]. Ac=acetate.

MOFs, combining the favourable characteristics of heterogeneous and homogeneous catalysts, have been explored as a novel class of model catalytic materials for understanding the electrochemical CO₂ reduction.

The application of MOF-related catalysts for CO₂ electrochemical reduction started in 2012 [21], when a copper rubeanate metal-organic framework (CR-MOF) was prepared by Hinogami *et al.* to electrochemically reduce CO₂ into valuable products. With an onset potential of \sim 200 mV more positive than that of a Cu electrode in the aqueous electrolyte, formic acid (HCOOH) was virtually the only CO₂

reduction product (FE = ~100%), whereas various products were generated on a Cu electrode. The partial current of HCOOH by CR-MOF electrode was ~7.1 mA cm⁻², which was also higher than for the Cu electrode.

Kumar *et al.*, also in 2012, reported cyclic voltammetry (CV) studies in 0.1 M KCl of Cu-BTC films on glassy carbon electrodes [22]. Well-defined Cu(II)/Cu(I) and Cu(I)/Cu(0) reversible redox responses were observed. The MOF film was then studied as electrocatalyst in N,N-dimethylformamide (DMF). The production of oxalic acid was confirmed by GC-MS with a FE of ~51% and a total current density of 19 mA cm⁻².

Following these pioneering works, additional MOF-based catalysts have been investigated for CO₂ER. ZIF-8, an archetypical MOF material, was synthesized with various zinc sources by Wang *et al.* and used as electrocatalyst for CO₂ reduction to CO [23]. ZIF-8 prepared with ZnSO₄ delivered the best catalytic activity towards CO₂ electroreduction, with a FE towards CO (FE_{CO}) of 65% and a total current density (j_{Total}) of ~3 mA cm⁻², establishing a relation between the CO₂ER performance and synthetic zinc sources. The main catalytic active sites were claimed to be the discrete Zn nodes in ZIF-8.

Jiang *et al.* further identified the imidazolate ligands coordinated with the Zn(II) centre in ZIFs as the catalytic sites of ZIFs for CO₂ER with the help of in-situ X-ray absorption spectroscopy (XAS) measurements and density functional theory (DFT) calculations [24]. They investigated ZIFs with the same sodalite topology and different organic ligands, including ZIF-8, ZIF-108, ZIF-7, and SIM-1 for CO₂ER in aqueous electrolyte. ZIF-8 showed the highest FE_{CO} of 81.0% at -1.1 V vs. RHE among all the ZIF

catalysts, and the CO current density could reach as high as 12.8 mA cm⁻² at -1.3 V vs. RHE over ZIF-108.

The effect of the linker on CO₂ER was also investigated by Albo *et al.* [25] Four Cu-based MOFs, namely, 1) Cu-BTC (HKUST-1); 2) Copper(II) adeninate acetate (Cu-AdeAce); 3) Copper bisbidentate dithiooxamidate (Cu-DTA) mesoporous metal-organic aerogel (MOA); and 4) CuZn-DTA MOA, were synthesized and supported on gas diffusion electrodes. The MOF-based electrodes showed electrocatalytic efficiency for the production of methanol and ethanol in the liquid phase. The maximum cumulative FE for CO₂ conversion was measured at Cu-BTC based electrodes, which was 15.9 % at a current density of 10 mA cm⁻². It was demonstrated that MOFs with coordinately unsaturated metal sites were favourable for the enhancement of the electrocatalytic reduction of CO₂ to alcohols. Furthermore, Cu-BTC based electrodes showed stable electrocatalytic performance for 17 h.

In addition to the structural effect, the linker of MOFs can also be functionalized to boost the catalytic activity. The poor conductivity of MOFs largely hinders their direct application as electrocatalysts, thus, Dou *et al.* reported a general strategy of ligand doping to enhance charge transfer, thereby improving the electrocatalytic activity [26]. A strong electron-donating molecule, 1,10-phenanthroline, was introduced into ZIF-8 as CO₂ reduction electrocatalyst. Experimental and theoretical results suggested that the electron-donating nature of phenanthroline enabled charge transfer, which facilitated the generation of •COOH. As a consequence, the ligand-doped ZIF-8 showed an FE_{CO} of 90% and a j_{Total} of 10.1 mA cm⁻², both significantly improved compared with pristine ZIF-8.

Ye *et al.* deposited a highly oriented monolithic Re-based MOF thin film onto a conductive fluorine-doped tin oxide (FTO) electrode using liquid-phase epitaxy [27]. The MOF film was grown exclusively along the [001] direction, and exhibited a high FE_{CO} of $\sim 93\%$ when operated as an electrocatalyst for the reduction of CO_2 , with a current density exceeding 2 mA cm^{-2} .

As discussed above, the overpotential is one of the key issues which needs to be addressed in CO_2ER . A combination of ionic liquids (ILs) as the electrolyte and Zn-BTC as the catalyst was applied by Kang *et al.* as a strategy to lower overpotentials in CO_2ER [28], which was the first work combining a MOF electrode and pure IL electrolyte in this field. The Zn-BTC electrode showed a higher selectivity to CH_4 ($>80\%$) and higher current density (3 mA cm^{-2}) at mild overpotentials (250 mV), than the commonly used metal electrodes.

1.3.2. MOFs as Active Phase Supports

In addition to the direct application as electrocatalysts, the unique textural properties of MOFs also offer a number of opportunities for their application as active phase supports for CO_2ER .

Porphyrin-based molecular catalysts have been widely used in CO_2ER [47]. The significance of molecular catalyst immobilization was highlighted by Hu *et al.* by comparing the performance of cobalt meso-tetraphenylporphyrin (CoTPP) in CO_2ER under both supported and unsupported conditions [48]. CoTPP performed poorly as a homogeneous electrocatalyst giving low product selectivity at a high overpotential, while a remarkable catalytic activity enhancement was seen with CO_2 selectively forming CO ($> 90\%$) at a low overpotential upon directly immobilizing

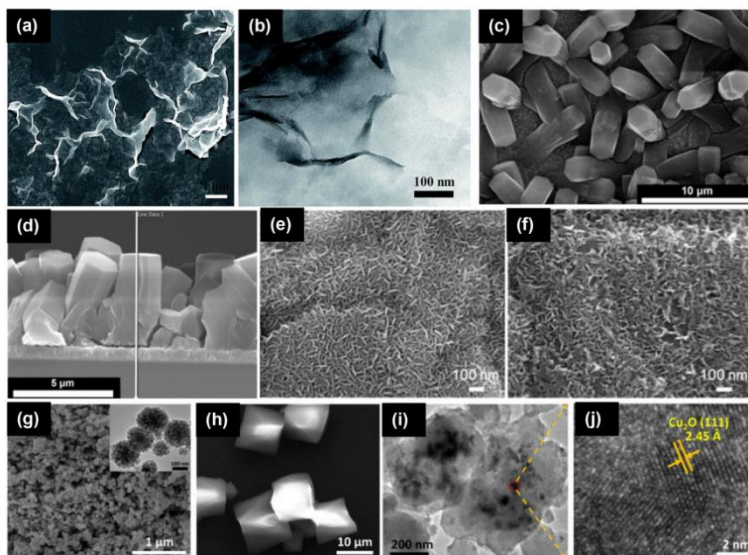


Figure 1.2. Representative electron micrograph of using MOF as catalyst supports. (a) SEM image and (b) TEM image of Cu₂(CuTCCP) nanosheets; [31] Top-view SEM images (c) and cross-sectional SEM image (d) of the Cu-SIM NU-1000 thin film; [34] SEM images of the MOF catalyst film before (e) and after electrolysis (f) revealing the retention of the plate-like morphology; [32] (g) SEM and TEM (inset in g) images of Cu₂O spheres, (h) SEM image of Cu-MOF, (i) TEM and (j) HRTEM images of Cu₂O@Cu-MOF after reacting for 12 h [35].

CoTPP onto carbon nanotubes. Kramer *et al.* demonstrated that the immobilization agent had an effect on the molecular catalyst's performance by comparing the CO₂ER activity of cobalt phthalocyanine (CoPc) supported on edge-plane graphite and poly-4-vinylpyridine (P4VP) thin films [49]. CoPc embedded in P4VP matrix displayed improved FE_{CO} and turnover frequency, which was attributed to the chemical coordination environment provided by the P4VP polymer matrix.

Hod *et al.* used Fe-porphyrin as CO₂ reduction catalyst, which was incorporated into MOF-525 as both a structural and functional element [29]. MOF-525 was first deposited onto a conductive indium tin oxide (ITO)

substrate, and then Fe-porphyrin was formed via a post-metalation strategy. The approach yielded a high surface coverage of electrochemically addressable Fe-porphyrin sites (~ 1015 sites cm^{-2}), forming a mixture of CO and H_2 in roughly equal amounts ($FE_{\text{CO}} = \sim 50\%$) as products with a j_{Total} of ~ 6 mA cm^{-2} . In spite of the low FE of CO_2ER , these results demonstrated that porphyrins can be electrochemically accessed when incorporated into a MOF structure.

Electroactive porphyrins can also be used as ligands to form MOFs. Dong *et al.* rationally introduced a Fe-TCPP porphyrin to form PCN-222(Fe) as CO_2ER catalyst [30]. After dip-coating onto carbon substrate, the composite catalyst PCN-222(Fe)/C (mass ratio = 1:2) exhibited a maximum 91% FE_{CO} with 494 mV overpotential (where $j_{\text{Total}} = 1.2$ mA cm^{-2}) in an aqueous solution, achieving a TOF of 0.336 $\text{site}^{-1} \text{ s}^{-1}$. The catalyst was found to retain its crystallinity and stability after 10 h of electrolysis at -0.60 V versus RHE (average $FE_{\text{CO}} = 80.4\%$).

Wu *et al.* used porphyrinic MOF nanosheets for CO_2ER [31]. The $\text{Cu}_2(\text{CuTCPP})$ nanosheets were cathodized on FTO glasses, and exhibited significant activity for formate production with a FE of 68.4% at -1.55 V vs. Ag/Ag^+ . Moreover, the C–C coupling product acetate was also generated from the same catalyst at a voltage range of $1.40 - 1.65$ V with the total liquid product FE of $38.8 - 85.2\%$. Characterization results showed the instability of $\text{Cu}_2(\text{CuTCPP})$, with Cu(II) being transformed into CuO, Cu_2O and Cu_4O_3 , which significantly catalyzed CO_2 to formate and acetate.

Kornienko *et al.* employed an aluminium porphyrin-based MOF-55 [32], comprising cobalt porphyrin active sites, for the electrocatalytic reduction of CO_2 to CO. An aluminium oxide thin film was first deposited via atomic

layer deposition (ALD) as metal precursor, followed by subsequent MOF formation through the reaction of the coated aluminium oxide with the linker under solvothermal conditions. The thickness of the precursor could easily be controlled by the number of ALD cycles, thereby controlling the thickness of catalyst layers. The performance of the resulting MOF catalyst initially improved with increasing film thickness until reaching a maximum of $\sim 2.8 \text{ mA cm}^{-2}$, and the appearance of maximum performance possibly indicated a trade-off between electron and mass transport. The optimized catalyst thickness exhibited a FE_{CO} production of up to 76 % in a 7 h test.

In addition to molecular catalysts, MOFs have also been used for supporting metal nanoparticles in CO₂ER. Jiang *et al.* reported the construction of Ag₂O/layered ZIF composite structure by mixing pre-synthesized layered ZIF-7 with AgNO₃ aqueous solution, followed by refluxing at 100 °C [33]. Ag₂O/layered ZIF composite showed much higher FE_{CO} ($\sim 80 \%$) and j_{CO} ($\sim 32 \text{ mA cm}^{-2}$) than the layered ZIF or Ag/C alone. The performance enhancement was attributed to the synergistic effect between Ag₂O nanoparticles and the layered ZIF, as well as the facilitated mass transport by the high specific surface area of Ag₂O/layered ZIF.

Kung *et al.* embedded copper nanoparticles into a thin film of NU-1000 [34], by first installing single-site Cu(II) into the NU-1000 thin film followed by electrochemical reduction of Cu(II) to metallic Cu. The obtained Cu nanoparticles were electrochemically addressable and exhibited a moderate electrocatalytic activity with a maximum FE towards HCOO⁻ of 28 % and -1.2 mA cm^{-2} at -0.82 V vs. RHE . Both the crystallinity and morphology of the thin film remained unchanged after electrocatalysis. The authors also found that the particle sizes were largely dependent on the pore

size of the MOF, which might offer an opportunity to achieve tunable catalyst sizes through this pore confinement effect of MOFs.

In a recent study, Tan *et al.* reported a tailor-made Cu₂O@Cu-MOF electrocatalyst [35] by in-situ etching Cu₂O spheres with H₃BTC to form a Cu-MOF shell. The as-prepared electrocatalyst resulted in an intriguing performance towards the formation of hydrocarbons from CO₂, with a high FE towards CH₄ and C₂H₄ of 79.4%, particularly, the FE of CH₄ as high as 63.2% at -1.71 V vs RHE.

1.3.3. MOFs as Electrocatalyst Precursors

Although quite a few works using MOFs directly as catalysts claimed that the MOF catalysts showed good stability during test, a lot of them failed to conduct post-reaction analysis to confirm these statements [50]. Indeed, stability is a serious issue for MOFs, especially under the highly negative potentials usually applied in CO₂ER. These potentials are more negative than the reduction potential of many metals used in MOF synthesis (see Table 1.2). In this spirit, using a MOF as catalyst precursor can be a favourable way to produce a stable and efficient catalyst.

The decomposition of MOFs under controlled conditions usually leads to the clustering of its metal component into small nanoparticles. Zhao *et al.* synthesized oxide-derived Cu/carbon (OD Cu/C) catalysts by facile carbonization of Cu-BTC MOF (HKUST-1) [36]. The resulting materials exhibited highly selective CO₂ reduction to alcohols with total FE of 71.2% at -0.7 V vs. RHE. High yields to methanol and ethanol were achieved on OD Cu/C-1000 with the peak production rates of 12.4 mg L⁻¹ h⁻¹ at -0.3V and 13.4 mg L⁻¹ h⁻¹ at -0.7V, respectively. Notably, the onset potential for

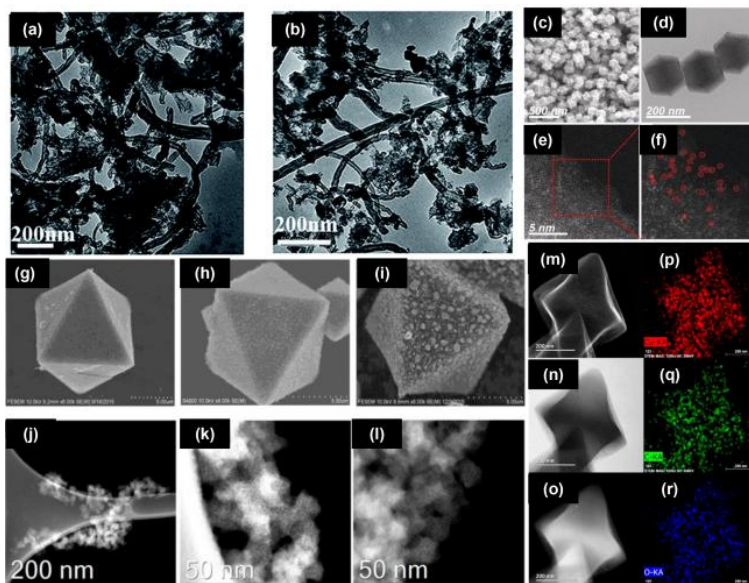


Figure 1.3. Representative electron micrograph of using MOF as catalyst precursors. TEM images of (a) ZIF-CNT-FA-p, and (b) ZIF-Fe-CNT-FA-p;[46] (c) SEM and (d) TEM images of N-coordinated Co. (e-f) Magnified high-angle annular dark-field-scanning transmission electron microscopy (HAADF-STEM) images of N-coordinated Co showing the atomic dispersion of Co atoms;[42] (g-i) SEM images of the OD-Cu/C processed with different temperature;[36] The HAADF-STEM images of (j-l) Fe-N-C;[40] Structural investigations of as-fabricated HKUST-1 by (m) SEM, (n) TEM bright field image, (o) TEM HAADF, and (p-r) TEM EDS [41].

C₂H₅OH formation was among the lowest overpotentials reported to date for the CO₂ reduction to C₂H₅OH. The improvement in activity and selectivity of the oxide-derived Cu/carbon were attributed to the synergistic effect between the highly dispersed copper and the matrix of porous carbon.

Kim *et al.* used an electrochemical reduction strategy to decompose MOFs [37], obtaining an efficient electrocatalyst for the synthesis of CH₄. Cu-based MOF-74 was chosen as the precursor, which was electrochemically reduced to Cu nanoparticles (NPs). The porous structure

Table 1.2. Standard electrode potentials of common metal nodes in MOFs [51].

Half reaction	Potential (V vs. RHE)
$\text{Co}^{3+} + \text{e}^- \rightleftharpoons \text{Co}^{2+}$	1.82
$\text{Ag}^+ + \text{e}^- \rightleftharpoons \text{Ag}$	0.8
$\text{Fe}^{3+} + \text{e}^- \rightleftharpoons \text{Fe}^{2+}$	0.77
$\text{Cu}^+ + \text{e}^- \rightleftharpoons \text{Cu}$	0.52
$\text{O}_2 + 2\text{H}_2\text{O} + 4\text{e}^- \rightleftharpoons 4\text{OH}^-$	0.4
$\text{Cu}^{2+} + 2\text{e}^- \rightleftharpoons \text{Cu}$	0.34
$\text{Cu}^{2+} + \text{e}^- \rightleftharpoons \text{Cu}^+$	0.15
$2\text{H}^+ + 2\text{e}^- \rightleftharpoons \text{H}_2$	0
$\text{Fe}^{3+} + 3\text{e}^- \rightleftharpoons \text{Fe}$	-0.04
$\text{Ni}^{2+} + 2\text{e}^- \rightleftharpoons \text{Ni}$	-0.25
$\text{Co}^{2+} + 2\text{e}^- \rightleftharpoons \text{Co}$	-0.29
$\text{Fe}^{2+} + 2\text{e}^- \rightleftharpoons \text{Fe}$	-0.41
$\text{Cr}^{3+} + \text{e}^- \rightleftharpoons \text{Cr}^{2+}$	-0.42
$\text{Cr}^{3+} + 3\text{e}^- \rightleftharpoons \text{Cr}$	-0.74
$\text{Zn}^{2+} + 2\text{e}^- \rightleftharpoons \text{Zn}$	-0.76
$\text{Ti}^{3+} + 3\text{e}^- \rightleftharpoons \text{Ti}$	-1.37
$\text{Zr}^{4+} + 4\text{e}^- \rightleftharpoons \text{Zr}$	-1.45
$\text{Ti}^{2+} + 2\text{e}^- \rightleftharpoons \text{Ti}$	-1.63
$\text{Al}^{3+} + 3\text{e}^- \rightleftharpoons \text{Al}$	-1.66

of the MOF serves as a template for the synthesis of isolated Cu NPs with high current densities and high FE towards CH₄ in the electrochemical CO₂ reduction reaction. The MOF-derived Cu NPs resulted in a FE_{CH₄} >50% and a 2.3-fold higher current density at -1.3 V vs. RHE than commercially available Cu NPs.

Besides metal nanoparticles, MOF-mediated synthesis can also act as a method to generate isolated metal-nitrogen sites with high exposure of active sites for efficient catalysis. Ye *et al.* fabricated isolated iron-nitrogen sites, located on the surface of carbon matrix, through the pyrolysis of ammonium ferric citrate (AFC)/ZIF-8 composites [38]. The AFC/ZIF-8 composite was synthesized by reacting the Zn precursor solution, in which the AFC was also dissolved, with 2-methylimidazole solution, followed by cleaning, centrifuging, and drying. The highly exposed iron-nitrogen sites demonstrated high selectivity to CO (peak $FE_{CO} = 93\%$) and high activity ($j_{CO} = 9.5\text{ mA cm}^{-2}$).

Zhao *et al.* adopted Ni ion exchanged ZIF-8 to assist the preparation of a catalyst containing single Ni sites for efficient CO₂ electroreduction [39]. The synthesis was based on an inexpensive ionic exchange between Zn nodes and adsorbed Ni ions within the cavities of the MOF, which was followed by pyrolysis of the ion-exchanged MOF. This single-atom catalyst exhibited an outstanding turnover frequency for CO₂ electroreduction (5273 h⁻¹), with a FE_{CO} of over 71.9% and a j_{Total} of 10.48 mA cm⁻² at an overpotential of 890 mV.

Pan *et al.* studied the reactivity and structure of atomically dispersed M-N₄ (M = Fe and Co) single sites in CO₂ER. Nitrogen coordinated Fe or Co single site atomically dispersed into a carbon matrix (M-N-C) were prepared

by using MOF precursors which were further studied as model catalysts [40]. Fe was intrinsically more active than Co in M-N₄ for the reduction of CO₂ to CO, in terms of a higher FE_{CO} (93% vs. 45%) and current density. First principle computations elucidated that the M-N₂₊₂-C₈ moieties, which were distributed at the edge of carbon matrix and bridged two adjacent armchair-like graphitic layers, were the active sites for the CO₂ER.

Selectivity is one of the key issues faced by CO₂ER, especially when Cu-based catalysts are used. Nam *et al.* reported a strategy involving MOF-regulated Cu cluster formation that shifted CO₂ electroreduction with Cu based catalysts towards multiple-carbon products [41]. The symmetric paddle-wheel Cu dimer secondary building block of HKUST-1 was distorted to an asymmetric motif by separating adjacent benzene tricarboxylate moieties using thermal treatment. By varying materials processing conditions, the asymmetric local atomic structure, oxidation state and bonding strain of Cu dimers were modulated. The formation of Cu clusters with low coordination numbers from distorted Cu dimers in HKUST-1 was observed during CO₂ electroreduction, leading to a FE towards C₂H₄ of 45%. The enhanced performance was closely related to maintaining a low Cu-Cu coordination number among the Cu clusters during the reaction.

Another example of regulating coordination number to tune the selectivity was reported by Wang *et al.* [42]. A series of atomically dispersed Co catalysts with different nitrogen coordination numbers were prepared for the CO₂ER. The best catalyst, atomically dispersed Co with two-coordinate nitrogen atoms, achieved both high selectivity ($FE_{CO} = 94\%$) and superior activity ($j_{Total} = 18.1 \text{ mAcm}^{-2}$) at an overpotential of 520 mV.

The CO formation turnover frequency reached a record value of 18200 h⁻¹. These results demonstrated that lower a coordination number facilitated activation of CO₂ to the •COO⁻ intermediate and hence enhanced CO₂ER activity.

Very recently, Guo *et al.* introduced a new method to tune the CO₂ER selectivity via MOF-derived bimetallic oxide catalyst [43]. MOF-derived In-Cu bimetallic oxides were synthesized by pyrolysis of a Cu-In bimetallic MOF. By controlling In-Cu ratios, the FE_{CO} could reach 92.1%, along with a j_{Total} of 11.2 mA cm⁻². The excellent performance was mainly attributed to stronger CO₂ adsorption, higher electrochemical surface area and lower charge transfer resistance by the bimetallic catalyst.

Besides metal-based catalysts, a carbon-rich organic linker, combined with the low-boiling point of some metal nodes, such as Zn, make MOFs a promising precursor to produce carbon-based electrocatalysts [52]. Following this strategy, Wang *et al.* synthesized a nitrogen-doped carbon (NC), through the pyrolysis of the well-known metal-organic framework ZIF-8 [44]. The resulting NC-based CO₂ER electrode showed a FE_{CO} as high as ~78%. It was also found that the pyrolysis temperature determined the amount and the accessibility of N species in the carbon electrode, in which pyridinic-N and quaternary-N species played key roles in the selective formation of CO. Generally the materials derived from Zn-based ZIFs are nothing less than nitrogen containing carbons and are active without other metal addition. Therefore it should be kept in mind to benchmark their performance against those materials prepared via other routes [53].

The pyrolysis temperature effect and the mechanism in the ZIF-8-derived NC was further studied by Zheng *et al.* [45]. NC catalysts were prepared by decomposing ZIF-8 at different temperatures in argon. The catalytic performances showed that the higher pyrolysis temperature resulted in a better CO₂ER activity. The NC catalyst with the best performance achieved high selectivity with 95.4 % FE_{CO} at -0.5 V vs. RHE. The catalyst also maintained stability during 20 h operation, after which the FE_{CO} was still greater than 90%. The experiments showed that a higher pyrolysis temperature reduced the total nitrogen contents but changed the nature and density of N-species. DFT calculations revealed that higher pyrolysis temperature led to enhanced activity by promoting the formation of pyridinic N, which provided more efficient active sites.

To relieve the electron transportation limit with MOF-mediated approach, Guo *et al.* synthesized a composite material by co-pyrolysis of in-situ grown ZIF-8 on multi-walled carbon nanotubes (MWCNTs) substrate [46]. This composite could selectively catalyze the electrochemical reduction of CO₂ to CO in aqueous solution with ~100 % FE and a current density up to 7.7 mA cm⁻² at an overpotential of 740 mV. By comparison, the pyrolyzed ZIF-8 without MWCNT only showed a FE_{CO} of ~50%. Addition of Fe to the ZIF could lower the overpotential, but also changed the selectivity. The MWCNT support was crucial to achieving superior efficiency, by enhancing electron transport through the MWCNT network and simultaneously expediting the CO₂ transport in the mesoporous structure constructed by the MWCNTs.

1.4. CONCLUDING REMARKS

CO₂ER is widely regarded as one of the most promising technologies to solve the CO₂ emission issue, though it is still faced by several challenges on the path towards commercialization. In this work, we have summarized recent works on CO₂ electroreduction with MOFs and MOF mediated catalysts. Generally speaking, the main advantages of MOFs in CO₂ER originate from their unique textural and structural properties. When MOFs are used directly as catalysts for CO₂ER, the atomically dispersed metal nodes can offer highly active sites, and the organic linkers can also be modified into catalytic sites or charge transfer agents. The porous structure, put up by the metal nodes and organic linkers, makes catalytic sites more accessible to CO₂ either if catalysis takes place on the MOF itself or on supported species. Moreover, the compatibility of MOFs with ILs facilitates their application in this medium. The use of MOFs as catalyst precursors usually leads to highly dispersed metal particles or carbon-based catalysts, maximizing catalyst utilization. The homogeneously dispersed metal sites can be inherited by the MOF-derived catalysts to form efficient single-site catalysts with unprecedented TOFs. And the highly tunable building blocks of MOFs enable the formation of bi-metallic structures, providing a facile route to the synthesis of metal alloys, opening the door to breaking scaling relationships in CO₂ER [10].

Although remarkable results have been reported with MOF-related catalysts, there are still issues that need to be carefully addressed in future research. Stability is one of the most concerning issues for CO₂ER. While most authors have claimed that pristine MOFs based on easily reducible metals are stable under reaction conditions, the catalyst stability has only

been confirmed in a few cases by post-analysis characterization [30, 32, 34-35]. Here, we would like to clarify that stability of the crystalline MOF does not necessarily need to be an issue. Indeed, from an application point of view, electrochemical reduction of MOFs to form small metal nanoparticles may render very interesting catalytic systems. However, as scientists, we should make sure that we do not jump into wrong conclusions by attributing the observed catalytic performance to the MOF scaffold.

As it is the case in thermal catalysis, probably the most exciting results in terms of performance have been reported for MOF-derived catalysts [7a, 54]. We believe that this route offers great possibilities for the further engineering of CO₂ER catalysts and for the optimization of metal use in catalysis, an aspect that may become critical if CO₂ electrolyzers are massively applied.

Last but not least, it is fair to admit that so far most catalytic results have been reported using aqueous electrolytes and semi-batch experiments, where only low current densities can be achieved due to the low solubility of CO₂ in the aqueous phase. We are sure that, as it is already happening for “traditional” electrocatalysts, MOF-derived systems will soon be tested under commercially more relevant conditions by making use of gas-diffusion electrochemical cells in which high current densities (>100 mA cm⁻²) have been achieved [55]. Through carbon capture technologies from point sources liquid CO₂ will become available at pressures exceeding 100 bar and solubility may not be limiting any more. Also aspects of molecular and electron transport require careful attention, as shown by Guo *et al.* [46].

Overall, we are confident that MOF-related catalysts engineering when combined with system integration of CO₂ER, will mark a substantial contribution to the field of electrocatalytic CO₂ reduction.

1.5. ABBREVIATIONS

BMIM	1-butyl-3-methylimidazolium
BTC	Benzene-1,3,5-Tricarboxylate
CN	Coordination Number
CR-MOF	Copper Rubeanate Metal-Organic Framework
EMIM	1-ethyl-3-methylimidazolium
FE	Faradaic Efficiency
HER	Hydrogen Evolution Reaction
MWCNT	Multi-walled Carbon Nanotube
NC	Nitrogen-doped Carbon
ORR	Oxygen Reduction Reaction
Pc	Phthalocynine
P4VP	Poly-4-vinylpyridine
PCN	Porous Coordination Network
RHE	Reversible Hydrogen Electrode
SHE	Standard Hydrogen Electrode
SIM	Substituted Imidazolate Material
TBAH	Tetrabutylammonium Hydroxide
TBATF ₆	Tetrabutylammonium Hexafluorophosphate
TBATFB	Tetrabutylammonium Tetrafluoroborate
TCPP	Tetrakis(4-carboxyphenyl)porphyrin

TFE	Trifluoroethanol
TOF	Turnover Frequency
ZIF	Zeolitic Imidazolate Framework

1.6. REFERENCES

1. Chen, C.; Kotyk, J. F. K.; Sheehan, S. W., Progress toward Commercial Application of Electrochemical Carbon Dioxide Reduction. *Chem* 2018, 4 (11), 2571-2586.
2. Dokania, A.; Ramirez, A.; Bavykina, A.; Gascon, J., Heterogeneous Catalysis for the Valorization of CO₂: Role of Bifunctional Processes in the Production of Chemicals. *ACS Energy Letters* 2019, 4 (1), 167-176.
3. Hori, Y. (2010). CO₂-reduction, catalyzed by metal electrodes. In *Handbook of Fuel Cells* (eds W. Vielstich, A. Lamm, H. A. Gasteiger and H. Yokokawa).
4. (a) Gao, D.; Cai, F.; Wang, G.; Bao, X., Nanostructured heterogeneous catalysts for electrochemical reduction of CO₂. *Current Opinion in Green and Sustainable Chemistry* 2017, 3, 39-44; (b) Ma, M.; Smith, W. A., Nanostructured Catalysts for the Electrochemical Reduction of CO₂. In *Anisotropic and Shape-Selective Nanomaterials: Structure-Property Relationships*, Hunyadi Murph, S. E.; Larsen, G. K.; Coopersmith, K. J., Eds. Springer International Publishing: Cham, 2017; pp 337-373; (c) Zhang, L.; Zhao, Z.-J.; Gong, J., Nanostructured Materials for Heterogeneous Electrocatalytic CO₂ Reduction and their Related Reaction Mechanisms. *Angewandte Chemie International Edition* 2017, 56 (38), 11326-11353.
5. (a) Corma, A.; García, H.; Llabrés i Xamena, F. X., Engineering Metal Organic Frameworks for Heterogeneous Catalysis. *Chemical Reviews* 2010, 110 (8), 4606-4655; (b) Czaja, A. U.; Trukhan, N.; Müller, U., Industrial applications of metal-organic frameworks. *Chemical Society Reviews* 2009, 38 (5), 1284-1293; (c) Dhakshinamoorthy, A.; Garcia, H., Catalysis by metal nanoparticles embedded on metal-organic frameworks. *Chemical Society Reviews* 2012, 41 (15), 5262-5284; (d) Farrusseng, D.; Aguado, S.; Pinel, C., Metal-Organic Frameworks: Opportunities for Catalysis. *Angewandte Chemie International Edition* 2009, 48 (41), 7502-7513; (e) Feng, D.; Gu, Z.-Y.; Li, J.-R.; Jiang, H.-L.; Wei, Z.; Zhou, H.-C., Zirconium-Metalloporphyrin PCN-222: Mesoporous Metal-Organic Frameworks with Ultrahigh Stability as Biomimetic Catalysts. *Angewandte Chemie International Edition* 2012, 51 (41), 10307-10310; (f) Furukawa, H.; Cordova, K. E.; O’Keeffe, M.; Yaghi, O. M., The Chemistry and Applications of Metal-Organic Frameworks. *Science* 2013, 341 (6149), 1230444; (g) James, S. L., Metal-organic frameworks. *Chemical Society*

Reviews 2003, 32 (5), 276-288; (h) Lee, J.; Farha, O. K.; Roberts, J.; Scheidt, K. A.; Nguyen, S. T.; Hupp, J. T., Metal–organic framework materials as catalysts. *Chemical Society Reviews* 2009, 38 (5), 1450-1459; (i) Liu, J.; Chen, L.; Cui, H.; Zhang, J.; Zhang, L.; Su, C.-Y., Applications of metal–organic frameworks in heterogeneous supramolecular catalysis. *Chemical Society Reviews* 2014, 43 (16), 6011-6061; (j) Liu, Y.; Xuan, W.; Cui, Y., Engineering Homochiral Metal–Organic Frameworks for Heterogeneous Asymmetric Catalysis and Enantioselective Separation. *Advanced Materials* 2010, 22 (37), 4112-4135; (k) Ma, L.; Falkowski, J. M.; Abney, C.; Lin, W., A series of isoreticular chiral metal–organic frameworks as a tunable platform for asymmetric catalysis. *Nature Chemistry* 2010, 2, 838; (l) Seo, J. S.; Whang, D.; Lee, H.; Jun, S. I.; Oh, J.; Jeon, Y. J.; Kim, K., A homochiral metal–organic porous material for enantioselective separation and catalysis. *Nature* 2000, 404 (6781), 982-986; (m) Wu, C.-D.; Hu, A.; Zhang, L.; Lin, W., A Homochiral Porous Metal–Organic Framework for Highly Enantioselective Heterogeneous Asymmetric Catalysis. *Journal of the American Chemical Society* 2005, 127 (25), 8940-8941; (n) Zhou, H.-C.; Long, J. R.; Yaghi, O. M., Introduction to Metal–Organic Frameworks. *Chemical Reviews* 2012, 112 (2), 673-674; (o) Alaerts, L.; Séguin, E.; Poelman, H.; Thibault-Starzyk, F.; Jacobs, P. A.; De Vos, D. E., Probing the Lewis Acidity and Catalytic Activity of the Metal–Organic Framework $[\text{Cu}_3(\text{btc})_2]$ (BTC=Benzen-1,3,5-tricarboxylate). *Chemistry – A European Journal* 2006, 12 (28), 7353-7363; (p) Alkordi, M. H.; Liu, Y.; Larsen, R. W.; Eubank, J. F.; Eddaoudi, M., Zeolite-like Metal–Organic Frameworks as Platforms for Applications: On Metalloporphyrin-Based Catalysts. *Journal of the American Chemical Society* 2008, 130 (38), 12639-12641; (q) Dang, D.; Wu, P.; He, C.; Xie, Z.; Duan, C., Homochiral Metal–Organic Frameworks for Heterogeneous Asymmetric Catalysis. *Journal of the American Chemical Society* 2010, 132 (41), 14321-14323; (r) Dhakshinamoorthy, A.; Alvaro, M.; Garcia, H., Metal–organic frameworks as heterogeneous catalysts for oxidation reactions. *Catalysis Science & Technology* 2011, 1 (6), 856-867; (s) Dhakshinamoorthy, A.; Alvaro, M.; Garcia, H., Commercial metal–organic frameworks as heterogeneous catalysts. *Chemical Communications* 2012, 48 (92), 11275-11288; (t) Dhakshinamoorthy, A.; Garcia, H., Metal–organic frameworks as solid catalysts for the synthesis of nitrogen-containing heterocycles. *Chemical Society Reviews* 2014, 43

- (16), 5750-5765; (u) Gascon, J.; Aktay, U.; Hernandez-Alonso, M. D.; van Klink, G. P. M.; Kapteijn, F., Amino-based metal-organic frameworks as stable, highly active basic catalysts. *Journal of Catalysis* 2009, 261 (1), 75-87; (v) Horike, S.; Dincă, M.; Tamaki, K.; Long, J. R., Size-Selective Lewis Acid Catalysis in a Microporous Metal-Organic Framework with Exposed Mn²⁺ Coordination Sites. *Journal of the American Chemical Society* 2008, 130 (18), 5854-5855.
6. (a) Gascon, J.; Corma, A.; Kapteijn, F.; Llabrés i Xamena, F. X., Metal Organic Framework Catalysis: Quo vadis? *ACS Catalysis* 2014, 4 (2), 361-378; (b) Rogge, S. M. J.; Bavykina, A.; Hajek, J.; Garcia, H.; Olivos-Suarez, A. I.; Sepúlveda-Escribano, A.; Vimont, A.; Clet, G.; Bazin, P.; Kapteijn, F.; Daturi, M.; Ramos-Fernandez, E. V.; Llabrés i Xamena, F. X.; Van Speybroeck, V.; Gascon, J., Metal-organic and covalent organic frameworks as single-site catalysts. *Chemical Society Reviews* 2017, 46 (11), 3134-3184.
7. (a) Oar-Arteta, L.; Wezendonk, T.; Sun, X.; Kapteijn, F.; Gascon, J., Metal organic frameworks as precursors for the manufacture of advanced catalytic materials. *Materials Chemistry Frontiers* 2017, 1 (9), 1709-1745; (b) Santos, V. P.; Wezendonk, T. A.; Jaén, J. J. D.; Dugulan, A. I.; Nasalevich, M. A.; Islam, H.-U.; Chojecki, A.; Sartipi, S.; Sun, X.; Hakeem, A. A.; Koeken, A. C. J.; Ruitenbeek, M.; Davidian, T.; Meima, G. R.; Sankar, G.; Kapteijn, F.; Makkee, M.; Gascon, J., Metal organic framework-mediated synthesis of highly active and stable Fischer-Tropsch catalysts. *Nature Communications* 2015, 6, 6451; (c) Sun, X.; Olivos-Suarez, A. I.; Oar-Arteta, L.; Rozhko, E.; Osadchii, D.; Bavykina, A.; Kapteijn, F.; Gascon, J., Metal-Organic Framework Mediated Cobalt/Nitrogen-Doped Carbon Hybrids as Efficient and Chemoselective Catalysts for the Hydrogenation of Nitroarenes. *ChemCatChem* 2017, 9 (10), 1854-1862; (d) Sun, X.; Suarez, A. I. O.; Meijerink, M.; van Deelen, T.; Ould-Chikh, S.; Zečević, J.; de Jong, K. P.; Kapteijn, F.; Gascon, J., Manufacture of highly loaded silica-supported cobalt Fischer-Tropsch catalysts from a metal organic framework. *Nature Communications* 2017, 8 (1), 1680.
8. Sun, X.; Olivos-Suarez, A. I.; Osadchii, D.; Romero, M. J. V.; Kapteijn, F.; Gascon, J., Single cobalt sites in mesoporous N-doped carbon matrix for selective catalytic hydrogenation of nitroarenes. *Journal of Catalysis* 2018, 357, 20-28.

9. Xia, W.; Mahmood, A.; Zou, R. Q.; Xu, Q., Metal-organic frameworks and their derived nanostructures for electrochemical energy storage and conversion. *Energy Environ Sci* 2015, 8 (7), 1837-1866.
10. Kortlever, R.; Shen, J.; Schouten, K. J.; Calle-Vallejo, F.; Koper, M. T., Catalysts and Reaction Pathways for the Electrochemical Reduction of Carbon Dioxide. *The journal of physical chemistry letters* 2015, 6 (20), 4073-82.
11. (a) Lu, Q.; Jiao, F., Electrochemical CO₂ reduction: Electrocatalyst, reaction mechanism, and process engineering. *Nano Energy* 2016, 29, 439-456; (b) Jhong, H. R.; Ma, S. C.; Kenis, P. J. A., Electrochemical conversion of CO₂ to useful chemicals: current status, remaining challenges, and future opportunities. *Current Opinion in Chemical Engineering* 2013, 2 (2), 191-199; (c) Jones, J.-P.; Prakash, G. K. S.; Olah, G. A., Electrochemical CO₂ Reduction: Recent Advances and Current Trends. *Israel Journal of Chemistry* 2014, 54 (10), 1451-1466; (d) Lu, X.; Wu, Y.; Yuan, X.; Huang, L.; Wu, Z.; Xuan, J.; Wang, Y.; Wang, H., High-Performance Electrochemical CO₂ Reduction Cells Based on Non-noble Metal Catalysts. *ACS Energy Letters* 2018, 3 (10), 2527-2532; (e) Liu, X.; Xiao, J.; Peng, H.; Hong, X.; Chan, K.; Nørskov, J. K., Understanding trends in electrochemical carbon dioxide reduction rates. *Nature Communications* 2017, 8, 15438.
12. (a) Gonen, S.; Elbaz, L., Metal organic frameworks as catalysts for oxygen reduction. *Current Opinion in Electrochemistry* 2018, 9, 179-188; (b) Kim, C.; Dionigi, F.; Beermann, V.; Wang, X.; Moller, T.; Strasser, P., Alloy Nanocatalysts for the Electrochemical Oxygen Reduction (ORR) and the Direct Electrochemical Carbon Dioxide Reduction Reaction (CO₂RR). *Adv Mater* 2018, e1805617; (c) Kim, Y.; Jo, A.; Ha, Y.; Lee, Y.; Lee, D.; Lee, Y.; Lee, C., Highly Dispersive Gold Nanoparticles on Carbon Black for Oxygen and Carbon Dioxide Reduction. *Electroanalysis* 2018, 30 (12), 2861-2868.
13. Mondal, B.; Sen, P.; Rana, A.; Saha, D.; Das, P.; Dey, A., Reduction of CO₂ to CO by an Iron Porphyrin Catalyst in the Presence of Oxygen. *ACS Catalysis* 2019, 9 (5), 3895-3899.
14. Rudnev, A. V.; Fu, Y. C.; Gjuroski, I.; Stricker, F.; Furrer, J.; Kovacs, N.; Vesztegom, S.; Broekmann, P., Transport Matters: Boosting CO₂ Electroreduction in Mixtures of

- [BMIm][BF₄]/Water by Enhanced Diffusion. *Chemphyschem* 2017, 18 (22), 3153-3162.
15. Han, L.; Zhou, W.; Xiang, C., High-Rate Electrochemical Reduction of Carbon Monoxide to Ethylene Using Cu-Nanoparticle-Based Gas Diffusion Electrodes. *ACS Energy Letters* 2018, 3 (4), 855-860.
 16. Rumayor, M.; Dominguez-Ramos, A.; Irabien, A., Environmental and economic assessment of the formic acid electrochemical manufacture using carbon dioxide: Influence of the electrode lifetime. *Sustainable Production and Consumption* 2019, 18, 72-82.
 17. Hori, Y.; Konishi, H.; Futamura, T.; Murata, A.; Koga, O.; Sakurai, H.; Oguma, K., "Deactivation of copper electrode" in electrochemical reduction of CO₂. *Electrochimica Acta* 2005, 50 (27), 5354-5369.
 18. (a) Won da, H.; Shin, H.; Koh, J.; Chung, J.; Lee, H. S.; Kim, H.; Woo, S. I., Highly Efficient, Selective, and Stable CO₂ Electroreduction on a Hexagonal Zn Catalyst. *Angew Chem Int Ed Engl* 2016, 55 (32), 9297-300; (b) Ma, M.; Liu, K.; Shen, J.; Kas, R.; Smith, W. A., In Situ Fabrication and Reactivation of Highly Selective and Stable Ag Catalysts for Electrochemical CO₂ Conversion. *ACS Energy Lett* 2018, 3 (6), 1301-1306; (c) Zhang, H.; Ma, Y.; Quan, F. J.; Huang, J. J.; Jia, F. L.; Zhang, L. Z., Selective electro-reduction of CO₂ to formate on nanostructured Bi from reduction of BiOCl nanosheets. *Electrochemistry Communications* 2014, 46, 63-66.
 19. Zhai, Y.; Chiachiarelli, L.; Sridhar, N., Effect of Gaseous Impurities on the Electrochemical Reduction of CO₂ on Copper Electrodes. *ECS Transactions* 2009, 19 (14), 1-13.
 20. (a) Lu, Q.; Rosen, J.; Jiao, F., Nanostructured Metallic Electrocatalysts for Carbon Dioxide Reduction. *Chemcatchem* 2015, 7 (1), 38-47; (b) He, J. F.; Huang, A. X.; Johnson, N. J. J.; Dettelbach, K. E.; Weekes, D. M.; Cao, Y.; Berlinguette, C. P., Stabilizing Copper for CO₂ Reduction in Low-Grade Electrolyte. *Inorganic Chemistry* 2018, 57 (23), 14624-14631.
 21. Hinogami, R.; Yotsuhashi, S.; Deguchi, M.; Zenitani, Y.; Hashiba, H.; Yamada, Y., Electrochemical Reduction of Carbon Dioxide Using a Copper Rubeanate Metal Organic Framework. *Ecs Electrochemistry Letters* 2012, 1 (4), H17-H19.

22. Kumar, R. S.; Kumar, S. S.; Kulandainathan, M. A., Highly selective electrochemical reduction of carbon dioxide using Cu based metal organic framework as an electrocatalyst. *Electrochemistry Communications* 2012, 25, 70-73.
23. Wang, Y. L.; Hou, P. F.; Wang, Z.; Kang, P., Zinc Imidazolate Metal-Organic Frameworks (ZIF-8) for Electrochemical Reduction of CO₂ to CO. *Chemphyschem* 2017, 18 (22), 3142-3147.
24. Jiang, X. L.; Li, H. B.; Xiao, J. P.; Gao, D. F.; Si, R.; Yang, F.; Li, Y. S.; Wang, G. X.; Bao, X. H., Carbon dioxide electroreduction over imidazolate ligands coordinated with Zn(II) center in ZIFs. *Nano Energy* 2018, 52, 345-350.
25. Albo, J.; Vallejo, D.; Beobide, G.; Castillo, O.; Castano, P.; Irabien, A., Copper-Based Metal-Organic Porous Materials for CO₂ Electrocatalytic Reduction to Alcohols. *ChemSusChem* 2017, 10 (6), 1100-1109.
26. Dou, S.; Song, J. J.; Xi, S. B.; Du, Y. H.; Wang, J.; Huang, Z. F.; Xu, Z. C. J.; Wang, X., Boosting Electrochemical CO₂ Reduction on Metal-Organic Frameworks via Ligand Doping. *Angew Chem Int Edit* 2019, 58 (12), 4041-4045.
27. Ye, L.; Liu, J.; Gao, Y.; Gong, C.; Addicoat, M.; Heine, T.; Wöll, C.; Sun, L., Highly oriented MOF thin film-based electrocatalytic device for the reduction of CO₂ to CO exhibiting high faradaic efficiency. *Journal of Materials Chemistry A* 2016, 4 (40), 15320-15326.
28. Kang, X.; Zhu, Q.; Sun, X.; Hu, J.; Zhang, J.; Liu, Z.; Han, B., Highly efficient electrochemical reduction of CO₂ to CH₄ in an ionic liquid using a metal-organic framework cathode. *Chem Sci* 2016, 7 (1), 266-273.
29. Hod, I.; Sampson, M. D.; Deria, P.; Kubiak, C. P.; Farha, O. K.; Hupp, J. T., Fe-Porphyrin-Based Metal-Organic Framework Films as High-Surface Concentration, Heterogeneous Catalysts for Electrochemical Reduction of CO₂. *Acs Catalysis* 2015, 5 (11), 6302-6309.
30. Dong, B.-X.; Qian, S.-L.; Bu, F.-Y.; Wu, Y.-C.; Feng, L.-G.; Teng, Y.-L.; Liu, W.-L.; Li, Z.-W., Electrochemical Reduction of CO₂ to CO by a Heterogeneous Catalyst of Fe-Porphyrin-Based Metal-Organic Framework. *ACS Applied Energy Materials* 2018, 1 (9), 4662-4669.
31. Wu, J. X.; Hou, S. Z.; Zhang, X. D.; Xu, M.; Yang, H. F.; Cao, P. S.; Gu, Z. Y., Cathodized copper porphyrin metal-organic framework nanosheets for selective

- formate and acetate production from CO₂ electroreduction. *Chemical Science* 2019, 10 (7), 2199-2205.
32. Kornienko, N.; Zhao, Y.; Kley, C. S.; Zhu, C.; Kim, D.; Lin, S.; Chang, C. J.; Yaghi, O. M.; Yang, P., Metal-organic frameworks for electrocatalytic reduction of carbon dioxide. *J Am Chem Soc* 2015, 137 (44), 14129-35.
 33. Jiang, X. L.; Wu, H. H.; Chang, S. J.; Si, R.; Miao, S.; Huang, W. X.; Li, Y. H.; Wang, G. X.; Bao, X. H., Boosting CO₂ electroreduction over layered zeolitic imidazolate frameworks decorated with Ag₂O nanoparticles. *Journal of Materials Chemistry A* 2017, 5 (36), 19371-19377.
 34. Kung, C. W.; Audu, C. O.; Peters, A. W.; Noh, H.; Farha, O. K.; Hupp, J. T., Copper Nanoparticles Installed in Metal-Organic Framework Thin Films are Electrocatalytically Competent for CO₂ Reduction. *Acs Energy Letters* 2017, 2 (10), 2394-2401.
 35. Tan, X. Y.; Yu, C.; Zhao, C. T.; Huang, H. W.; Yao, X. C.; Han, X. T.; Guo, W.; Cui, S.; Huang, H. L.; Qiu, J. S., Restructuring of Cu₂O to Cu₂O@Cu-Metal-Organic Frameworks for Selective Electrochemical Reduction of CO₂. *Acs Applied Materials & Interfaces* 2019, 11 (10), 9904-9910.
 36. Zhao, K.; Liu, Y. M.; Quan, X.; Chen, S.; Yu, H. T., CO₂ Electroreduction at Low Overpotential on Oxide-Derived Cu/Carbons Fabricated from Metal Organic Framework. *Acs Applied Materials & Interfaces* 2017, 9 (6), 5302-5311.
 37. Kim, M. K.; Kim, H. J.; Lim, H.; Kwon, Y.; Jeong, H. M., Metal-organic framework-mediated strategy for enhanced methane production on copper nanoparticles in electrochemical CO₂ reduction. *Electrochimica Acta* 2019, 306, 28-34.
 38. Ye, Y. F.; Cai, F.; Li, H. B.; Wu, H. H.; Wang, G. X.; Li, Y. S.; Miao, S.; Xie, S. H.; Si, R.; Wang, J.; Bao, X. H., Surface functionalization of ZIF-8 with ammonium ferric citrate toward high exposure of Fe-N active sites for efficient oxygen and carbon dioxide electroreduction. *Nano Energy* 2017, 38, 281-289.
 39. Zhao, C. M.; Dai, X. Y.; Yao, T.; Chen, W. X.; Wang, X. Q.; Wang, J.; Yang, J.; Wei, S. Q.; Wu, Y. E.; Li, Y. D., Ionic Exchange of Metal Organic Frameworks to Access Single Nickel Sites for Efficient Electroreduction of CO₂. *Journal of the American Chemical Society* 2017, 139 (24), 8078-8081.

40. Pan, F. P.; Zhang, H. G.; Liu, K. X.; Cullen, D.; More, K.; Wang, M. Y.; Feng, Z. X.; Wang, G. F.; Wu, G.; Li, Y., Unveiling Active Sites of CO₂ Reduction on Nitrogen-Coordinated and Atomically Dispersed Iron and Cobalt Catalysts. *Acs Catalysis* 2018, 8 (4), 3116-3122.
41. Nam, D. H.; Bushuyev, O. S.; Li, J.; De Luna, P.; Seifitokaldani, A.; Dinh, C. T.; de Arquer, F. P. G.; Wang, Y. H.; Liang, Z. Q.; Proppe, A. H.; Tan, C. S.; Todorovic, P.; Shekiah, O.; Gabardo, C. M.; Jo, J. W.; Choi, J. M.; Choi, M. J.; Baek, S. W.; Kim, J.; Sinton, D.; Kelley, S. O.; Eddaoudi, M.; Sargent, E. H., Metal-Organic Frameworks Mediate Cu Coordination for Selective CO₂ Electroreduction. *Journal of the American Chemical Society* 2018, 140 (36), 11378-11386.
42. Wang, X. Q.; Chen, Z.; Zhao, X. Y.; Yao, T.; Chen, W. X.; You, R.; Zhao, C. M.; Wu, G.; Wang, J.; Huang, W. X.; Yang, J. L.; Hong, X.; Wei, S. Q.; Wu, Y.; Li, Y. D., Regulation of Coordination Number over Single Co Sites: Triggering the Efficient Electroreduction of CO₂. *Angew Chem Int Edit* 2018, 57 (7), 1944-1948.
43. Guo, W. W.; Sun, X. F.; Chen, C. J.; Yang, D. X.; Lu, L.; Yang, Y. D.; Han, B. X., Metal-organic framework-derived indium-copper bimetallic oxide catalysts for selective aqueous electroreduction of CO₂. *Green Chemistry* 2019, 21 (3), 503-508.
44. Wang, R.; Sun, X.; Ould-Chikh, S.; Osadchii, D.; Bai, F.; Kapteijn, F.; Gascon, J., Metal-Organic-Framework-Mediated Nitrogen-Doped Carbon for CO₂ Electrochemical Reduction. *ACS Applied Materials & Interfaces* 2018, 10 (17), 14751-14758.
45. Zheng, Y.; Cheng, P.; Xu, J.; Han, J.; Wang, D.; Hao, C.; Alanagh, H. R.; Long, C.; Shi, X.; Tang, Z., MOF-derived nitrogen-doped nanoporous carbon for electroreduction of CO₂ to CO: the calcining temperature effect and the mechanism. *Nanoscale* 2019, 11 (11), 4911-4917.
46. Guo, Y.; Yang, H. J.; Zhou, X.; Liu, K. L.; Zhang, C.; Zhou, Z. Y.; Wang, C.; Lin, W. B., Electrocatalytic reduction of CO₂ to CO with 100% faradaic efficiency by using pyrolyzed zeolitic imidazolate frameworks supported on carbon nanotube networks. *Journal of Materials Chemistry A* 2017, 5 (47), 24867-24873.
47. (a) Weng, Z.; Jiang, J.; Wu, Y.; Wu, Z.; Guo, X.; Materna, K. L.; Liu, W.; Batista, V. S.; Brudvig, G. W.; Wang, H., Electrochemical CO₂ Reduction to Hydrocarbons on a Heterogeneous Molecular Cu Catalyst in Aqueous Solution. *J Am Chem Soc* 2016,

- 138 (26), 8076-9; (b) Zhu, G.; Li, Y.; Zhu, H.; Su, H.; Chan, S. H.; Sun, Q., Curvature-Dependent Selectivity of CO₂ Electrocatalytic Reduction on Cobalt Porphyrin Nanotubes. *ACS Catalysis* 2016, 6 (9), 6294-6301; (c) Lin, S.; Diercks, C. S.; Zhang, Y.-B.; Kornienko, N.; Nichols, E. M.; Zhao, Y.; Paris, A. R.; Kim, D.; Yang, P.; Yaghi, O. M.; Chang, C. J., Covalent organic frameworks comprising cobalt porphyrins for catalytic CO₂ reduction in water. *Science* 2015, 349 (6253), 1208-1213.
48. Hu, X. M.; Ronne, M. H.; Pedersen, S. U.; Skrydstrup, T.; Daasbjerg, K., Enhanced Catalytic Activity of Cobalt Porphyrin in CO₂ Electroreduction upon Immobilization on Carbon Materials. *Angew Chem Int Ed Engl* 2017, 56 (23), 6468-6472.
49. Kramer, W. W.; McCrory, C. C. L., Polymer coordination promotes selective CO₂ reduction by cobalt phthalocyanine. *Chemical Science* 2016, 7 (4), 2506-2515.
50. Schuth, F.; Ward, M. D.; Buriak, J. M., Common Pitfalls of Catalysis Manuscripts Submitted to Chemistry of Materials. *Chemistry of Materials* 2018, 30 (11), 3599-3600.
51. Lide, David R., ed. *CRC handbook of chemistry and physics*. Vol. 85. CRC press, 2004.
52. Liu, B.; Shioyama, H.; Akita, T.; Xu, Q., Metal-organic framework as a template for porous carbon synthesis. *J Am Chem Soc* 2008, 130 (16), 5390-1.
53. (a) Walczak, R.; Kurpil, B.; Savateev, A.; Heil, T.; Schmidt, J.; Qin, Q.; Antonietti, M.; Oschatz, M., Template- and Metal-Free Synthesis of Nitrogen-Rich Nanoporous "Noble" Carbon Materials by Direct Pyrolysis of a Preorganized Hexaazatriphenylene Precursor. *Angew Chem Int Edit* 2018, 57 (33), 10765-10770; (b) Antonietti, M.; Oschatz, M., The Concept of "Noble, Heteroatom-Doped Carbons," Their Directed Synthesis by Electronic Band Control of Carbonization, and Applications in Catalysis and Energy Materials. *Advanced Materials* 2018, 30 (21).
54. Ramirez, A.; Gevers, L.; Bavykina, A.; Ould-Chikh, S.; Gascon, J., Metal Organic Framework-Derived Iron Catalysts for the Direct Hydrogenation of CO₂ to Short Chain Olefins. *ACS Catalysis* 2018, 8 (10), 9174-9182.
55. Burdyny, T.; Smith, W. A., CO₂ reduction on gas-diffusion electrodes and why catalytic performance must be assessed at commercially-relevant conditions. *Energy Environ Sci* 2019, 12, 1442-1453.

OBJECTIVE AND OUTLINE OF THIS THESIS

Among the various CO₂ utilization methods, electrochemical CO₂ reduction shows promising potential to counteract the anthropogenic CO₂ emissions, because of its mild operation conditions and its ability to promptly reach steady operation, ideal for transient operation under fluctuating renewable electricity supply. The commercialization of this process still awaits efficient and stable catalysts. Meanwhile, metal-organic frameworks have recently emerged as precursors for catalyst synthesis. MOF-mediated synthesized catalysts usually have a highly porous structure and uniformly dispersed active sites, which both favour catalysis. This thesis serves to explore the potential of MOF-mediated approaches in electrochemical CO₂ reduction, by expanding the toolkit of MOF-mediated synthesis (MOFMS), designing and optimizing active sites by MOF-mediated synthesis.

This thesis consists of three parts.

Part I (**Chapter 1**) gives an introduction to the progress made in the application of MOF-related electrocatalysts in the electrochemical reduction of CO₂.

Part II (**Chapter 2 and 3**) focuses on the utilization of the metal content of MOFs to fabricate CO₂ER electrodes. In **Chapter 2**, we use an innovative method of electro-decomposing a Ag-coordination polymer to construct a gas-diffusion electrode for high-rate CO₂ER. In **Chapter 3**, this method is extended to the production of a Ag-Cu composite electrode to tune the selectivity of CO₂ER toward ethylene production.

Part III (**Chapter 4 and 5**) focuses on the utilization of the organic constituent of MOFs to prepare carbon-based electrocatalysts for CO₂ER. In **Chapter 4**, ZIF-8 is used as sacrificial template to synthesize Nitrogen-doped carbon electrocatalysts. In **Chapter 5**, to introduce a mesoporous structure in the carbon matrix of the pyrolyzed ZIF-8 (**Chapter 4**) a silica template-assisted approach is applied. At the same time, the silica template can stabilize single atom Fe-sites, which is reported to facilitate CO₂ER.

Overall, this thesis highlights the potential of MOF-mediated catalyst engineering in CO₂ER. This MOF-mediated approach can offer inexpensive and facile routes for designing CO₂ER catalyst structures.

The chapters in the thesis are written as independent papers, so some introductory overlap may exist.

Maximizing Ag Utilization in High Rate CO₂ Electrochemical Reduction with a Coordination Polymer Mediated Gas Diffusion Electrode

2

This chapter is based on the following publication:

Riming Wang, Henrik Haspel, Alexey Pustovarenko, Alla Dikhtiarenko, Artem Russkikh, Genrikh Shterk, Dmitrii Osadchii, Samy Ould-Chikh, Ming Ma, Wilson A. Smith, Kazuhiro Takanebe, Freek Kapteijn, and Jorge Gascon, *ACS Energy Lett.* 2019, 4, 8, 2024-2031

Abstract: We report the preparation and electrocatalytic performance of silver-containing gas diffusion electrodes (GDE) derived from a silver coordination polymer (Ag-CP). Layer-by-layer growth of the Ag-CP onto porous supports was applied to control Ag loading. Subsequent electro-decomposition of the Ag-CP resulted in highly selective and efficient CO₂-to-CO GDE in aqueous CO₂ electroreduction. Afterwards, the MOF-mediated approach was transferred to a gas-fed flow electrolyzer for high-current density tests. The in-situ formed GDE, with a low silver loading of 0.2 mg cm⁻², showed a peak performance of $j_{CO} \approx 385 \text{ mA cm}^{-2}$ at around -1.0 V vs. RHE and stable operation with high FE_{CO} (> 95%) at $j_{Total} = 300 \text{ mA cm}^{-2}$ over a 4 h run. These results demonstrate that the MOF-mediated approach offers a facile route to manufacture uniformly dispersed Ag catalysts for CO₂ER by eliminating ill-defined deposition steps (drop-casting *etc.*), while allowing control of the catalyst structure through self-assembly.

2.1. INTRODUCTION

Atmospheric CO₂ concentration has been increasing drastically since the industrial revolution, this has spurred different initiatives into reducing emissions and directly utilizing CO₂ [1]. Among the various methods proposed, CO₂ electrochemical reduction (CO₂ER) is one of the most promising technologies due to the relatively mild operating conditions and the increasing sources of green electricity [2]. Moreover, the electrochemical reduction of CO₂ can be driven towards one single product, avoiding expensive purification and separation steps. In this sense, the selective electrochemical conversion of CO₂ to CO constitutes an excellent perspective technology. Au [3], Ag [4], and Zn [5] have been identified as the most efficient catalysts for this process. The high price of Au and the low stability of Zn place Ag as the most attractive option [4b, 6]. As it is the case in classical heterogeneous catalysis, optimization of the final catalyst composition and metal loading are critical to the commercialization of CO₂ER. Most studies to date have focused on the application of metal plates [4b, 7] or supported nanoparticles [3-4, 5, 8]. In the former case, the high metal content per electrode area results in such high Capital Expenditures (CAPEX) that these technologies become non-viable. Therefore, the use of supported metal catalysts seems more realistic. Catalyst layer morphology has an effect on cathode performance: a more uniform active phase distribution and lower particle agglomeration lead to better catalytic performance [9]. However, the fabrication of uniformly dispersed catalysts remains a significant challenge. Herein, we propose the MOF-mediated synthesis as a facile and scalable method to manufacture highly dispersed supported Ag catalysts with very low metal loadings for CO₂ER.

The use of metal-organic frameworks as catalyst precursors has gained significant attention in the last few years [10]. Following this approach, a pre-synthesized MOF is treated at high temperature in a controlled atmosphere and transformed into a supported metal nanoparticle catalyst [11]. The high activities per metal atom exhibited by the resulting catalysts, even when the total metal content can be as high as a 50 wt% [10a], demonstrate the enormous potential of this approach. In this work, we demonstrate that MOF mediated synthesis (MOFMS) can also be realized through electro-decomposition.

Here, an Ag coordination polymer (Ag-CP) is grown directly onto carbon based microporous layer (MPL) gas diffusion electrodes by a layer-by-layer (LBL) method, followed by the electro-decomposition of the coordination polymer to achieve a well-defined carbon supported Ag structure (denoted as Ag/MPL). The *in-situ* formed carbon cloth supported Ag gas diffusion electrodes exhibit high CO₂ER efficiency in both, the traditional aqueous three-electrode system and a gas-fed flow electrolyzer. Overcoming CO₂ transport limitations in the latter resulted in a peak performance of $j_{CO} = 385 \text{ mA cm}^{-2}$ CO partial current density and 1864 mA mg⁻¹ mass activity due to the extremely low Ag loading. The work opens up the possibility for the direct manufacture of CO₂ER electrodes with optimum catalyst utilization using the MOF-mediated approach.

2.2. RESULTS AND DISCUSSION

The self-assembly between 2,5-pyridinedicarboxylic (pydc) acid and AgNO₃ in several common solvents at room temperature leads to the formation of an Ag-CP microcrystalline powder (Table S2.1-2.2 and Figure S2.1) [12]. The crystal structure of Ag-CP was elucidated from powder X-

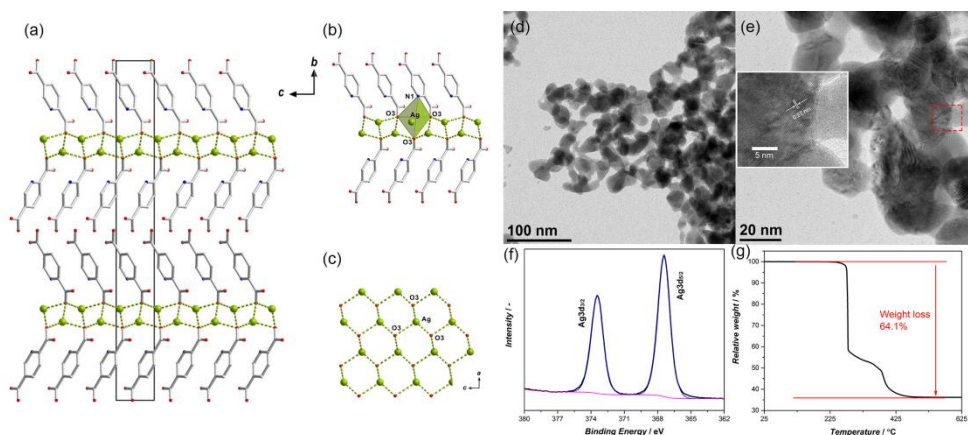


Figure 2.1. (a) Representation of the lamellar crystal packing and the unit cell of Ag-CP viewed along the *a*-axis. (b) Coordination mode of 2,5-pyridinedicarboxylic acid (μ_3 -bridging through O3 atom). (c) Hexagonal arrangement of Ag in the polymeric layer. Color scheme of the atoms: silver – green, carbon – grey, oxygen – red, nitrogen – blue. Hydrogen atoms are omitted for clarity. (d) Low-, and (e) high-magnification TEM images of Ag-CP (inset in e is a magnified image of the red box area). (f) XPS Ag3*d* regional spectrum of Ag-CP, and (g) TGA curve of Ag-CP in air.

ray diffraction (PXRD) data by means of simulated annealing procedure followed by Rietveld refinement [13]. The Ag-CP crystallizes in orthorhombic *Pbn*2₁ space group (Figure S2.2-2.3, Table S2.3) and reveals a layered arrangement of silver atoms coordinated to 2,5-pydc ligands (Figure S2.4, Table S2.4). The linker moieties lie on both sides of the Ag ion double layer: one carboxylic group is bonded to three crystallographically equivalent silver atoms exhibiting a μ_3 -bridging mode; another one is protonated and participates in the formation of hydrogen bonds between two Ag-CP 2D networks (Figure 2.1a-c and Figure S2.5).

Characterization results of Ag-CP are displayed in Figure 2.1d-g. The Ag-CP particles have a particle size ranging from 25 nm to 35 nm (Figure 2.1d). The high-magnification TEM image (inset of Figure 2.1e) shows

well-defined d -spacing with a distance of ~ 0.27 nm. Ag $3d$ XPS spectrum of Ag-CP (Figure 2.1f) exhibits two highly symmetric peaks with binding energies of 367.4 eV and 373.4 eV, corresponding to Ag $3d_{5/2}$ and Ag $3d_{3/2}$ photoelectron lines, respectively. Photoelectron shift of Ag $3d$ line reveals that only oxidized Ag is present in the sample, which agrees with the Ag-O interaction in the crystal structure. Survey XPS spectrum of Ag-CP (Figure S2.6) proves the presence of Ag, C, N and O in the sample, and the atomic content of each element is summarized in Table S5. The TGA curve of Ag-CP (Figure 2.1g) exhibits a total weight loss of $\sim 64.1\%$. Since Ag $_2$ O is thermodynamically unfavourable at high temperature [14], the final product is metallic Ag with a silver content of $\sim 35.9\%$. The formation of metallic Ag after the high-temperature calcination of Ag-CP in air can also be confirmed by XRD (Figure S2.7). N $_2$ physisorption of Ag-CP (Figure S2.8) shows a type II isotherm and absence of microporosity.

Ag-CP was deposited onto the support by the subsequent adsorption of pydc and Ag $^+$ from their DMF solutions (Figure 2.2a). The Ag-CP loading increases strictly linearly from the 2. deposition step (LBL cycle) up to 12 or 20 cycles, as it is seen in Figure 2.2b for bare carbon fibre and MPL containing carbon cloth alike. Utilizing the top part of the microporous layer, however, helps to achieve good surface coverage at lower Ag-CP loading ($0.144 - 0.375$ mg cm $^{-2}$ step $^{-1}$). Taking the theoretical density of the unit cell (2.557 g cm $^{-3}$) from Table S3 into consideration, a 0.563 μ m thick Ag-CP layer - and since the longest cell parameter is around 3.2 nm, practically 150-200 unit cell thickness is deposited in each cycle onto the MPL support. The higher-than-linear deposition in the 1. LBL cycle (Figure 2.2b inset) is due to the high surface area of the carbon grains in the MPL,

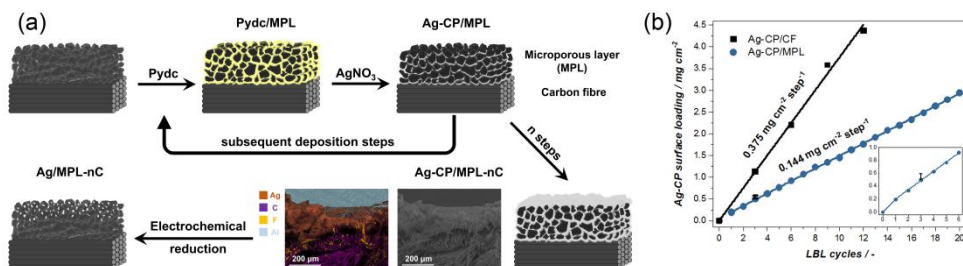


Figure 2.2. (a) Scheme of the preparation of Ag/MPL catalysts; the sequential deposition of Ag-CP via the alternating adsorption of the dicarboxylic linker and the metal node, and the cross-sectional elemental maps of C, F, Ag and Al. Fluorine can be found on the PTFE-treated carbon fabric, while Al signal comes from the sample holder. (b) Increasing surface loading in subsequent deposition steps on bare carbon fibre and MPL/carbon cloth. The error bar at the 3 LBL point was determined from 8 parallel samples.

as first the Ag-CP is built up directly onto the carbon surface (see EDS elemental maps of a 20 LBL sample in Figure 2.2a and S2.9). The actual CO₂ER catalyst is then formed by the in-situ electrochemical reduction of the supported coordination polymer (Figure 2.2a). The final Ag loading also changes linearly with the number of deposition steps as it is seen in the bare carbon fibre based samples (Ag/CF-nC, $n = 3, 6, 9, 12$) in Figure S2.10. The difference between the Ag-CP and Ag loading was ~ 35.2 wt%, which is in good agreement with the Ag content in the crystallographically determined formula (39.4 wt%) and with the previous TGA analysis (~ 35.9 wt%).

Although several MOF-derived electrocatalysts have been reported in the literature lately, to the best of our knowledge, no detailed mechanistic description of the electrochemical reduction and transformation of MOFs into the resulting NPs exists. We propose, that as the reducing potential is applied to the electrode and the metal node is reduced back to zero valence silver, the linker molecules are not able to coordinate and hence maintaining

the continuous polymeric structure anymore. The collapsing structure releases silver atoms at the surface of the support, and nanoparticles and – with increasing Ag-CP coverage – agglomerated silver network are formed through conventional aggregation.

According to the SEM images (Figure 2.3 and Figure S2.11-2.14), Ag-CP fully covers the MPL of the gas diffusion electrode after at least 2 LBL cycles (Figure 2.3a-d). A spot of Ag-CP on the 1 LBL sample is clearly seen in Figure S11a, whereas in Figure S12a-14a the CP coverage is continuous. The subsequent electro-decomposition of Ag-CP resulted in well-dispersed of Ag nanoparticles (Figure 2.3e-h) due to the homogeneous distribution of the Ag-CP precursor. The Ag/MPL-1C electrode (Figure 2.3e) has a relatively sparse distribution of Ag particles, while Ag/MPL-6C shows an agglomerated network of silver structures. Well-dispersed individual Ag particles were obtained by using 2 and 3 LBL cycles (Figure 2.3f-g). Although the thick carbon fabric supported Ag NPs are not suitable for TEM investigation, we removed the MPL grains by ultra-sonication and the Ag particle size distributions were determined (Figure S2.15). Since no significant differences in the PSDs were found, we propose that there is no direct connection between variation of activity and particle size in our system.

After the L-B-L growth process, the PXRD pattern of the carbon cloth-supported Ag-CP is compared with the simulated pattern of the pure Ag-CP in Figure S2.16a. The sharp reflections demonstrate good crystallinity of Ag-CP. The position of the Ag-CP/CF reflections corresponds well to those

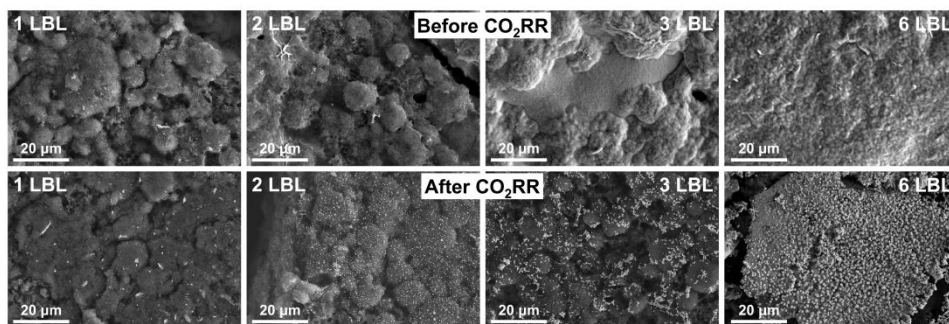


Figure 2.3. SEM images of electrodes prepared with (a, e) 1, (b, f) 2, (c, g) 3, and (d, h) 6 LBL cycles before and after electro-decomposition.

metallic Ag is formed (Figure S2.16b), with three major reflections centered at 44.6° , 52.5° , and 77.2° corresponding to the (111), (200), and (220) crystal facets of metallic Ag. The broad peak centered at $\sim 27^\circ$ is likely to be generated by the amorphous carbon in the carbon support. And after CO₂ER, the metallic Ag pattern is maintained, demonstrating the stability of the electrode.

Evolution of Ag chemical states in the sample before and after *in-situ* catalyst formation (*i.e.*, in CO₂ electrolysis) were determined by XPS (Figure S2.17). After deconvolution, two doublets can be distinguished in the Ag3d line, corresponding to metallic Ag (red peaks in Figure S2.17 centered at 374.2 eV and 368.2 eV) and Ag₂O (blue peaks centered at 373.6 eV and 367.6 eV) [4b, 15]. The ratio of metallic Ag: oxidized Ag increases from 2.4 to 6 after one CO₂ER performance test, indicating the reduction of Ag₂O during this process.

In order to demonstrate the advantage of the LBL method over drop-casting, a carbon fiber (CF) supported Ag-CP electrode was prepared via the L-B-L method and the widely-used drop-casting (DC) method (Scheme S2.1). When drop-casted, the Ag-CP particles spread around the carbon

fibres, filling the space in between them (Figure S2.18a,b). After electro-decomposition, large flower-like Ag particles grow onto the fibres, leaving a large part of the carbon support uncoated (Figure S2.18c,d). By comparison, the L-B-L method with 9 cycles produced uniformly dispersed Ag-CP (Figure S2.18e,f) and Ag particles (Figure S2.18g,h) fully covering the surface of carbon fibers.

Chronoamperometric (*i.e.*, controlled-potential) electrochemical CO₂ reduction tests were carried out in a traditional two-compartment aqueous cell in 0.1 M KHCO₃ electrolyte using a Pt counter electrode. The CO₂ electroreduction performance of Ag/MPL-nC electrodes is presented in Figure 2.4. Only CO and H₂ were detected as products by gas and liquid chromatography (GC and UPLC), and all the catalysts show stable CO₂ER performance after an initial 15 min period, where the *in-situ* formation of the Ag/MPL takes place *via* electro-decomposition (Figure S2.19).

As shown in Figure 2.4a, the total geometrical current density increases with increasing cathode potential ($j_{Total, max} \approx 43\text{-}44 \text{ mA cm}^{-2}$ at around -1.05 V vs. RHE for Ag/MPL-3,6C) along with the steady increase in the FE_{CO} (Figure 2.4b), reaching a maximum FE_{CO} of 90-95% ($FE_{H_2} = 10\text{-}5\%$) between -0.6 and -1.1 V vs RHE for the Ag/MPL-1,2,3C electrodes. The number of LBL cycles also plays an important role in electrode performance with 3 cycles showing the optimal compromise between the wide potential window for high FE_{CO} and the high j_{CO} ($\sim 30 \text{ mA cm}^{-2}$ at -1.0 V vs. RHE) at a minimum Ag loading (Figure 2.4c and Table S2.6).

In order to investigate if the presence of linker molecules and Ag in the electrolyte solution affects CO₂ER performance, electrolysis were carried out at -2.0 and -1.6 V vs SCE using fresh electrolyte right after the *in-situ*

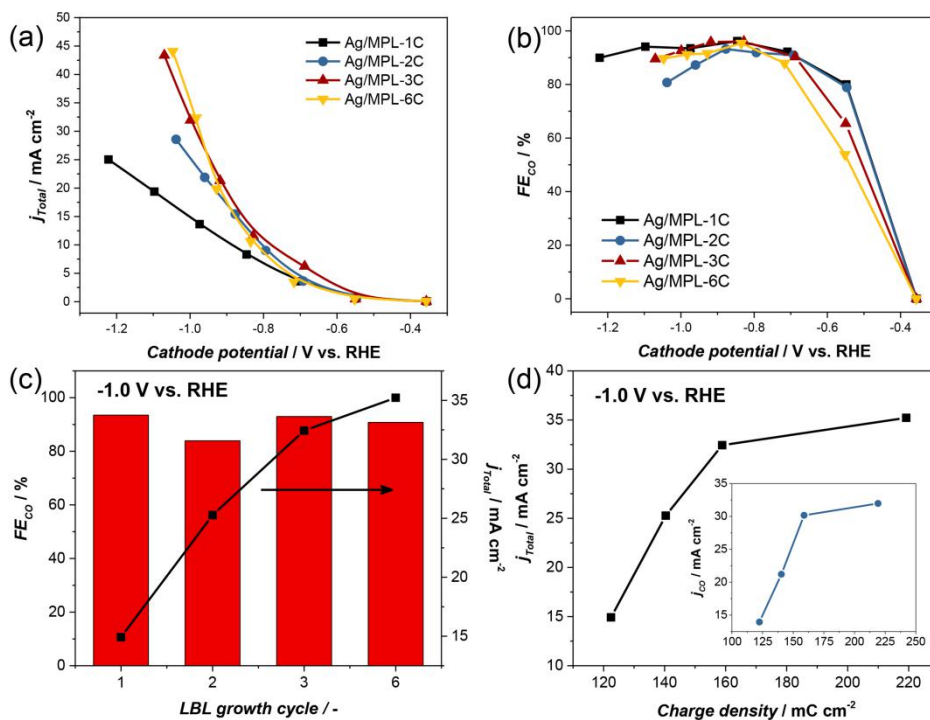


Figure 2.4. CO₂ electrochemical reduction performance of Ag/MPL-nC electrodes. (a) Total current density, (b) FE for CO, and (c) their LBL cycle dependency at -1.0 V vs RHE. (d) Variation of j_{Total} and j_{CO} with the electrochemical active surface area (EASA) at the same potential.

formation of the Ag/MPL-3C catalyst from the Ag-CP/MPL-3C precursor (Figure S2.20). No significant change in the product distribution was seen, however, the total current density drops by 15-25% after the change of the solution. We speculate that this is due to the loss of Ag from the surface rinsing the electrode. The long-term stability of the CO₂ER performance was also tested using the Ag/MPL-3C sample in a refreshed electrolyte solution, and stable CO₂-to-CO activity was attained in a 5-hour electrolysis (Figure S2.21). The CO₂ER performance of the Ag/MPL-3C electrode was compared to similar Ag catalysts reported in the literature (Table S2.7) [4b, 6, 16].

To address the increased j_{Total} and j_{CO} , the electrochemical active surface area (EASA) of the Ag-CP and Ag/MPL-nC samples was determined by the monolayer silver oxide method in 0.1 M KOH [16-17]. The charge for monolayer oxide formation was calculated in Figure S2.22. EASA almost linearly increases with ongoing LBL cycles (Figure S2.23), which then does not accompanied by the same increase in the total and CO current density. The latter levels off at 3 deposition cycles (Figure 2.4d). Even though the total amount of silver in Ag/MPL-6C increased considerably compared to Ag/MPL-3C (twice as many LBL cycles), it is not accompanied by the increase in the number of accessible active sites. The effect of electro-decomposition, *i.e.*, the formation of Ag particles can be followed in Figure S2.23. The EASA saturates after 2 LBL cycles at a lower level, as the increase in Ag loading (in the form of Ag-CP) is not followed by an increase of the number of active sites, demonstrating that only Ag in the outer surface acts as a CO₂-to-CO electrocatalyst.

CO₂ mass transport limitation is one of the bottlenecks that prevent achieving high current densities in aqueous phase CO₂ electrolysis [18]. Therefore, we turned to a gas-fed flow electrolyzer to perform high current density chronopotentiometric CO₂ electrolysis on the Ag/MPL-3C electrode [19]. The cathode side was fed by a humidified CO₂ stream without using any liquid catholyte, and a nickel mesh was used as an oxygen evolution catalyst in recirculated 1 M KOH anolyte at the anode side. The two compartments were separated by Sustainion S-50 polyimidazolium-based anion exchange membrane. The catalytically active Ag particles were *in-situ* formed from the pre-synthesized Ag-CP *via* an initial chronoamperometric

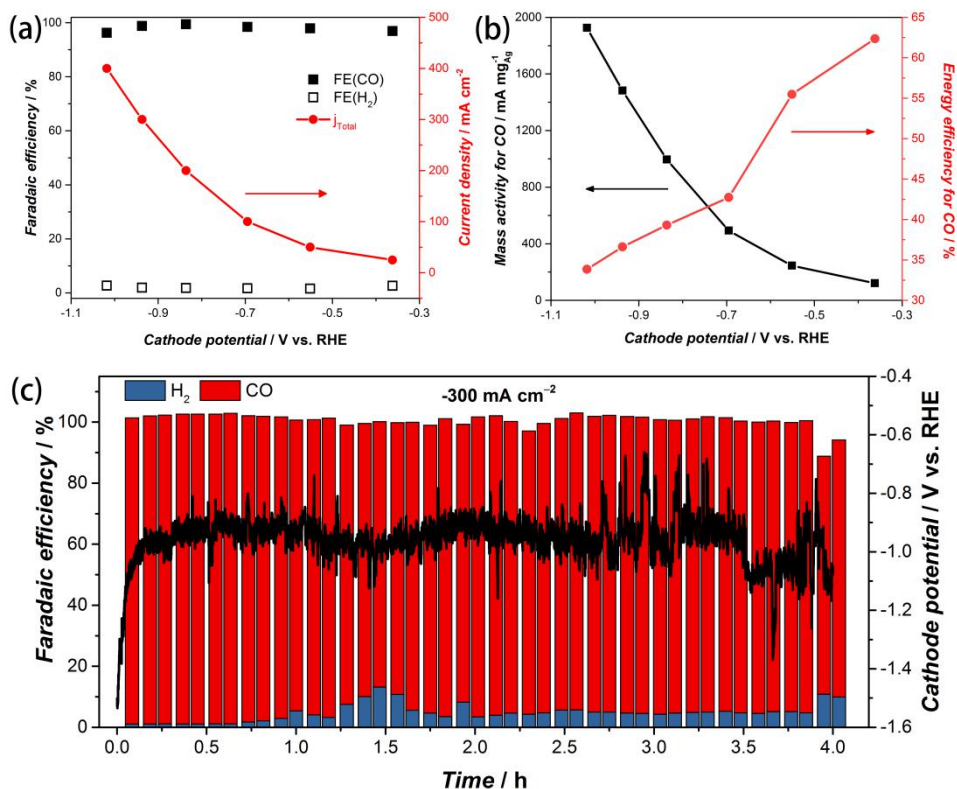


Figure 2.5. CO₂ER performance of the Ag/MPL-3C electrode in a gas-fed zero gap flow electrolyzer. (a) Faradaic efficiency and total current density, and (b) mass activity and energy efficiency for CO. (c) Stability test at -300 mA cm^{-2} for 4 h, the bar diagram represents the FE (left y-axis) of CO (red) and H₂ (blue), and the black line represents the cathode potential (right y-axis).

run at constant -2 V vs Hg/HgO potential under CO₂ electroreduction conditions (Figure S2.24). CO was formed with high selectivity right from the beginning of the activation step, and j_{CO} levels off after about 20 min at typically around $200\text{-}300 \text{ mA cm}^{-2}$.

Immediately after the initial CA run, chronopotentiometric CO₂ electrolysis was done at different current densities. A moderately high current density of -25 mA cm^{-2} was achieved at a cathode potential of around -0.36 V vs RHE (Figure 2.5a). Towards higher current densities the

cathode potential climbed to -1.04 V vs. RHE, which corresponds to a cell voltage of 3.78 V, at $j_{Total} = -400$ mA cm $^{-2}$. High FE_{CO} ($> 96\%$) was achieved in the whole tested current density range, peaking at $FE_{CO} = 99.5\%$ at $j_{Total} = -200$ mA cm $^{-2}$ ($E_{Cathode} = -0.84$ V vs. RHE). The flow cell CO $_2$ ER performance of the Ag/MPL-3C catalyst are summarized in Table S2.8, and compared to literature data on high current density flow cell CO $_2$ -to-CO electrolysis (Table S2.9, Figure S2.25a) [6c, 20].

Active phase dispersion and accessibility plays a crucial role in catalytic performance. To this end, the MOF mediated synthesis, combined with electro-decomposition, offers a straightforward approach to achieving high mass activity of the catalyst. In Ag/MPL-3C the Ag-CP and Ag loadings are 0.55 mg cm $^{-2}$ and 0.20 - 0.21 mg cm $^{-2}$, respectively, which in turn results in a mass activity of 1864 - 1926 mA mg $_{Ag}^{-1}$ (Figure 2.5b), one of the highest values ever reported (Table S2.9, Figure S2.25b) [6c, 20]. The energy efficiency of CO formation remains above 50% at moderate current densities (< 100 mA cm $^{-2}$), and drops to the 32 - 42% range during high current density operation due to the elevated cell potential (Figure 2.5b). The main source of the low energy efficiencies is either the high overvoltage (energy wasted as dissipated heat) and/or low CO selectivity (energy wasted as undesired products) [18a].

Ag/MPL-3C showed stable high current density performance at -300 mA cm $^{-2}$ for 4 h (Figure 2.5c). The estimated average potential was -0.94 V vs RHE in the first 3.5 h. The fluctuation in the potential reading is due to the intensive bubble formation at the nickel mesh anode catalyst, as the counter electrode potential was directly determined in this setup. The cell potential oscillated at around 3.2 V in the first 3 h, then it shifted to higher

voltages (Figure S2.26). Moreover, gas flow fluctuation due to carbonate precipitation in the cathode flow channels is a further issue to be solved in industrial scale high rate operations in alkaline environment CO₂ electrolysis [18a, 20e]. Images of a crystalline precipitate is seen after a long-term electrolysis in Figure S2.27 without (a) and with (b) reactant stream humidification, its XRD pattern (Figure S2.28) shows that mainly KHCO₃ was formed in the flow channels and on the macroporous side of the carbon cloth GDE. The temporary increase in FE_{H_2} at around 1.5 h is most probably the result of the building-up of the KHCO₃ layer on the cathode side of the cell. This on one hand, partly blocks the CO₂ flow, but on the other hand provides a suitable environment for CO₂ER as HCO₃⁻ ion layer at the cathode is known for stabilizing the CO₂ER performance in flow electrolyzers [18a, 20e].

2.3. CONCLUSIONS

In summary, the MOF-mediated approach, *i.e.*, LBL deposition of Ag-CP followed by electro-decomposition, offers a facile route to manufacture uniformly dispersed Ag catalysts for CO₂ER. In spite of the small amount of Ag in the final electrodes (0.2 mg cm⁻²), gas diffusion electrodes show excellent CO₂ER performance in traditional aqueous cells ($FE_{CO} \approx 90-95\%$ and $j_{CO, max} = 38.8 \text{ mA cm}^{-2}$ at -1.07 V vs RHE) and in a gas-fed electrolyzer ($j_{CO, max} = 385 \text{ mA cm}^{-2}$ at -1.04 V vs. RHE). The enhanced catalyst dispersion and utilization resulted in one of the highest silver mass activities (1864 mA mg_{Ag}⁻¹) in the literature to date. The direct synthesis of metal electrocatalyst eliminates the need for ill-defined deposition steps (drop-casting *etc.*), while allowing tight control of the catalyst structure through self-assembly.

2.4. REFERENCES

1. (a) Kondratenko, E. V.; Mul, G.; Baltrusaitis, J.; Larrazabal, G. O.; Perez-Ramirez, J., Status and perspectives of CO₂ conversion into fuels and chemicals by catalytic, photocatalytic and electrocatalytic processes. *Energ Environ Sci* 2013, 6 (11), 3112-3135; (b) Saeidi, S.; Amin, N. A. S.; Rahimpour, M. R., Hydrogenation of CO₂ to value-added products-A review and potential future developments. *Journal of CO₂ Utilization* 2014, 5, 66-81; (c) Sharma, S.; Hu, Z. P.; Zhang, P.; McFarland, E. W.; Metiu, H., CO₂ methanation on Ru-doped ceria. *Journal of Catalysis* 2011, 278 (2), 297-309; (d) Thampi, K. R.; Kiwi, J.; Gratzel, M., Methanation and Photo-Methanation of Carbon-Dioxide at Room-Temperature and Atmospheric-Pressure. *Nature* 1987, 327 (6122), 506-508; (e) Wang, W.; Wang, S.; Ma, X.; Gong, J., Recent advances in catalytic hydrogenation of carbon dioxide. *Chem Soc Rev* 2011, 40 (7), 3703-27.
2. (a) Whipple, D. T.; Kenis, P. J. A., Prospects of CO₂ Utilization via Direct Heterogeneous Electrochemical Reduction. *J Phys Chem Lett* 2010, 1 (24), 3451-3458; (b) Lu, Q.; Jiao, F., Electrochemical CO₂ reduction: Electrocatalyst, reaction mechanism, and process engineering. *Nano Energy* 2016, 29, 439-456; (c) Ganesh, I., Electrochemical conversion of carbon dioxide into renewable fuel chemicals - The role of nanomaterials and the commercialization. *Renew Sust Energ Rev* 2016, 59, 1269-1297.
3. (a) Zhu, W.; Michalsky, R.; Metin, O.; Lv, H.; Guo, S.; Wright, C. J.; Sun, X.; Peterson, A. A.; Sun, S., Monodisperse Au nanoparticles for selective electrocatalytic reduction of CO₂ to CO. *J Am Chem Soc* 2013, 135 (45), 16833-6; (b) Mistry, H.; Reske, R.; Zeng, Z.; Zhao, Z. J.; Greeley, J.; Strasser, P.; Cuenya, B. R., Exceptional size-dependent activity enhancement in the electroreduction of CO₂ over Au nanoparticles. *J Am Chem Soc* 2014, 136 (47), 16473-6.
4. (a) Sastre, F.; Munoz-Batista, M. J.; Kubacka, A.; Fernandez-Garcia, M.; Smith, W. A.; Kapteijn, F.; Makkee, M.; Gascon, J., Efficient Electrochemical Production of Syngas from CO₂ and H₂O by using a Nanostructured Ag/g-C₃N₄ Catalyst. *Chemelectrochem* 2016, 3 (9), 1497-1502; (b) Ma, M.; Trzesniewski, B. J.; Xie, J.; Smith, W. A., Selective and Efficient Reduction of Carbon Dioxide to Carbon Monoxide on Oxide-

- Derived Nanostructured Silver Electrocatalysts. *Angewandte Chemie* 2016, 55 (33), 9748-52.
5. Won da, H.; Shin, H.; Koh, J.; Chung, J.; Lee, H. S.; Kim, H.; Woo, S. I., Highly Efficient, Selective, and Stable CO₂ Electroreduction on a Hexagonal Zn Catalyst. *Angewandte Chemie* 2016, 55 (32), 9297-300.
 6. (a) Daiyan, R.; Lu, X. Y.; Ng, Y. H.; Amal, R., Highly Selective Conversion of CO₂ to CO Achieved by a Three-Dimensional Porous Silver Electrocatalyst. *Chemistryselect* 2017, 2 (3), 879-884; (b) Liu, S.; Tao, H.; Zeng, L.; Liu, Q.; Xu, Z.; Liu, Q.; Luo, J. L., Shape-Dependent Electrocatalytic Reduction of CO₂ to CO on Triangular Silver Nanoplates. *J Am Chem Soc* 2017, 139 (6), 2160-2163; (c) Lu, Q.; Rosen, J.; Zhou, Y.; Hutchings, G. S.; Kimmel, Y. C.; Chen, J. G.; Jiao, F., A selective and efficient electrocatalyst for carbon dioxide reduction. *Nat Commun* 2014, 5, 3242; (d) Mistry, H.; Choi, Y. W.; Bagger, A.; Scholten, F.; Bonifacio, C. S.; Sinev, I.; Divins, N. J.; Zegkinoglou, I.; Jeon, H. S.; Kisslinger, K.; Stach, E. A.; Yang, J. C.; Rossmeisl, J.; Roldan Cuenya, B., Enhanced Carbon Dioxide Electroreduction to Carbon Monoxide over Defect-Rich Plasma-Activated Silver Catalysts. *Angewandte Chemie* 2017, 56 (38), 11394-11398; (e) Peng, X.; Karakalos, S. G.; Mustain, W. E., Preferentially Oriented Ag Nanocrystals with Extremely High Activity and Faradaic Efficiency for CO₂ Electrochemical Reduction to CO. *ACS Appl Mater Interfaces* 2018, 10 (2), 1734-1742; (f) Rosen, B. A.; Salehi-Khojin, A.; Thorson, M. R.; Zhu, W.; Whipple, D. T.; Kenis, P. J.; Masel, R. I., Ionic liquid-mediated selective conversion of CO(2) to CO at low overpotentials. *Science* 2011, 334 (6056), 643-4.
 7. Hori, Y.; Kikuchi, K.; Suzuki, S., Production of CO and CH₄ in Electrochemical Reduction of CO₂ at Metal-Electrodes in Aqueous Hydrogen carbonate Solution. *Chem Lett* 1985, (11), 1695-1698.
 8. Wang, R.; Sun, X.; Ould-Chikh, S.; Osadchii, D.; Bai, F.; Kapteijn, F.; Gascon, J., Metal-Organic-Framework-Mediated Nitrogen-Doped Carbon for CO₂ Electrochemical Reduction. *ACS Appl Mater Interfaces* 2018, 10 (17), 14751-14758.
 9. Jhong, H.-R. M.; Brushett, F. R.; Kenis, P. J. A., The Effects of Catalyst Layer Deposition Methodology on Electrode Performance. *Advanced Energy Materials* 2013, 3 (5), 589-599.

10. (a) Sun, X.; Suarez, A. I. O.; Meijerink, M.; van Deelen, T.; Ould-Chikh, S.; Zecevic, J.; de Jong, K. P.; Kapteijn, F.; Gascon, J., Manufacture of highly loaded silica-supported cobalt Fischer-Tropsch catalysts from a metal organic framework. *Nat Commun* 2017, 8 (1), 1680; (b) Sun, X.; Olivos-Suarez, A. I.; Osadchii, D.; Romero, M. J. V.; Kapteijn, F.; Gascon, J., Single cobalt sites in mesoporous N-doped carbon matrix for selective catalytic hydrogenation of nitroarenes. *Journal of Catalysis* 2018, 357, 20-28; (c) Sun, X.; Olivos-Suarez, A. I.; Oar-Arteta, L.; Rozhko, E.; Osadchii, D.; Bavykina, A.; Kapteijn, F.; Gascon, J., Metal-Organic Framework Mediated Cobalt/Nitrogen-Doped Carbon Hybrids as Efficient and Chemoselective Catalysts for the Hydrogenation of Nitroarenes. *Chemcatchem* 2017, 9 (10), 1854-1862; (d) Santos, V. P.; Wezendonk, T. A.; Jaen, J. J.; Dugulan, A. I.; Nasalevich, M. A.; Islam, H. U.; Chojecki, A.; Sartipi, S.; Sun, X.; Hakeem, A. A.; Koeken, A. C.; Ruitenbeek, M.; Davidian, T.; Meima, G. R.; Sankar, G.; Kapteijn, F.; Makkee, M.; Gascon, J., Metal organic framework-mediated synthesis of highly active and stable Fischer-Tropsch catalysts. *Nat Commun* 2015, 6, 6451; (e) Oar-Arteta, L.; Wezendonk, T.; Sun, X. H.; Kapteijn, F.; Gascon, J., Metal organic frameworks as precursors for the manufacture of advanced catalytic materials. *Materials Chemistry Frontiers* 2017, 1 (9), 1709-1745.
11. Wang, R.; Kapteijn, F.; Gascon, J., Engineering Metal–Organic Frameworks for the Electrochemical Reduction of CO₂: A Minireview. *Chemistry – An Asian Journal* doi:10.1002/asia.201900710
12. Lu, X.; Ye, J.; Zhang, D.; Xie, R.; Bogale, R. F.; Sun, Y.; Zhao, L.; Zhao, Q.; Ning, G., Silver carboxylate metal-organic frameworks with highly antibacterial activity and biocompatibility. *J Inorg Biochem* 2014, 138, 114-121.
13. (a) Pawley, G. S., Unit-Cell Refinement from Powder Diffraction Scans. *J Appl Crystallogr* 1981, 14 (Dec), 357-361; (b) Boulton, A.; Louer, D., Powder pattern indexing with the dichotomy method. *J Appl Crystallogr* 2004, 37, 724-731; (c) Altomare, A.; Corriero, N.; Cuocci, C.; Falcicchio, A.; Moliterni, A.; Rizzi, R., EXPO software for solving crystal structures by powder diffraction data: methods and application. *Cryst Res Technol* 2015, 50 (9-10), 737-742.
14. L'vov, B. V., Kinetics and mechanism of thermal decomposition of silver oxide. *Thermochim Acta* 1999, 333 (1), 13-19.

15. Gao, X. Y.; Wang, S. Y.; Li, J.; Zheng, Y. X.; Zhang, R. J.; Zhou, P.; Yang, Y. M.; Chen, L. Y., Study of structure and optical properties of silver oxide films by ellipsometry, XRD and XPS methods. *Thin Solid Films* 2004, 455, 438-442.
16. Ma, M.; Liu, K.; Shen, J.; Kas, R.; Smith, W. A., In Situ Fabrication and Reactivation of Highly Selective and Stable Ag Catalysts for Electrochemical CO₂ Conversion. *ACS Energy Letters* 2018, 3 (6), 1301-1306.
17. Rosen, J.; Hutchings, G. S.; Lu, Q.; Rivera, S.; Zhou, Y.; Vlachos, D. G.; Jiao, F., Mechanistic Insights into the Electrochemical Reduction of CO₂ to CO on Nanostructured Ag Surfaces. *Acs Catal* 2015, 5 (7), 4293-4299.
18. (a) Martín, A. J.; Larrazábal, G. O.; Pérez-Ramírez, J., Towards sustainable fuels and chemicals through the electrochemical reduction of CO₂: lessons from water electrolysis. *Green Chemistry* 2015, 17 (12), 5114-5130; (b) Schwarz, H. A.; Dodson, R. W., Reduction potentials of CO₂- and the alcohol radicals. *The Journal of Physical Chemistry* 1989, 93 (1), 409-414.
19. (a) Han, L.; Zhou, W.; Xiang, C., High-Rate Electrochemical Reduction of Carbon Monoxide to Ethylene Using Cu-Nanoparticle-Based Gas Diffusion Electrodes. *ACS Energy Letters* 2018, 3 (4), 855-860; (b) Burdyny, T.; Smith, W. A., CO₂ reduction on gas-diffusion electrodes and why catalytic performance must be assessed at commercially-relevant conditions. *Energy Environ Sci* 2019; (c) Higgins, D.; Hahn, C.; Xiang, C.; Jaramillo, T. F.; Weber, A. Z., Gas-Diffusion Electrodes for Carbon Dioxide Reduction: A New Paradigm. *ACS Energy Letters* 2019, 4 (1), 317-324; (d) Wu, J.; Risalvato, F. G.; Sharma, P. P.; Pellechia, P. J.; Ke, F.-S.; Zhou, X.-D., Electrochemical Reduction of Carbon Dioxide. *J Electrochem Soc* 2013, 160 (9), F953-F957; (e) Merino-Garcia, I.; Alvarez-Guerra, E.; Albo, J.; Irabien, A., Electrochemical membrane reactors for the utilisation of carbon dioxide. *Chem Eng J* 2016, 305, 104-120; (f) Endrődi, B.; Bencsik, G.; Darvas, F.; Jones, R.; Rajeshwar, K.; Janáky, C., Continuous-flow electroreduction of carbon dioxide. *Progress in Energy and Combustion Science* 2017, 62, 133-154; (g) Weekes, D. M.; Salvatore, D. A.; Reyes, A.; Huang, A.; Berlinguette, C. P., Electrolytic CO₂ Reduction in a Flow Cell. *Accounts Chem Res* 2018, 51 (4), 910-918.
20. (a) Ma, S.; Luo, R.; Gold, J. I.; Yu, A. Z.; Kim, B.; Kenis, P. J. A., Carbon nanotube containing Ag catalyst layers for efficient and selective reduction of carbon dioxide. *J*

Mater Chem A 2016, 4 (22), 8573-8578; (b) Ma, S.; Luo, R.; Moniri, S.; Lan, Y.; Kenis, P. J. A., Efficient Electrochemical Flow System with Improved Anode for the Conversion of CO₂ to CO. *J Electrochem Soc* 2014, 161 (10), F1124-F1131; (c) Ma, S.; Lan, Y.; Perez, G. M. J.; Moniri, S.; Kenis, P. J. A., Silver Supported on Titania as an Active Catalyst for Electrochemical Carbon Dioxide Reduction. *ChemSusChem* 2014, 7 (3), 866-874; (d) Tornow, C. E.; Thorson, M. R.; Ma, S.; Gewirth, A. A.; Kenis, P. J. A., Nitrogen-Based Catalysts for the Electrochemical Reduction of CO₂ to CO. *Journal of the American Chemical Society* 2012, 134 (48), 19520-19523; (e) Verma, S.; Hamasaki, Y.; Kim, C.; Huang, W.; Lu, S.; Jhong, H.-R. M.; Gewirth, A. A.; Fujigaya, T.; Nakashima, N.; Kenis, P. J. A., Insights into the Low Overpotential Electroreduction of CO₂ to CO on a Supported Gold Catalyst in an Alkaline Flow Electrolyzer. *ACS Energy Letters* 2018, 3 (1), 193-198; (f) Verma, S.; Lu, X.; Ma, S.; Masel, R. I.; Kenis, P. J. A., The effect of electrolyte composition on the electroreduction of CO₂ to CO on Ag based gas diffusion electrodes. *Physical Chemistry Chemical Physics* 2016, 18 (10), 7075-7084; (g) Dinh, C.-T.; García de Arquer, F. P.; Sinton, D.; Sargent, E. H., High Rate, Selective, and Stable Electroreduction of CO₂ to CO in Basic and Neutral Media. *ACS Energy Letters* 2018, 3 (11), 2835-2840; (h) Haas, T.; Krause, R.; Weber, R.; Demler, M.; Schmid, G., Technical photosynthesis involving CO₂ electrolysis and fermentation. *Nature Catalysis* 2018, 1 (1), 32-39; (i) Jhong, H.-R. M.; Tornow, C. E.; Kim, C.; Verma, S.; Oberst, J. L.; Anderson, P. S.; Gewirth, A. A.; Fujigaya, T.; Nakashima, N.; Kenis, P. J. A., Gold Nanoparticles on Polymer-Wrapped Carbon Nanotubes: An Efficient and Selective Catalyst for the Electroreduction of CO₂. *Chemphyschem* 2017, 18 (22), 3274-3279; (j) Jhong, H.-R. M.; Tornow, C. E.; Smid, B.; Gewirth, A. A.; Lyth, S. M.; Kenis, P. J. A., A Nitrogen-Doped Carbon Catalyst for Electrochemical CO₂ Conversion to CO with High Selectivity and Current Density. *ChemSusChem* 2017, 10 (6), 1094-1099; (k) Kim, B.; Hillman, F.; Ariyoshi, M.; Fujikawa, S.; Kenis, P. J. A., Effects of composition of the micro porous layer and the substrate on performance in the electrochemical reduction of CO₂ to CO. *J Power Sources* 2016, 312, 192-198; (l) Ma, S.; Liu, J.; Sasaki, K.; Lyth, S. M.; Kenis, P. J. A., Carbon Foam Decorated with Silver Nanoparticles for Electrochemical CO₂ Conversion. *Energy Technology* 2017, 5 (6), 861-863; (m) Möller, T.; Ju, W.; Bagger, A.; Wang, X.; Luo, F.; Ngo

Thanh, T.; Varela, A. S.; Rossmeisl, J.; Strasser, P., Efficient CO₂ to CO electrolysis on solid Ni–N–C catalysts at industrial current densities. *Energ Environ Sci* 2019, 12 (2), 640-647.

2.5. Supporting Information for Chapter 2

2.5.1. Optimization of the synthetic conditions for Ag-CP

In Ag-CP synthesis, the resulting coordination polymer is precipitated from the DMF solution forming a gel-like product. In order to optimize the crystallization conditions, a series of screening experiments have been performed varying solvent and Ag : 2,5-pydc molar ratio, which are presented in Table S2.1. The screening results suggest that the appearance of the Ag coordination polymer is solvent driven. The use of DMF as a solvent media results in the formation of gel-like precipitation which can be separated from mother liquor by several centrifugation runs, while DMSO and aqueous solutions yield the microcrystalline precipitates.

Since the Ag : pydc molar ratio did not show to be a very influential parameter to increase the crystal size of Ag-CP, another set of screening experiments were performed varying solvents and temperatures. Due to the low solubility of the 2,5-pyridine dicarboxylic acid (2,5-pydc) in water, the experiment involving aqueous medium was performed by partial neutralization of the corresponding organic acid with 0.5 equivalent of Na_2CO_3 . In all experiments the amounts of the reacting components were kept unchanged at Ag : 2,5-pydc molar ratio of 1:1. Table S2.2 represents the appearance of distinct chemical phases as a function of solvent and temperature, indicating that the Ag-CP appears as a predominant crystal phase from DMF, DMSO and H_2O solvents only at room temperature. Increasing the synthesis temperature for DMF and DMSO resulted in a mixture of Ag-CP and Ag_2O , whereas the same thermal effect in case of an aqueous solution gives Ag_2O as the main reaction product.

Table S2.1. Summary of the optimization experiments at room temperature representing the appearance of Ag-CP as function of Ag: 2,5-pydc molar ratio and solvent.

Ag : 2,5-pydc Solvent	5 : 1	3 : 1	1 : 1	2 : 3	1 : 3
DMF*	<i>gel</i>	<i>gel</i>	<i>gel</i>	<i>gel</i>	<i>gel</i>
DMSO**	<i>solid</i>	<i>solid</i>	<i>solid</i>	<i>solid</i>	<i>solid</i>
H ₂ O***	<i>solid</i>	<i>solid</i>	<i>solid</i>	<i>solid</i>	<i>solid</i>

*DMF: N,N'-dimethylformamide.

**DMSO: dimethyl sulfoxide.

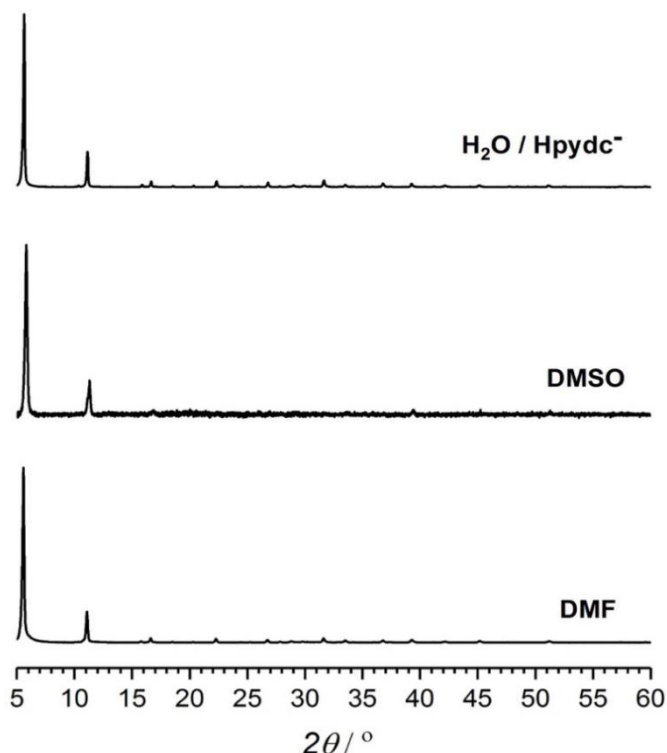
*** Clear reaction mixture was prepared by partially deprotonating 2,5-pyridine dicarboxylic acid (2,5-pydc) with 0.5 equivalent of Na₂CO₃ in deionized water and adding the former one to AgNO₃ aqueous solution.**Figure S2.1.** Experimental powder X-ray diffraction patterns of the solid products resulting from the reaction between equimolar amounts of AgNO₃ and 2,5-pyridinedicarboxylic acid in different solvent media at room temperature.

Table S2.2. The resulting products in solvent screening and products observed during the optimization of the synthetic conditions for Ag-CP.

Solvent Temperature	DMF	DMSO	H ₂ O*
RT			
80 °C			
90 °C			
100 °C			
110 °C			
120 °C			
130 °C			
140 °C			
Color scheme for identifications of phases appeared as a solid product:			
<i>Ag₂O</i>		<i>Ag-CP</i>	

* Clear reaction mixture was prepared by partially deprotonating 2,5-pyridine dicarboxylic acid (2,5-pydc) with 0.5 equivalent of Na₂CO₃ in deionized water and adding the former one to AgNO₃ aqueous solution.

2.5.2. Crystal structure of silver 2,5-pyridinedicarboxylate coordination polymer (Ag-CP): determination and details

In order to optimize the count statistics and peak shape profiles, data collection was carried out in the 2θ range of 4-80° with a step size of 0.02° and a scan speed of 15 s/step. The indexing procedure was performed by DICVOL [1] followed by intensity extraction and unit cell refinement applying a Pawley fitting procedure (Figure S2.2) [2]. The lattice type and space group were assigned based on the evaluation of systematic absences. Foregoing analyses suggest that the Ag-CP crystallized in the orthorhombic

Pbn21 space group with the lattice parameters listed in Table S2.3. The structure solution proceeded by simulated annealing procedure using EXPO2014 software[3] yielding the trial models comprised of silver and 2,5-pyridinedicarboxylate fragments. The chemically rational model was chosen as a final structure model and, subsequently, has been subjected to Rietveld refinement involving silver coordinates, scale factor, zero-point, cell parameters, four background parameters, peak asymmetry and preferred orientation corrections. Details of structure refinement are summarized in Table S2.3 and the final Rietveld plot is shown in Figure S2.3. Atomic coordinates, the principal bond distances and angles are given in Table S2.4.

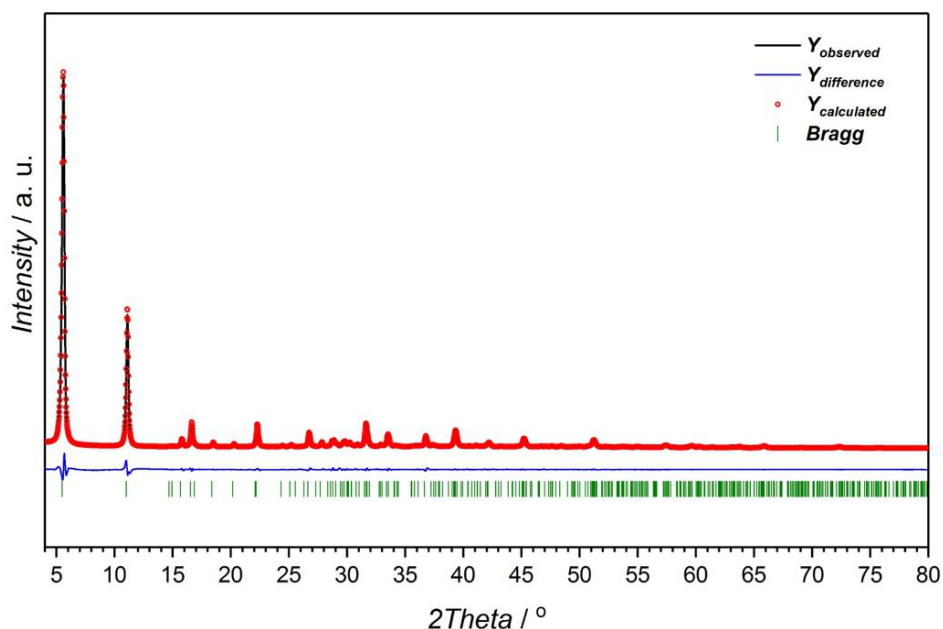


Figure S2.2. Representation of Pawley fit made on Ag-CP experimental data and indexed in orthorhombic Pbn21 space group with the unit cell parameters: $a = 6.0320(5) \text{ \AA}$, $b = 32.1632(6) \text{ \AA}$, $c = 3.6147(8) \text{ \AA}$, $\alpha = \beta = \gamma = 90^\circ$. Experimental pattern is plotted as black line, Pawley fit – red dots, difference as solid blue line and observed reflections are green sticks. Obtained figures of merit are $R_p = 3.99$ and $R_{wp} = 5.51$.

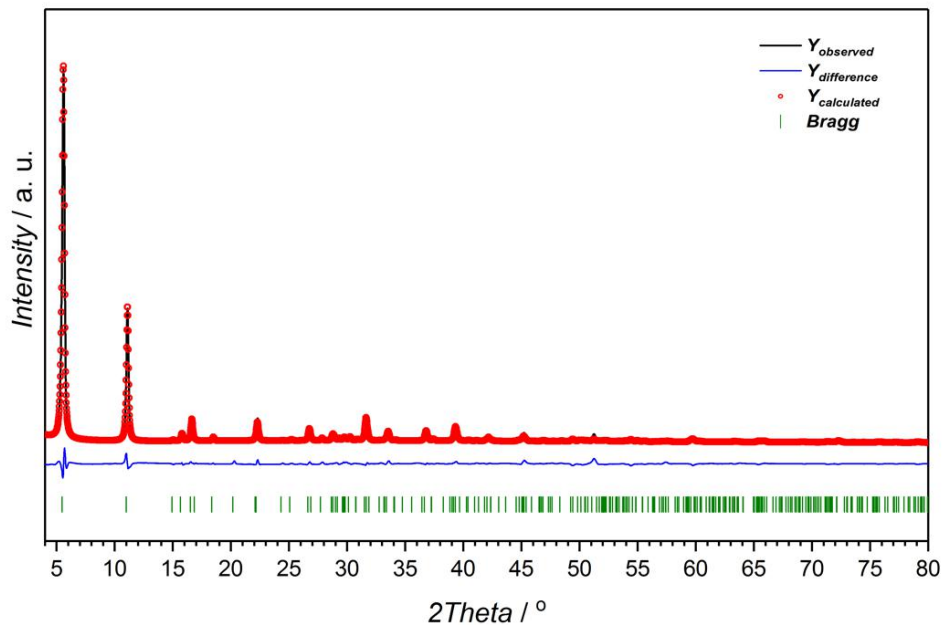


Figure S2.3. Rietveld refinement plot made on Ag-CP experimental data using the model obtained by simulated annealing. Experimental pattern is plotted as black line, Pawley fit – red dots, difference as solid blue line and observed reflections are green sticks. Obtained figures of merit are $R_p = 10.76$ and $R_{wp} = 16.60$.

Table S2.3. Crystal structure parameters and refinement details for Ag-CP.

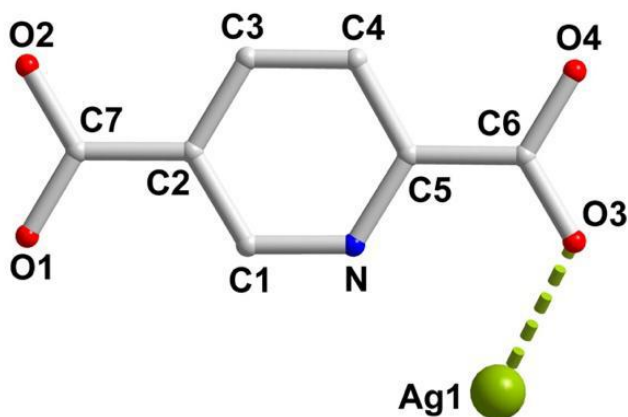
Compound	Ag-CP
Empirical formula	AgC ₇ H ₄ NO ₄
Formula weight / g·mol ⁻¹	273.95
Temperature / K	293
Wavelength / Å	1.5406
Crystal system	orthorhombic
Space group	<i>Pbn</i> 2 ₁
<i>a</i> / Å	6.0320(5)
<i>b</i> / Å	32.1632(6)
<i>c</i> / Å	3.6147(8)
$\alpha, \beta, \gamma / ^\circ$	90, 90, 90
<i>V</i> / Å ³	701.3
<i>Z</i>	4
Calculated density / g·cm ⁻³	2.557
Data collection	powder X-ray diffraction
Data collection range $2\theta / ^\circ$	4 – 80
<i>R</i> factors	$R_p = 10.74, R_{wp} = 16.60, R_{Bragg} = 5.69$

Table S2.4. Final atomic coordinates, selected bond distances (Å) and bond angles (°) for Ag-CP.

Atom	x	y	z	Bond	Length, Å	Angle	Degree, °
Ag1	0.20610	0.23075	0.40667	Ag1–O3 *	2.293	O3–Ag1–O3 ^a	92.18
C1	0.22810	0.10860	0.39081	Ag1–O3 ^a *	2.708	O3–Ag1–O3 ^b	134.81
C2	0.34625	0.07112	0.38480	Ag1–O3 ^b *	2.297	O3 ^a –Ag1–O3 ^b	115.46
C3	0.54564	0.06962	0.18899	Ag1–N1 *	2.982	Ag1–O3–C6	124.19
C4	0.62333	0.10484	1.00502	O1–C7	1.270	Ag1–O3–Ag1 ^d	92.18
C5	0.50082	0.14180	0.01696	O2–C7 ^c	1.271	Ag1–O3–Ag1 ^e	95.99
C6	0.58368	0.17933	0.82084	O3–C6	1.273	Ag1 ^d –O3–C6	124.19
C7	0.26244	0.03402	0.58057	O4–C6	1.272	Ag1 ^e –O3–C6	111.25
N1	0.30630	0.14270	0.20969	C5–C6 ^a	1.486	Ag1 ^d –O3–Ag1 ^e	95.26
O1	0.14349	0.03795	0.86824	C2–C7	1.476		
O2	0.30829	0.99775	0.46366				
O3	0.47505	0.21328	0.82727				
O4	0.76552	0.17805	0.64266				

Translation of symmetry code to equivalent position: (a) $x, y, 1+z$; (b) $-1/2+x, 1/2-y, -1/2+z$; (c) $x, 1+y, z$; (d) $x, y, 1+z$; (e) $1/2+x, 1/2-y, 1/2+z$.

* The values agree with those reported for silver (I) pyridinecarboxylate fragments found in the Cambridge Structural Database (CSD)[4] with the MOGUL software [5].

**Figure S2.4.** Representation of asymmetric unit for Ag-CP with the corresponding atomic labelling scheme. Hydrogen atoms are omitted for clarity.

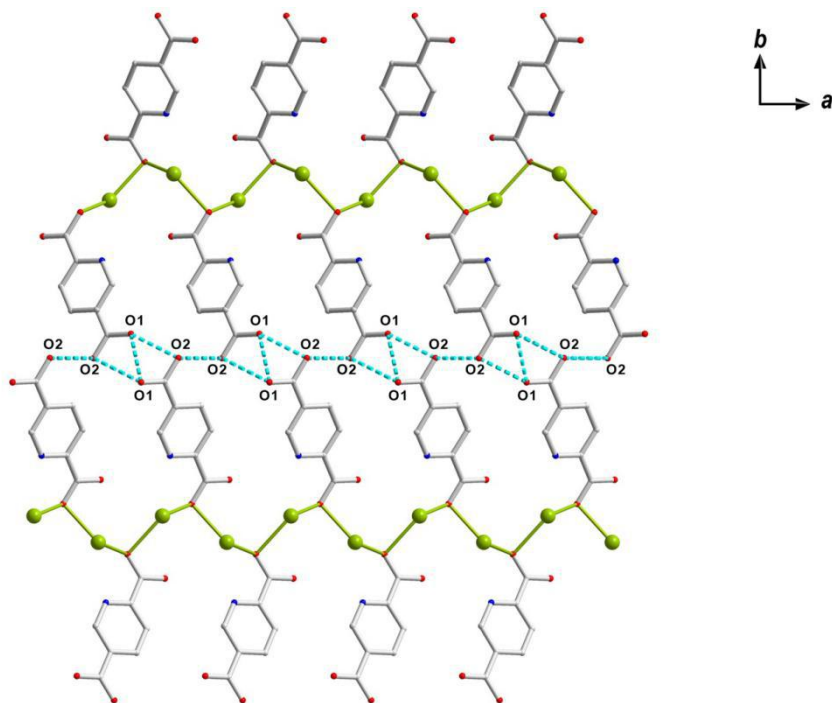


Figure S2.5. Network of hydrogen bonds formed in Ag-CP by protonated carboxylic group in 5-position viewed along c-axis. Hydrogen bonding formed by O2...O2a (2.739 Å), O1...O2a (2.747 Å) and O1...O1b (2.944 Å): a 1-x, -y, -1/2+z and b -x, -y, -1/2+z.

2.5.3. Experimental details

Materials. Silver nitrate (>99% purity), 2,5-pyridinedicarboxylic acid (2,5-pydc, 98% purity), potassium hydroxide (99.99% purity), potassium bicarbonate (99.99% purity) and N,N-dimethylformamide (DMF, 99.8% purity) were purchased from Sigma-Aldrich and were used without further purification. Both, bare macroporous woven carbon cloth (SPUN Carbon Fibres Technology Quintech) and microporous layer containing gas diffusion layer (ELAT LT1400 from Fuel Cell Store) was used throughout the study. The woven nickel mesh anode (300 μm thickness) and the titanium plate (250 μm thickness) were acquired from Nilaco Corporation,

while the anion-exchange membrane (Sustainion S-50) and the reference electrodes, Ag/AgCl (Sat'd KCl), Standard Calomel Electrode, Hg/HgO (1 M NaOH), were purchased from Dioxide Materials and BAS Corporation, respectively. High-purity CO₂ (99.9999%) gas was used in the CO₂ electroreduction tests, obtained from AHG Industrial Gases.

Synthesis of Ag coordination polymer. This method was inspired by a report on the synthesis of a silver carboxylate metal-organic framework [6]. In a typical synthesis, 3.84 g AgNO₃ (22.6 mmol) and 1.2 g 2,5-pydc (7.2 mmol) were separately dissolved in 200 mL DMF under vigorous stirring, forming clear solutions. Then these two solutions were mixed and kept under stirring for 24 h. After that, the slurry was centrifuged and the collected precipitate was washed twice, first with methanol and then with distilled water. The solid was finally dried in a vacuum oven at 80 °C. The synthesis yielded microcrystalline powder composed of tiny crystallites not suitable for single crystal structural analysis. Thus, in order to grow bigger crystals and improve the crystallinity of the compound, an extensive screening study was performed to optimize the synthetic conditions for Ag-CP (see section 1).

Preparation of Ag/carbon fiber (Ag/CF) electrodes. Ag/CF electrodes were prepared by layer-by-layer growth of Ag-CP onto the carbon fibres (green box in Scheme S1a) followed by electro-decomposition (orange box in Scheme S1a). A carbon cloth electrode, composed of weaved carbon fibres, was immersed into 0.1 M KOH for 1 hour and dried in air to activate the surface of the carbon fibres [7]. 0.3 g 2,5-pydc (1.8 mmol) was dissolved in 50 mL DMF (36 mM) as organic linker solution, and 0.96 g AgNO₃ (5.64 mmol) was dissolved in 50 mL DMF (113 mM) as metal precursor solution.

Another 50 mL DMF was used as cleaning agent in between the immersion in the organic linker and the metal precursor solutions. The successive immersion of the carbon cloth electrode in the organic linker solution, pure DMF, and metal precursor solution is denoted as one growth cycle. Each immersion lasted for 2 min. The resulting electrodes were denoted as Ag-CP/CF-9C (9 being the number of LBL growth cycles). After the layer-by-layer growth of Ag-CP, the electrode was fitted into a 3-electrode electrochemical cell with the Ag-CP/CF acting as the working electrode, and 0.1 M KHCO₃ was used as electrolyte. A potential of -1.8 V vs Ag/AgCl was applied by an Autolab PGSTAT302N potentiostat for 2 h to reduce the Ag-CP and obtain the final Ag/CF-9C samples.

Preparation of drop-casted Ag/carbon fiber (Ag/CF-DC) electrode. Ag/CF-DC electrodes were prepared from the powdered coordination polymer via drop-casting (DC) of Ag-CP onto the bare woven carbon cloth (red box in Scheme S1b) from a suspension of 50 mg Ag-CP in 5 mL ethanol and 0.2 mL Nafion solution, followed by electro-decomposition (orange box in Scheme S1b). The resulting electrode was denoted as Ag-CP/CF-DC, and it underwent the same electro-decomposition process as described above to obtain the final Ag/CF-DC electrode. The Ag-CP and Ag loadings on the carbon cloth are determined by weighing the electrodes after each preparation step, and summarized in Table S2.6.

Preparation of Ag/microporous layer (Ag/MPL) electrodes. For the CO₂ electroreduction experiments (both in a traditional 3-electrode liquid cell and in the flow cell electrolyzer) Ag/CF electrodes were prepared in a similar way described above. The major difference was, that only the microporous layer (MPL) of the carbon cloth substrate was (pre-)treated during the synthesis (surface version of the Scheme S1a method). We took

advantage of the high PTFE content, and thus, the hydrophobicity of the cloth, as it floats on top of the aqueous solution. The MPL side got in contact with the KOH solution and was etched to make it more hydrophilic due to the formation of OH-containing functional groups. The same two-step synthesis was applied using 2,5-pydc linker and AgNO₃ silver source in DMF at the same concentration (36 and 113 mM, respectively). The carbon cloth was floating on top of the DMF-based solution as well, depositing the silver containing coordination polymer (Ag/CP) only on top of the MPL. This further reduces the silver loading needed for high performance CO₂ER with decreasing the thickness of the active area and facilitating the dispersion of the metal on the support. Furthermore, this catalytically active top layer becomes important in flow cell CO₂ electrolysis performed in a zero gap cell, meaning the MPL side (along with the catalyst layer) of the porous carbon substrate was pressed against an anion exchange membrane. This leaves the macroporous structure intact for gas diffusion, while utilizing the top skin of the substrate. The resulting electrodes were denoted as Ag-CP/MPL-*n*C (*n* being the number of LBL growth cycles, *n* = 1, 2, 3, 6). A potential of -1.8 V vs Ag/AgCl was applied by a potentiostat to reduce Ag-CP/MPL-*n*C into the final Ag/MPL-*n*C electrodes.

Characterization techniques. X-ray diffraction (XRD) patterns of Ag-CP, Ag particles supported on carbon fibres were collected using a Bruker D8 Advance X-ray diffractometer, and the radiation source was a Co-*K* α radiation ($\lambda = 0.179026$ nm). The Ag content in Ag-CP was determined by thermogravimetric (TG) analysis. TG analysis was conducted on a Mettler Toledo TGA/SDTA851e instrument. The temperature was increased from room temperature to 1000 °C with a ramp of 5 °C·min⁻¹ in air, at a flow rate

of 100 mL min⁻¹. N₂ adsorption-desorption isotherms were recorded to determine the porous structure of Ag-CP. A Micromeritics Tristar 3020 apparatus was used to collect N₂ isotherms at 77 K. The sample was degassed beforehand at 120 °C under N₂ atmosphere. Scanning electron microscopy (SEM) analysis was performed on either a Nova Nano 630 or a Teneo scanning electron microscope from FEI Company. A FEI TEM (model Titan 80-300 ST) operated at 300 kV was used for transmission electron microscopy (TEM) analysis. A K-alpha Thermo Fisher Scientific spectrometer was used for the XPS investigation using monochromatic Al-K α radiation at ambient temperature and a chamber pressure of about 10⁻⁸ mbar. All spectra measured were corrected by setting the reference binding energy of carbon (1s) at 284.8 eV. Spectra were analyzed using the Thermo Avantage software package. The deconvolution of spectra was performed using a mixed Gauss-Lorentzian function, the quantification was done by using the Scofield sensitivity factors. Difference in depth of analysis for different photoelectron lines was accounted using the TPP-2M method.

Low- and high current density electrochemical CO₂ reduction. Screening of the Ag/MPL-nC (n = 1, 2, 3, 6) samples in CO₂ER was conducted in a custom-made airtight, two-compartment, three-electrode cell, Ag/MPL-nC samples were used as working electrode and Pt as counter electrode separated from the cathode part by a glass frit. A standard calomel electrode was used (SCE) was used as the reference electrode. The CO₂ electroreduction was carried out using in CO₂-saturated 0.1 M KHCO solution (pH = 6.8) under stirring at a CO₂ flow rate of 10 mL min⁻¹ in all experiments. All potentials for CO₂ reduction are reported with respect to the reversible hydrogen electrode (RHE).

The high current density continuous-flow CO₂ electrolysis was performed in a custom-built zero-gap electrochemical cell. The flow electrolyzer was modified from a Fuel Cell Technologies 5 cm² PEM single cell to fit to the specific task of CO₂ER. A membrane electrode assembly (MEA) is a sandwich-like structure of an ion-exchange membrane and a cathode and anode side catalyst layer on gas diffusion electrodes pressed against it. MEAs first found widespread use in polymer electrolyte fuel cells, and water electrolyzers, and recently it is being spread in flow CO₂ electrolysis using zero-gap flow cells [8]. We constructed our MEAs with a catalyst active area of 1.9 cm² of the Ag/ microporous layer covered carbon cloth (ELAT LT1400) cathode and 5.0 cm² of a woven nickel mesh anode. An imidazolium-functionalized anion-exchange membrane (Sustainion S-50) separated the two compartments. The MEA was sandwiched between two flow-field blocks of stainless steel (Type 316L) and PTFE as cathode and anode, respectively. Since PTFE is an insulator, a patterned titanium plate used as anode charge collector. Silicone gaskets (15 mil, Fuel Cell Store) were used to make the cell gas tight, and the aluminium end plates were screwed together using a torque wrench at 20-30 in-lbs (~2.3-3.4 N m). 1 M KOH aqueous anolyte solution was recirculated in the anode compartment by a Watson Marlow 323 peristaltic pump at 10 mL min⁻¹. The cathode side was fed with humidified CO₂ stream with ~1-5 vol% N₂ as internal standard at 40 ml min⁻¹ total flow rate, controlled by a calibrated Brooks Delta Smart II mass flow controller. CO₂ electrolysis was conducted under constant current conditions (CP, chronopotentiometry) using a potentiostat (BioLogic SP-150). The potential of the counter electrode was continuously monitored via a Hg/HgO (1 M NaOH) reference electrode inserted into the anolyte

chamber right behind the Ti anode current collector. The product distribution in CO₂ electroreduction experiments was determined by gas chromatography in the gas phase. Gas products were analyzed every 5 min via a SRI Instruments T-3000 micro gas chromatograph equipped with MolSieve 5A and Poraplot Q columns and a micro TCD detector. The reported Faradaic efficiencies are averages over the time of the electrolysis. No liquid products were obtained in the experiments reported herein.

In a typical experiment, the Ag-CP layer on the microporous side of the carbon cloth was first transformed into an Ag/carbon cloth catalyst via a 30-min-long chronoamperometric (CA) run at a constant potential of -2 V (vs. Hg/HgO). The in-situ formed catalysts were then tested via chronopotentiometry at constant current densities of -25 , -50 , -100 , -200 , -300 , and -400 mA cm⁻² for 30 min. Since we used a GDL based electrolyzer, fluctuations in the potential readings were observed due to the intensive bubble formation. The reported cell and cathode potentials are averages over the respective electrolysis run. Since it is a zero-gap cell without using a liquid catholyte, the working electrode potential could be approximated from the directly determined counter electrode potential and the full cell voltage. The raw cathode potential readings were manually corrected to the RHE scale via eq. (1) taking the membrane resistance into account as an iR drop. The uncorrected R_u resistance between the counter and reference electrode was determined via EIS connecting the originally counter electrode nickel mesh as working electrode. Due to the small distance between the CE and RE and the high conductivity of the electrolyte solution, the resulting iR_u was negligible even at the highest applied current density -400 mA cm⁻².

The parameters characterizing the electrochemical performance of the catalysts were calculated according to the following equations.

RHE correction:

The measured potentials vs. Ag/AgCl (sat'd KCl) and Hg/HgO (1 M NaOH) in the H-cell and the flow cell, respectively, were converted to the reversible hydrogen electrode (RHE) scale according to the following equation:

$$E(\text{vs. RHE}) = E(\text{vs. RE}) + E_{RE}^{\circ}(\text{vs. SHE}) + 0.059 \text{ V} \cdot \text{pH} \quad (1)$$

$E(\text{vs. RE})$: the experimentally measured potential vs. the respective reference electrode;

$$E^{\circ}\text{Ag/AgCl}(\text{sat'd KCl}) = 0.197 \text{ (V vs. SHE) at } 23 \text{ }^{\circ}\text{C};$$

$$E^{\circ}\text{Hg/HgO}(1 \text{ M NaOH}) = 0.118 \text{ (V vs. SHE) at } 23 \text{ }^{\circ}\text{C};$$

SHE: Standard hydrogen electrode;

pH: The pH of the used electrolyte solution: 13.5 for 1 M KOH, and 6.8 for CO₂ saturated 0.1 M KHCO₃;

Faradaic efficiency (FE):

The fraction of the total charge consumed to form product 'x' was calculated according to

$$FE_x = \frac{n \cdot F \cdot v_x \cdot f}{V_m \cdot j} \quad (2)$$

FE_x : the Faradaic efficiency of product 'x';

n : the number of electrons consumed to produce one molecule of product, $n = 2$ for both CO and H₂;

v_x : the volume fraction of a certain gas product;

f : the overall gas flow rate at ambient pressure and temperature (m³ s⁻¹);

F : Faraday constant ($F=96\,485.3329 \text{ C mol}^{-1}$);

V_m : the molar volume constant at ambient pressure and temperature
($V_m=24.465 \text{ L mol}^{-1}$);

j : steady-state cell total current at each applied potential (mA).

Partial current density:

$$j_x = \frac{FE_x \cdot j_{Total}}{100} \quad (3)$$

j_x : partial current density of product x (mA cm⁻²);

FE_x : Faraday efficiency of product x (%);

j_{Total} : total current density all product combined (mA cm⁻²);

Energy efficiency:

The ratio of between the stored energy in product ‘x’ and the electrical energy applied to the system was determined according to eq. (4):

$$EE_x = \frac{E^\circ}{U_{Cell}} \cdot FE_x \quad (4)$$

EE_x : energy efficiency of product x (%);

E° : equilibrium cell potential ($E^\circ = E^\circ_{cathode} - E^\circ_{anode} = -0.10 \text{ V} - 1.23 \text{ V} = -1.33 \text{ V}$ for CO₂ to CO);[9]

U_{Cell} : overall cell potential (V).

Electrochemical active surface area (EASA) experiment. The electrochemical active surface areas of Ag electrodes were compared using the monolayer oxidation method in a traditional three-electrode aqueous electrochemical cell with platinum and Ag/AgCl (Sat’d KCl) counter and reference electrodes, respectively [10]. The current density peak at about

1.15-1.20 V vs. RHE corresponds to the formation of monolayer silver oxide or AgOH (Figure S2.22a).

The measurement was carried out in 0.1 M KOH with bubbling N₂. The electrodes were reduced at -0.4 V vs RHE for 10 min in order to reduce the already existing silver oxide layer, and then immediately oxidized by a constant potential of 1.15 V vs RHE to form monolayer silver oxide. By measuring the charge used during oxidation, the relative active surface area of a Ag catalyst can be calculated. The reported values are averages of four consecutive measurements (Figure S22b). Both, the Ag-CP/MPL-nC and the Ag/MPL-nC electrodes (Figure S22c-f) were tested.

2.5.4. Supplementary experimental results

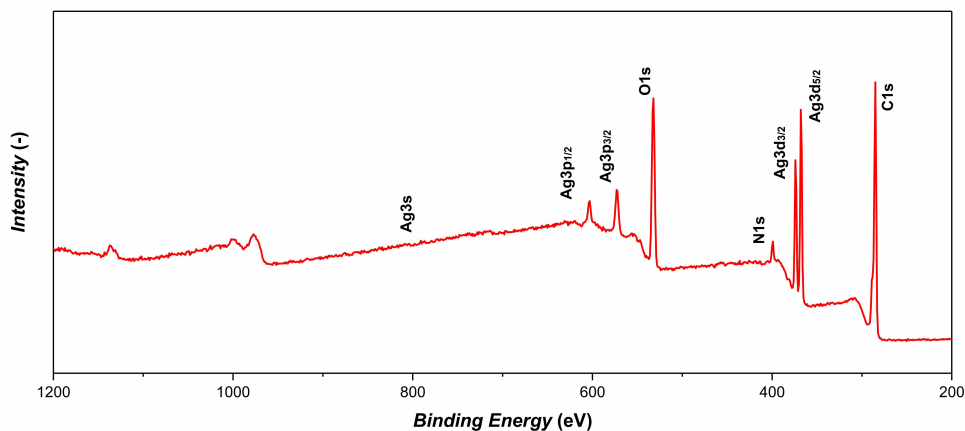
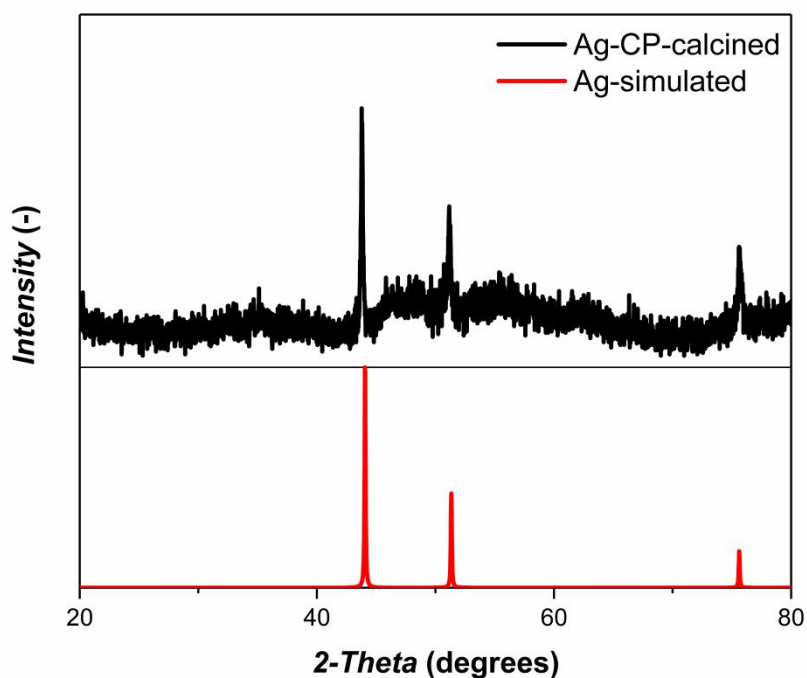


Figure S2.6. XPS survey spectrum of Ag-CP.

Table S2.5. Atomic (surface) content of elements in Ag-CP determined by XPS.

Element	Atomic content (%)
C	68.8
Ag	3.5
N	3.2
O	24.5

**Figure S2.7.** XRD pattern of Ag-CP after calcination at 600 °C in air (*black*) and the simulated XRD pattern of metallic Ag (*red*).

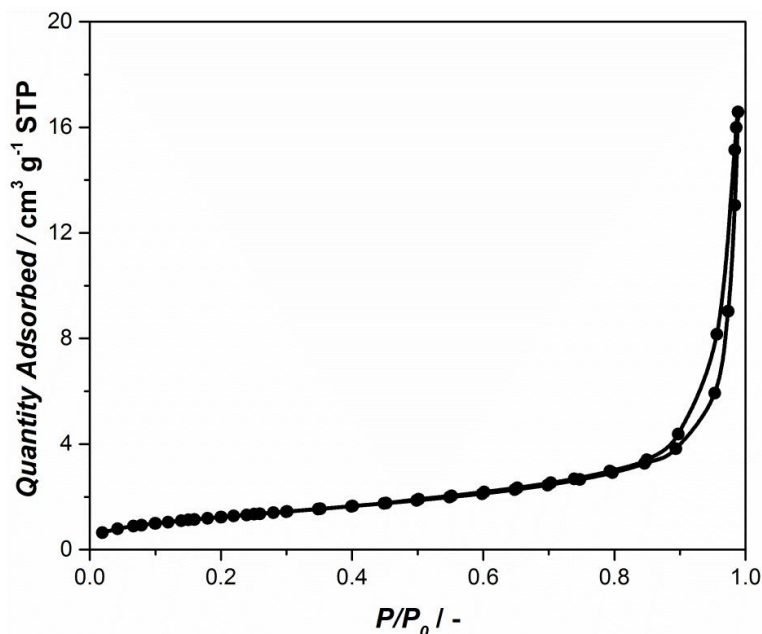
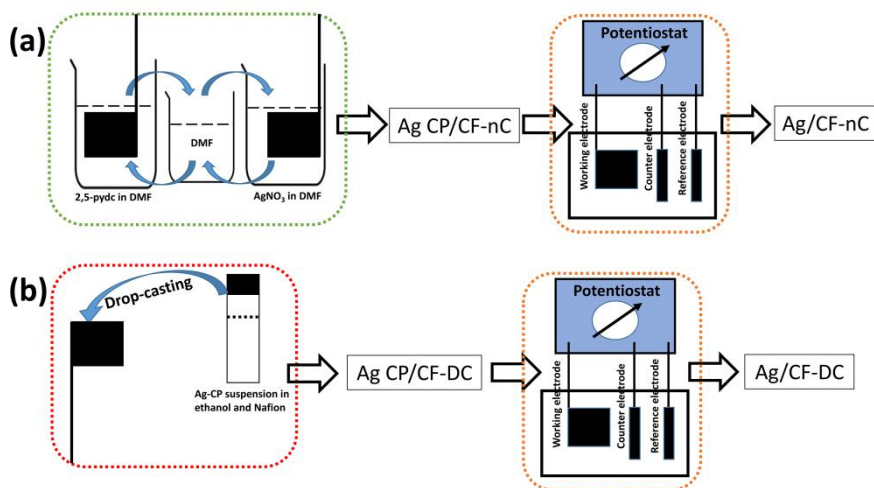


Figure S2.8. N_2 isotherm of Ag-CP at 77 K.



Scheme S2.1. Schematic synthesis route of (a) Ag/CF-nC electrode and (b) Ag/CF-DC electrode. Green, orange, and red boxes represent LBL growth of Ag-CP, electro-decomposition of Ag-CP, and drop-casting of Ag-CP on carbon cloth, respectively.

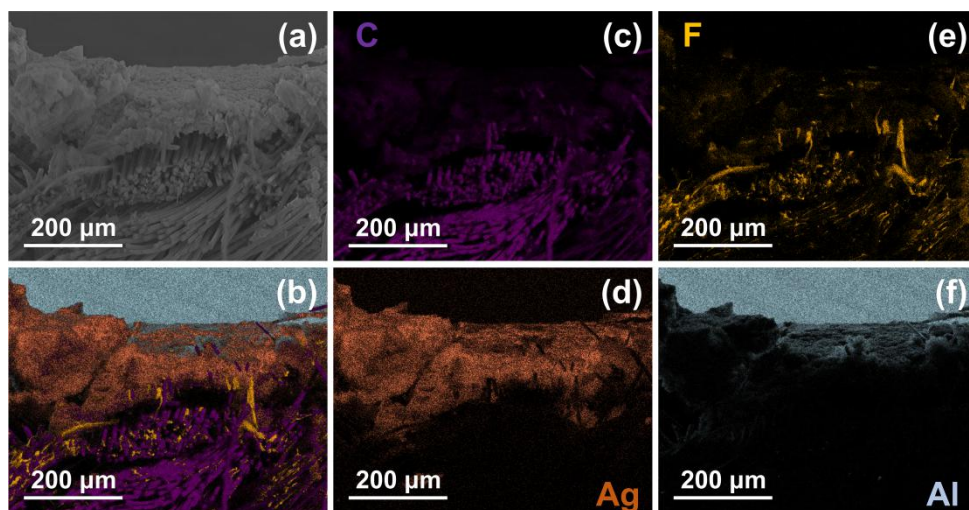


Figure S2.9. Cross-sectional SEM image (a) and the corresponding EDS elemental map (b) of the 20 LBL cycle sample (Ag-CP/MPL-20C). The component maps of (c) carbon, (d) silver, (e) fluorine and (f) Al are also shown. The fluorine signal comes from the PTFE treated carbon fabric, while Al is the sample holder.

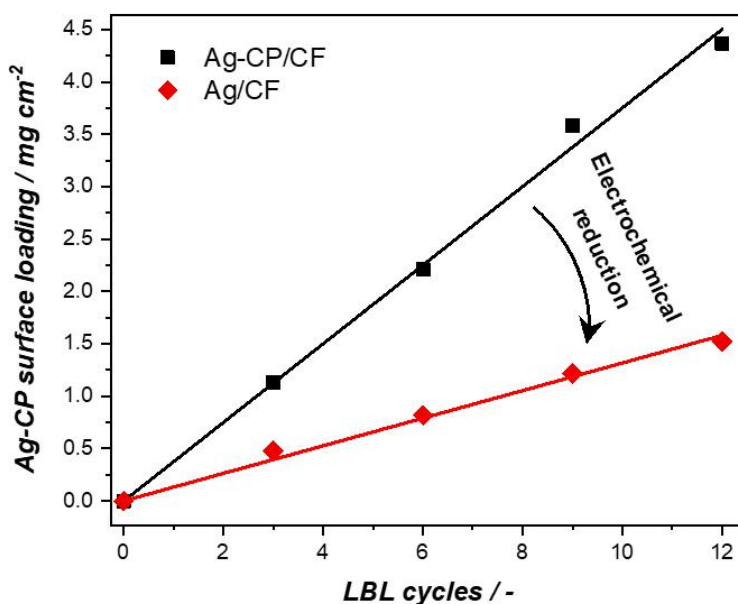


Figure S2.10. Variation of the Ag-CP and Ag (before and after in-situ electro-decomposition) loading with the number of sequential deposition steps (LBL cycles) on bare carbon fibre support.

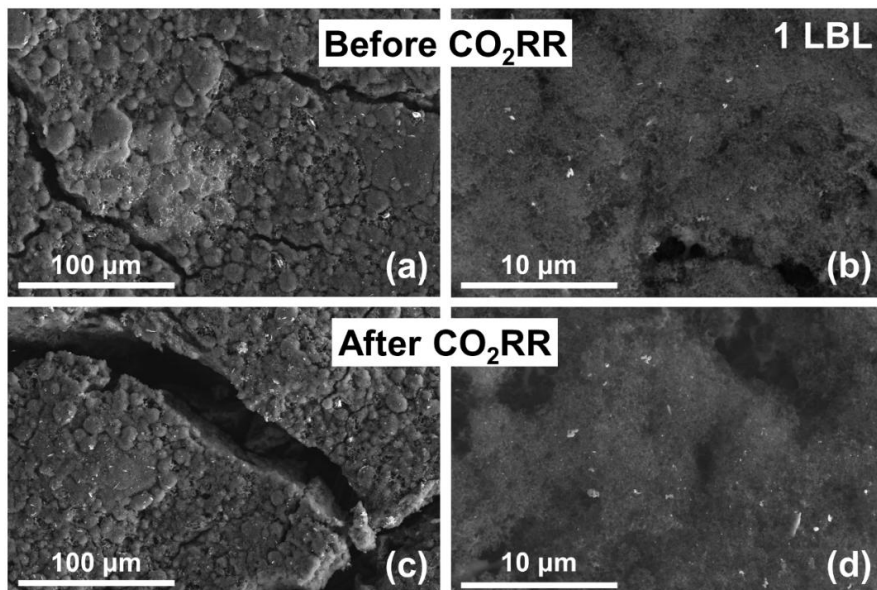


Figure S2.11. SEM images of the 1 LBL cycle sample (Ag/MPL-1C) before (a-b) and after (c-d) in-situ electro-decomposition.

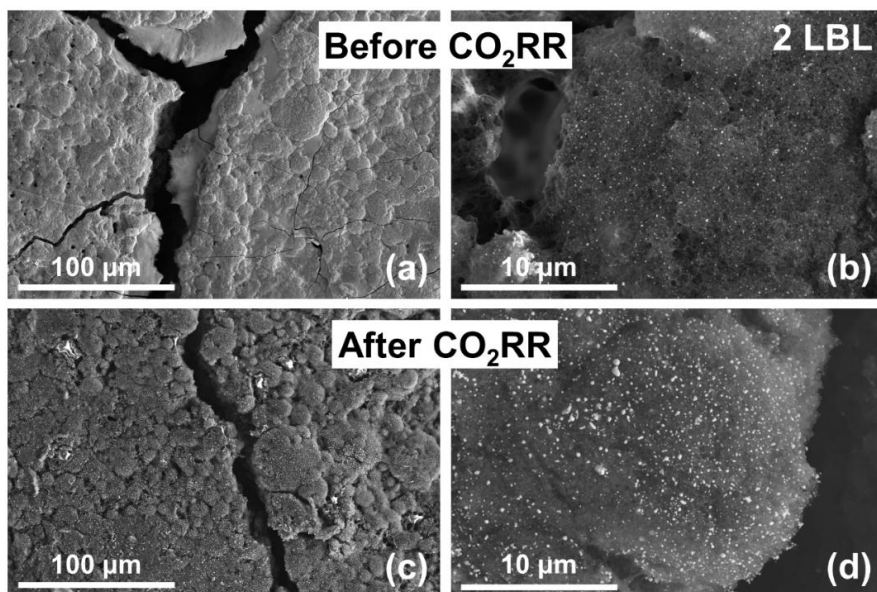


Figure S2.12. SEM images of the 2 LBL cycle sample (Ag/MPL-2C) before (a-b) and after (c-d) in-situ electro-decomposition.

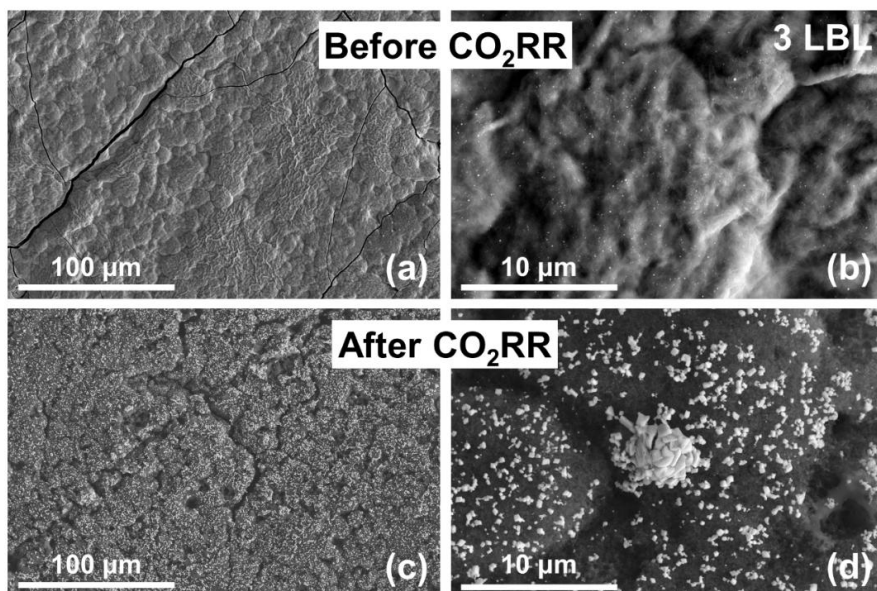


Figure S2.13. SEM images of the 3 LBL cycle sample (Ag/MPL-3C) before (a-b) and after (c-d) in-situ electro-decomposition.

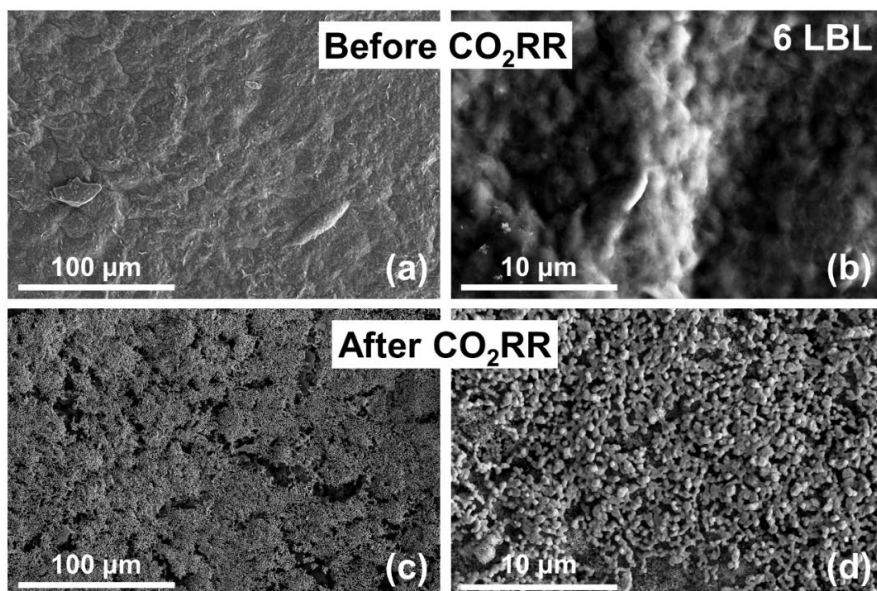


Figure S2.14. SEM images of the 6 LBL cycle sample (Ag/MPL-6C) before (a-b) and after (c-d) in-situ electro-decomposition.

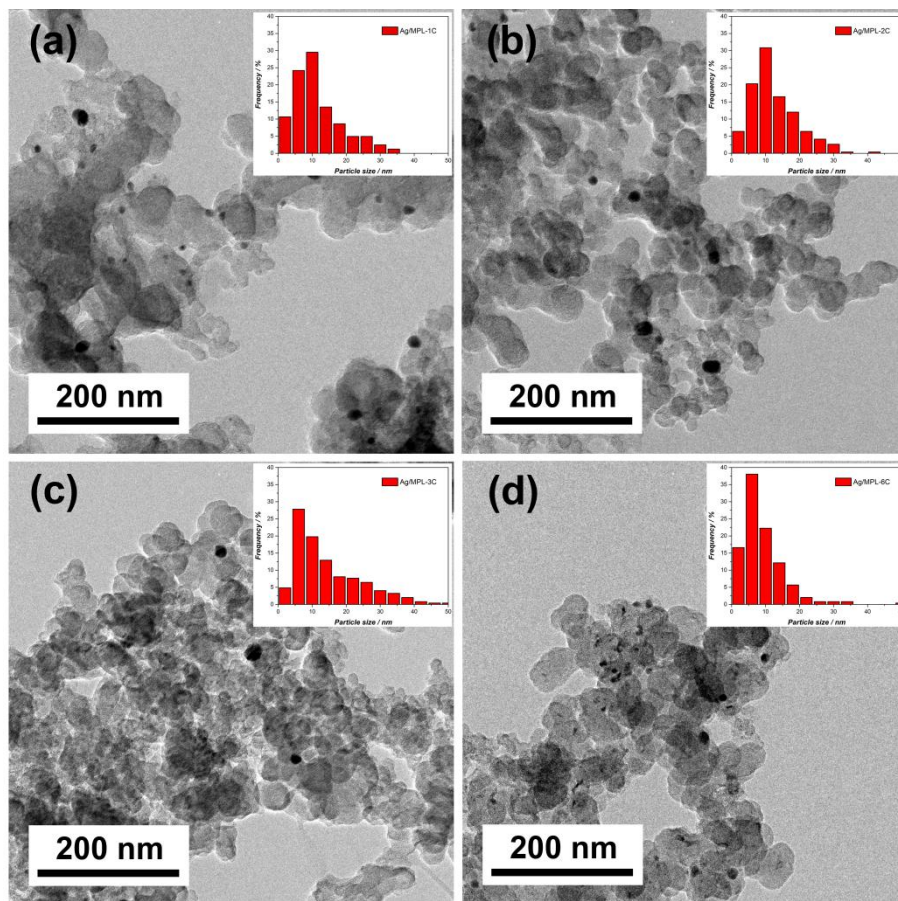


Figure S2.15. TEM images of the microporous layer supported Ag nanoparticles and the corresponding particle size distributions of the $n =$ (a) 1, (b) 2, (c) 3, (d) 6 Ag/MPL- n C samples.

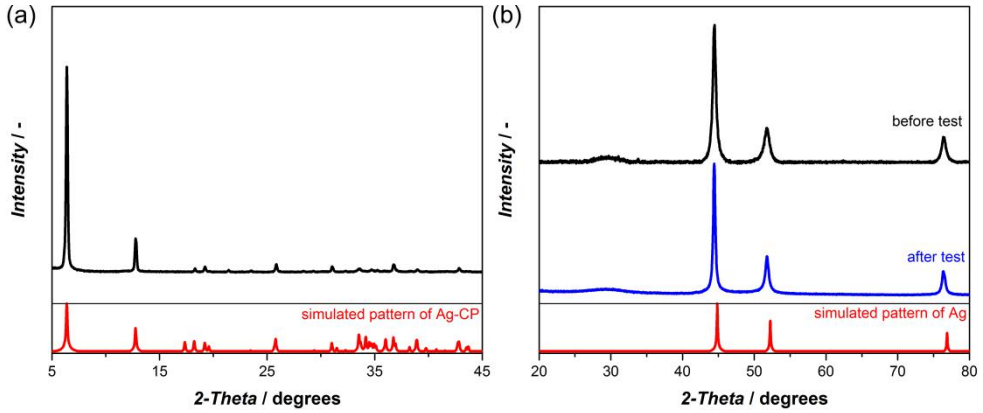


Figure S2.16. XRD patterns of the (a) carbon supported Ag-CP (*black*) and the simulated pattern of Ag-CP (*red*); (b) as-prepared carbon supported Ag electrode before (*black*) and after (*blue*) one CO₂ER test and simulated pattern of metallic Ag (*red*).

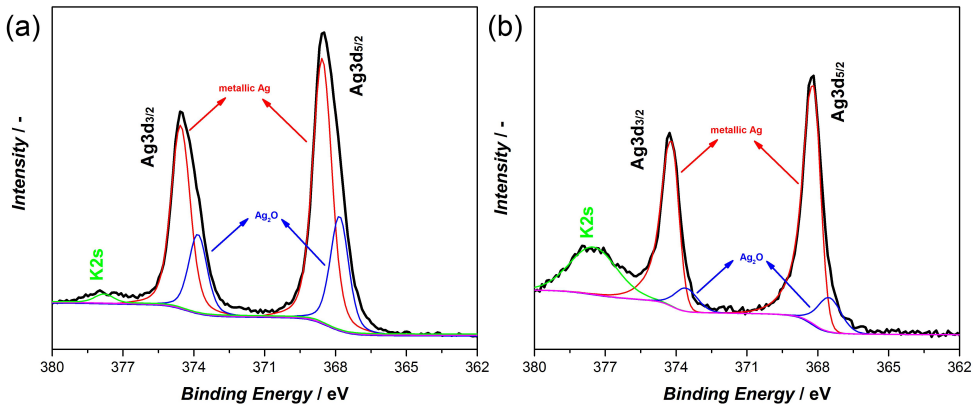


Figure S2.17. Ag 3d region XPS spectra of the Ag powders collected from carbon supported Ag electrode before (a) and after (b) one CO₂ER test with blue, red, and green peaks representing Ag₂O, metallic Ag and K, respectively.

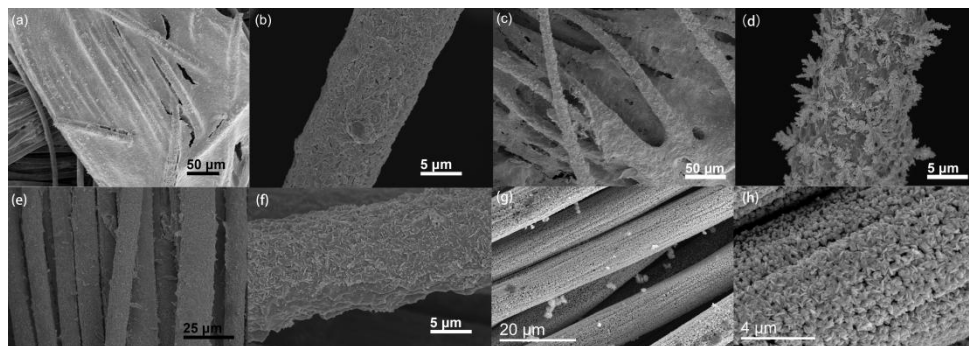


Figure S2.18. SEM images of an electrode prepared onto bare woven carbon fibers by conventional drop casting (a-b) before and (c-d) after electro-decomposition. SEM images of an electrode prepared onto bare woven carbon fibers by L-B-L method (e-f) before and (g-h) after electro-decomposition.

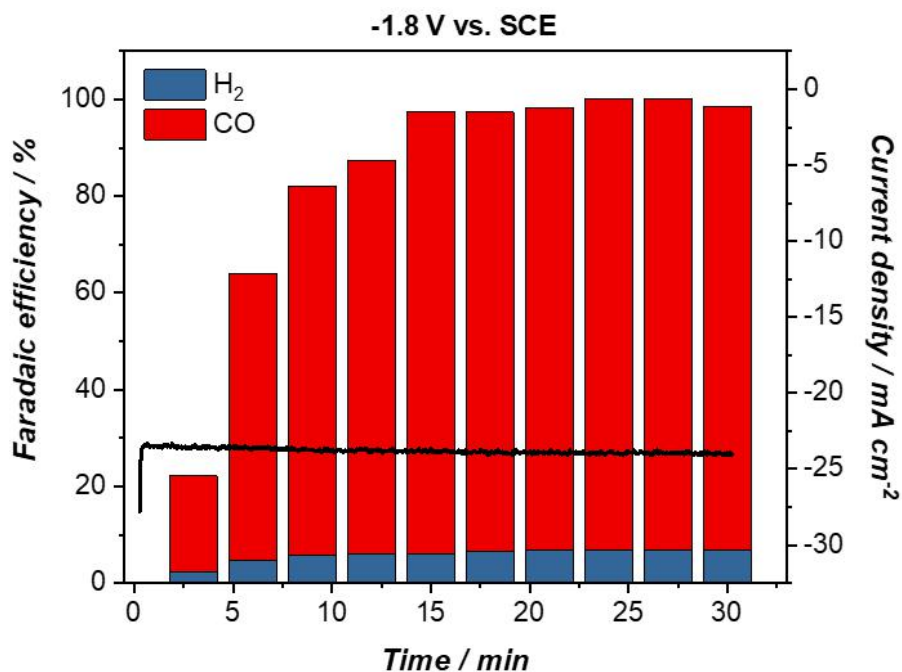


Figure S2.19. Typical chronoamperometric in-situ reduction of the Ag-CP/MPL-3C sample in the liquid cell at -1.8 V vs SCE (-0.88 V vs RHE). Stable CO_2 reduction performance was achieved from 15 min of the reaction.

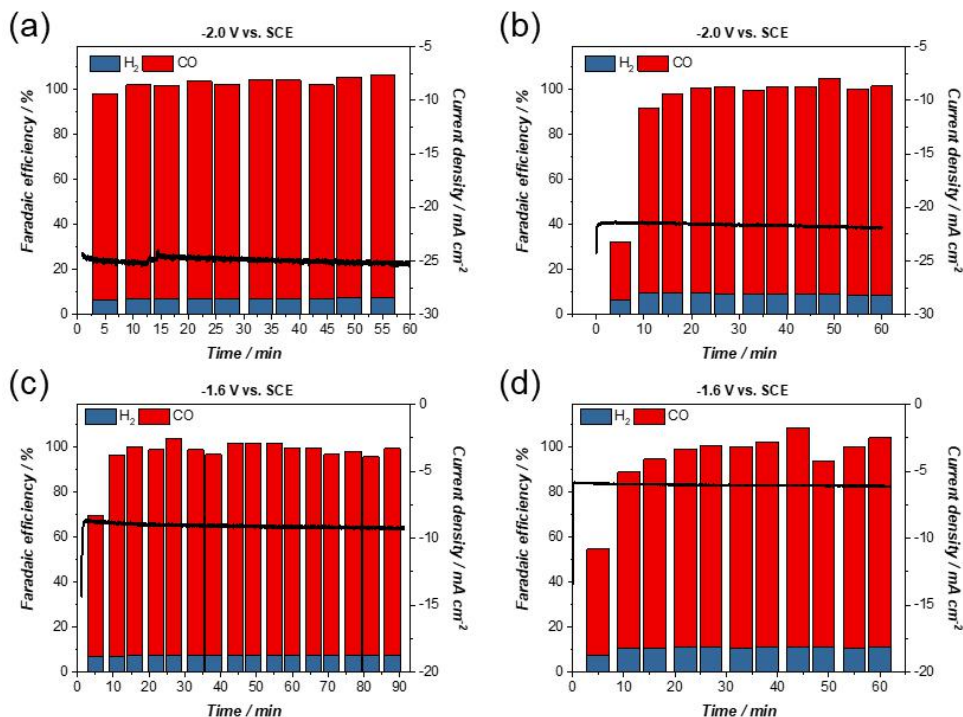


Figure S2.20. Chronoamperometric CO₂ electroreduction using the Ag/MPL-3C sample in the liquid cell at -2.0 V and -1.6 V vs SCE (-0.94 - 0.98 and -0.78 - 0.81 V vs. RHE). In (a) and (c) the CO₂ER tests were conducted in the original electrolyte solutions, where the catalysts were in-situ reduced, while in (b) and (d) the previously reduced samples were re-measured in fresh electrolyte.

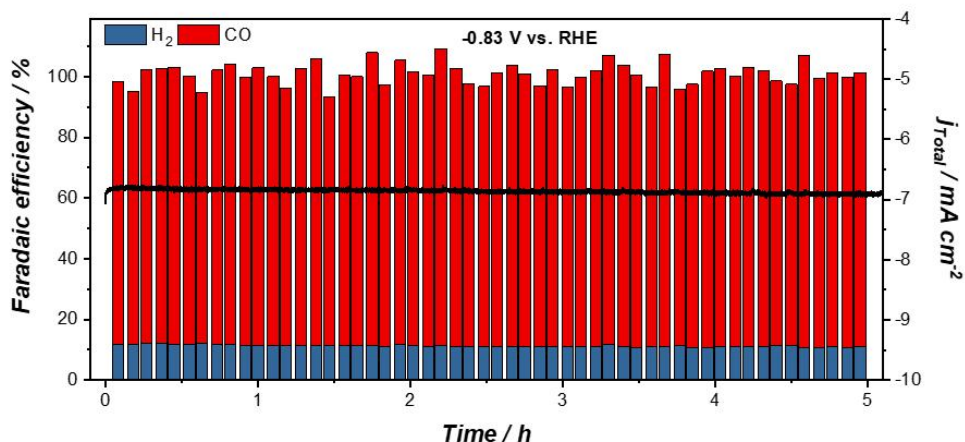


Figure S2.21. Chronoamperometric CO₂ER stability test using the Ag/MPL-3C sample in the liquid cell at -1.6 V vs SCE (-0.83 V vs. RHE). Stable CO₂ reduction performance was achieved in the 5-hour electrolysis.

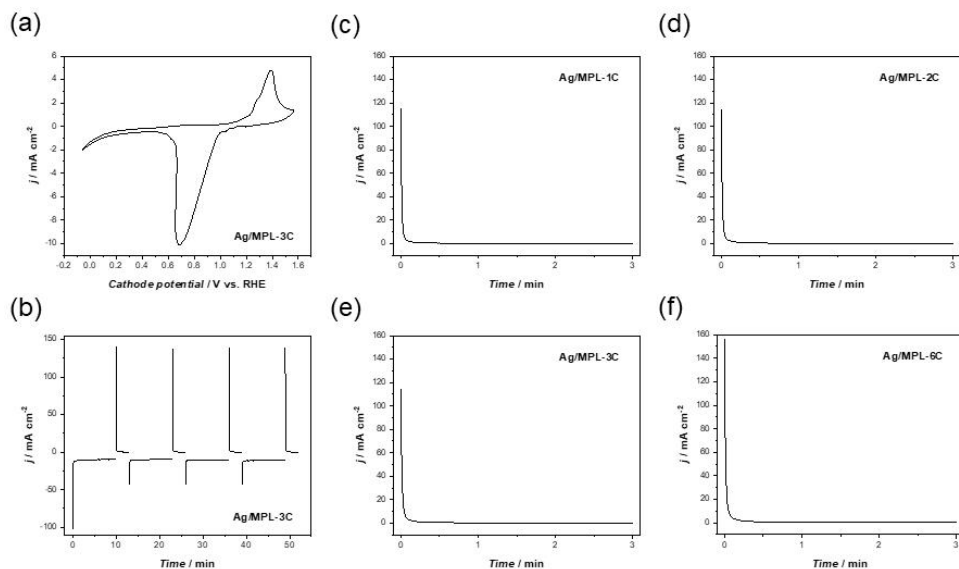


Figure S2.22. (a) Cyclic voltammetry of Ag-CP/MPL-3C in 0.1 M KOH at 20 mV s⁻¹ scan rate. Current density as a function of time at around 1.18 V vs RHE for the determination of EASA in Ag/MPL-3C (4 parallel measurements), and the first monolayer reduction curves for Ag/MPL-*n*C, where *n* = (c) 1, (d) 2, (e) 3, and (f) 6.

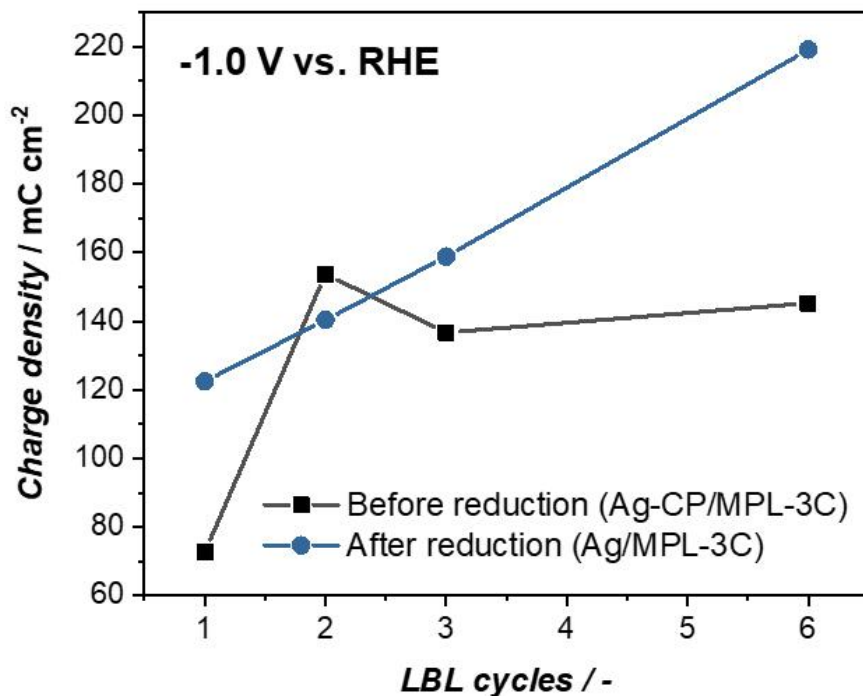


Figure S2.23. Variation of the electrochemical active area (EASA) of the Ag-CP/MPL-3C and Ag/MPL-3C with ongoing LBL cycles.

Table S2.6. Loading amount of Ag-CP and Ag on carbon cloth electrodes.

Electrode	Ag-CP loaded (mg)	Ag loaded (mg)	Ag loading density (mg cm ⁻²)
Dropcasted	46.5	19.4	3.10
Ag/CF-3C	7.1	3	0.48
Ag/CF -6C	13.8	5.1	0.82
Ag/CF -9C	22.4	7.6	1.22
Ag/CF -12C	27.3	9.5	1.52
Ag/MPL-3C	0.55	0.38-0.4	0.20-0.21

Table S2.7. Summary of recently reported Ag-based electrodes in H-type CO₂ electrolyzers.

Catalyst	Loading	Electrolyte		FE_{CO} (%)	j_{CO} (mA/cm ⁻²)	Mass activity (mA/mg)	Ref.
Polycrystalline Ag	Bulk (thickness 0.25mm)	0.1 KHCO ₃	M	~85	~2.1	~0.008	[11]
Oxide-derived Ag	Bulk (thickness 0.25mm)	0.1 KHCO ₃	M	~95	~2.7	~0.011	[12]
3-D porous Ag	Bulk (thickness 0.5mm)	0.1 KHCO ₃	M	94.7	~10.0	~0.020	[13]
Triangular Ag nanoplate	~0.637 mg cm ⁻²	-		90	3.0	4.710	[14]
Nanoporous Ag	10 mg cm ⁻²	0.5 KHCO ₃	M	~92	8.0	~2.000	[15]
Plasma-activated Ag	Bulk (thickness 0.008mm)	0.1 KHCO ₃	M	>90	2.25	~0.280	[16]
Preferentially oriented Ag	Bulk (thickness 0.1mm)	0.5 KHCO ₃	M	96.7	~9.0	~0.090	[17]
Ag nanoparticle	10 mg/cm ²	EMIM-BF ₄		>96	~0.92	0.137	[18]
Anodic-etched Ag	Bulk (thickness 0.25mm)	0.1 KHCO ₃	M	92%	1.50	~0.006	[10a]
Ag/MPL-3C	0.205 mg/cm ²	0.1 KHCO ₃	M	93.0%	30.2	147.15	This work

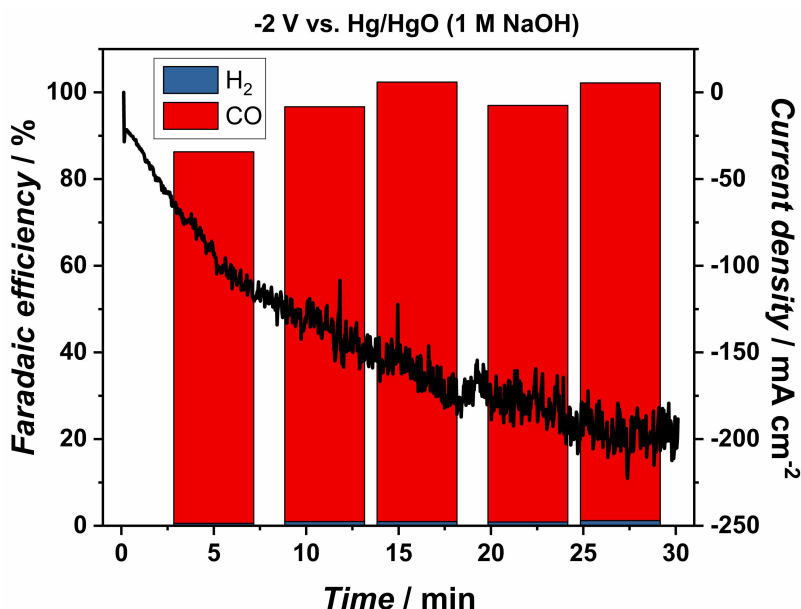


Figure S2.24. Typical chronoamperometric curve of the in-situ reduction of a Ag/CP-3C/carbon cloth sample into a Ag/carbon cloth catalyst in the zero gap flow cell during the first half hour of the CO₂ electrolysis. The catalyst was selective to CO right from the beginning of the reaction, and reaches stable high current between 20 and 30 min of the run.

Table S2.8. CO₂ to CO electroreduction performance in a gas-fed flow electrolyzer in terms of cell (U_{Cell}) and cathode potentials ($E_{Cathode}$), Faradaic efficiency (FE_{CO}), mass activity, and energetic efficiency (EE_{CO}) on the Ag/MPL electrode.

j_{Total} (mA cm ⁻²)	U_{Cell} (V)	$E_{Cathode}$ (V vs. RHE)	FE_{CO} (%)	Mass activity for CO (mA mg _{Ag} ⁻¹)	EE_{CO} (%)
-25	-2.07	-0.36	96.9	117.3	62.4
-50	-2.35	-0.55	97.9	237.0	55.5
-100	-3.07	-0.70	98.5	476.7	42.7
-200	-3.37	-0.84	99.5	962.9	39.3
-300	-3.59	-0.94	98.8	1435.1	36.6
-400	-3.78	-1.02	96.3	1864.3	33.8

Table S2.9. A comparison of CO₂-to-CO electroreduction literature data achieved with flow cell in terms of maximum CO current density (j_{CO}), cell voltage (U_{cell}), cathode potential ($E_{Cathode}$), CO Faradaic efficiency (FE_{CO}) and CO energy efficiency (EE_{CO}).

Catalyst	U_{cell} (V)	$E_{Cathode}$ (V vs. RHE)	FE_{CO} (%)	j_{CO} (mA cm ⁻²)	Mass activity (mA/mg)	EE_{CO} (%)	Ref.
AgDAT	-3.5	-0.90	93.0	109.3	1267.8	35.4	[19]
AgPz	-3.5	-0.77	90.4	76.8	1780.9	34.4	[19]
AgPc	-3.5	-0.98	75.7	107.6	1721.0	28.8	[19]
Ag NP	-3.0	-0.91	94.7	248.4	276.0	42.0	[20]
Nanoporous Ag	-	-0.80	93.1	34.7	0.9	-	[15]
Ag NP/MWNT	-3.0	-0.80	102.1	356.6	1782.9	45.3	[21]
Ag NP/XC-72R	-3.0	-0.85	98.9	116.2	112.9	43.9	[22]
40 wt% Ag NP/P25 TiO ₂	-3.0	-0.81	93.3	100.6	257.6	41.4	[22]
20 wt% Ag NP/P25 TiO ₂	-3.0	-0.84	92.6	102.4	533.2	41.1	[22]
5 wt% Ag NP/P25 TiO ₂	-3.0	-0.79	45.6	45.6	2695.7	23.9	[22]
Ag NP	-3.0	-1.08	91.2	436.4	218.2	40.4	[23]
Ag NP	-3.0	-1.21	97.5	280.9	351.1	43.2	[24]
Au/PyPBI/MWNT	-	-1.18	62.1	159.9	940.3	-	[25]
g-C ₃ N ₄ /MWNT	-3.0	-1.01	98.1	90.2	37.7	43.5	[26]
Ag/carbon foam	-3.0	-1.07	65.0	121.6	211.8	32.5	[27]
Au/PyPBI/MWNT	-2.5	-0.65	63.6	203.0	1127.5	33.3	[9]
Covestro Ag ODC	-4.7	-	73.5	232.4	~0.9-1.7	21.9-24.2	[28]
Sputtered Ag/PTFE	-	-0.67	89.7	180.0	-	-	[29]
CD-Ag/PTFE	-	-0.81	90.6	157.7	-	-	[29]
Ag/PTFE	-5.9	-0.84	84.3	252.9	126.5	19.1	[30]
Ag NP/carbon felt	-	-	60.4	108.7	72.4	-	[31]
Ni-N-C	-	-1.11	73.5	220.8	220.8	-	[32]
Porous Zn GDE	-	-0.68	73.0	218.9	33.7	-	[33]
Ag/MPL-3C	-3.8	-1.02	96.3	385.2	1864.3	33.8	This work

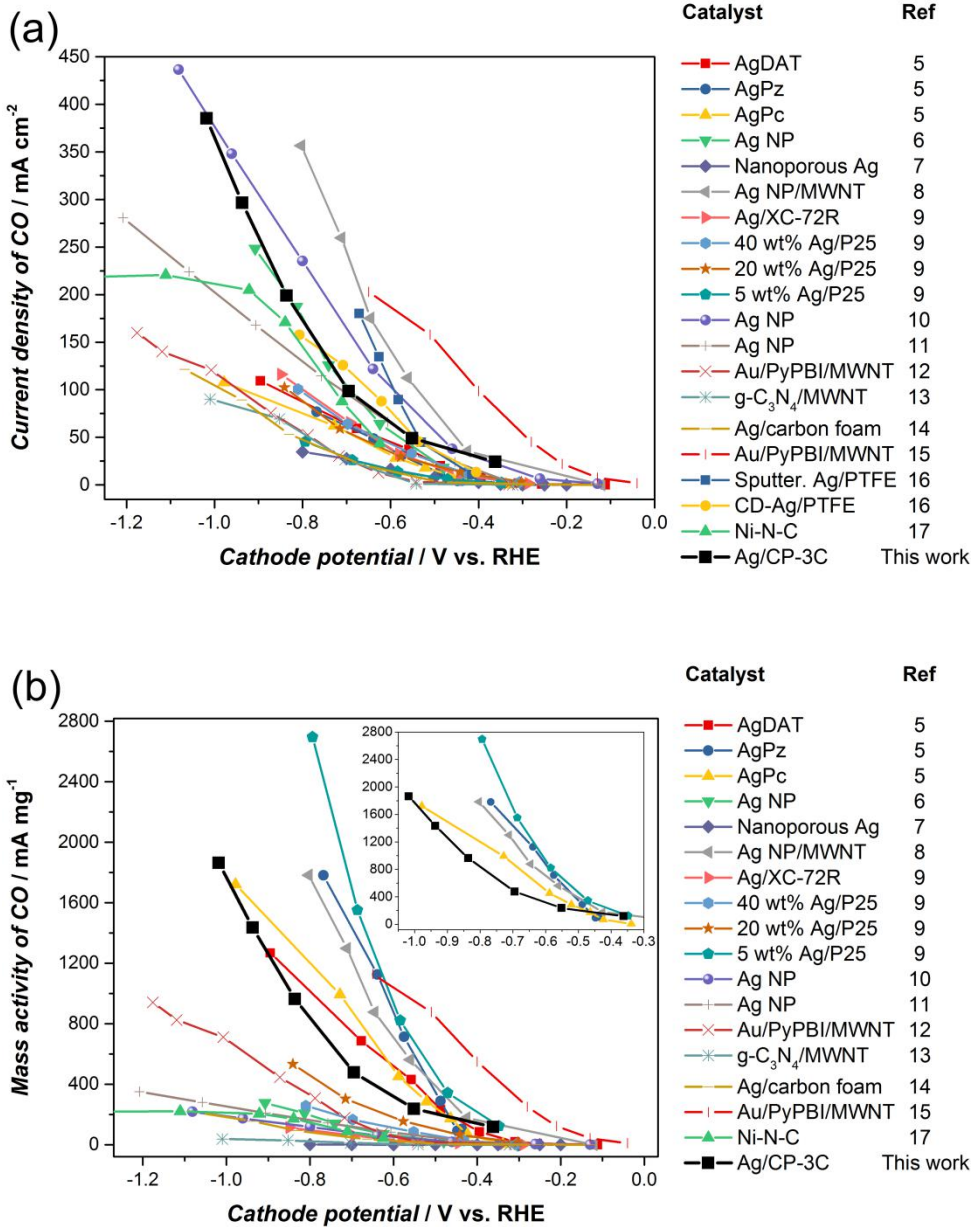


Figure S2.25. A comparison of flow cell CO₂-to-CO electroreduction literature data in terms of (a) maximum CO current density (j_{CO}) and (b) mass activity for CO against cathode potential ($E_{Cathode}$). The inset graph in panel b shows mass activity curves for catalysts with a reported maximum mass activity of higher than 1500 mA mg⁻¹.

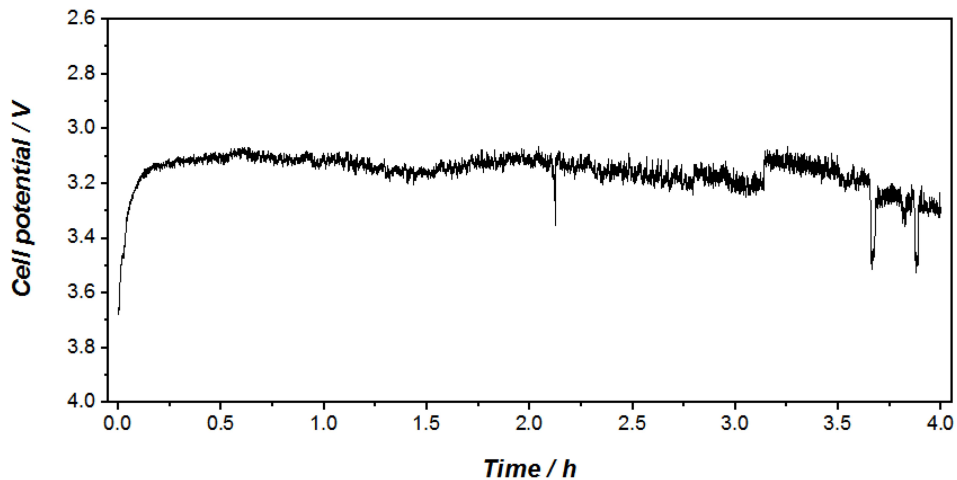


Figure S2.26. Cell potential in the long-term stability test of the Ag/CP-3C sample derived Ag/carbon cloth sample in a flow electrolyzer.

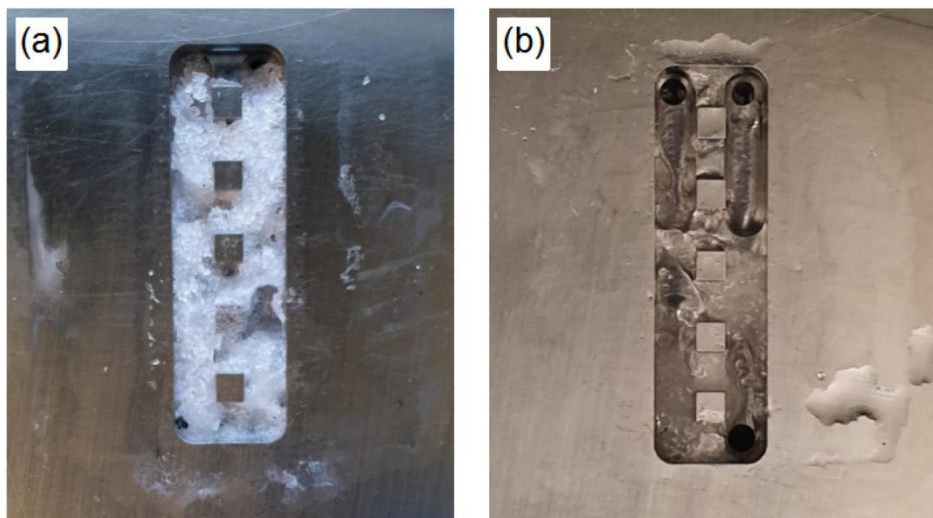


Figure S2.27. Crystal precipitates in the cathode flow channels after long-term electrolysis (a) without and (b) with humidifying the CO₂ gas feed.

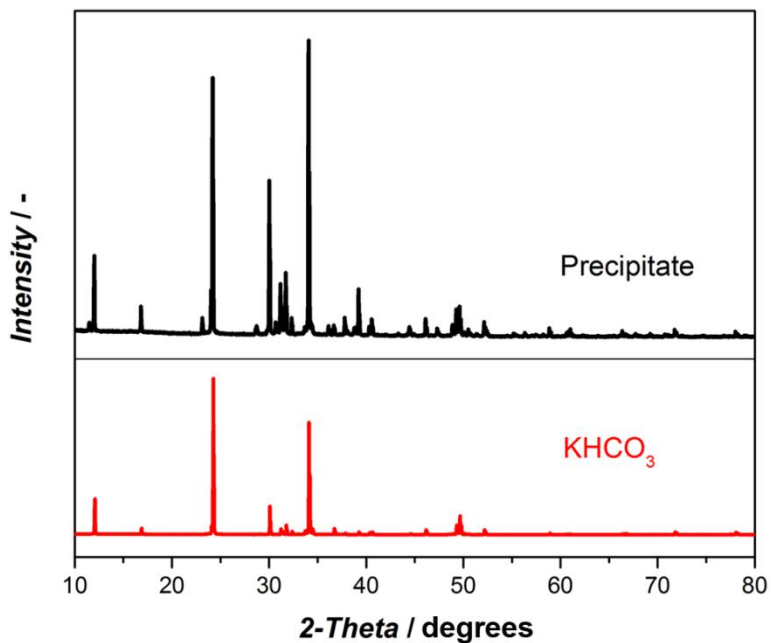


Figure S2.28. XRD pattern of the crystalline precipitate from the cathode gas flow channels. The pattern for KHCO₃ is plotted for comparison.

2.5.5. References for supporting information

1. Boultif, A.; Louer, D., Powder pattern indexing with the dichotomy method. *J Appl Crystallogr* 2004, 37, 724-731.
2. Pawley, G. S., Unit-Cell Refinement from Powder Diffraction Scans. *J Appl Crystallogr* 1981, 14 (Dec), 357-361.
3. Altomare, A.; Corriero, N.; Cuocci, C.; Falcicchio, A.; Moliterni, A.; Rizzi, R., EXPO software for solving crystal structures by powder diffraction data: methods and application. *Cryst Res Technol* 2015, 50 (9-10), 737-742.
4. Groom, C. R.; Bruno, I. J.; Lightfoot, M. P.; Ward, S. C., The Cambridge Structural Database. *Acta Crystallogr B Struct Sci Cryst Eng Mater* 2016, 72 (Pt 2), 171-9.
5. Bruno, I. J.; Cole, J. C.; Kessler, M.; Luo, J.; Motherwell, W. D.; Purkis, L. H.; Smith, B. R.; Taylor, R.; Cooper, R. I.; Harris, S. E.; Orpen, A. G., Retrieval of crystallographically-derived molecular geometry information. *J Chem Inf Comput Sci* 2004, 44 (6), 2133-44.
6. Lu, X.; Ye, J.; Zhang, D.; Xie, R.; Bogale, R. F.; Sun, Y.; Zhao, L.; Zhao, Q.; Ning, G., Silver carboxylate metal–organic frameworks with highly antibacterial activity and biocompatibility. *Journal of Inorganic Biochemistry* 2014, 138, 114-121.
7. Endrődi, B.; Kecsenovity, E.; Samu, A.; Darvas, F.; Jones, R. V.; Török, V.; Danyi, A.; Janáky, C., Multilayer Electrolyzer Stack Converts Carbon Dioxide to Gas Products at High Pressure with High Efficiency. *ACS Energy Letters* 2019, 4 (7), 1770-1777.
8. Weekes, D. M.; Salvatore, D. A.; Reyes, A.; Huang, A.; Berlinguette, C. P., Electrolytic CO₂ Reduction in a Flow Cell. *Accounts Chem Res* 2018, 51 (4), 910-918.
9. Verma, S.; Hamasaki, Y.; Kim, C.; Huang, W.; Lu, S.; Jhong, H.-R. M.; Gewirth, A. A.; Fujigaya, T.; Nakashima, N.; Kenis, P. J. A., Insights into the Low Overpotential Electroreduction of CO₂ to CO on a Supported Gold Catalyst in an Alkaline Flow Electrolyzer. *ACS Energy Letters* 2018, 3 (1), 193-198.
10. (a) Ma, M.; Liu, K.; Shen, J.; Kas, R.; Smith, W. A., In Situ Fabrication and Reactivation of Highly Selective and Stable Ag Catalysts for Electrochemical CO₂ Conversion. *ACS Energy Letters* 2018, 3 (6), 1301-1306; (b) Rosen, J.; Hutchings, G. S.; Lu, Q.; Rivera, S.; Zhou, Y.; Vlachos, D. G.; Jiao, F., Mechanistic Insights into the

- Electrochemical Reduction of CO₂ to CO on Nanostructured Ag Surfaces. *ACS Catal* 2015, 5 (7), 4293-4299.
11. Ma, M.; Trzesniewski, B. J.; Xie, J.; Smith, W. A., Selective and Efficient Reduction of Carbon Dioxide to Carbon Monoxide on Oxide-Derived Nanostructured Silver Electrocatalysts. *Angewandte Chemie* 2016, 55 (33), 9748-52.
 12. Won da, H.; Shin, H.; Koh, J.; Chung, J.; Lee, H. S.; Kim, H.; Woo, S. I., Highly Efficient, Selective, and Stable CO₂ Electroreduction on a Hexagonal Zn Catalyst. *Angewandte Chemie* 2016, 55 (32), 9297-300.
 13. Daiyan, R.; Lu, X. Y.; Ng, Y. H.; Amal, R., Highly Selective Conversion of CO₂ to CO Achieved by a Three-Dimensional Porous Silver Electrocatalyst. *Chemistryselect* 2017, 2 (3), 879-884.
 14. Liu, S.; Tao, H.; Zeng, L.; Liu, Q.; Xu, Z.; Liu, Q.; Luo, J. L., Shape-Dependent Electrocatalytic Reduction of CO₂ to CO on Triangular Silver Nanoplates. *J Am Chem Soc* 2017, 139 (6), 2160-2163.
 15. Lu, Q.; Rosen, J.; Zhou, Y.; Hutchings, G. S.; Kimmel, Y. C.; Chen, J. G.; Jiao, F., A selective and efficient electrocatalyst for carbon dioxide reduction. *Nat Commun* 2014, 5, 3242.
 16. Mistry, H.; Choi, Y. W.; Bagger, A.; Scholten, F.; Bonifacio, C. S.; Sinev, I.; Divins, N. J.; Zegkinoglou, I.; Jeon, H. S.; Kisslinger, K.; Stach, E. A.; Yang, J. C.; Rossmeisl, J.; Roldan Cuenya, B., Enhanced Carbon Dioxide Electroreduction to Carbon Monoxide over Defect-Rich Plasma-Activated Silver Catalysts. *Angewandte Chemie* 2017, 56 (38), 11394-11398.
 17. Peng, X.; Karakalos, S. G.; Mustain, W. E., Preferentially Oriented Ag Nanocrystals with Extremely High Activity and Faradaic Efficiency for CO₂ Electrochemical Reduction to CO. *ACS Appl Mater Interfaces* 2018, 10 (2), 1734-1742.
 18. Rosen, B. A.; Salehi-Khojin, A.; Thorson, M. R.; Zhu, W.; Whipple, D. T.; Kenis, P. J.; Masel, R. I., Ionic liquid-mediated selective conversion of CO(2) to CO at low overpotentials. *Science* 2011, 334 (6056), 643-4.
 19. Tornow, C. E.; Thorson, M. R.; Ma, S.; Gewirth, A. A.; Kenis, P. J. A., Nitrogen-Based Catalysts for the Electrochemical Reduction of CO₂ to CO. *Journal of the American Chemical Society* 2012, 134 (48), 19520-19523.

20. Ma, S.; Luo, R.; Moniri, S.; Lan, Y.; Kenis, P. J. A., Efficient Electrochemical Flow System with Improved Anode for the Conversion of CO₂ to CO. *J Electrochem Soc* 2014, 161 (10), F1124-F1131.
21. Ma, S.; Luo, R.; Gold, J. I.; Yu, A. Z.; Kim, B.; Kenis, P. J. A., Carbon nanotube containing Ag catalyst layers for efficient and selective reduction of carbon dioxide. *J Mater Chem A* 2016, 4 (22), 8573-8578.
22. Ma, S.; Lan, Y.; Perez, G. M. J.; Moniri, S.; Kenis, P. J. A., Silver Supported on Titania as an Active Catalyst for Electrochemical Carbon Dioxide Reduction. *ChemSusChem* 2014, 7 (3), 866-874.
23. Verma, S.; Lu, X.; Ma, S.; Masel, R. I.; Kenis, P. J. A., The effect of electrolyte composition on the electroreduction of CO₂ to CO on Ag based gas diffusion electrodes. *Physical Chemistry Chemical Physics* 2016, 18 (10), 7075-7084.
24. Kim, B.; Hillman, F.; Ariyoshi, M.; Fujikawa, S.; Kenis, P. J. A., Effects of composition of the micro porous layer and the substrate on performance in the electrochemical reduction of CO₂ to CO. *J Power Sources* 2016, 312, 192-198.
25. Jhong, H.-R. M.; Tornow, C. E.; Kim, C.; Verma, S.; Oberst, J. L.; Anderson, P. S.; Gewirth, A. A.; Fujigaya, T.; Nakashima, N.; Kenis, P. J. A., Gold Nanoparticles on Polymer-Wrapped Carbon Nanotubes: An Efficient and Selective Catalyst for the Electroreduction of CO₂. *Chemphyschem* 2017, 18 (22), 3274-3279.
26. Jhong, H.-R. M.; Tornow, C. E.; Smid, B.; Gewirth, A. A.; Lyth, S. M.; Kenis, P. J. A., A Nitrogen-Doped Carbon Catalyst for Electrochemical CO₂ Conversion to CO with High Selectivity and Current Density. *ChemSusChem* 2017, 10 (6), 1094-1099.
27. Ma, S.; Liu, J.; Sasaki, K.; Lyth, S. M.; Kenis, P. J. A., Carbon Foam Decorated with Silver Nanoparticles for Electrochemical CO₂ Conversion. *Energy Technology* 2017, 5 (6), 861-863.
28. Haas, T.; Krause, R.; Weber, R.; Demler, M.; Schmid, G., Technical photosynthesis involving CO₂ electrolysis and fermentation. *Nature Catalysis* 2018, 1 (1), 32-39.
29. Dinh, C.-T.; Garcia de Arquer, F. P.; Sinton, D.; Sargent, E. H., High Rate, Selective, and Stable Electroreduction of CO₂ to CO in Basic and Neutral Media. *ACS Energy Letters* 2018, 3 (11), 2835-2840.
30. Gabardo, C. M.; Seifitokaldani, A.; Edwards, J. P.; Dinh, C.-T.; Burdyny, T.; Kibria, M. G.; O'Brien, C. P.; Sargent, E. H.; Sinton, D., Combined high alkalinity and

- pressurization enable efficient CO₂ electroreduction to CO. *Energ Environ Sci* 2018, 11 (9), 2531-2539.
31. Salvatore, D. A.; Weekes, D. M.; He, J.; Dettelbach, K. E.; Li, Y. C.; Mallouk, T. E.; Berlinguette, C. P., Electrolysis of Gaseous CO₂ to CO in a Flow Cell with a Bipolar Membrane. *ACS Energy Letters* 2018, 3 (1), 149-154.
 32. Möller, T.; Ju, W.; Bagger, A.; Wang, X.; Luo, F.; Ngo Thanh, T.; Varela, A. S.; Rossmeisl, J.; Strasser, P., Efficient CO₂ to CO electrolysis on solid Ni–N–C catalysts at industrial current densities. *Energ Environ Sci* 2019, 12 (2), 640-647.
 33. Luo, W.; Zhang, J.; Li, M.; Züttel, A., Boosting CO Production in Electrocatalytic CO₂ Reduction on Highly Porous Zn Catalysts. *Acs Catal* 2019, 9 (5), 3783-3791.

Metal-Organic Framework Mediated Ag-Cu Composite for Enhanced Production of Ethylene in Electrochemical CO₂ Reduction

3

This chapter is based on the following publication:

R. Wang, F. Kapteijn, J. Gascon, *Metal-organic Framework Mediated Ag-Cu Composite for Enhanced Production of Ethylene in CO₂ Electrochemical Reduction*, in preparation.

Abstract: Electrochemical reduction of CO₂ to value-added products has been attracting tremendous attention because of its economic and environmental impact. The combination of Cu with another metal to form alloys or composites shows promising potential in directing the CO₂ electroreduction selectivity towards C₂H₄. In this chapter, a facile construction is reported of an Ag-Cu composite by spin-coating of a Ag coordination polymer (CP) on Cu, followed by electro-reduction of the Ag-CP. H₂ evolution is suppressed after Ag coating while CO production is boosted, with peak *FE* towards CO as high as 45%. Moreover, by tuning the content of Ag, the *FE* towards C₂H₄ can reach 43%. The total current density of Ag-Cu composites is also enhanced by more than 50% compared with the Cu foil.

3.1. INTRODUCTION

Anthropogenic activities have caused tremendous increase of atmospheric CO₂ concentration during the last two centuries, and the high CO₂ concentration is widely considered to be a major reason for the environmental problems faced by the human society. To tackle this problem, several CO₂ utilization technologies have been proposed [1], such as photocatalytic methods [2], thermo-catalytic methods [3], and electrocatalytic methods [4]. Among these methods, CO₂ electrochemical reduction is of great industrial potential owing to the mild operation conditions and the possibility to generate some highly value-added products [4].

Researchers have demonstrated that the products of CO₂ electrochemical reduction were closely related to the catalyst [4a, 5]. Metal catalysts are divided into four categories based on their main products, and when it comes to the formation of hydrocarbons, Cu stands out as the sole metal to catalyze CO₂ electrochemical reduction into various products, with methane and ethylene as dominant ones [5a]. Although methane is a useful fuel, especially for power plants, the market price of methane is actually much inferior to ethylene [6]. Thus, from an economic point of view, the development of catalysts that do not stimulate methane formation in electrochemical CO₂ reduction would be highly desirable for the commercialization of CO₂ER. The suppression of CH₄ production on Cu has been demonstrated through several engineering methods, such as plasma activation of Cu [7], choice of electrolyte [7], and nanostructuring Cu [7-8], *etc.* Recently, researchers have been exploring metal alloys or composites to

tune the selectivity of Cu-based electrocatalysts, especially towards C₂H₄ production [9].

Feng *et al.* [10] used laser ablation to prepare Cu-Zn alloy catalysts that exhibited a FE towards C₂H₄ as high as 33.3% at -1.1 V vs. RHE. The high proximity of Cu and Zn atoms on the electrocatalyst surface was shown to facilitate the stabilization of the *CO intermediate and the transfer of the *CO intermediate from Zn atoms to their neighbouring Cu atoms, where dimerization and protonation of the *CO intermediate occurred to form ethylene. Hoang *et al.* [11] constructed Cu-Ag alloy films with homogeneous mixture through co-electrodeposition. The alloy film exhibited a FE for C₂H₄ as high as 60% at -0.7 V vs. RHE and a total current density of approximately -300 mA cm⁻². Mechanistic studies suggested that the high selectivity towards C₂ products originates from a synergistic effect of the enhanced stabilization of the Cu₂O overlayer and the optimal availability of the CO intermediate, both of which resulted from the incorporation of Ag in the alloy. Wang *et al.* [12] reported the efficient production of ethylene by constructing a Ag-Cu bimetallic catalyst by sequential precipitation of Ag/Cu₂O heterostructure followed by electroreduction, enhancing FE to ethylene to 42%. The high yield of ethylene can be rationalized by the relay catalysis of the Ag and Cu component around the Ag/Cu interface, with CO forming on Ag and then transferring to Cu for further reduction. As for the mechanisms of the catalysis by the combination of Ag and Cu, Gurudayal *et al.* [13] demonstrated a sequential cascade pathway to convert CO₂ to C₂+ hydrocarbons and oxygenates in a two-step electrocatalytic process using CO as the intermediate. CO₂ to CO conversion was performed by using Ag, and further conversion of CO to C-C coupled products is performed with

Cu. Huang *et al.* [14] used Ag/Cu nanocrystals to uncover the key role played by the Ag/Cu interface in promoting CO₂RR. Segregated Ag and Cu domains sharing a tunable interface were obtained by a seeded growth synthesis, wherein preformed Ag nanoparticles were used as nucleation seeds for the Cu domain. It was found that the tandem catalysis and electronic effects, both enabled by the addition of Ag to Cu in the form of segregated nanodomains, synergistically account for an enhancement in the Faradaic efficiency for C₂H₄.

Here a facile MOF-mediated strategy is introduced to produce a Ag-Cu composite for electrochemical CO₂ reduction. A Ag coordination polymer (Ag-CP) was synthesized and spin-coated onto Cu foil, followed by electrochemical reduction of the Ag-CP into metallic Ag, thereby generating in-situ a composite of Ag and Cu. The loading amount of Ag can be tightly controlled through spin-coating cycles. The Ag-Cu electrode was measured for CO₂ electrochemical reduction with a H-cell, and shows a Faradaic efficiency towards C₂H₄ as high as 43% and a current density of -9.3 mA cm⁻² at -1.13 V vs. RHE, with H₂ and CO as the main by-products. With the increase of the Ag loading on the electrode, the H₂ evolution was gradually suppressed. This MOF-mediated strategy opens a door for facile synthesis of composite catalysts for electrochemical reduction of CO₂ into valuable hydrocarbon products.

3.2. EXPERIMENTAL

3.2.1. Materials

Silver nitrate (>99%), 2,5-pyridinedicarboxylic acid (2,5-pydc, 98%), potassium hydroxide (99.99%), potassium bicarbonate (99.99%) and N,N-

dimethylformamide (DMF, 99.8%), hydrochloric acid (36.5-38 wt.%), Cu foil (thickness 0.25 mm, 99.98% trace metal basis) were purchased from Sigma-Aldrich and were used without further purification. Nafion solution (5 %, in ethanol) was purchased from Fuel Cell Store.

3.2.2. *Synthesis of Ag-CP*

This synthesis method was adopted from literature [15] and Chapter 2. In a typical synthesis, 3.84 g AgNO₃ (22.56 mmol) and 1.2 g 2,5-pydc (7.2 mmol) were separately dissolved in 200 mL DMF each under vigorous stirring to form clear solutions. Then these two solutions were mixed and kept under stirring for 24 h. After that, the slurry was centrifuged and the collected precipitate was washed twice, first with methanol and then with distilled water. The solid was finally dried in a vacuum oven at 80 °C.

3.2.3. *Hydrochloric acid (HCl) etching of Cu foil*

The concentrated HCl was first diluted to 0.1 M with distilled water. Pristine Cu foils were cut into small pieces of 2.5 cm × 2.5 cm. The Cu foils were placed in a plastic box and immersed in 0.1 M HCl solution (Figure S3.1a). The plastic box was then wrapped with aluminium foil, and kept in the fume hood for overnight treatment (Figure S3.1b), after which the Cu foils were washed 3 times with distilled water and dried in a vacuum oven overnight at 60 °C. The Cu foils after HCl etching were denoted as ***etched Cu foil***. The etched Cu foils appeared significantly different in comparison with the pristine Cu foils (Figure S3.2).

3.2.4. Spin-coating of Ag-CP onto etched Cu foil.

A suspension of Ag-CP in ethanol and Nafion was prepared by mixing 100 mg Ag-CP into 8 mL ethanol and 2 mL Nafion solution, and kept under magnetic stirring for 2 h to form a uniform suspension.

For the spin-coating process, one piece of etched Cu foil was fixed on the holder of spin-coater, the rotation speed of the spin-coater started from zero to 2000 rpm in 4 s, and then was kept at 2000 rpm for 10 s, during which 1 mL Ag-CP suspension was casted on etched Cu foil in a drop-by-drop manner; after that, the rotating speed was further increased to 3000 rpm in 5 s, and kept at 3000 rpm for 10 s to guarantee the uniform dispersion of Ag-CP. The spin-coating process was repeated for various cycles to control the Ag loading amount. The sample after spin-coating of Ag-CP was denoted as *Ag-CP/Cu-n* (*n* represents the spin-coating cycles, *n* = 2, 4, 6).

3.2.5. Electroreduction of Ag-CP.

To fabricate an electrode, a silver wire was soldered on the uncoated side of Cu foil, and the uncoated side was sealed with metal glue to prevent its contact with electrolyte. The Ag-CP/Cu-*n* electrodes were put in a three-electrode electrochemical cell, with 0.1 M KHCO₃ as electrolyte, Ag/AgCl (sat'd KCl) as reference electrode, and Pt gauze as counter electrode. A potential of -1.8 V vs. Ag/AgCl was applied for 10 min to electrochemically reduce the Ag-CP to metallic Ag. The electrodes after electroreduction of Ag-CP were denoted as *AgCu-n*. As seen from Figure S3.3, with more spin-coating cycles, the coated side of the electrode became darker.

3.2.6. Controlled-potential CO₂ electrolysis.

CO₂ electroreduction experiments were performed in a H-type electrochemical cell as previously reported [16]. The cell was divided into two compartments, the anode compartment and cathode compartment, by a proton-exchange membrane (Nafion 117). The anode compartment contained a counter electrode (Pt gauze), while the cathode electrode contained the working electrode and a reference electrode (Ag/AgCl electrode). Both compartments had a volume of 100 mL, and were filled with 85 mL electrolyte prior to the performance tests, leaving a headspace of 15 mL. CO₂ was then fed into the reactor by bubbling through the liquid with a flow rate of 100 mL min⁻¹ until the electrolyte was saturated, after which the CO₂ flow was fixed at 10 ml min⁻¹. To start the controlled-potential electrolysis, an operation potential was applied by a potentiostat (Autolab PGSTAT302N) in the range of -1.0 to -2.0 V vs. Ag/AgCl. The cathode compartment was connected to an on-line gas chromatograph (Global Analyzer Solution Compact GC), which was triggered every 24 min to analyze the gas product. The online-GC is equipped with a thermal conductivity detector (TCD), connected with Parabond (Q 2 m x 0.32 mm) and Carboxen 1010 (20 m x 0.32 mm) columns, and flame ionization detector (FID), connected with a Porabond Q (15 m x 0.32 mm x 10 μm) column. He is used as carrier gas, and the online-GC is pre-calibrated with mixture gas bottle (5% CH₄, C₂H₄, C₂H₆, C₃H₃, C₃H₈, and CO, diluted with N₂) and H₂ bottle (5% H₂ diluted with N₂). All the experiments lasted 120 min. At the end of the electrocatalytic test, a liquid sample (~0.2 mL) was collected from the electrolyte solution for ultra-performance liquid chromatography (UPLC) analysis. The UPLC is equipped with a RI detector

and a TUV detector, and a Shodex KC811 column. The UPLC is pre-calibrated for the analysis of liquid phase product, such as methanol, ethanol, and formate, *etc.* After each experiment, the electrochemical reactor was cleaned with distilled water, and the proton-exchange membrane was immersed into 0.1 M H₂SO₄ for regeneration.

Faradaic efficiency (FE) of a gas product i was calculated based on the following equation:

$$FE_i = (n \times F \times v_i \times f) / (V_m \times j) \quad (1)$$

Where:

n : the number of electrons consumed to produce one product molecule;

v_i : the volume fraction of a certain gas product;

f : the overall gas flow rate (in the unit of m³ s⁻¹);

F : Faraday constant ($F=96485$ C mol⁻¹);

V_m : the molar volume constant at ambient pressure ($V_m=0.024465$ m³ mol⁻¹);

j : steady-state cell total current at each applied potential (A).

3.2.7. Electrochemical active surface area measurement.

The electrochemically active surface area (ECSA) for each electrode was estimated from the electrochemical double-layer capacitance of the catalytic surface [17]. The electrochemical capacitance was determined by measuring the non-Faradaic capacitive current associated with double-layer charging from the scan-rate dependence of cyclic voltammograms (CVs). To measure double-layer charging via CV, a potential range in which no apparent Faradaic processes occur was determined from static CV. This range is typically a 0.1 V potential window centred at the open-circuit potential (OCP) of the system. The OCPs for each electrode are given in Table S3.1.

All measured current in this non-Faradaic potential region is assumed to be due to double-layer charging. The charging current, i_c , was then measured from CVs at multiple scan rates. The double-layer charging current is equal to the product of the scan rate, ν , and the electrochemical double-layer capacitance, C_{DL} , as given by the equation below:

$$i_c = \nu \cdot C_{DL} \quad (2)$$

Thus, a plot of i_c as a function of ν yields a straight line with a slope equal to C_{DL} .

The CV curves of pristine Cu foil, etched Cu foil, and AgCu-n electrodes at different scan rates are shown in Figure S3.4, and the linear slopes of charging currents vs. scan rates were calculated and displayed in Figure S3.5. The related data are summarized in Table S3.1. The roughness factor is defined as the ratio between the ECSA of one electrode and ECSA of pristine Cu foil, which represents the relative ECSA.

3.2.8. Characterization techniques.

X-ray diffraction (XRD) patterns of etched Cu foils, Ag-CP/Cu-n, and AgCu-n electrodes were collected using a Bruker D8 Advance X-ray diffractometer, and the radiation source was a Co- $K\alpha$ radiation ($\lambda = 0.179026$ nm). The Ag content in Ag-CP was determined by thermogravimetric (TG) analysis. Scanning electron microscopy (SEM) analysis was performed on either a Nova Nano 630 or a Teneo scanning electron microscope from FEI Company. A K-alpha Thermo Fischer Scientific spectrometer was used for the XPS investigation using monochromatic Al- $K\alpha$ radiation at ambient temperature and a chamber pressure of about 10^{-8} mbar. All spectra measured were corrected by setting the reference binding energy of carbon (C1s) at 284.8 eV. Spectra were

analyzed using the Thermo Advantage software package. The deconvolution of spectra was performed using a mixed Gauss-Lorentzian function, the quantification was done by using the Scofield sensitivity factors. Difference in analysis depth for different photoelectron lines was accounted for by the TPP-2M method.

3.3. RESULTS AND DISCUSSION

In the XRD analysis two sets of reflections are observed in AgCu-n samples (Figure 3.1), corresponding to those of metallic Cu and Ag. More spin-coating cycles of Ag-CP lead to stronger Ag reflections, indicating higher Ag loadings. The coating of Ag-CP onto Cu foil does not directly result in AgCu composites, as follows from the XRD patterns of Ag-CP/Cu-n samples. Clear reflections of Ag-CP can be observed for Ag-CP/Cu-n electrodes (Figure S3.6), showing the presence of Ag-CP on the Cu surface.

Figure 3.2a-c reveals a small amount of Ag₂O (with Ag3d_{5/2} and Ag3d_{3/2} peaks centred at ~367.6 eV and ~373.6 eV, respectively)^[18] in the Ag-CP, while the electro-reduced AgCu-4 samples only show metallic Ag peaks (with Ag3d_{5/2} and Ag3d_{3/2} peaks centred at ~368.2 eV and ~374.2 eV, respectively), indicating a complete reduction of Ag₂O to the detection limit after the electro-reduction of Ag-CP. The Cu2p results (Figure 3.2d-f) exhibit a mixture of CuO (with Cu2p_{3/2} centred at ~934.6 eV and Cu2p_{1/2} centred at ~954.4 eV) and metallic Cu (with Cu2p_{3/2} centred at ~932.7eV and Cu2p_{1/2} centred at ~952.5 eV) [19]. The satellite peaks of Cu2p are typical for the presence of Cu²⁺. CuO is partially reduced to metallic Cu

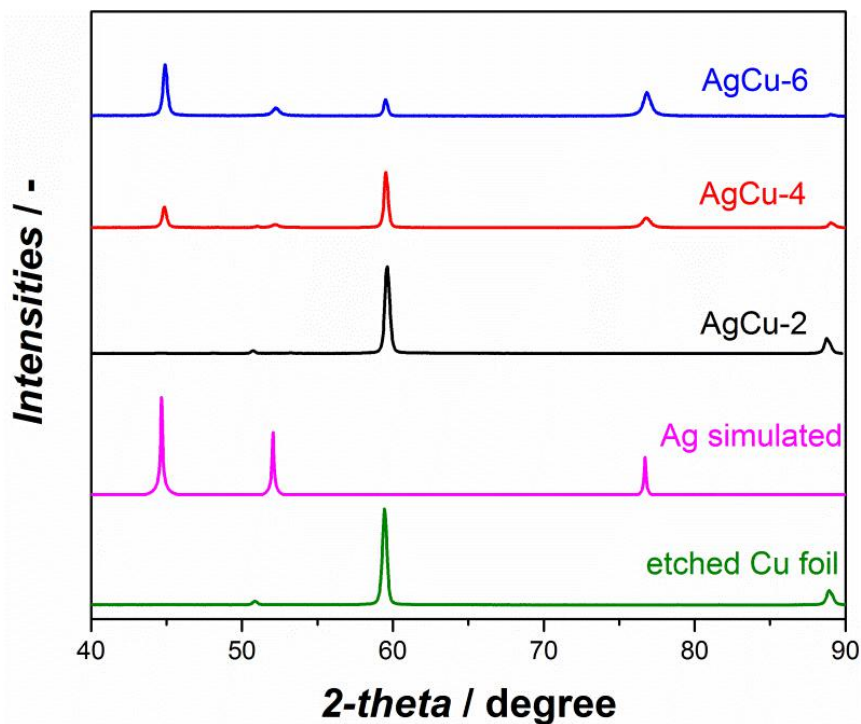


Figure 3.1. XRD patterns of AgCu-n samples, simulated Ag, and etched Cu foil.

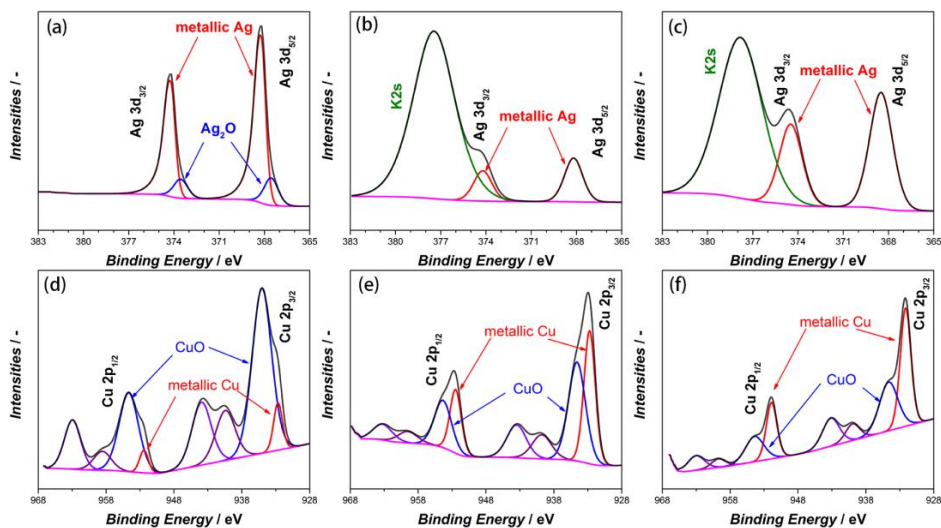


Figure 3.2. Regional Ag3d and Cu2p XPS peaks of (a, d) Ag-CP/Cu-4, (b, e) AgCu-4 before CO₂ electrolysis, and (c, f) AgCu-4 after CO₂ electrolysis.

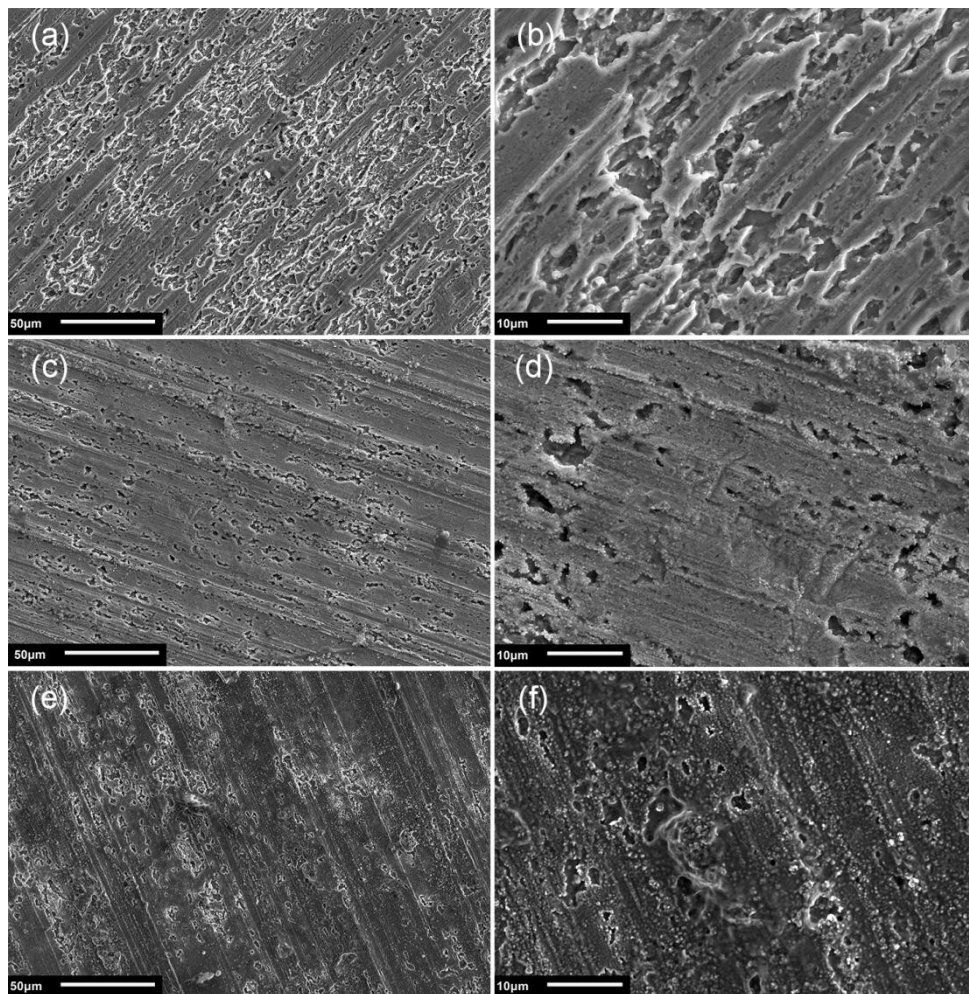


Figure 3.3. SEM images of (a-b) AgCu-2, (c-d) AgCu-4, and (e-f) AgCu-6.

when a negative potential is applied (during both the electro-reduction of Ag-CP and the CO₂ electrolysis), because the ratio of CuO : metallic Cu shows a clear decreasing trend (Table S3.2).

The HCl etching caused a difference in the appearance between pristine and etched Cu foils. The Cu foil surface structure at the micro level was also affected, as shown by the SEM analysis (Figure S3.7). After HCl etching, the Cu foil surface was highly roughened. The etched roughness was

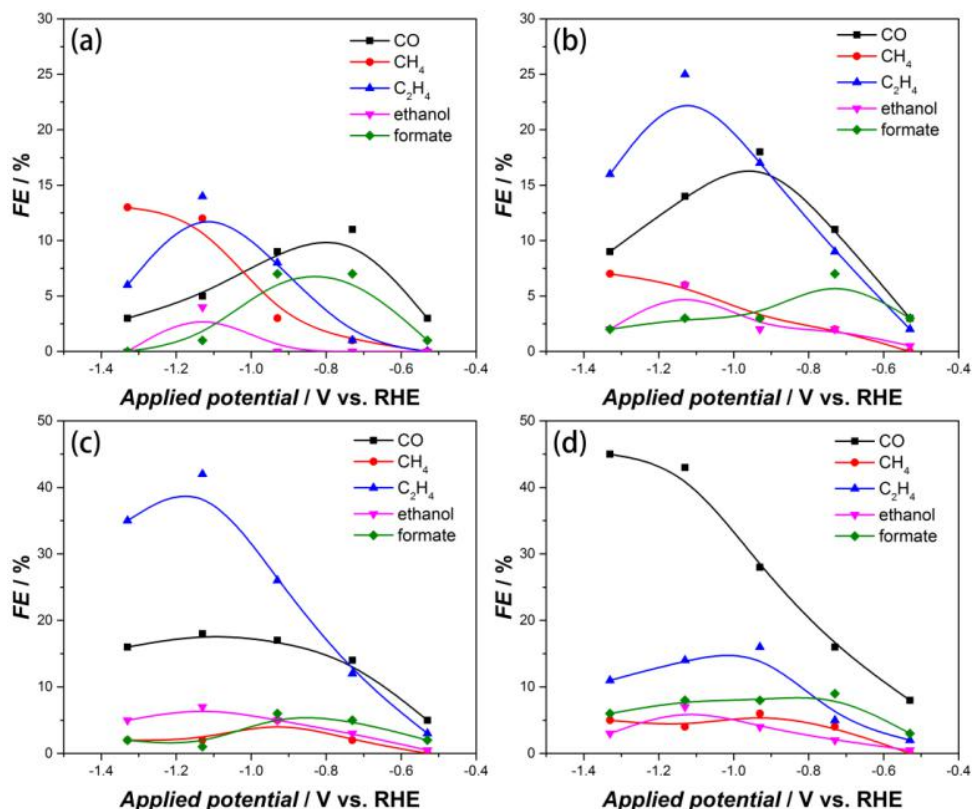


Figure 3.4. Faradaic efficiencies of CO, CH₄, C₂H₄, ethanol, and formate measured on (a) etched Cu foil, (b) AgCu-2, (c) AgCu-4, and (d) AgCu-6 in controlled-potential CO₂ electrolysis.

possibly a reason for the increased ECSA of etched Cu foil compared to the pristine Cu foil (Table S3.1).

The SEM images of AgCu-*n* samples (Figure 3.3) demonstrate that more cycles of Ag-CP lead to a higher surface coverage of Ag particles. AgCu-2 still has a highly roughened surface, while the roughness induced by HCl treatment on AgCu-4 and AgCu-6 has been largely mitigated by an increased Ag coverage. Moreover, AgCu-6 has larger Ag particles than AgCu-2 and AgCu-4.

Although loading of Ag particles does not add to an observed surface roughness, the ECSA after Ag loading is boosted compared with pristine and etched Cu foils, and the ECSA shows a high dependence on the spin-coating cycles, *i.e.*, the more Ag loading, the higher ECSA (Figure S3.4-S3.5 and Table S3.1).

The uniformity of Ag dispersion on the surface is demonstrated by the EDX elemental mapping (Figure S3.8-3.10), and the elemental content is summarized in table S3.3. Specifically, the Ag content shows an almost linear relation with Ag-CP coating cycles, demonstrating that the MOF-mediated approach, especially in combination with spin-coating, can be a precise way to tune the loading quantity when preparing metal composites. The elemental content ratio of Ag:Cu as determined from the XPS survey spectra (Figure S3.12 and Table S3.4) also exhibits a clearly increasing trend with the number of spin-coating cycles, indicating the decreased exposure of the Cu surface with higher Ag loadings.

The Faradaic efficiency distribution of the CO₂ reduction reaction (CO₂RR) products on etched Cu foil and AgCu-n electrodes as a function of the applied potential is shown in Figure 3.4. For all these four electrodes CO, CH₄, and C₂H₄ are the main gas-phase CO₂RR products, while ethanol and formate are the detectable liquid-phase CO₂RR products. For etched Cu foil, no product is formed with a FE above 15%. After Ag loading, CO and C₂H₄ start to stand out as dominant products, especially for AgCu-4 and AgCu-6, C₂H₄ (on AgCu-4) and CO (on AgCu-6) exhibit a significantly higher FE than all the other products. The Ag loading also results in an improvement in the production of ethanol, which exhibits a peak $FE_{ethanol}$ of 7% at -1.13 V vs. RHE on AgCu-6. Formate production is slightly decreased on AgCu-2

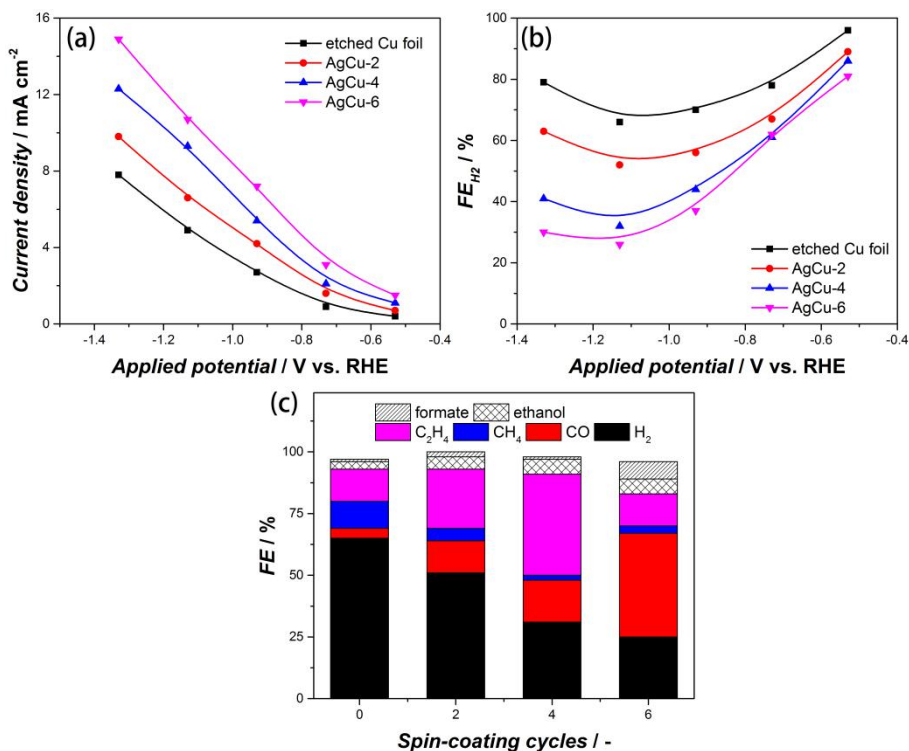


Figure 3.5. (a) Total current density, and (b) Faradaic efficiency for H₂ for etched Cu foil and AgCu-*n* samples; (c) Faradaic efficiencies towards formate, ethanol, C₂H₄, CH₄, CO, and H₂ at -1.13V vs. RHE.

and AgCu-4, but finally enhanced on AgCu-6, with a peak $FE_{formate}$ of $\sim 10\%$. Moreover, the Ag loading also mitigate the overpotentials for the formation of C₂H₄ and ethanol. For AgCu-*n* electrodes, significant amount of C₂H₄ and ethanol can already be observed at -0.53 V vs. RHE, while almost no C₂H₄ and ethanol is formed on etched Cu foil at the same overpotential.

The decoration of Ag on the Cu surface significantly improves the current density (Figure 3.5a), and the higher Ag loading the higher the current density. Specifically, the current density at -1.33V vs. RHE is increased by more than 50% (from 7.9 mA cm⁻² to 13.5 mA cm⁻²) after 6

cycles of Ag-CP. The increased current density can be explained by ECSA improvement by Ag loading (Figure S3.4-S3.5 and Table S3.1).

The Faradaic efficiency towards H_2 shows an opposite trend with total current density (Figure 3.5b), that is the higher Ag loading suppresses FE of H_2 . An optimum FE_{H_2} occurs at $-1.13V$ vs. RHE, where the FE_{H_2} is lowered from $\sim 70\%$ (etched Cu foil) to $\sim 25\%$ (AgCu-6). The Faradaic efficiencies of all the products (hydrocarbons, ethanol, formatted, and H_2) from cathode add up to slightly less than 100%, and the missing FE is likely to originate from those products which are small in amount and cannot be accurately detected. The Faradaic efficiencies of several major products, C_2H_4 , CH_4 , CO , and H_2 , at $-1.13V$ vs. RHE are plotted in Figure 3.5c. Along with the suppression of H_2 evolution with higher Ag loading, CO production is gradually boosted from 5% (etched Cu foil) to 44% (AgCu-6), possibly indicating the loaded Ag particles mainly function as independent CO evolution sites. In addition to H_2 evolution, loading Ag on the Cu surface also suppresses CH_4 production. At $-1.13V$ vs. RHE, the FE of CH_4 was reduced from 12% (etched Cu foil) to less than 5% (AgCu-4 and AgCu-6). The FE of C_2H_4 first increases from 14% (etched Cu foil) to 43% (AgCu-4). Increasing the Ag loading from AgCu-4 to AgCu-6 likely boosts the formation of large Ag particles on the surface, as observed from SEM (Figure 3.3), making Ag the dominant catalytic phase on the surface, resulting in the decrease in FE of C_2H_4 and increasing the FE_{CO} .

Based on the 'relay' (bifunctional) catalysis model proposed by Wang *et al.* [12], the CO_2 molecule first adsorbs on the Ag surface, and $*CO$ intermediate is formed by transferring two electron-proton pairs to the adsorbed CO_2 molecule. Afterwards, the CO intermediate is transported to

Cu surface for further reduction to hydrocarbons and alcohols. Although a detailed pathway still needs to be examined by DFT calculation, this model can be used to explain the performance of the bifunctional Ag-Cu composites that were constructed. By decorating the Cu foil by Ag particles, which are favorable for CO production, a relatively large amount of CO is fed to the Cu surface instead of pure CO₂, resulting in an increased production of C₂H₄, being a major product in electrochemical CO reduction on Cu surface [20].

A compilation of recent studies on Cu-based electrodes for electrochemical CO₂ reduction into C₂H₄ under similar experimental conditions as ours is listed in Table S3.5. By comparison, the Ag-Cu composites constructed by the MOF-mediated approach exhibit an outstanding $FE_{C_2H_4}$, and a relatively higher current density than most of the reported works.

3.4. CONCLUSIONS

In summary, we have shown here a facile route to construct a Ag-Cu composite electrocatalyst for CO₂ reduction through spin-coating of Ag-CP on the Cu foil, followed by the electro-reduction of Ag-CP. The spin-coating method ensures the uniform dispersion of Ag, and exhibits a tight control over the coating amount of Ag. The Ag loading on Cu surface can significantly suppress the H₂ evolution while facilitating CO production and increasing the current density in CO₂ER. Furthermore, the Ag-Cu composite favours the production of C₂H₄ over Cu, with increasing Ag contents the FE of C₂H₄ first increases to as high as 43% on AgCu-4, but decreases on AgCu-6, attributed to the larger Ag particles becoming the dominant catalytic phase on the surface. The construction of metal composites through

MOF-mediated approach hold a promising potential for the scalable fabrication of electrodes for the electrochemical reduction of CO₂ into valuable hydrocarbons, here demonstrated for a bifunctional Ag-Cu system.

3.5. REFERENCES

1. Kondratenko, E. V.; Mul, G.; Baltrusaitis, J.; Larrazábal, G. O.; Pérez-Ramírez, J., Status and perspectives of CO₂ conversion into fuels and chemicals by catalytic, photocatalytic and electrocatalytic processes. *Energ Environ Sci* 2013, 6 (11), 3112-3135.
2. (a) Habisreutinger, S. N.; Schmidt-Mende, L.; Stolarczyk, J. K., Photocatalytic Reduction of CO₂ on TiO₂ and Other Semiconductors. *Angewandte Chemie International Edition* 2013, 52 (29), 7372-7408; (b) Corma, A.; Garcia, H., Photocatalytic reduction of CO₂ for fuel production: Possibilities and challenges. *Journal of Catalysis* 2013, 308, 168-175; (c) Sekizawa, K.; Maeda, K.; Domen, K.; Koike, K.; Ishitani, O., Artificial Z-Scheme Constructed with a Supramolecular Metal Complex and Semiconductor for the Photocatalytic Reduction of CO₂. *Journal of the American Chemical Society* 2013, 135 (12), 4596-4599; (d) Thampi, K. R.; Kiwi, J.; Grätzel, M., Methanation and photo-methanation of carbon dioxide at room temperature and atmospheric pressure. *Nature* 1987, 327 (6122), 506-508.
3. (a) Centi, G.; Perathoner, S., Opportunities and prospects in the chemical recycling of carbon dioxide to fuels. *Catal Today* 2009, 148 (3), 191-205; (b) Wang, W.; Wang, S.; Ma, X.; Gong, J., Recent advances in catalytic hydrogenation of carbon dioxide. *Chemical Society Reviews* 2011, 40 (7), 3703-3727; (c) Dorner, R. W.; Hardy, D. R.; Williams, F. W.; Willauer, H. D., Heterogeneous catalytic CO₂ conversion to value-added hydrocarbons. *Energ Environ Sci* 2010, 3 (7), 884-890; (d) Sharma, S.; Hu, Z.; Zhang, P.; McFarland, E. W.; Metiu, H., CO₂ methanation on Ru-doped ceria. *Journal of Catalysis* 2011, 278 (2), 297-309.
4. (a) Gattrell, M.; Gupta, N.; Co, A., A review of the aqueous electrochemical reduction of CO₂ to hydrocarbons at copper. *J Electroanal Chem* 2006, 594 (1), 1-19; (b) Whipple, D. T.; Kenis, P. J. A., Prospects of CO₂ Utilization via Direct Heterogeneous Electrochemical Reduction. *The Journal of Physical Chemistry Letters* 2010, 1 (24), 3451-3458; (c) Lu, Q.; Jiao, F., Electrochemical CO₂ reduction: Electrocatalyst, reaction mechanism, and process engineering. *Nano Energy* 2016, 29, 439-456.
5. (a) CO₂-reduction, catalyzed by metal electrodes. In *Handbook of Fuel Cells*; (b) Hori, Y.; Takahashi, I.; Koga, O.; Hoshi, N., Electrochemical reduction of carbon dioxide at various series of copper single crystal electrodes. *Journal of Molecular Catalysis A*:

- Chemical 2003, 199 (1), 39-47; (c) Hori, Y.; Murata, A.; Takahashi, R., Formation of hydrocarbons in the electrochemical reduction of carbon dioxide at a copper electrode in aqueous solution. *Journal of the Chemical Society, Faraday Transactions 1: Physical Chemistry in Condensed Phases* 1989, 85 (8), 2309-2326.
- Chen, C.; Khosrowabadi Kotyk, J. F.; Sheehan, S. W., Progress toward Commercial Application of Electrochemical Carbon Dioxide Reduction. *Chem* 2018, 4 (11), 2571-2586.
 - Gao, D.; Scholten, F.; Roldan Cuenya, B., Improved CO₂ Electroreduction Performance on Plasma-Activated Cu Catalysts via Electrolyte Design: Halide Effect. *Acs Catal* 2017, 7 (8), 5112-5120.
 - Kim, J.; Choi, W.; Park, J. W.; Kim, C.; Kim, M.; Song, H., Branched Copper Oxide Nanoparticles Induce Highly Selective Ethylene Production by Electrochemical Carbon Dioxide Reduction. *Journal of the American Chemical Society* 2019, 141 (17), 6986-6994.
 - (a) Kottakkat, T.; Klingan, K.; Jiang, S.; Jovanov, Z. P.; Davies, V. H.; El-Nagar, G. A. M.; Dau, H.; Roth, C., Electrodeposited AgCu Foam Catalysts for Enhanced Reduction of CO₂ to CO. *Acs Appl Mater Inter* 2019, 11 (16), 14734-14744; (b) Liu, K.; Ma, M.; Wu, L.; Valenti, M.; Cardenas-Morcoso, D.; Hofmann, J. P.; Bisquert, J.; Gimenez, S.; Smith, W. A., Electronic Effects Determine the Selectivity of Planar Au-Cu Bimetallic Thin Films for Electrochemical CO₂ Reduction. *Acs Appl Mater Inter* 2019, 11 (18), 16546-16555; (c) Lee, S.; Park, G.; Lee, J., Importance of Ag-Cu Biphasic Boundaries for Selective Electrochemical Reduction of CO₂ to Ethanol. *Acs Catal* 2017, 7 (12), 8594-8604; (d) Birhanu, M. K.; Tsai, M.-C.; Kahsay, A. W.; Chen, C.-T.; Zeleke, T. S.; Ibrahim, K. B.; Huang, C.-J.; Su, W.-N.; Hwang, B.-J., Copper and Copper-Based Bimetallic Catalysts for Carbon Dioxide Electroreduction. *Advanced Materials Interfaces* 2018, 5 (24), 1800919.
 - Feng, Y.; Li, Z.; Liu, H.; Dong, C.; Wang, J.; Kulinich, S. A.; Du, X., Laser-Prepared CuZn Alloy Catalyst for Selective Electrochemical Reduction of CO₂ to Ethylene. *Langmuir* 2018, 34 (45), 13544-13549.
 - Hoang, T. T. H.; Verma, S.; Ma, S.; Fister, T. T.; Timoshenko, J.; Frenkel, A. I.; Kenis, P. J. A.; Gewirth, A. A., Nanoporous Copper-Silver Alloys by Additive-Controlled

- Electrodeposition for the Selective Electroreduction of CO₂ to Ethylene and Ethanol. *Journal of the American Chemical Society* 2018, 140 (17), 5791-5797.
12. Wang, J.; Li, Z.; Dong, C.; Feng, Y.; Yang, J.; Liu, H.; Du, X., Silver/Copper Interface for Relay Electroreduction of Carbon Dioxide to Ethylene. *ACS Appl Mater Inter* 2019, 11 (3), 2763-2767.
 13. Gurudayal; Perone, D.; Malani, S.; Lum, Y.; Haussener, S.; Ager, J. W., Sequential Cascade Electrocatalytic Conversion of Carbon Dioxide to C–C Coupled Products. *ACS Applied Energy Materials* 2019, 2 (6), 4551-4559.
 14. Huang, J.; Mensi, M.; Oveisi, E.; Mantella, V.; Buonsanti, R., Structural Sensitivities in Bimetallic Catalysts for Electrochemical CO₂ Reduction Revealed by Ag–Cu Nanodimers. *Journal of the American Chemical Society* 2019, 141 (6), 2490-2499.
 15. Wang, R.; Haspel, H.; Pustovarenko, A.; Dikhtiarenko, A.; Russkikh, A.; Shterk, G.; Osadchii, D.; Ould-Chikh, S.; Ma, M.; Smith, W. A.; Takanebe, K.; Kapteijn, F.; Gascon, J., Maximizing Ag Utilization in High-Rate CO₂ Electrochemical Reduction with a Coordination Polymer-Mediated Gas Diffusion Electrode. *ACS Energy Letters* 2019, 4 (8), 2024-2031.
 16. (a) Sastre, F.; Muñoz-Batista, M. J.; Kubacka, A.; Fernández-García, M.; Smith, W. A.; Kapteijn, F.; Makkee, M.; Gascon, J., Efficient Electrochemical Production of Syngas from CO₂ and H₂O by using a Nanostructured Ag/g-C₃N₄ Catalyst. *Chemelectrochem* 2016, 3 (9), 1497-1502; (b) Wang, R.; Sun, X.; Ould-Chikh, S.; Osadchii, D.; Bai, F.; Kapteijn, F.; Gascon, J., Metal-Organic-Framework-Mediated Nitrogen-Doped Carbon for CO₂ Electrochemical Reduction. *Acs Appl Mater Inter* 2018, 10 (17), 14751-14758.
 17. McCrory, C. C. L.; Jung, S.; Peters, J. C.; Jaramillo, T. F., Benchmarking Heterogeneous Electrocatalysts for the Oxygen Evolution Reaction. *Journal of the American Chemical Society* 2013, 135 (45), 16977-16987.
 18. Boronin, A. I.; Koscheev, S. V.; Zhidomirov, G. M., XPS and UPS study of oxygen states on silver. *Journal of Electron Spectroscopy and Related Phenomena* 1998, 96 (1), 43-51.
 19. Deroubaix, G.; Marcus, P., X-ray photoelectron spectroscopy analysis of copper and zinc oxides and sulphides. *Surface and Interface Analysis* 1992, 18 (1), 39-46.

20. (a) Han, L.; Zhou, W.; Xiang, C., High-Rate Electrochemical Reduction of Carbon Monoxide to Ethylene Using Cu-Nanoparticle-Based Gas Diffusion Electrodes. *ACS Energy Letters* **2018**, 3 (4), 855-860; (b) Wang, L.; Nitopi, S. A.; Bertheussen, E.; Orazov, M.; Morales-Guio, C. G.; Liu, X.; Higgins, D. C.; Chan, K.; Nørskov, J. K.; Hahn, C.; Jaramillo, T. F., Electrochemical Carbon Monoxide Reduction on Polycrystalline Copper: Effects of Potential, Pressure, and pH on Selectivity toward Multicarbon and Oxygenated Products. *ACS Catal* **2018**, 8 (8), 7445-7454.

3.6. Supporting Information for Chapter 3

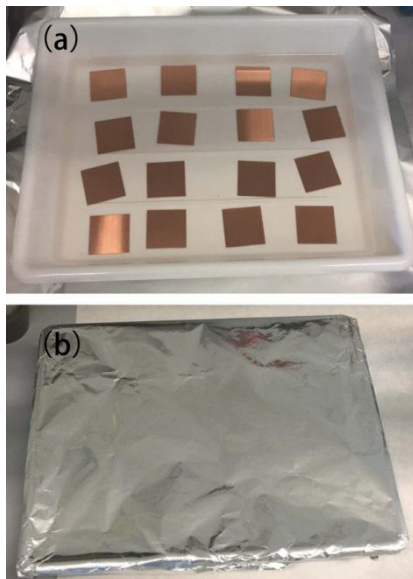


Figure S3.1. HCl etching of Cu foils. (*Top*) all samples collected in the treatment box, (*bottom*) covered with Al-foil for overnight treatment in fume hood.

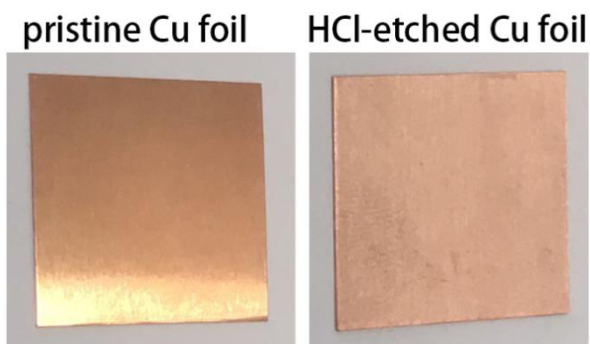


Figure S3.2. Appearance of Cu foil before (*left*) and after (*right*) HCl etching.

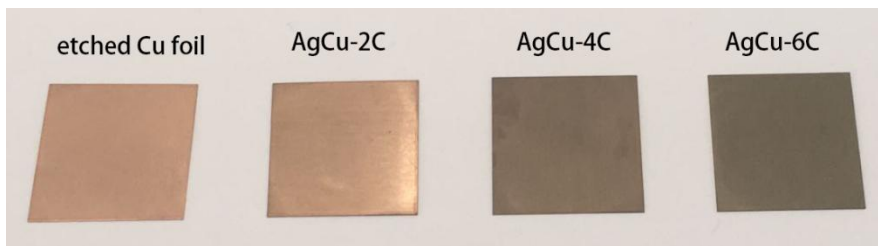


Figure S3.3. Appearance of etched Cu foil and AgCu-n electrodes.

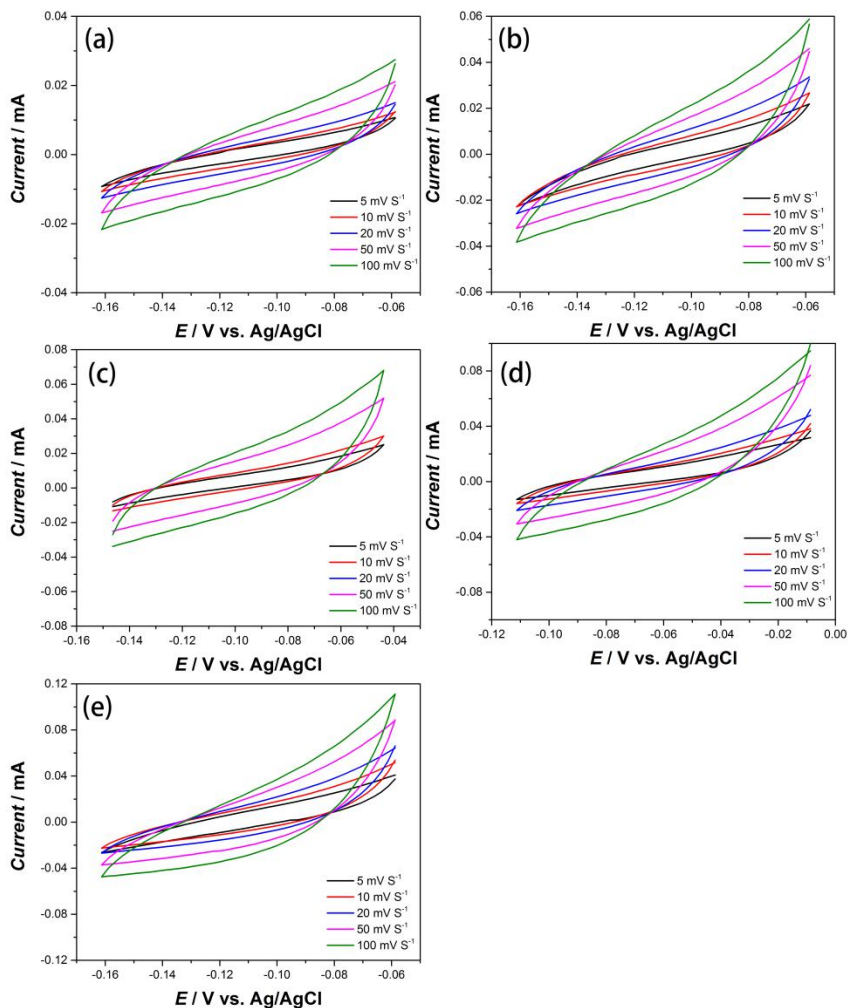


Figure S3.4. CV curves at different scan rates for (a) pristine Cu foil, (b) etched Cu foil, (c) AgCu-2, (d) AgCu-4, and (e) AgCu-6.

As described in experimental section, the cyclic voltammograms at different scan rate were measured to determine electrochemical capacitance, which is proportional to the electrochemically active surface areas. To measure double-layer charging via CV, a potential range in which no apparent Faradaic processes occur was determined from static CV. This range is typically a 0.1 V potential window centered at the open-circuit potential (OCP) of the system. All measured current in this non-Faradaic potential region is assumed to be due to double-layer charging. The charging currents constitute a linear relation with scan rate, as shown in Figure S3.5, and a higher value of slope represents a higher electrochemically active surface area.

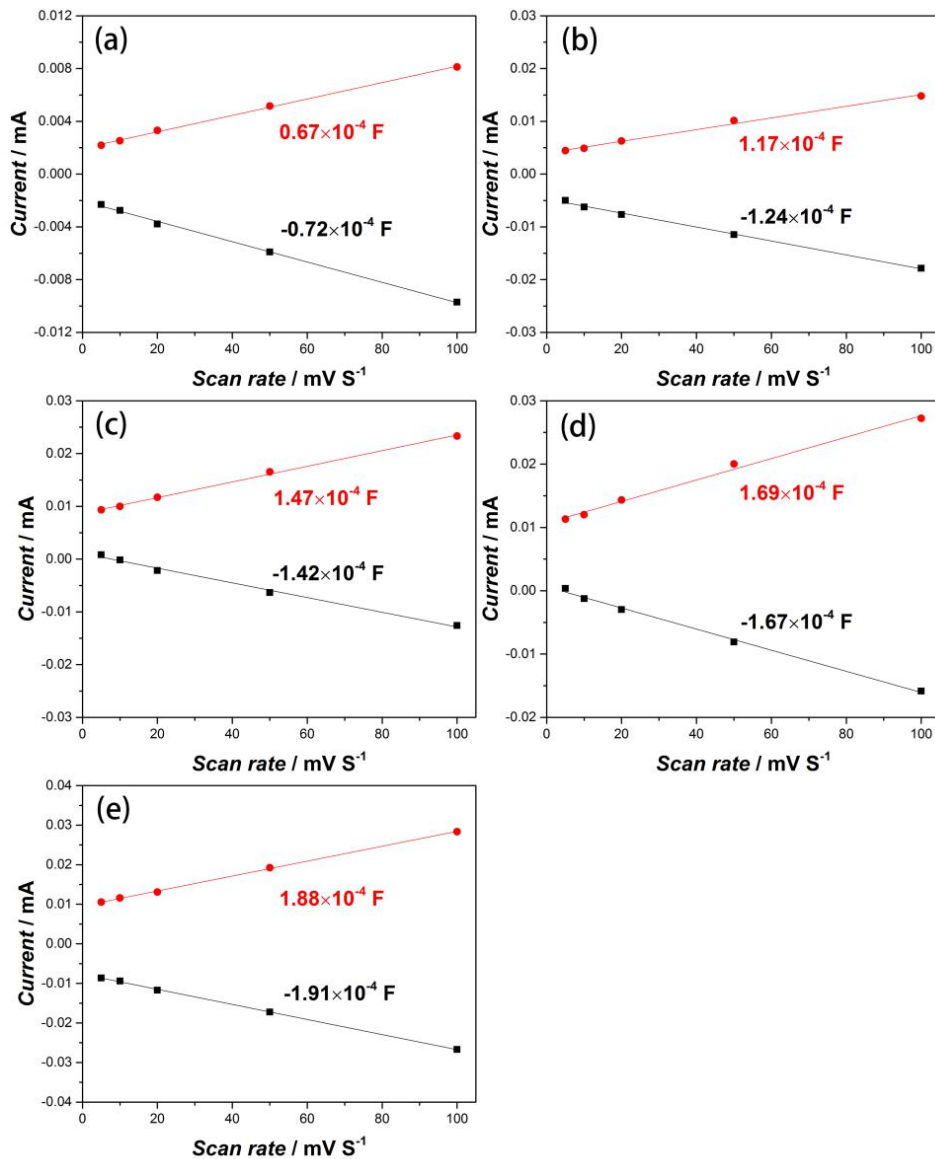


Figure S3.5. Charging current vs. scan rate for (a) pristine Cu foil, (b) etched Cu foil, (c) AgCu-2, (d) AgCu-4, and (e) AgCu-6.

Table S3.1. Summary of ECSA-related data.

Sample	Open-circuit potential (V)	$C_{DL}(\text{anode}) - C_{DL}(\text{cathode})$ (mF)	Roughness factor
Pristine Cu foil	-0.11	0.14	1
Etched Cu foil	-0.11	0.24	1.75
AgCu-2	-0.095	0.29	2.06
AgCu-4	-0.06	0.34	2.42
AgCu-6	-0.11	0.38	2.73

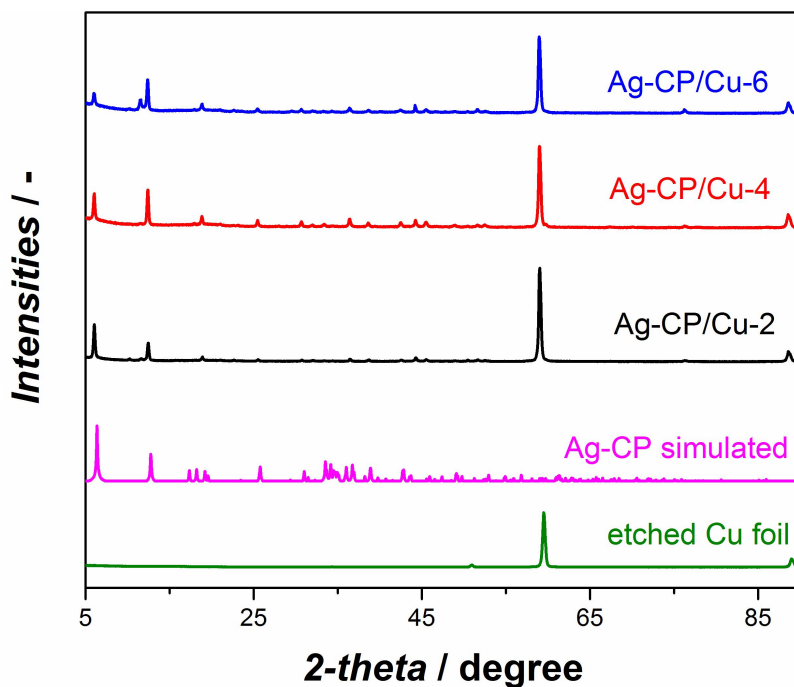
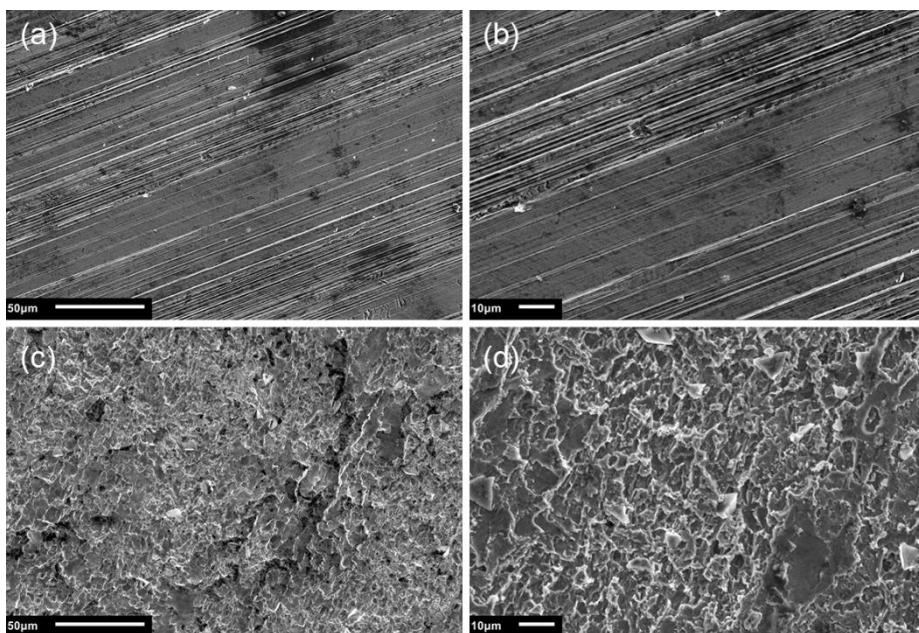
**Figure S3.6.** XRD patterns of Ag-CP coated Cu foil samples, simulated Ag-CP, and etched Cu foil.

Table S3.2. Elemental Ag and Cu contents of Ag-CP/Cu-4 and AgCu-4 before and after CO₂ER as determined by XPS.

Sample	Element content	
	Ag Ag ₂ O: Metallic Ag	Cu Metallic Cu:CuO
Ag-CP/Cu-4	0.18	0.13
AgCu-4 before CO ₂ ER	--[a]	0.9
AgCu-4 after CO ₂ ER	--[a]	1.4

[a] Ag₂O is not detected in these samples.

**Figure S3.7.** SEM images of non-treated (a-b) Cu foil and (c-d) etched Cu foil.

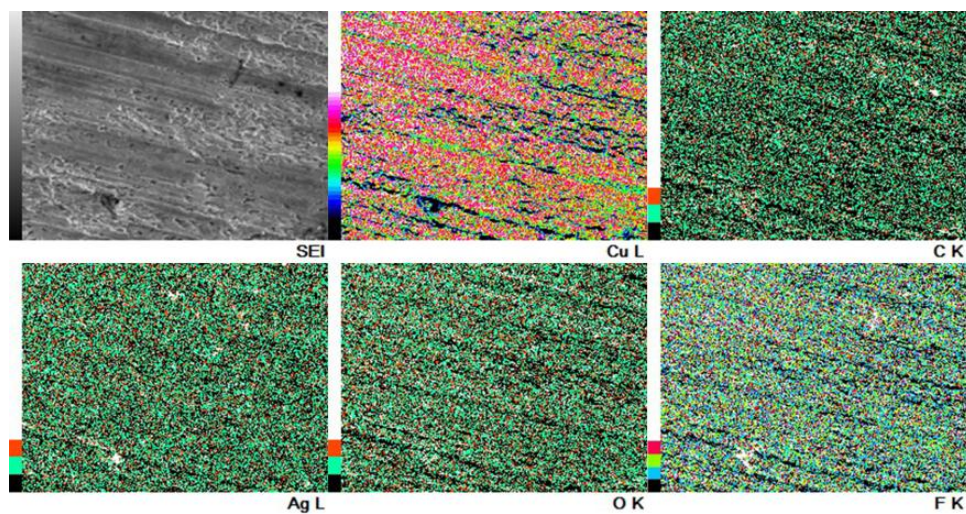


Figure S3.8. EDX element mapping of AgCu-2.

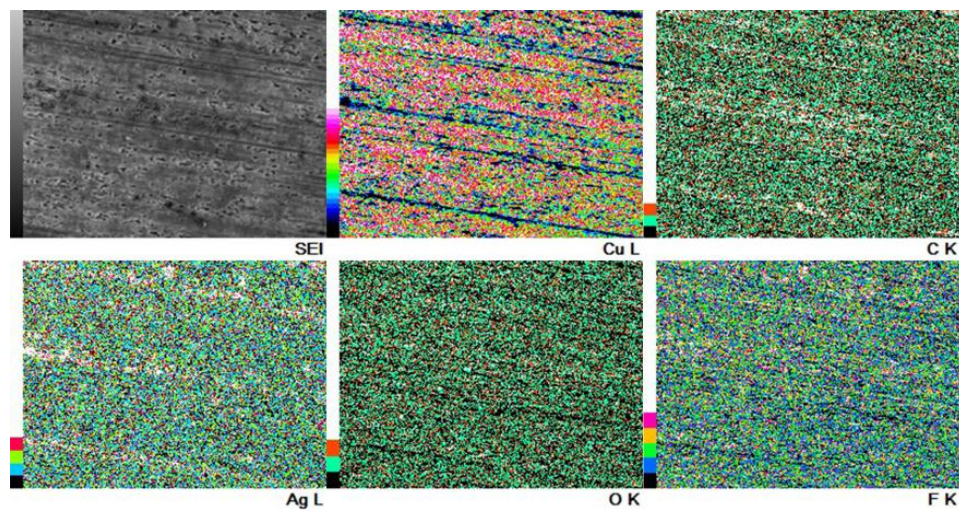


Figure S3.9. EDX element mapping of AgCu-4.

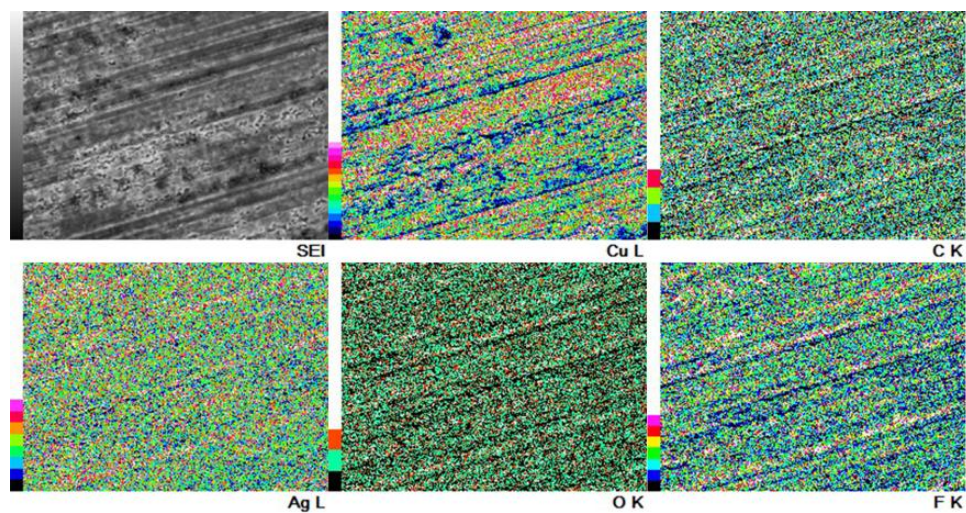


Figure S3.10. EDX element mapping of AgCu-6.

Table S3.3. Element content of AgCu-*n* samples as determined by EDX.

Spin-coating cycles	Elemental content (atom%)				
	Cu	Ag	C	O	F
2	44.4	6.7	35.6	4.1	9.2
4	27.6	12.5	33.5	4.8	21.8
6	20.2	18.1	35.8	4.4	21.5

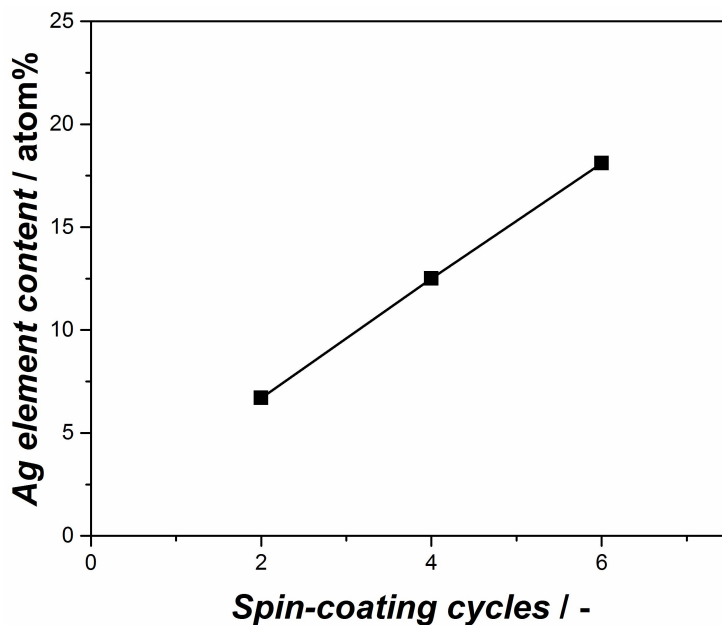


Figure S3.11. Linear relation of Ag element contents determined by EDX with spin-coating cycles.

Table S3.4. Elemental surface ratio of Ag:Cu as determined by XPS.

Spin-coating cycles	Elemental content ratio of Ag:Cu
2	0.06
4	0.37
6	1.92

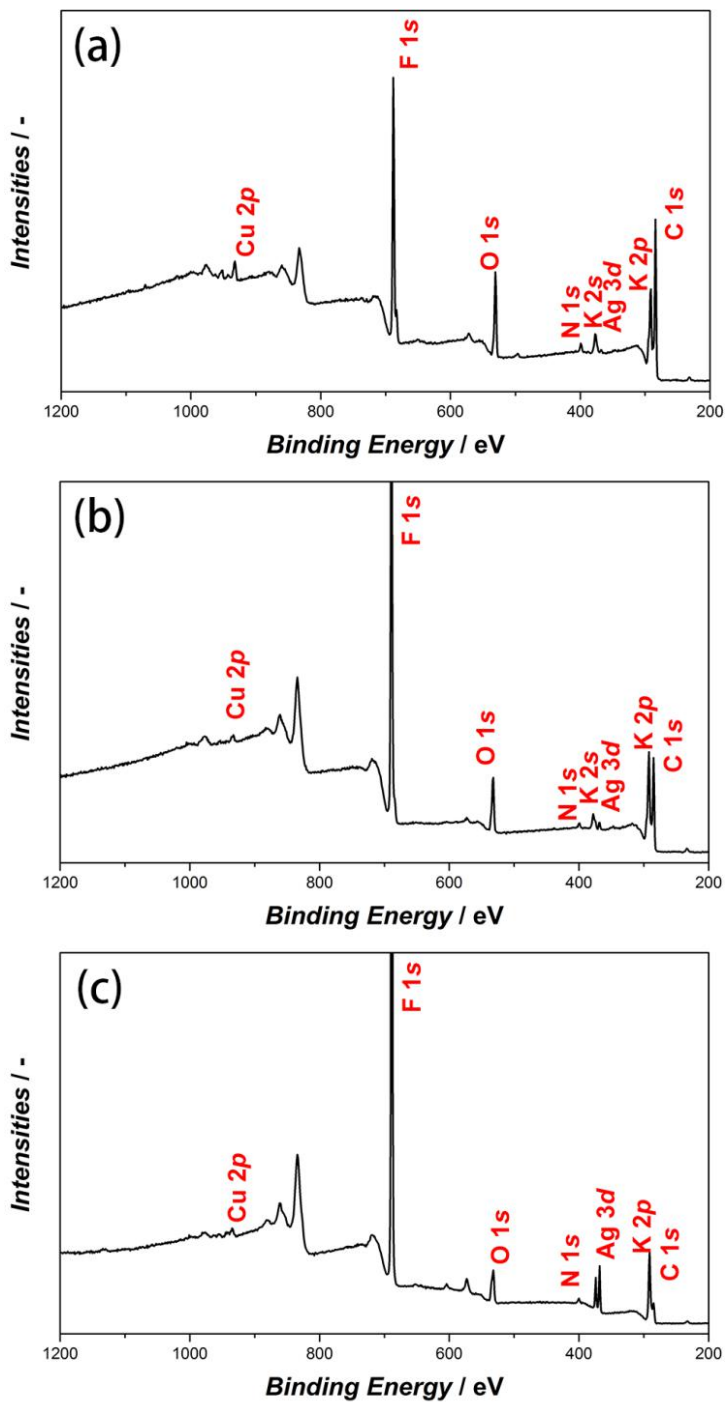


Figure S3.12. XPS survey spectra of (a) AgCu-2, (b) AgCu-4, and (c) AgCu-6.

Table S3.5. Faradaic efficiencies to C₂H₄ obtained on Cu-based alloys and composites.

Electrode	Peak $FE_{C_2H_4}$	Corresponding Potential of Peak $FE_{C_2H_4}$ (V vs. RHE)	J_{Total} (mA cm ⁻²)	Catholyte	Ref [a]
Ag-Cu bimetallic catalyst	42%	-1.1	~6	0.1 M KHCO ₃	1
Ag-Cu Nanodimers	~40%	-1.1	~1	0.1 M KHCO ₃	2
Cu-Zn alloy	33.3%	-1.1	6.1	0.1 M KHCO ₃	3
Ag-Cu ₂ O electrode	11%	-1.3	~4	0.1 M K ₂ CO ₃	4
Cu ₁₀ Zn	15	-0.95	~20	0.1 M KHCO ₃	5
Cu ₃ Ag	~20	-	30	0.1 M KHCO ₃	5
Ag-Cu composite	43%	-1.13	~9	0.1 M KHCO ₃	This work

[a] The references listed in the table are as follows:

1. Wang, J.; Li, Z.; Dong, C.; Feng, Y.; Yang, J.; Liu, H.; Du, X., Silver/Copper Interface for Relay Electroreduction of Carbon Dioxide to Ethylene. *ACS Appl Mater Inter* 2019, 11 (3), 2763-2767.
2. Huang, J.; Mensi, M.; Oveisi, E.; Mantella, V.; Buonsanti, R., Structural Sensitivities in Bimetallic Catalysts for Electrochemical CO₂ Reduction Revealed by Ag-Cu Nanodimers. *Journal of the American Chemical Society* 2019, 141 (6), 2490-2499.
3. Feng, Y.; Li, Z.; Liu, H.; Dong, C.; Wang, J.; Kulinich, S. A.; Du, X., Laser-Prepared CuZn Alloy Catalyst for Selective Electrochemical Reduction of CO₂ to Ethylene. *Langmuir* 2018, 34 (45), 13544-13549.
4. Lee, S.; Park, G.; Lee, J., Importance of Ag-Cu Biphasic Boundaries for Selective Electrochemical Reduction of CO₂ to Ethanol. *ACS Catal* 2017, 7 (12), 8594-8604.
5. Ren, D.; Ang, B. S.-H.; Yeo, B. S., Tuning the Selectivity of Carbon Dioxide Electroreduction toward Ethanol on Oxide-Derived CuxZn Catalysts. *ACS Catal* 2016, 6 (12), 8239-8247.

**Metal-organic Framework
Mediated Nitrogen-doped Carbon
for Electrochemical
CO₂ Reduction**

4

This chapter is based on the following publication:

R. Wang, X. Sun, S. Ould-Chikh, D. Osadchii, F. Bai, F. Kapteijn, J. Gascon. *ACS Appl. Mater. Interfaces*. 2018, 10, 17, 14751-14758.

Abstract: A Nitrogen-doped carbon was synthesized through the pyrolysis of the well-known metal-organic framework ZIF-8, followed by a subsequent acid treatment, and has been applied as catalyst in the electrochemical reduction of carbon dioxide. The resulting electrode shows Faradaic efficiencies to carbon monoxide as high as ~80%, with hydrogen being the only by-product. Pyrolysis temperature determines the amount and the accessibility of N-species in the carbon electrode, in which pyridinic-N and quaternary-N species play key roles in the selective formation of carbon monoxide.

4.1. INTRODUCTION

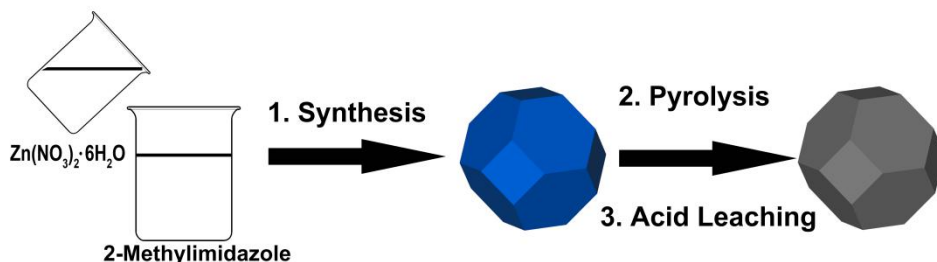
The CO₂ concentration in the atmosphere has increased drastically since the first industrial revolution. The current CO₂ level is considered to be the cause of severe environmental problems [1], increasing the need to find solutions both to revert CO₂ emissions and to utilize the CO₂ already present in the atmosphere. In both cases, valorization of CO₂ may provide human society with new routes for the production of important chemical commodities traditionally manufactured from oil. Several pathways have been proposed to utilize CO₂ [2], such as CO₂ methanation [3], reverse water gas shift [4], CO₂ hydrogenation to hydrocarbons or alcohols [5], CO₂ electrochemical reduction [6], and CO₂ photocatalytic reduction [7], *etc.* Among the above-mentioned CO₂ utilization methods, the electrochemical reduction of CO₂ seems to hold great promise in a more than likely future scenario with affordable green electricity at moderate prices. In such a scenario, the selective formation of one single product is highly desired, while the integration of potential products with existing chemo-catalytic technologies would be ideal. In this sense, the direct production of carbon monoxide is regarded as one of the most promising alternatives, since CO is an essential feed-stock for the chemical industry.

Various electrocatalysts, including noble and earth-abundant metals and their coordination complexes, have been widely studied in the CO₂ electroreduction reaction [8]. Copper is found to be active in the direct synthesis of hydrocarbons and oxygenates from CO₂ [9]. Silver and gold electrodes are reported to selectively convert CO₂ to CO [10]. Nevertheless, their limited availability and sensitivity to poisoning impede to a large extent their practical applications. Hence, the exploration of alternative

materials with high energy efficiency, selectivity, and durability remains challenging.

Recently, introduction of heteroatoms (*e.g.* nitrogen) into the carbon structure has been reported to improve the chemical, electrical, and functional properties of carbon materials [11]. For instance, a carbon nanotubes (CNTs) with N as dopant show a high efficiency in CO₂ reduction to CO, while the nitrogen-free CNTs only produce very little amount of CO. The high CO selectivity was later attributed to the presence of pyridinic-N and quaternary-N [12]. Zhang *et al.* also investigated the effect of N-content in the N-doped CNTs on the catalytic activity in this reaction, and found an linear increase of the Faradaic efficiency towards formate with the N-content [13].

Metal-organic-frameworks (MOFs) have emerged as promising precursors for the synthesis of nanomaterials, because of their unique structure, atomic dispersion, and textural properties [14]. Controlled thermal decomposition of MOFs in an inert gas atmosphere has been demonstrated as a facile route to synthesize carbon materials with well-developed porosity [15]. In this study, a prototypical nitrogen containing MOF, ZIF-8, was chosen as a sacrificial template for the synthesis of N-doped carbon catalysts (NC-T, T referring the pyrolysis temperature). The synthesis involves a high-temperature pyrolysis and a subsequent acid treatment (Scheme 1). The as-synthesized N-doped carbon samples were then used for electrochemical CO₂ reduction.



Scheme 4.1. Schematic illustration of the synthesis of the NC-T catalysts. (1) Room temperature synthesis of ZIF-8 crystals. (2) Pyrolysis of the ZIF-8 crystals in N₂ at different temperatures. (3) Acid leaching to generate the NC-T catalysts.

4.2. EXPERIMENTAL SECTION

4.2.1. Materials

2-Methylimidazole (MeIm, purity 99%), zinc nitrate hexahydrate (Zn(NO₃)₂·6H₂O, >98%), and methanol (>99.8%) were purchased from Sigma-Aldrich Chemical Co. All the chemicals were used without further purification.

4.2.2. Characterization techniques

X-ray diffraction (XRD) patterns were recorded on a Bruker D8 Advance X-ray diffractometer equipped with a Co-K α radiation ($\lambda = 0.179026$ nm). Raman spectra were obtained with a commercial Renishaw in Via Reflex confocal microscope using a 532 nm laser, and measurements were carried out in samples without any pre-treatment at ambient conditions. Thermogravimetric (TG) analysis was carried out using a Mettler Toledo TGA/SDTA851e instrument. The experiments were performed from room temperature to 1000 °C with a ramp of 5 °C min⁻¹ under a N₂ flow (100 mL min⁻¹). The N₂ adsorption-desorption measurements were performed by

using a Micromeritics Tristar 3020 apparatus at 77 K. Scanning electron microscopy (SEM) analysis and the EDX element mapping were performed on a Nova Nano 630 scanning electron microscope from FEI Company. Transmission electron microscopy (TEM) analysis was performed using a FEI TEM (model Titan 80-300 ST) at 300 kV. XPS measurements were performed on a K-alpha Thermo Fisher Scientific spectrometer using monochromatic Al-K α radiation at ambient temperature and chamber pressure of about 10^{-8} mbar. All the spectra measured were corrected by setting the reference binding energy of carbon (*1s*) at 284.8 eV. Spectra were analyzed using the Thermo Avantage software package. The deconvolution of spectra was performed using a mixed Gauss-Lorentz function where the Lorentzian contribution was set to 20% for *Cl*s, *N*1s and *O*1s, and to 30% for *Zn*2p. Quantification was done by using the Scofield sensitivity factors. Difference in depth of analysis for different photoelectron lines was accounted using the TPP-2M method.

4.2.3. Catalysts synthesis

Synthesis of ZIF-8. ZIF-8 precursors were synthesized according to a previous report with some modification [16]. Typically, 2.933 g $\text{Zn}(\text{NO}_3)_2 \cdot 6\text{H}_2\text{O}$ and 6.489 g 2-methylimidazole were separately dissolved in 200 mL methanol. The clear linker solution was rapidly poured into the metal precursor solution under magnetic stirring and kept at room temperature for 24 h. Afterwards, the bright white product was collected by filtration, washed three times with methanol, and dried at 80 °C under vacuum.

Synthesis of MOF-5. MOF-5 precursors were synthesized based on the method previously reported with some modification [17]. In a typical

synthesis, 5.065 g terephthalic acid and 16.99 g Zn(OAc)₂·2H₂O was dissolved in 400 mL and 500 mL DMF, respectively. After stirring for 15 min, the zinc salt solution was added to the organic solution, and the mixture was stirred for another 2.5 h. The product was filtered and washed three times with DMF. The final product was dried at 80 °C under vacuum.

Synthesis of NC-T and C-900. For the preparation of NC-T, 1 g ZIF-8 was pyrolyzed in a ceramic crucible inside a quartz tubular reactor (approx. $L = 1.0 \text{ m} \times \text{ID} = 5.0 \text{ cm}$) horizontally situated in a ceramic fiber oven (Carbolite, Sheffield). The reactor was flushed with nitrogen (100 ml min⁻¹) at 30 °C for 0.5 h, followed by further carbonization at different temperature for 4 h under N₂ (100 ml min⁻¹) at a ramp of 2 °C min⁻¹. The obtained black powders were further immersed in 400 mL 0.5 M H₂SO₄ solution for 24 h at 80 °C and then dried at 60 °C in a vacuum oven for 24 h. These samples are denoted as 'NC-T', where T refers to the pyrolysis temperature ($T = 700, 800, 900 \text{ °C}$). For the synthesis of C-900, 1 g MOF-5 was pyrolyzed at 900 °C, washed in 0.5 M H₂SO₄ solution, and dried under vacuum at the same conditions as that of NC-900.

4.2.4. Electrochemical performance

Preparation of working electrode. For preparation of the electrode, 50 mg catalyst was weighed and suspended in a mixture of tetrahydrofuran (4 mL), Nafion solution (0.5 mL) and isopropyl alcohol (4 mL). Then the mixture was kept in an ultrasonic bath for 2 h. The suspension was drop casted onto a carbon cloth electrode with an area of 12.5 cm² (2.5 cm × 2.5 cm, both sides effective). The electrode was then dried overnight at 80 °C under vacuum. The final catalyst loading of ~50 mg was confirmed by

weighing the working electrode before and after drop-casting, so the catalyst per area was $\sim 4 \text{ mg cm}^{-2}$.

CO₂ electrochemical reduction performance. CO₂ electroreduction experiments were performed in a continuous flow reactor as previously reported [6d]. The reactor was divided into two compartments, the anode and cathode compartment, by a proton-exchange membrane. The anode compartment contained a counter electrode (Pt gauze), while the cathode electrode contained the working electrode and a reference electrode (Ag/AgCl electrode). Both compartments had a volume of 100 mL, and were filled with 85 mL electrolyte prior to the performance tests, leaving a headspace of 15 mL. CO₂ was then fed into the reactor by bubbling through the liquid with a flow rate of 100 mL min^{-1} until the electrolyte was saturated, after which the CO₂ flow was fixed at 10 mL min^{-1} . To start the controlled potential electrolysis, an operation potential was applied by a potentiostat (Autolab PGSTAT302N) in the range of -1.0 to $-2.0 \text{ V vs. Ag/AgCl}$. The cathode compartment was connected to an on-line gas chromatograph (Global Analyzer Solution Compact GC), and the on-line GC would be triggered every 24 min to analyze the gas product. All the experiments last 120 min. At the end of the electrocatalytic test, a liquid sample ($\sim 1 \text{ mL}$) was collected from the electrolyte solution for ultra-performance liquid chromatography (UPLC) measurement. After each experiment, the electrochemical reactor was cleaned with distilled water, and the proton-exchange membrane was immersed into $0.1 \text{ M H}_2\text{SO}_4$ for regeneration.

Faradaic efficiency (FE) of the gas product was calculated based on the following equation:

$$FE = \frac{(n \times F \times v \times f)}{(V_m \times j)} \quad (1)$$

Where:

n : the number of electrons consumed to produce one product molecule, for the product of CO or H₂ ($n=2$), while for the product of CH₄ ($n=8$);

v : the volume fraction of a certain gas product;

f : the overall gas flow rate (m³ s⁻¹);

F : Faraday constant ($F= 96485$ C mol⁻¹);

V_m : the molar volume constant at ambient pressure ($V_m=0.024465$ m³ mol⁻¹);

j : steady-state cell total current at each applied potential (A).

4.3. RESULTS AND DISCUSSION

4.3.1. Synthesis and Structural Characterization

ZIF-8 was synthesized by mixing methanolic solutions of zinc nitrate and MeIm (2-methylimidazole) at room temperature. The powder X-ray diffraction (PXRD) pattern confirms the formation of pure crystalline ZIF-8 (Figure 4.1a) [18]. After pyrolysis and a subsequent acid treatment, the characteristic peaks of ZIF-8 disappear, and two broad reflections positioned at $2\theta = 30^\circ$ and 50.5° are observed in the N-doped carbon samples (Figure 4.1b), attributed to the (002) and (100) planes of the graphitic carbon, respectively [19].

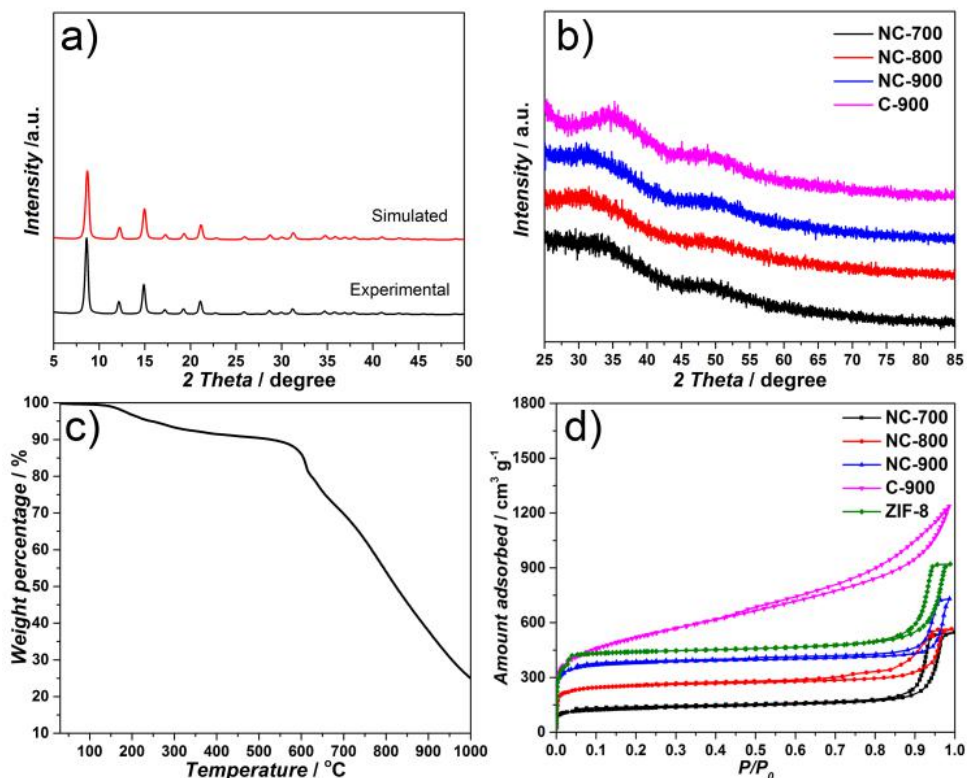


Figure 4.1. XRD pattern of ZIF-8 (a) and carbon-based samples (b); TG profile of ZIF-8 (c); N_2 sorption isotherms of the as-synthesized materials (d).

The graphitization degree of the carbon matrix in the N-doped carbon samples was analyzed by Raman spectroscopy (Figure S4.1). All the Raman spectra of NC-T exhibit the characteristic G and D bands of carbon at 1580 cm^{-1} and 1350 cm^{-1} , which are correlated to graphitic sp^2 carbon and disordered or defect carbon, respectively [14c]. The Raman spectra exhibit an apparent correlation with pyrolysis temperature. The intensity ratio between G and D band (I_G/I_D) is similar between NC-800 and NC-900, suggesting a comparable graphitization degree of the carbon matrix [20]. For the Raman spectrum of NC-700, a shoulder at 1500 cm^{-1} can also be

observed. This peak is likely to originate from the non-pyrolyzed imidazolates [21], and leads to an overestimation of the I_G/I_D ratio. Indeed, the presence of non-pyrolyzed imidazolates in NC-700 can be further confirmed by thermogravimetric (TG) analysis (Figure 4.1c). In the TGA curve, a mass loss of ~ 10 wt.% can be observed until 600 °C, probably attributed to the release of moisture and residual MeIm molecules from the porosity of ZIF-8 [18]. The sample mass then decreases sharply with elevating temperature, which can be ascribed to the decomposition of the organic linker (MeIm) and the gradual evaporation of metallic zinc (boiling point of metallic Zn is 907 °C) [22].

The Brunauer-Emmett-Teller (BET) area (S_{BET}) and pore volume (V_{pore}) of ZIF-8 and NC-T samples were determined by N₂ adsorption-desorption isotherms at 77 K (Figure 4.1d), and the corresponding textural properties are summarized in Table S4.1. ZIF-8 with a high S_{BET} of 1752 m² g⁻¹ and V_{pore} of 1.42 cm³ g⁻¹, exhibits a typical microporous structure with some intergranular mesoporosity, as concluded from the presence of hysteresis loop above $P/P_0 \approx 0.8$ [23]. After pyrolysis and acid leaching, the S_{BET} and V_{pore} of NC-T samples decrease drastically, attributed to the collapse of the well-defined microporous structure of ZIF-8 during the pyrolysis process. Besides, an apparent dependence between surface area and pore volume with pyrolysis temperature can be observed in NC-T samples. Specifically, the NC-900 sample exhibits the highest S_{BET} and micropore volume (V_{micro}), but the lowest mesopore volume (V_{meso}) among all NC-T samples, suggesting that a higher pyrolysis temperature can remove more organic residuals from the pores but lead to more agglomeration of carbon nanoparticles [20a].

The morphology of the synthesized materials was studied using electron microscopy. Transmission electron microscopy (TEM) image (Figure 4.2a) of the as-prepared ZIF-8 exhibits a typical rhombic dodecahedral shape with a size of 30-50 nm. The corresponding energy-dispersive X-ray spectroscopy (EDX) element mapping images (Figure S4.2a-d) demonstrate the homogeneous dispersion of carbon, nitrogen, and zinc throughout the ZIF-8 crystal. After high-temperature pyrolysis and acid treatment, highly dispersed C, N, and Zn EDX-signals in the pyrolyzed NC-T samples can be detected (Figure S4.2e-p). The absence of any observable zinc (oxide) nanoparticles in the carbon matrix of the as-synthesized NC-T samples are further verified by TEM analysis (Figure 4.2b-d), indicating that the acid treatment is sufficient to remove all zinc (oxide) nanoparticles from these nitrogen-doped carbon samples. In addition, some large pores are observed in the NC-T samples (*e.g.* the yellow circle in Figure 4.2b), attributed to the presence of voids between nanoparticles, in line with the N₂ sorption results.

The as synthesized precursors and catalysts were further characterized by means of X-ray photoelectron spectroscopy (XPS). The XPS survey spectra clearly demonstrate the presence of C, N, O, and some Zn in the structure of all the samples (Figure S4.3 a,b and Table S4.2). XPS survey spectra indicate that these NC-T samples exhibit similar oxygen and zinc contents, and the presence of the *O1s* signal can be attributed to the oxidation of the carbon surface after exposure to the air and the subsequent acid leaching. The similar Zn contents of NC-T samples detected by XPS analysis further confirm that the acid leaching easily removes those Zn (oxide) nanoparticles in the carbon porosity, while the remaining Zn signals

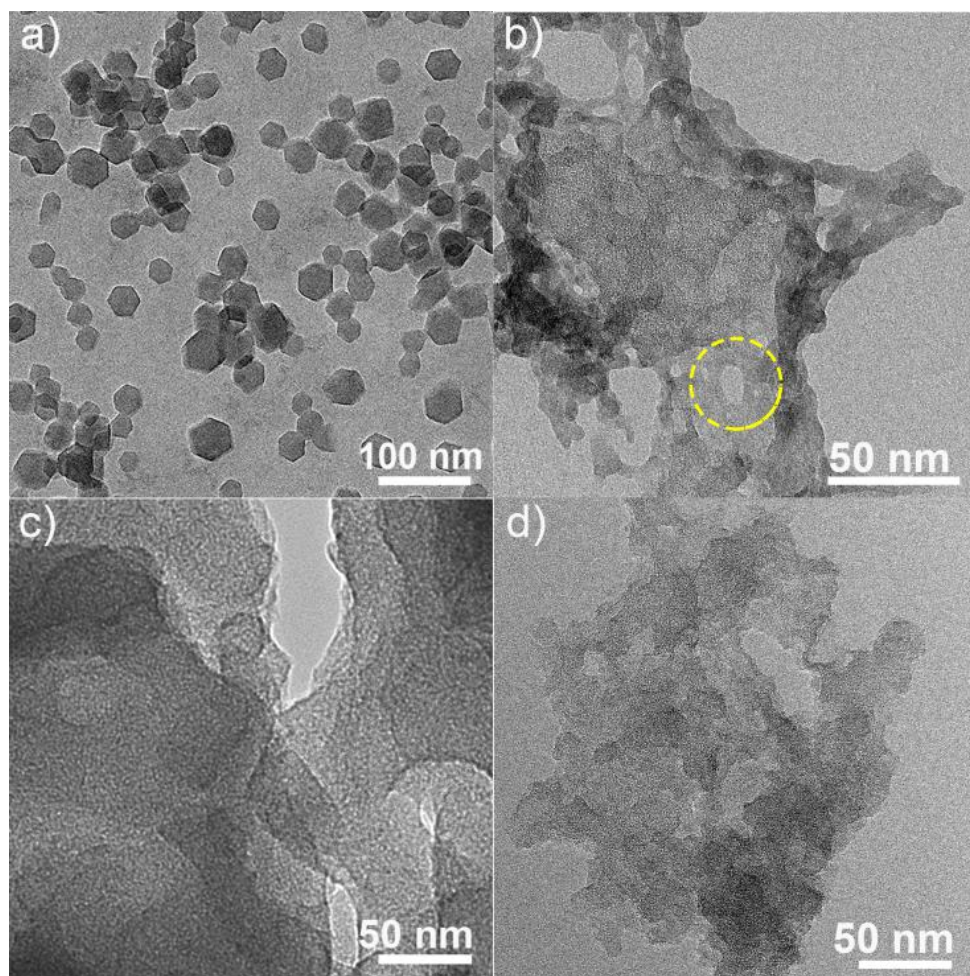


Figure 4.2. TEM images of ZIF-8 (a), NC-700 (b), NC-800 (c), and NC-900 (d).

in all these NC-T samples have been proven by Wang *et al.* to be porphyrin-like Zn (Zn-N_x) with high resistance against acid leaching [24]. *N*1s signals of NC-T samples can be deconvoluted into four types of nitrogen species with binding energy around 398.3 eV, 399.9 eV, 401.2 eV, and 402.5 eV, which can be attributed to pyridinic-N, pyrrolic-N, quaternary-N, and oxidized-N, respectively [25], as shown in Figure 4.3a-c. We speculate that, upon pyrolysis, N-atoms in the pentagonal ring of the original imidazole

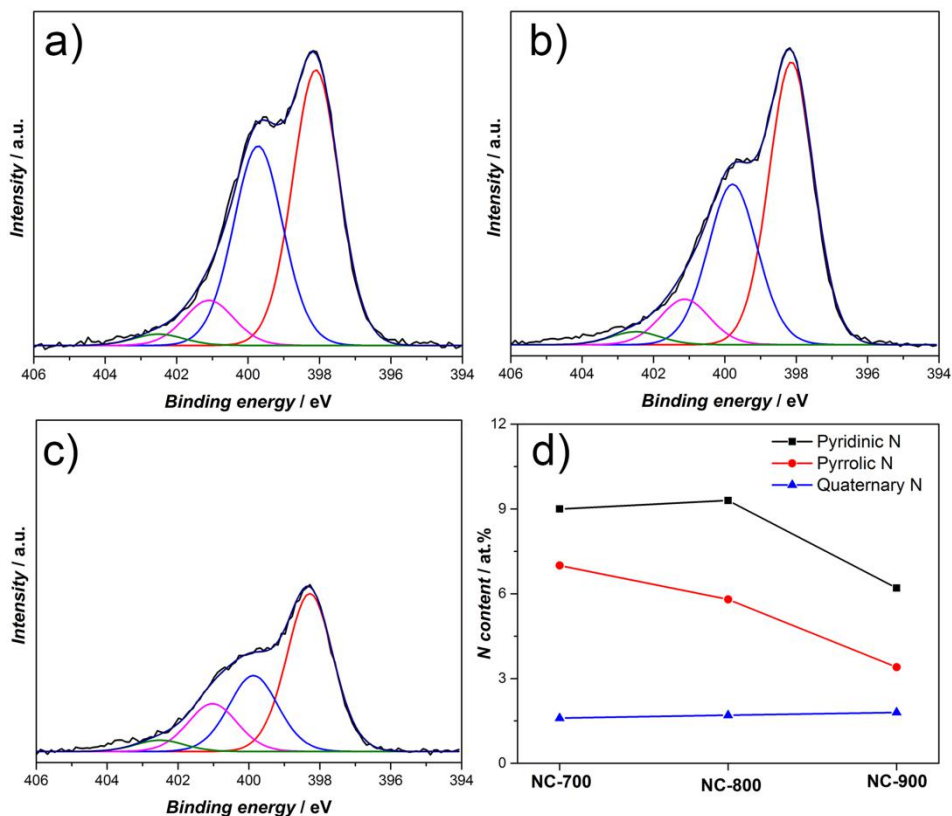


Figure 4.3. N $1s$ XPS region spectra of (a) NC-700, (b) NC-800, and (c) NC-900; (d) N-species distribution in NC-900 from XPS.

units are mostly converted into pyridinic-, pyrrolic-, and quaternary-N species. The percentage of each N species is calculated from XPS analysis and included in Figure 4.3d and Table S4.2. Obviously, the NC-T sample synthesized at a higher pyrolysis temperature contains a lower overall N-content, which can be attributed to the removal of some relatively unstable N-species such as pyridinic and/or pyrrolic-N at high temperature, consistent with previous reports [25-26]. Pyridinic-N dominates in all NC-T samples, and the NC-800 sample has the highest pyridinic-N content of 9.3 at.%.

4.3.2. Catalytic Performance

The performance of the N-doped carbon catalysts in the electrocatalytic reduction of carbon dioxide was evaluated in 0.1 M KHCO₃ solution saturated with CO₂ under controlled potential electrolysis. No liquid-phase products could be detected during the reaction by ultra-performance-liquid chromatography (UPLC), and the gas products were analyzed by on-line gas chromatography (GC). CO and H₂ are the only detectable reduction products over the whole potential range (Figure 4.4a and b), except at -1.33 V vs. RHE (reversible hydrogen electrode), where some CH₄ is produced (Figure S4.4). When the Faradaic efficiency of CO (FE_{CO}) is plotted as a function of the potential in the range of -0.53 to -1.33 V vs. RHE, a volcano-like curve is obtained, with an optimum at -0.93 V vs. RHE for all these N-doped carbon samples. At the same time, the FE_{CO} of NC-T samples depends on the pyrolysis temperature, and the N-doped carbon pyrolyzed at a higher temperature exhibits a higher FE_{CO} , with NC-900 showing the highest FE_{CO} of ~78% at -0.93 V vs. RHE, which is comparable to the data reported recently from nitrogen-doped carbon catalysts (Table S4.3) [12-13, 27]. Figure 4.4c shows the partial current density to CO (j_{CO}) for the N-doped carbon samples within the potential range from -0.53 to -1.33 V vs. RHE. NC-900 exhibits the highest j_{CO} among these catalysts. The electrocatalytic stability of the NC-900 sample in CO₂ reduction is as well evaluated by constant potential electrolysis of CO₂ (Figure S4.5a). At an applied potential of -0.93 V vs. RHE, the NC-900 sample exhibits a stable current density of -1.1 mA cm⁻² and FE_{CO} of ~80 % during 120 min reaction time, without obvious deactivation.

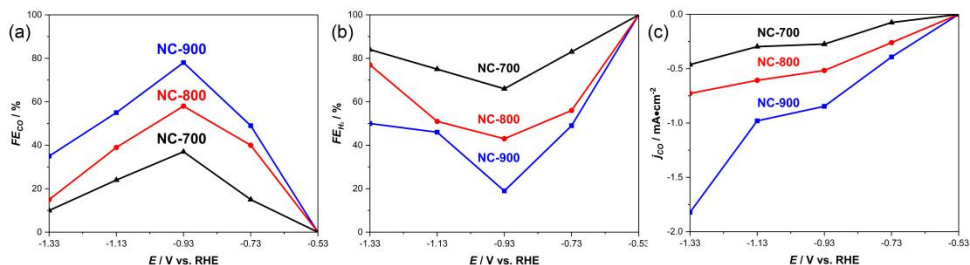


Figure 4.4. CO₂ electrochemical reduction performance of NC-T samples. (a) Faradaic efficiency to CO, (b) Faradaic efficiency to H₂, and (c) Partial CO current density.

To probe the origin of the CO₂ reduction catalytic activity obtained with the NC-900 sample, a carbon material (C-900) was also prepared by pyrolysis of MOF-5 ([Zn₄O(bdc)₃], bdc = benzene-1,4-dicarboxylate) [15a], followed by acid leaching under the same conditions as NC-900. As expected, C, O, and Zn signals but no N-species can be detected in the XPS survey spectrum of C-900 (Figure S4.3 and Table S4.2). Although C-900 exhibits a higher S_{BET} than that of NC-900 (Figure 4.1d and Table S4.1), it shows a FE_{CO} as low as ~2%, along with a poor current density of -0.6 mA cm⁻² at -0.93 V vs. RHE (Figure S4.5b). This result indicates that the presence of N in the carbon structure significantly improves the activity for CO₂ electroreduction, and that residual Zn has a negligible contribution. It has been reported that pyridinic-N and quaternary-N species in the carbon matrix can facilitate the transfer of a proton-electron pair to CO₂, thereby lowering the energy barrier for the production of COOH*, an intermediate for CO formation, resulting in a high catalytic activity, while the pyrrolic-N plays a less important role in this process [12]. Unexpectedly, NC-800 is less active although it has a higher content of pyridinic-N than NC-900. On the one hand, a zinc-porphyrin complex (Zn-N_x) was indeed reported to

preferably produce hydrogen under a similar electrochemical measurement conditions [28], but since NC-900 and NC-800 exhibit similar Zn contents, as proven by XPS analysis, the lower activity of NC-800 cannot be simply attributed to the presence of these Zn-species. On the other hand, NC-800 and NC-900 samples also show similar graphitization degrees according to Raman measurement. Thus, we attribute the lower activity of NC-800 mainly to the lower S_{BET} of NC-800, which probably impedes the accessibility of active sites during CO₂ electroreduction process.

4.4. CONCLUSIONS

A facile route is proposed for the preparation of nitrogen-doped carbon materials via pyrolysis of ZIF-8 and subsequent acid treatment. In CO₂ electroreduction, these N-doped carbon samples are up to 78% selective to CO formation, the higher the pyrolysis temperature the better the catalytic performance. The high activity can be attributed to the presence of a large amount of pyridinic-N and quaternary-N species in the carbon structure, which are known to lower the energy barrier for the formation of COOH*, an intermediate to produce CO. In addition, the well-developed porosity further promotes the activity by making more active sites accessible.

4.5. REFERENCES

1. Princiotta, F. T., Global climate change - the technology challenge. *Wit Trans Ecol Envir* 2007, 101, 533-551.
2. Kondratenko, E. V.; Mul, G.; Baltrusaitis, J.; Larrazabal, G. O.; Perez-Ramirez, J., Status and perspectives of CO₂ conversion into fuels and chemicals by catalytic, photocatalytic and electrocatalytic processes. *Energy Environ Sci* 2013, 6 (11), 3112-3135.
3. (a) Du, G. A.; Lim, S.; Yang, Y. H.; Wang, C.; Pfefferle, L.; Haller, G. L., Methanation of carbon dioxide on Ni-incorporated MCM-41 catalysts: The influence of catalyst pretreatment and study of steady-state reaction. *Journal of Catalysis* 2007, 249 (2), 370-379; (b) Park, J. N.; McFarland, E. W., A highly dispersed Pd-Mg/SiO₂ catalyst active for methanation of CO₂. *Journal of Catalysis* 2009, 266 (1), 92-97; (c) Sharma, S.; Hu, Z. P.; Zhang, P.; McFarland, E. W.; Metiu, H., CO₂ methanation on Ru-doped ceria. *Journal of Catalysis* 2011, 278 (2), 297-309; (d) Shin, H. H.; Lu, L.; Yang, Z.; Kiely, C. J.; McIntosh, S., Cobalt Catalysts Decorated with Platinum Atoms Supported on Barium Zirconate Provide Enhanced Activity and Selectivity for CO₂ Methanation. *Acs Catal* 2016, 6 (5), 2811-2818; (e) Wang, F.; He, S.; Chen, H.; Wang, B.; Zheng, L.; Wei, M.; Evans, D. G.; Duan, X., Active Site Dependent Reaction Mechanism over Ru/CeO₂ Catalyst toward CO₂ Methanation. *J Am Chem Soc* 2016, 138 (19), 6298-305; (f) Wang, W.; Wang, S.; Ma, X.; Gong, J., Recent advances in catalytic hydrogenation of carbon dioxide. *Chem Soc Rev* 2011, 40 (7), 3703-27.
4. (a) Bustamante, F.; Enick, R. M.; Cugini, A. V.; Killmeyer, R. P.; Howard, B. H.; Rothenberger, K. S.; Ciocco, M. V.; Morreale, B. D., High-temperature kinetics of the homogeneous reverse water-gas shift reaction. *Aiche Journal* 2004, 50 (5), 1028-1041; (b) Daza, Y. A.; Kent, R. A.; Yung, M. M.; Kuhn, J. N., Carbon Dioxide Conversion by Reverse Water-Gas Shift Chemical Looping on Perovskite-Type Oxides. *Ind Eng Chem Res* 2014, 53 (14), 5828-5837; (c) Dietz, L.; Piccinin, S.; Maestri, M., Mechanistic Insights into CO₂ Activation via Reverse Water-Gas Shift on Metal Surfaces. *The Journal of Physical Chemistry C* 2015, 119 (9), 4959-4966; (d) Upadhye, A. A.; Ro, I.; Zeng, X.; Kim, H. J.; Tejedor, I.; Anderson, M. A.; Dumesic, J. A.; Huber, G. W., Plasmon-enhanced reverse water gas shift reaction over oxide

- supported Au catalysts. *Catalysis Science & Technology* 2015, 5 (5), 2590-2601; (e) Wang, L. H.; Liu, H.; Liu, Y.; Chen, Y.; Yang, S. Q., Effect of precipitants on Ni-CeO₂ catalysts prepared by a co-precipitation method for the reverse water-gas shift reaction. *Journal of Rare Earths* 2013, 31 (10), 969-974.
5. (a) Centi, G.; Perathoner, S., Opportunities and prospects in the chemical recycling of carbon dioxide to fuels. *Catal Today* 2009, 148 (3-4), 191-205; (b) Iablokov, V.; Beaumont, S. K.; Alayoglu, S.; Pushkarev, V. V.; Specht, C.; Gao, J.; Alivisatos, A. P.; Kruse, N.; Somorjai, G. A., Size-controlled model Co nanoparticle catalysts for CO(2) hydrogenation: synthesis, characterization, and catalytic reactions. *Nano Lett* 2012, 12 (6), 3091-6; (c) Owen, R. E.; Mattia, D.; Plucinski, P.; Jones, M. D., Kinetics of CO₂ Hydrogenation to Hydrocarbons over Iron-Silica Catalysts. *Chemphyschem* 2017, 18 (22), 3211-3218; (d) Rungtaweewanit, B.; Baek, J.; Araujo, J. R.; Archanjo, B. S.; Choi, K. M.; Yaghi, O. M.; Somorjai, G. A., Copper Nanocrystals Encapsulated in Zr-based Metal-Organic Frameworks for Highly Selective CO₂ Hydrogenation to Methanol. *Nano Lett* 2016, 16 (12), 7645-7649; (e) Saeidi, S.; Amin, N. A. S.; Rahimpour, M. R., Hydrogenation of CO₂ to value-added products-A review and potential future developments. *Journal of CO₂ Utilization* 2014, 5, 66-81; (f) Sathawong, R.; Koizumi, N.; Song, C.; Prasassarakich, P., Comparative Study on CO₂ Hydrogenation to Higher Hydrocarbons over Fe-Based Bimetallic Catalysts. *Top Catal* 2013, 57 (6-9), 588-594; (g) Xie, C.; Chen, C.; Yu, Y.; Su, J.; Li, Y.; Somorjai, G. A.; Yang, P., Tandem Catalysis for CO₂ Hydrogenation to C₂-C₄ Hydrocarbons. *Nano Lett* 2017, 17 (6), 3798-3802.
6. (a) Ganesh, I., Electrochemical conversion of carbon dioxide into renewable fuel chemicals - The role of nanomaterials and the commercialization. *Renew Sust Energ Rev* 2016, 59, 1269-1297; (b) Lu, Q.; Jiao, F., Electrochemical CO₂ reduction: Electrocatalyst, reaction mechanism, and process engineering. *Nano Energy* 2016, 29, 439-456; (c) Pletcher, D., The cathodic reduction of carbon dioxide—What can it realistically achieve? A mini review. *Electrochem Commun* 2015, 61, 97-101; (d) Sastre, F.; Munoz-Batista, M. J.; Kubacka, A.; Fernandez-Garcia, M.; Smith, W. A.; Kapteijn, F.; Makkee, M.; Gascon, J., Efficient Electrochemical Production of Syngas from CO₂ and H₂O by using a Nanostructured Ag/g-C₃N₄ Catalyst. *Chemelectrochem* 2016, 3 (9), 1497-1502; (e) Whipple, D. T.; Kenis, P. J. A., Prospects of CO₂

- Utilization via Direct Heterogeneous Electrochemical Reduction. *J Phys Chem Lett* 2010, 1 (24), 3451-3458; (f) Zhao, C.; Dai, X.; Yao, T.; Chen, W.; Wang, X.; Wang, J.; Yang, J.; Wei, S.; Wu, Y.; Li, Y., Ionic Exchange of Metal-Organic Frameworks to Access Single Nickel Sites for Efficient Electroreduction of CO₂. *J Am Chem Soc* 2017, 139 (24), 8078-8081.
7. Thampi, K. R.; Kiwi, J.; Gratzel, M., Methanation and Photo-Methanation of Carbon-Dioxide at Room-Temperature and Atmospheric-Pressure. *Nature* 1987, 327 (6122), 506-508.
 8. (a) Costentin, C.; Robert, M.; Saveant, J. M., Catalysis of the electrochemical reduction of carbon dioxide. *Chem Soc Rev* 2013, 42 (6), 2423-36; (b) Qiao, J.; Liu, Y.; Hong, F.; Zhang, J., A review of catalysts for the electroreduction of carbon dioxide to produce low-carbon fuels. *Chem Soc Rev* 2014, 43 (2), 631-75.
 9. Ma, M.; Djanashvili, K.; Smith, W. A., Controllable Hydrocarbon Formation from the Electrochemical Reduction of CO₂ over Cu Nanowire Arrays. *Angewandte Chemie* 2016, 55 (23), 6680-4.
 10. (a) Back, S.; Kim, J. H.; Kim, Y. T.; Jung, Y., Bifunctional Interface of Au and Cu for Improved CO₂ Electroreduction. *ACS Appl Mater Interfaces* 2016, 8 (35), 23022-7; (b) Ma, M.; Trzesniewski, B. J.; Xie, J.; Smith, W. A., Selective and Efficient Reduction of Carbon Dioxide to Carbon Monoxide on Oxide-Derived Nanostructured Silver Electrocatalysts. *Angewandte Chemie* 2016, 55 (33), 9748-52.
 11. Liu, Y.; Chen, S.; Quan, X.; Yu, H., Efficient Electrochemical Reduction of Carbon Dioxide to Acetate on Nitrogen-Doped Nanodiamond. *J Am Chem Soc* 2015, 137 (36), 11631-6.
 12. (a) Sharma, P. P.; Wu, J.; Yadav, R. M.; Liu, M.; Wright, C. J.; Tiwary, C. S.; Yakobson, B. I.; Lou, J.; Ajayan, P. M.; Zhou, X. D., Nitrogen-Doped Carbon Nanotube Arrays for High-Efficiency Electrochemical Reduction of CO₂: On the Understanding of Defects, Defect Density, and Selectivity. *Angewandte Chemie* 2015, 54 (46), 13701-5; (b) Wu, J.; Yadav, R. M.; Liu, M.; Sharma, P. P.; Tiwary, C. S.; Ma, L.; Zou, X.; Zhou, X. D.; Yakobson, B. I.; Lou, J.; Ajayan, P. M., Achieving Highly Efficient, Selective, and Stable CO₂ Reduction on Nitrogen-Doped Carbon Nanotubes. *Acs Nano* 2015, 9 (5), 5364-71.

13. Zhang, S.; Kang, P.; Ubnoske, S.; Brennaman, M. K.; Song, N.; House, R. L.; Glass, J. T.; Meyer, T. J., Polyethylenimine-enhanced electrocatalytic reduction of CO₂ to formate at nitrogen-doped carbon nanomaterials. *J Am Chem Soc* 2014, 136 (22), 7845-8.
14. (a) Oar-Arteta, L.; Wezendonk, T.; Sun, X. H.; Kapteijn, F.; Gascon, J., Metal organic frameworks as precursors for the manufacture of advanced catalytic materials. *Materials Chemistry Frontiers* 2017, 1 (9), 1709-1745; (b) Santos, V. P.; Wezendonk, T. A.; Jaen, J. J.; Dugulan, A. I.; Nasalevich, M. A.; Islam, H. U.; Chojecki, A.; Sartipi, S.; Sun, X.; Hakeem, A. A.; Koeken, A. C.; Ruitenbeek, M.; Davidian, T.; Meima, G. R.; Sankar, G.; Kapteijn, F.; Makkee, M.; Gascon, J., Metal organic framework-mediated synthesis of highly active and stable Fischer-Tropsch catalysts. *Nat Commun* 2015, 6, 6451; (c) Sun, X.; Olivos-Suarez, A. I.; Oar-Arteta, L.; Rozhko, E.; Osadchii, D.; Bavykina, A.; Kapteijn, F.; Gascon, J., Metal-Organic Framework Mediated Cobalt/Nitrogen-Doped Carbon Hybrids as Efficient and Chemoselective Catalysts for the Hydrogenation of Nitroarenes. *Chemcatchem* 2017, 9 (10), 1854-1862; (d) Sun, X.; Olivos-Suarez, A. I.; Osadchii, D.; Romero, M. J. V.; Kapteijn, F.; Gascon, J., Single cobalt sites in mesoporous N-doped carbon matrix for selective catalytic hydrogenation of nitroarenes. *Journal of Catalysis* 2018, 357, 20-28; (e) Sun, X.; Suarez, A. I. O.; Meijerink, M.; van Deelen, T.; Ould-Chikh, S.; Zecevic, J.; de Jong, K. P.; Kapteijn, F.; Gascon, J., Manufacture of highly loaded silica-supported cobalt Fischer-Tropsch catalysts from a metal organic framework. *Nat Commun* 2017, 8 (1), 1680.
15. (a) Liu, B.; Shioyama, H.; Akita, T.; Xu, Q., Metal-organic framework as a template for porous carbon synthesis. *J Am Chem Soc* 2008, 130 (16), 5390-1; (b) Zhang, L.; Su, Z.; Jiang, F.; Yang, L.; Qian, J.; Zhou, Y.; Li, W.; Hong, M., Highly graphitized nitrogen-doped porous carbon nanopolyhedra derived from ZIF-8 nanocrystals as efficient electrocatalysts for oxygen reduction reactions. *Nanoscale* 2014, 6 (12), 6590-602.
16. Venna, S. R.; Jasinski, J. B.; Carreon, M. A., Structural evolution of zeolitic imidazolate framework-8. *J Am Chem Soc* 2010, 132 (51), 18030-3.

17. Tranchemontagne, D. J.; Hunt, J. R.; Yaghi, O. M., Room temperature synthesis of metal-organic frameworks: MOF-5, MOF-74, MOF-177, MOF-199, and IRMOF-0. *Tetrahedron* 2008, 64 (36), 8553-8557.
18. Park, K. S.; Ni, Z.; Cote, A. P.; Choi, J. Y.; Huang, R.; Uribe-Romo, F. J.; Chae, H. K.; O'Keeffe, M.; Yaghi, O. M., Exceptional chemical and thermal stability of zeolitic imidazolate frameworks. *Proceedings of the National Academy of Sciences of the United States of America* 2006, 103 (27), 10186-10191.
19. Fei, H.; Dong, J.; Arellano-Jimenez, M. J.; Ye, G.; Dong Kim, N.; Samuel, E. L.; Peng, Z.; Zhu, Z.; Qin, F.; Bao, J.; Yacaman, M. J.; Ajayan, P. M.; Chen, D.; Tour, J. M., Atomic cobalt on nitrogen-doped graphene for hydrogen generation. *Nat Commun* 2015, 6, 8668.
20. (a) Chaikittisilp, W.; Hu, M.; Wang, H.; Huang, H. S.; Fujita, T.; Wu, K. C.; Chen, L. C.; Yamauchi, Y.; Ariga, K., Nanoporous carbons through direct carbonization of a zeolitic imidazolate framework for supercapacitor electrodes. *Chem Commun (Camb)* 2012, 48 (58), 7259-61; (b) Deng, J.; Ren, P.; Deng, D.; Bao, X., Enhanced electron penetration through an ultrathin graphene layer for highly efficient catalysis of the hydrogen evolution reaction. *Angewandte Chemie* 2015, 54 (7), 2100-4.
21. Carter, D. A.; Pemberton, J. E., Raman spectroscopy and vibrational assignments of 1- and 2-methylimidazole. *J Raman Spectrosc* 1997, 28 (12), 939-946.
22. (a) Torad, N. L.; Hu, M.; Kamachi, Y.; Takai, K.; Imura, M.; Naito, M.; Yamauchi, Y., Facile synthesis of nanoporous carbons with controlled particle sizes by direct carbonization of monodispersed ZIF-8 crystals. *Chem Commun (Camb)* 2013, 49 (25), 2521-3; (b) Zhong, H. X.; Wang, J.; Zhang, Y. W.; Xu, W. L.; Xing, W.; Xu, D.; Zhang, Y. F.; Zhang, X. B., ZIF-8 derived graphene-based nitrogen-doped porous carbon sheets as highly efficient and durable oxygen reduction electrocatalysts. *Angewandte Chemie* 2014, 53 (51), 14235-9.
23. Xia, B. Y.; Yan, Y.; Li, N.; Wu, H. B.; Lou, X. W.; Wang, X., A metal-organic framework-derived bifunctional oxygen electrocatalyst. *Nat Energy* 2016, 1, 15006.
24. Wang, S.; Shang, L.; Li, L.; Yu, Y.; Chi, C.; Wang, K.; Zhang, J.; Shi, R.; Shen, H.; Waterhouse, G. I.; Liu, S.; Tian, J.; Zhang, T.; Liu, H., Metal-Organic-Framework-Derived Mesoporous Carbon Nanospheres Containing Porphyrin-Like Metal Centers for Conformal Phototherapy. *Adv Mater* 2016, 28 (38), 8379-8387.

25. Wu, J.; Liu, M.; Sharma, P. P.; Yadav, R. M.; Ma, L.; Yang, Y.; Zou, X.; Zhou, X. D.; Vajtai, R.; Yakobson, B. I.; Lou, J.; Ajayan, P. M., Incorporation of Nitrogen Defects for Efficient Reduction of CO₂ via Two-Electron Pathway on Three-Dimensional Graphene Foam. *Nano Lett* 2016, 16 (1), 466-70.
26. Arrigo, R.; Havecker, M.; Schlogl, R.; Su, D. S., Dynamic surface rearrangement and thermal stability of nitrogen functional groups on carbon nanotubes. *Chem Commun (Camb)* 2008, (40), 4891-3.
27. (a) Guo, Y.; Yang, H. J.; Zhou, X.; Liu, K. L.; Zhang, C.; Zhou, Z. Y.; Wang, C.; Lin, W. B., Electrocatalytic reduction of CO₂ to CO with 100% faradaic efficiency by using pyrolyzed zeolitic imidazolate frameworks supported on carbon nanotube networks. *J Mater Chem A* 2017, 5 (47), 24867-24873; (b) Jhong, H. M.; Tornow, C. E.; Smid, B.; Gewirth, A. A.; Lyth, S. M.; Kenis, P. J., A Nitrogen-Doped Carbon Catalyst for Electrochemical CO₂ Conversion to CO with High Selectivity and Current Density. *ChemSusChem* 2017, 10 (6), 1094-1099; (c) Kumar, B.; Asadi, M.; Pisasale, D.; Sinha-Ray, S.; Rosen, B. A.; Haasch, R.; Abiade, J.; Yarin, A. L.; Salehi-Khojin, A., Renewable and metal-free carbon nanofibre catalysts for carbon dioxide reduction. *Nature Communications* 2013, 4; (d) Li, W.; Seredych, M.; Rodriguez-Castellon, E.; Bandoz, T. J., Metal-free Nanoporous Carbon as a Catalyst for Electrochemical Reduction of CO₂ to CO and CH₄. *ChemSusChem* 2016, 9 (6), 606-16; (e) Lu, X.; Tan, T. H.; Ng, Y. H.; Amal, R., Highly Selective and Stable Reduction of CO₂ to CO by a Graphitic Carbon Nitride/Carbon Nanotube Composite Electrocatalyst. *Chemistry* 2016, 22 (34), 11991-6; (f) Wang, H.; Jia, J.; Song, P.; Wang, Q.; Li, D.; Min, S.; Qian, C.; Wang, L.; Li, Y. F.; Ma, C.; Wu, T.; Yuan, J.; Antonietti, M.; Ozin, G. A., Efficient Electrocatalytic Reduction of CO₂ by Nitrogen-Doped Nanoporous Carbon/Carbon Nanotube Membranes: A Step Towards the Electrochemical CO₂ Refinery. *Angewandte Chemie* 2017, 56 (27), 7847-7852; (g) Xu, J.; Kan, Y.; Huang, R.; Zhang, B.; Wang, B.; Wu, K. H.; Lin, Y.; Sun, X.; Li, Q.; Centi, G.; Su, D., Revealing the Origin of Activity in Nitrogen-Doped Nanocarbons towards Electrocatalytic Reduction of Carbon Dioxide. *ChemSusChem* 2016, 9 (10), 1085-9.
28. Weng, Z.; Jiang, J.; Wu, Y.; Wu, Z.; Guo, X.; Materna, K. L.; Liu, W.; Batista, V. S.; Brudvig, G. W.; Wang, H., Electrochemical CO₂ Reduction to Hydrocarbons on a

Heterogeneous Molecular Cu Catalyst in Aqueous Solution. *J Am Chem Soc* 2016, 138 (26), 8076-9.

4.6. Supporting Information for Chapter 4

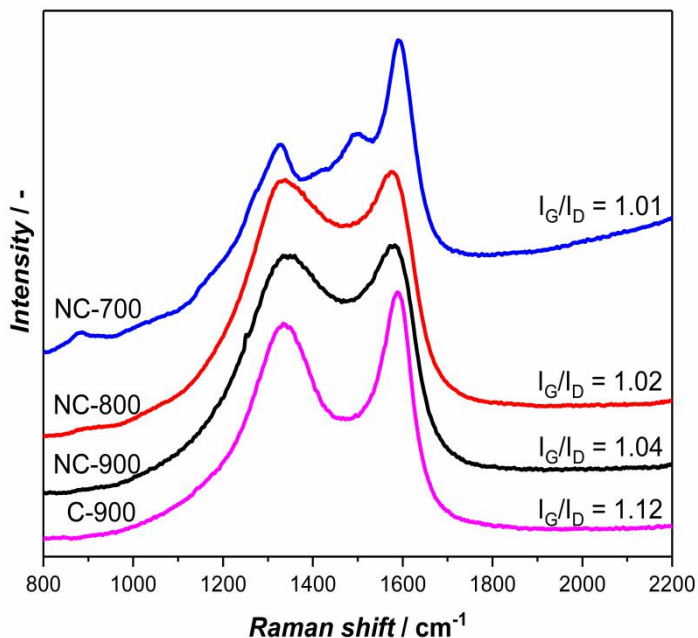


Figure S4.1. Raman spectra of NC-T and C-900 samples.

Table S4.1. N₂-adsorption-desorption data of as-synthesized samples.

Samples	$S / (\text{m}^2/\text{g})$			$V / (\text{cm}^3/\text{g})$		
	Total	Micro	Meso	Total	Micro	Meso
ZIF-8	1752	1615	137	1.42	0.62	0.80
NC-700	392	273	119	0.80	0.12	0.68
NC-800	488	399	89	0.65	0.15	0.50
NC-900	740	672	68	0.53	0.26	0.27
C-900	1833	703	1130	1.84	0.31	1.53

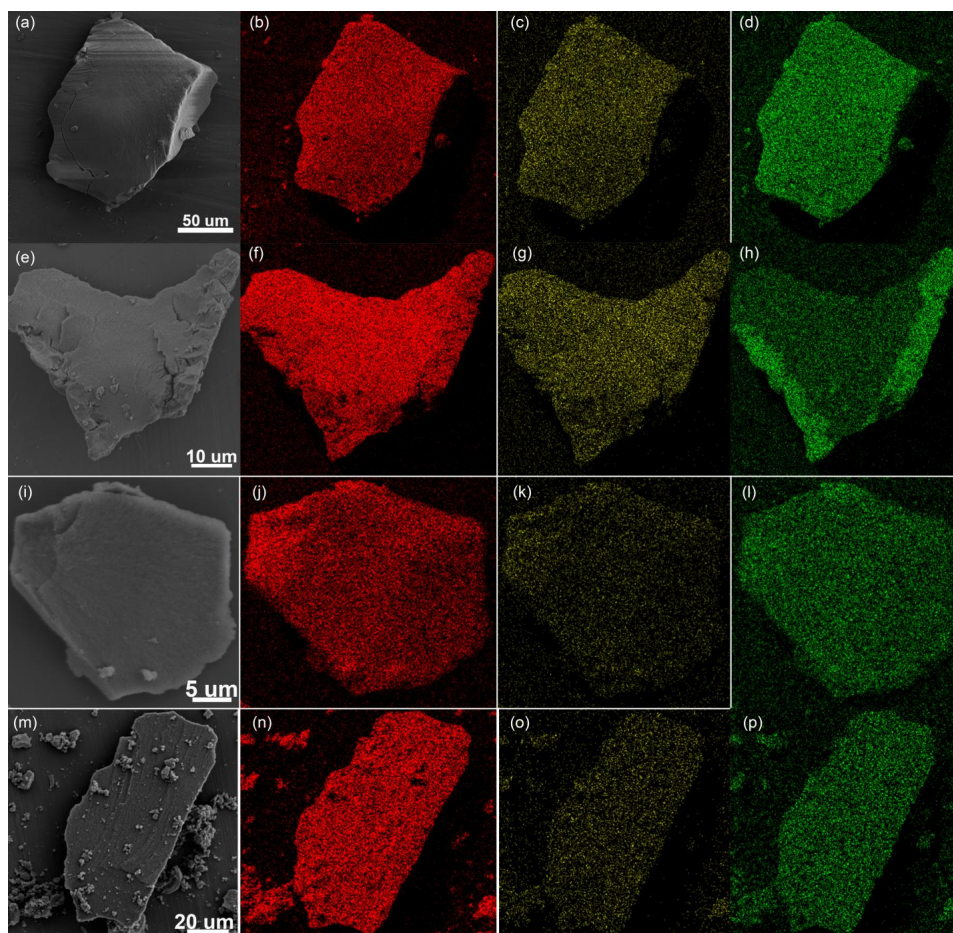


Figure S4.2. SEM and the corresponding EDX analysis of ZIF-8 (a-d), NC-700 (e-h), NC-800 (i-l) and NC-900 (m-p) with EDX elements of C (*red*), N (*yellow*), and Zn (*green*).

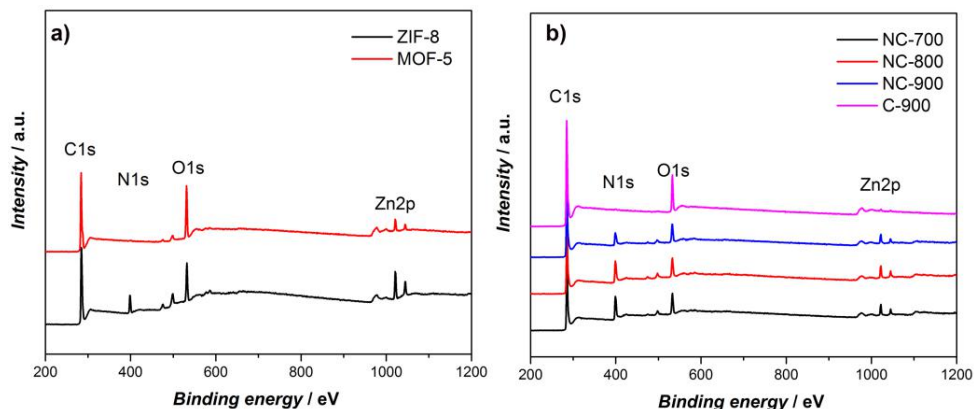


Figure S4.3. XPS survey spectra of (a) ZIF-8 and MOF-5 precursors and (b) final catalyst samples.

There are two small peaks appearing around 472 eV and 495 eV for the NC-T samples (Figure S4.3b) correspond to the Auger lines of zinc: Zn L₂M₄₅M₄₅ at ~472 eV and Zn L₃M₄₅M₄₅ at ~495 eV, so they should be observed in XPS if the sample contains zinc.

Table S4.2. Content of elements in N-doped carbon samples obtained from XPS analysis.

Samples	C	O	Zn	N _{total}	N			
					Pyridinic -N (398.3 eV)	Pyrrolic-N (399.9 eV)	Quaternary -N (401.2 eV)	N- oxide (402. 5 eV)
ZIF-8	72.4	15.3	2.4	9.9	-	-	-	-
MOF-5	76.9	21.7	1.4	-	-	-	-	-
NC-700	70.0	10.8	1.2	18.0	9.0	7.0	1.6	0.4
NC-800	70.9	10.5	1.2	17.4	9.3	5.8	1.7	0.6
NC-900	77.2	10.2	1.0	11.6	6.2	3.4	1.8	0.3
C-900	86.3	13.4	0.3	-	-	-	-	-

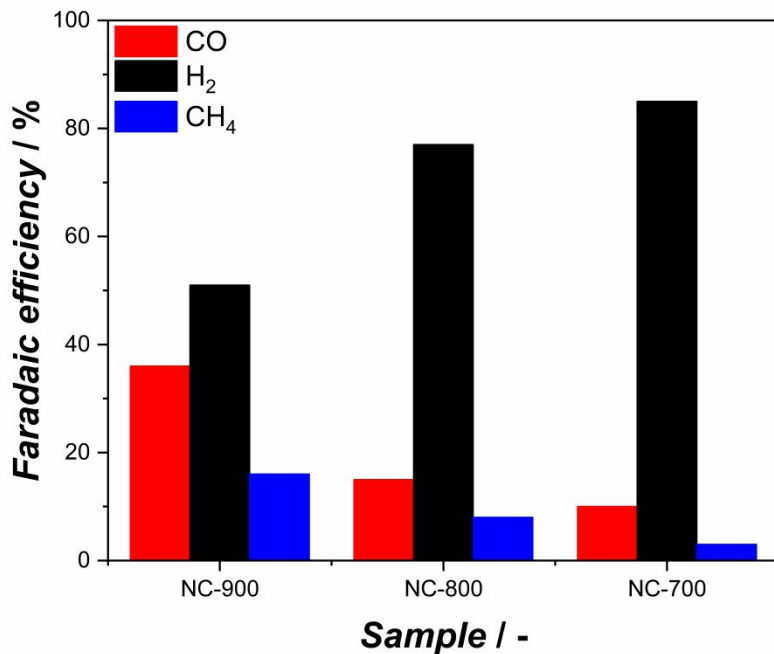


Figure S4.4. Faradaic efficiency distribution of NC-T samples at -1.33 V vs. RHE.

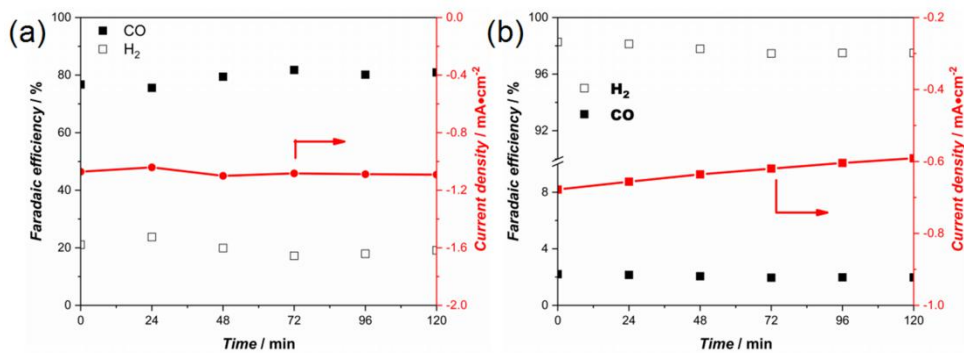


Figure S4.5. Stability test of CO₂ electrochemical reduction of (a) NC-900 and (b) C-900 at -0.93 V vs. RHE.

Table S4.3. Faradaic efficiencies to CO obtained for carbon-based electrocatalysts.

Electrocatalyst	Peak FE	Corresponding Potential (V vs. RHE) of Peak FE	FE around -0.93 V vs. RHE	Electrolyte	Ref [a]
Pyrolyzed ZIF supported on carbon nanotube	~100%	-0.86	~100%	0.1 M NaHCO ₃	1
Pyrolyzed ZIF	50%	-0.56	~26%	0.1 M NaHCO ₃	1
N-doped carbon nanotube	80%	-1.05	~62%	0.1 M KHCO ₃	2
N-doped nanoporous carbon/CNT membrane	81%	-0.80	~65%	0.1 M KHCO ₃	3
N-doped nanocarbon	85%	-0.90	~82%	0.5 M NaHCO ₃	4
PEI enhanced N-doped carbon nanomaterial	82%	-1.12	~60%	0.1 M KHCO ₃	5
N-doped carbon nanotube	80%	-0.80	~75%	0.1 M KHCO ₃	6
Carbon nanofiber	98%	-0.70	-	EMIM-BF ₄	7
g-C ₃ N ₄ /carbon nanotube composite	60%	-0.65	47%	0.1 M KHCO ₃	8
N-doped carbon coated multi-walled carbon nanotube	95%	-0.79	~95%	1 M KCl	9
S,N-codoped nanoporous carbon	11.3%	-0.99	~8%	0.1 M KHCO ₃	10
N-doped carbon	78%	-0.93	78%	0.1 M KHCO ₃	This work

[a] The references listed in the table are as follows:

- Guo, Y., Yang, H., Zhou, X., Liu, K., Zhang, C., Zhou, Z., Wang, C. and Lin, W., 2017. Electrocatalytic reduction of CO₂ to CO with 100% faradaic efficiency by using pyrolyzed zeolitic imidazolate frameworks supported on carbon nanotube networks. *Journal of Materials Chemistry A*, 5(47), pp.24867-24873.
- Sharma, P.P., Wu, J., Yadav, R.M., Liu, M., Wright, C.J., Tiwary, C.S., Yakobson, B.I., Lou, J., Ajayan, P.M. and Zhou, X.D., 2015. Nitrogen-Doped Carbon Nanotube Arrays for High-Efficiency Electrochemical Reduction of CO₂: On the Understanding of Defects, Defect Density, and Selectivity. *Angewandte Chemie International Edition*, 54(46), pp.13701-13705.
- Wang, H., Jia, J., Song, P., Wang, Q., Li, D., Min, S., Qian, C., Wang, L., Li, Y.F., Ma, C. and Wu, T., 2017. Efficient Electrocatalytic Reduction of CO₂ by Nitrogen-Doped Nanoporous Carbon/Carbon Nanotube Membranes: A Step Towards the Electrochemical CO₂ Refinery. *Angewandte Chemie International Edition*, 56(27), pp.7847-7852.

- Xu, J., Kan, Y., Huang, R., Zhang, B., Wang, B., Wu, K.H., Lin, Y., Sun, X., Li, Q., Centi, G. and Su, D., 2016. Revealing the Origin of Activity in Nitrogen-Doped Nanocarbons towards Electrocatalytic Reduction of Carbon Dioxide. *ChemSusChem*, 9(10), pp.1085-1089.
- Zhang, S., Kang, P., Ubnoske, S., Brennaman, M.K., Song, N., House, R.L., Glass, J.T. and Meyer, T.J., 2014. Polyethylenimine-enhanced electrocatalytic reduction of CO₂ to formate at nitrogen-doped carbon nanomaterials. *Journal of the American Chemical Society*, 136(22), pp.7845-7848.
- Wu, J., Yadav, R.M., Liu, M., Sharma, P.P., Tiwary, C.S., Ma, L., Zou, X., Zhou, X.D., Yakobson, B.I., Lou, J. and Ajayan, P.M., 2015. Achieving highly efficient, selective, and stable CO₂ reduction on nitrogen-doped carbon nanotubes. *ACS nano*, 9(5), pp.5364-5371.
- Kumar, B., Asadi, M., Pisasale, D., Sinha-Ray, S., Rosen, B.A., Haasch, R., Abiade, J., Yarin, A.L. and Salehi-Khojin, A., 2013. Renewable and metal-free carbon nanofibre catalysts for carbon dioxide reduction. *Nature communications*, 4, p.2819.
- Lu, X., Tan, T.H., Ng, Y.H. and Amal, R., 2016. Highly selective and stable reduction of CO₂ to CO by a graphitic carbon nitride/carbon nanotube composite electrocatalyst. *Chemistry-A European Journal*, 22(34), pp.11991-11996.
- Jhong, H.R.M., Tornow, C.E., Smid, B., Gewirth, A.A., Lyth, S.M. and Kenis, P.J., 2017. A Nitrogen-Doped Carbon Catalyst for Electrochemical CO₂ Conversion to CO with High Selectivity and Current Density. *ChemSusChem*, 10(6), pp.1094-1099.
- Li, W., Seredych, M., Rodríguez-Castellón, E. and Bandosz, T.J., 2016. Metal-free Nanoporous Carbon as a Catalyst for Electrochemical Reduction of CO₂ to CO and CH₄. *ChemSusChem*, 9(6), pp.606-616.

Structure-Activity Relationships in Metal-organic Framework Derived Mesoporous Nitrogen- doped Carbon Containing Atomically Dispersed Iron Sites for Electrochemical CO₂ Reduction

5

This chapter is based on the following publication:

Xiaohui Sun, [Riming Wang](#), Samy Ould-Chikh, Dmitrii Osadchii, Guanna Li, Antonio Aguilar, Jean-louis Hazemann, Freek Kapteijn, and Jorge Gascon, *Structure-Activity Relationships in Metal Organic Framework Derived Mesoporous Nitrogen-doped Carbon Containing Atomically Dispersed Iron Sites for CO₂ Electrochemical Reduction*, *J. Catal*, 2019, 378, 320-330.

Abstract: Mesoporous nitrogen-doped carbon nanoparticles with atomically dispersed iron sites (named mesoNC-Fe) are synthesized via the pyrolysis of a bi-metallic (Fe/Zn) ZIF-8. Hydrolysis of tetramethyl orthosilicate (TMOS) in the framework prior to pyrolysis plays an essential role in maintaining a high surface area during the formation of the carbon structure, impeding the formation of iron (oxide) nanoparticles. To gain insight on the nature of the resulting atomically dispersed Fe moieties, HERFD-XANES, EXAFS and valence-to-core X-ray emission spectroscopies have been used. The experimental spectra combined with theoretical calculations suggest that iron has a coordination sphere of a porphyrinic environment and OH/H₂O moieties, which is responsible for the high activity in CO₂ electroreduction. DFT calculations further demonstrate that the favourable CO formation in these structures originates from the decreased free energy barriers of *COOH formation and the impeded adsorption of *H.

5.1. INTRODUCTION

The increasing global demand for energy has inevitably led to rising CO₂ emissions due to the combustion of fossil fuels (*e.g.* coal, petroleum and natural gas), which is considered to accelerate global warming and climate deterioration [1]. Two major approaches can be followed to decrease CO₂ content in the atmosphere: to capture and geologically store CO₂, or to convert CO₂ into valuable chemical fuels. The latter approach seems to be more attractive, especially considering the stability of CO₂ storage [2]. Various catalytic approaches for CO₂ reduction, such as thermocatalytic reduction, photocatalytic reduction and electrocatalytic reduction have been proposed [3]. The mild operation conditions and the various valuable products make electrochemical CO₂ reduction a promising candidate for CO₂ utilization.

Numerous metal catalysts are active in CO₂ electroreduction, such as Au, Ag, Cu, *etc.* [4]. The catalytic performances of different metals were found to depend on the binding energy between the metal atoms and CO, a key intermediate in CO₂ reduction. Metals having an intermediate binding energy with CO are found to be active in the synthesis of hydrocarbons and oxygenates that require a transfer of more than two electrons [4c]. When the binding energy between the metal and CO becomes weak, CO is the main product, as CO molecules can easily desorb from the metal surface prior to further reduction to alcohols and/or hydrocarbons [5]. In the latter case, CO can be used as feedstock in an additional heterogeneous catalysis processes (*e.g.* Fischer-Tropsch synthesis) in order to obtain fuels and other valuable chemicals [6].

Nitrogen-doped carbon (hereafter denoted as NC) supported transition metal catalysts exhibit unique chemical and electrical properties, and are supposed to act as alternatives to expensive noble metal catalysts in electrocatalysis [7]. Interestingly, the catalytic activity and product selectivity to a large extent depend on the configuration of the transition metal in the carbon framework. For instance, iron nanoparticles anchored on NC supports were reported to mainly produce H_2 [8]. In contrast, atomically dispersed iron atoms prefer to bond with heteroatoms, such as N, C and/or O in the carbon matrix, and CO is the primary product from these isolated iron sites [7a]. Until now, extensive efforts have been made to understand the local structure of these atomically dispersed metal sites in the NC matrixes, and the coordination environment of metal centers largely depends on the materials and methods of preparation [9].

As a subclass of metal organic frameworks (MOFs), zeolitic imidazolate frameworks (ZIFs) have recently emerged as promising templates to synthesize novel materials, because of their unique textural properties and atomic metal dispersion [10]. For instance, NC with atomically dispersed metal sites in the framework has been successfully prepared by adding little amount of their inorganic metal salts in the synthesis solution of ZIF-8, followed by thermal treatment at high temperature under inert atmosphere [11]. The preferred formation of these atomically dispersed metal sites can be attributed to the generation of free N-coordination sites in the carbon matrix after Zn evaporates, which helps to stabilize the foreign metal atoms (FMA) [11b, 12]. However, thermal treatment at high temperature inevitably causes severe fusion and aggregation of carbon nanoparticles,

which shows low surface area and pore volume, and therefore reduces the number of accessible active sites during catalysis [13].

Herein, we report a facile approach to prepare mesoporous NC with atomically dispersed iron sites (mesoNC-Fe). This approach consists of (i) hydrolysis of tetramethyl orthosilicate (TMOS) in the structure of an iron-containing ZIF-8 material (ZIF-8-Fe), (ii) high-temperature pyrolysis and (iii) SiO₂ template leaching. The SiO₂-assisted approach is vital to (i) inhibit the formation of iron nanoparticles, (ii) preferentially generate atomically dispersed iron sites, and (iii) create high surface area and mesoporosity in the carbon matrix. This catalyst was tested in CO₂ electroreduction and showed high CO Faradaic efficiency (FE_{CO}), partial current density of CO (j_{CO}) and good catalytic stability. Because of the non-crystalline nature of the iron active phase, specific X-ray spectroscopies are applied to unravel the chemical environment of iron: HERFD-XANES, EXAFS and valence-to-core X-ray emission spectroscopies. Comparison of the experimental spectra (both XAS and XES) with the theoretical spectra calculated for various plausible models allows us to approximate to the coordination sphere of iron.

5.2. EXPERIMENTAL

5.2.1. Materials

2-Methylimidazole (MeIm, purity 99%), zinc nitrate hexahydrate (Zn(NO₃)₂·6H₂O, >98%), iron nitrate nonahydrate (Fe(NO₃)₃·9H₂O, >99%), tetramethyl orthosilicate (TMOS ≥99%), and methanol (>99.8%) were purchased from Sigma-Aldrich Chemical Co. All the chemicals were used without further purification.

5.2.2 Catalyst synthesis

For the synthesis of ZIF-8-Fe, a mixture of $\text{Zn}(\text{NO}_3)_2 \cdot 6\text{H}_2\text{O}$ and $\text{Fe}(\text{NO}_3)_3 \cdot 9\text{H}_2\text{O}$ with Zn/Fe molar ratio of 25 ($n_{\text{Zn}}/n_{\text{Fe}}=25$) was dissolved in 200 mL methanol. A mixture of MeIm (6.489 g) in 200 mL methanol was rapidly poured into the above solution with vigorous stirring for 24 h at room temperature. The total molar amount of (Zn + Fe) was fixed to be 10 mmol. Afterwards, the products were collected by filtration, washed thoroughly with methanol, and dried overnight at 80 °C under vacuum.

For the preparation of ZIF-8-Fe@SiO₂, 1 g ZIF-8-Fe was suspended in 5 mL TMOS in an autoclave, and further transferred into a rotation oven and heated up to 333 K and kept at 333 K overnight. After the oven was cooled down to room temperature, the mixture was carefully washed with ethanol by filtration. Then the obtained ZIF-8-Fe@TMOS material was placed in a cotton thimble of 22 mm diameter inside a glass tube of 25 mm diameter. The glass tube was fitted to a round bottom flask containing 500 mL water. A needle to bubble $\sim 10 \text{ ml min}^{-1}$ N₂ flow into water was also fitted. The temperature was raised to 50 °C to create a wet N₂ stream to hydrolyze the TMOS molecules for 24 h, after which the sample was collected and dried in an oven at 60 °C overnight.

NC-Fe@SiO₂ was prepared by pyrolysis of 1 g ZIF-8-Fe@SiO₂ at 900 °C for 4 h under N₂ at a ramp of 2 °C min⁻¹ in a ceramic crucible inside a quartz tubular reactor (approx. $L = 1.0 \text{ m} \times \text{ID} = 4.0 \text{ cm}$) horizontally situated in a ceramic fiber oven (Carbolite, Sheffield). The obtained NC-Fe@SiO₂ was further leached in 1 M NaOH solution for 24 h to remove the SiO₂ template, followed by washing with deionized water until the pH

reached neutral, and dried at 50 °C overnight under vacuum to yield mesoNC-Fe.

As reference, mesoNC was prepared by hydrolysis of TMOS in ZIF-8, followed by pyrolysis and SiO₂ leaching under the same conditions as the preparation of mesoNC-Fe. Further for comparison, microNC and microNC-Fe were prepared by direct pyrolysis of 1 g ZIF-8 and ZIF-8-Fe, respectively, at 900 °C for 4 h.

5.2.3. Characterization

Transmission electron microscopy (TEM) and high-resolution TEM (HR-TEM) were performed by using a Talos F200X microscope (FEI, Hillsboro, OR, USA) at an acceleration voltage of 200 kV. X-ray diffraction (XRD) patterns were recorded on a Bruker D8 Advance X-ray diffractometer equipped with a Co-*K*α radiation ($\lambda = 0.179026$ nm). Raman spectra analysis was performed by using a commercial Renishaw in Via Reflex confocal microscope with a 532 nm laser. The N₂ adsorption-desorption isotherms were measured at 77 K using a Micromeritics Tristar 3020 apparatus. Prior to measurement, samples were degassed under vacuum at 383 K overnight. XPS measurements were performed on a *K*-alpha Thermo Fisher Scientific spectrometer using monochromatic Al-*K* radiation at ambient temperature and chamber pressure of about 10⁻⁸ mbar. All the spectra measured were corrected by setting the reference binding energy of carbon (*1s*) at 284.8 eV. Spectra were analyzed using the Thermo Advantage software package. Background subtraction was done using the setting “SMART” (based on the Shirley background with the additional constraint that the background should not be of a greater intensity than the actual data at any point in the region). The deconvolution of spectra was

performed using a mixed Gauss-Lorentz function where the Lorentzian contribution was set to 20%. Linear sweep voltammetry (LSV) was conducted with a potentiostat (Autolab PGSTAT302N) in the potential range of 0.40 V to -1.40 V vs. Ag/AgCl at a sweep rate of 0.05 V s⁻¹.

5.2.4. Catalyst performance

For the preparation of the electrode, 50 mg catalyst was suspended in a mixture of tetrahydrofuran (4 mL), Nafion solution (0.5 mL), and isopropyl alcohol (4 mL). This mixture was transferred to an ultrasonic bath and kept for 2 h. The suspension was drop-casted onto a carbon cloth electrode with an area (two-sided) of 12.5 cm² (2.5 cm × 2.5 cm). The electrode was then dried overnight at 80 °C under evacuation.

CO₂ electrochemical reduction experiments were performed in the previously described continuous flow reactor [14]. A proton-exchange membrane separated reactor into an anode and cathode compartment. The anode compartment contained a counter electrode (Pt gauze), whereas the cathode compartment contained the working electrode and a reference electrode (Ag/AgCl electrode). Both compartments had a volume of 100 mL and were filled with 85 mL of 0.1 M KHCO₃ prior to the performance tests, leaving a headspace of 15 mL. CO₂ was then fed into the reactor by bubbling through the liquid with a flow rate of 100 mL min⁻¹ until the electrolyte was saturated, after which the CO₂ flow was fixed at 10 mL min⁻¹. An operation potential was applied by a potentiostat (Autolab PGSTAT302N) in the range of -1.0 to -2.0 V versus Ag/AgCl to initiate the controlled potential electrolysis. The cathode compartment was connected to an online gas chromatograph (GC, Global Analyzer Solution Compact GC) to analyze the gas product. All experiments lasted 120 min, and for each

potential applied in the controlled potential performance test, a new electrode was prepared. At the end of the electrocatalytic test, a liquid sample (~1 mL) was collected from the electrolyte solution for ultraperformance liquid chromatography (UPLC) measurements. After each experiment, the electrochemical reactor was cleaned with distilled water and the proton-exchange membrane was immersed into 0.1 M H₂SO₄ for regeneration.

The Faradaic efficiency (*FE*) of the gas product was calculated on the basis of the following equation:

$$FE = \frac{(n \times F \times v \times f)}{(V_m \times j)} \quad (1)$$

where *n* is the number of electrons consumed to produce one product molecule, for the product of CO or H₂, *n* = 2; *v* is the molar fraction of a certain gas product; *f* is the overall gas molar flow rate (mol s⁻¹); *F* is the Faraday constant (*F* = 96 485 C mol⁻¹); *j* is the steady-state cell current at each applied potential (A).

5.3. RESULTS AND DISCUSSION

5.3.1. Characterization of mesoNC-Fe catalyst

The preparation process for mesoNC-Fe is illustrated in Figure 5.1. In the first step, ZIF-8-Fe was synthesized by adding Fe(NO₃)₃ into a solution containing Zn(NO₃)₂, 2-methylimidazole (MeIm) and methanol. Then tetramethyl orthosilicate (TMOS) was hydrolyzed in the structure of ZIF-8-Fe, followed by pyrolysis under N₂ and SiO₂ leaching with a NaOH solution to generate the mesoNC-Fe catalyst (see Experimental Section for the details).

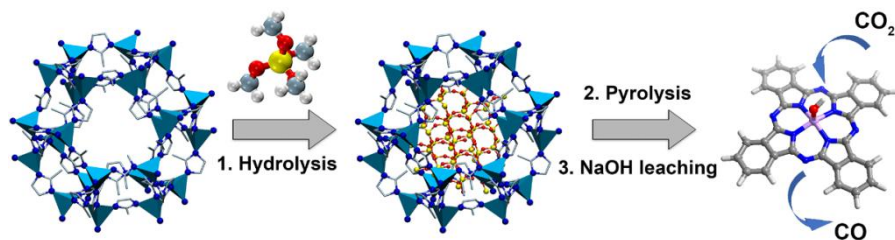


Figure 5.1. Schematic illustration of the synthesis of the mesoNC-Fe catalyst. (1) Impregnation and hydrolysis of TMOS molecules in ZIF-8-Fe. (2) Pyrolysis of ZIF-8-Fe@SiO₂ in N₂ to decompose ZIF-8-Fe and form NC-Fe@SiO₂. (3) NaOH leaching to remove SiO₂ to generate the mesoNC-Fe catalyst.

The structure of the synthesized ZIF-8-Fe was analyzed by XRD, which matches well with that of ZIF-8 (Figure S5.6). Hydrolysis of TMOS led to a homogeneous dispersion of Si in the structure of ZIF-8-Fe (Figure S5.7). After a following pyrolysis and a subsequent NaOH leaching, mesoNC-Fe is obtained. Metal (oxide) nanoparticles can hardly be observed in mesoNC-Fe, suggesting a high dispersion state of metal in the carbon matrix (Figure 5.2a, b). X-ray spectroscopy (EDX) further validates a uniform dispersion of C, N and Fe throughout the carbon matrix (Figure 5.2c-e). In contrast, iron (oxide) nanoparticles are present in microNC-Fe (Figure S5.8a), highlighting the important role of SiO₂ to inhibit the agglomeration of iron atoms to form nanoparticles during high temperature pyrolysis. The absence of iron (oxide) nanoparticles in mesoNC-Fe is further supported by powder XRD analysis, where only two broad reflections at $2\theta = 30^\circ$ and 50.5° are identified, ascribed to the (002) and (100) planes of carbon, respectively (Figure 5.3a) [15]. Raman spectra of all these as-synthesized materials (Figure S5.8d) exhibit two peaks at around 1350 cm^{-1} and 1580 cm^{-1} , which can be correlated to graphitic disordered or

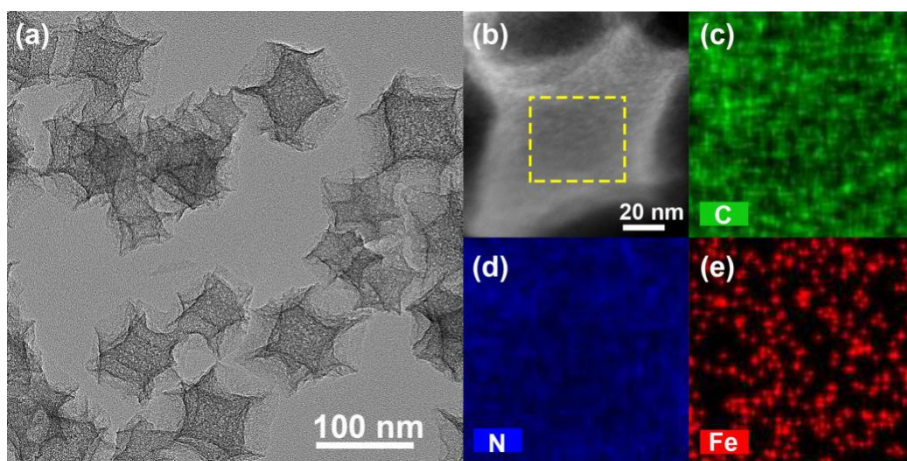


Figure 5.2. Bright field TEM and dark field STEM images of mesoNC-Fe (a, b); EDX mapping of C, N and Fe (c-e).

defective carbon (D-band) and sp^2 -bonded graphitic carbon sheets (G-band), respectively [10b]. These samples exhibit similar intensity ratio between D band and G band (I_D/I_G), suggesting a similar degree of (dis-)order.

The parent ZIF-8 and ZIF-8-Fe samples have a high BET area (S_{BET}) and pore volume (V_{pore}), and display a typical microporous structure with intergranular mesoporosity, as indicated by the steep N_2 uptake at low relative pressures and the hysteresis loop above $P/P_0 \approx 0.8$, respectively (Figure S5.9a) [16]. The mesoNC and mesoNC-Fe samples exhibit a slightly lower S_{BET} and V_{pore} than their parent ZIFs, probably attributed to the collapse of the well-defined microporous structure of ZIF materials and slight agglomeration of nanoparticles during pyrolysis (Figure 5.3b and Figure S5.9b). At the same time, an H_3 hysteresis loop that closes at $P/P_0 \approx 0.4$ can be as well observed, suggesting the presence of ill-defined mesopores in mesoNC and mesoNC-Fe. In contrast, microNC and microNC-Fe show a much lower S_{BET} and V_{pore} (Table S5.1), ascribed to the

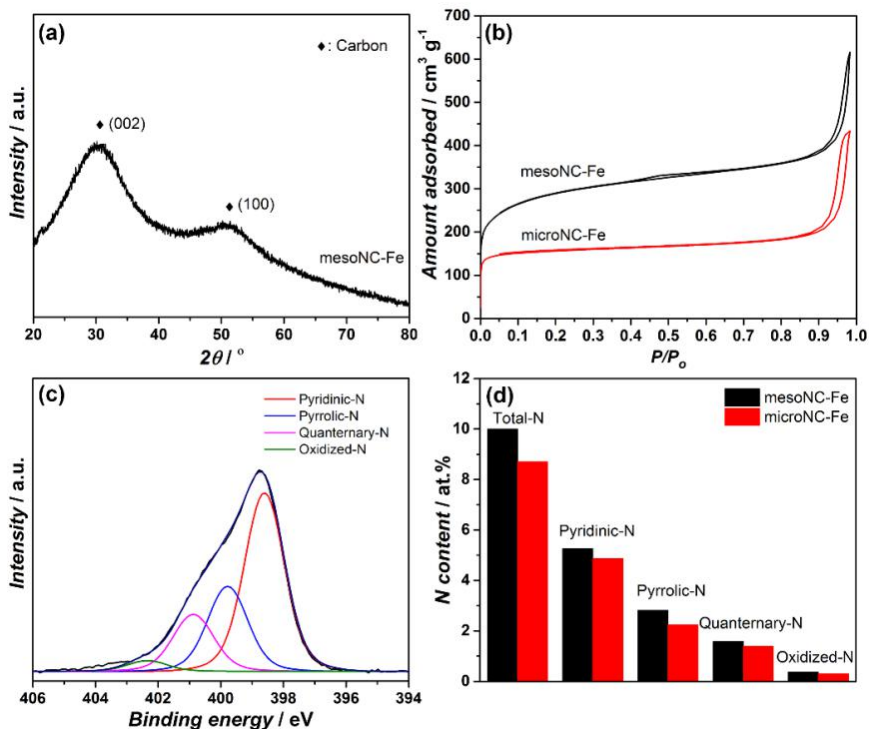


Figure 5.3. X-ray diffraction (XRD) patterns of mesoNC-Fe (a); N_2 -sorption isotherms of mesoNC-Fe and microNC-Fe (b); $N1s$ XPS regions of mesoNC-Fe with deconvolution into the N-speciation (c) and N distribution mesoNC-Fe and microNC-Fe (d).

more severe destruction of the ZIF nanoparticles during pyrolysis in the absence of SiO_2 . The XPS survey data prove the presence of C, N, O, Fe (depending on the sample) and Zn in these samples without detectable Si and Na (Table S5.2). The residual Zn signals in the pyrolyzed samples have been demonstrated to be porphyrin-like Zn (Zn-N_x) species in the nitrogen doped carbon matrix [17]. The $N1s$ spectra were deconvoluted into four types of species with binding energies around 398.5 eV, 399.9 eV, 400.9 eV, and 402.4 eV, attributed to pyridinic-N, pyrrolic-N, quaternary-N and

oxidized-N, respectively (Figure 5.3c and Figure S5.10a-c) [18]. Obviously, pyridinic-N dominates in all these samples.

5.3.2. The coordination environment of iron sites in mesoNC-Fe

X-ray absorption spectroscopy (XAS) was further performed at Fe *K*-edge to explore the structural and valence information of iron in mesoNC-Fe. As shown in Figure 5.4a, simple qualitative comparison of the XANES data with selected references indicates that the spectrum of mesoNC-Fe is almost identical to that of $[\text{Fe}(\text{H}_2\text{O})_6]^{3+}$ in solution [19]. A common statement of the structure of iron doped in nitrogen-doped carbon is Fe-N₄ pyridinic moieties in a square planar configuration [20]. In that case, a sharp pre-edge peak around 7,118 eV is present (*cf.* the XANES spectrum of FePc, Figure 5.4a), due to the $\text{Fe}(1s) \rightarrow \text{Fe}(4p_z)$ transition coupled to a ligand-to-metal charge transfer (shake-down) [21]. However, the latter pre-edge feature is absent from the spectrum of mesoNC-Fe, indicative of at least a broken D_{4h} symmetry or an O_h symmetry. Instead, a weak and broad peak is observed at 7115 eV in the pre-edge region due to $\text{Fe}(1s) \rightarrow \text{Fe}(3d)$ transitions as in the $[\text{Fe}(\text{H}_2\text{O})_6]^{3+}$ spectrum. These transitions gain their intensity *via* quadrupolar coupling or by *3d-4p* mixing in distorted octahedral field. The position of the pre-edge is also consistent with a trivalent iron [22].

The FT-EXAFS spectrum of mesoNC-Fe displays a main peak that is typical of metal-ligand distance ($\approx 1.5 \text{ \AA}$, no phase correction, Figure 5.4b). Comparison with the EXAFS spectra of standards also points towards structural similarities with $[\text{Fe}(\text{H}_2\text{O})_6]^{3+}$ in solution. However, there is an additional weak peak at 2.8 \AA which may arise from a Fe-Fe scattering path

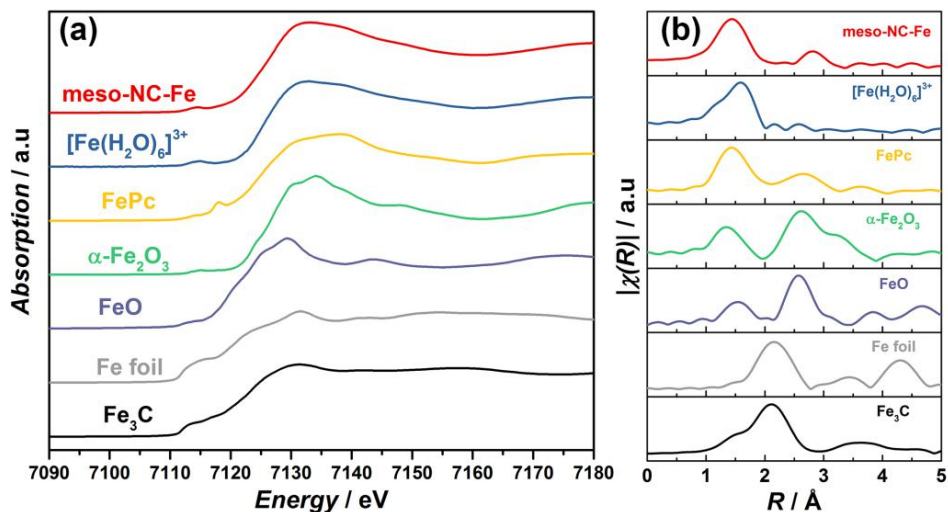


Figure 5.4. (a) Fe K-edge XANES spectra and (b) FT-EXAFS $k^2\chi(k)$ functions for meso-NC-Fe, $[\text{Fe}(\text{H}_2\text{O})_6]^{3+}$ in water (0.01M), FePc, $\alpha\text{-Fe}_2\text{O}_3$, FeO, Fe foil, and Fe_3C . Spectrum of $[\text{Fe}(\text{H}_2\text{O})_6]^{3+}$ in water was retrieved from the F. W. Lytle database: the International X-ray absorption society website at <http://ixs.iit.edu/database/>; and the spectrum of FePc was kindly provided by Zitolo, *et al* [9c].

as suggested by the comparison with the iron oxide references. Consequently, several models based on the combination of various scattering paths (Fe-O, Fe-N, Fe-C, Fe-Si, Fe-Fe, Fe-Zn) were tested to perform the quantitative analysis of the EXAFS data. The best-fit model includes a Fe-N scattering path for the first shell and a Fe-C scattering path for the second shell (Table S4). Note that the Fe-N scattering path also accounts for the presence of oxygen atoms since nitrogen and oxygen are indistinguishable by EXAFS spectroscopy [23]. The final parameters extracted from the EXAFS fit indicate a Fe-O/N bond at $1.96 \pm 0.03 \text{ \AA}$ with a coordination number (CN) of 5.6 ± 1.2 , and a Fe-C bond at $2.98 \pm 0.04 \text{ \AA}$

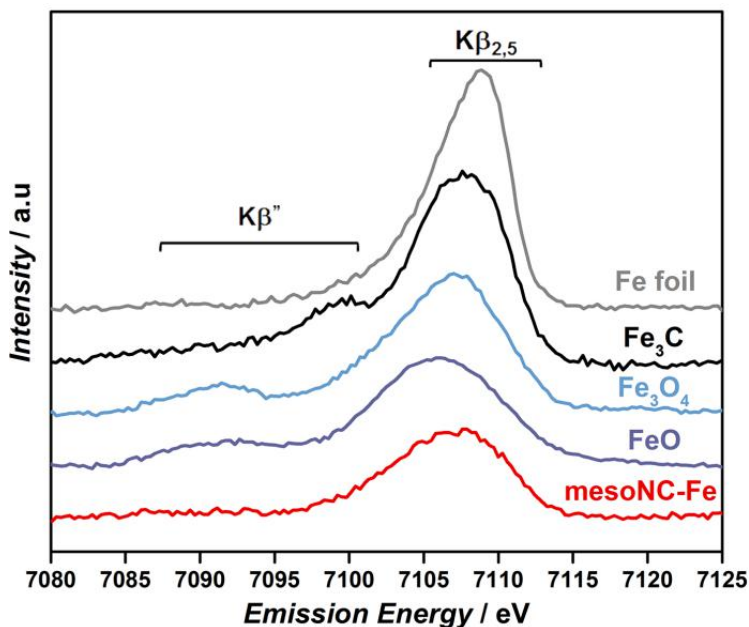


Figure 5.5. VTC- $K\beta$ spectra for a selected set of Fe-based compounds and mesoNC-Fe after removal of the $K\beta_{1,3}$ background.

($CN = 7.2 \pm 2.4$). Importantly, in the fittings of the EXAFS signal for mesoNC-Fe, it was not possible to include Fe-Fe scattering paths with reasonable parameters. Therefore, the negligible contribution of Fe-Fe scattering paths further confirms that nanocrystals are barely present in mesoNC-Fe.

Thus, XANES and EXAFS spectroscopies rule out the reduction of iron to its carbidic or metallic state, exclude the square-planar configuration of a simple Fe-N₄ moiety, and confirm a high dispersion of atomic iron in its trivalent state in mesoNC-Fe. Note that during the investigation of various EXAFS models, it was possible to obtain reasonable agreement using five- or six-coordinated iron (square pyramidal or octahedral geometry). Furthermore, previous characterizations on similar materials proposed various alternative structures: the coordination of the Fe-N₄ moiety is often

expanded by a water molecule, hydroxyl group or molecular dioxygen (for ORR studies) [9c, 24]. Given the on-going debate on the structure of iron active sites immobilized on nitrogen-doped graphene and the limits of the above characterization, valence-to-core X-ray emission spectroscopy and HERFD-XANES spectroscopy coupled to DFT calculations were conducted to further refine our structural model [25].

Non-resonant X-ray emission spectroscopy starts with the ionization of $1s$ electron on iron by incident X-ray photons with energies well-above the K -edge energy threshold. Then, an electron decays to fill the $1s$ core-hole with a simultaneous emission of photons [26]. The VTC-XES spectrum arises from transitions from occupied orbitals a few eV below the Fermi level (the valence band for solids or the highest occupied molecular orbitals for complexes). This valence-to-core region is traditionally divided into two emission lines: the $K\beta''$ and $K\beta_{2,5}$ transitions which are respectively attributed to orbitals mixed metal-ligand ns and np states. One of the first application of VTC-XES for chemistry is related to the sensitivity in energy position of the $K\beta''$ peak which depends of the identity of the ligand (*e.g.* C, N, O, S) [27]. Since the XANES spectrum of mesoNC-Fe is similar to the spectrum of $[\text{Fe}(\text{H}_2\text{O})_6]^{3+}$ cation, we had suspicions that nitrogen atoms are not even coordinated to iron despite the XPS spectroscopic evidence of a significant amount of pyridinic nitrogen. Thus, the initial motivation for the XES study was to overcome the limitation of EXAFS concerning the discrimination between oxygen and nitrogen atoms. The VTC- $K\beta$ spectrum of mesoNC-Fe is shown in Figure 5.5 with several standards for comparison (Fe foil, Fe_3C , Fe_3O_4 , FeO). Unexpectedly, the VTC- $K\beta$ spectrum of mesoNC-Fe presents only a broad peak centered at ≈ 7107 eV in the $K\beta_{2,5}$

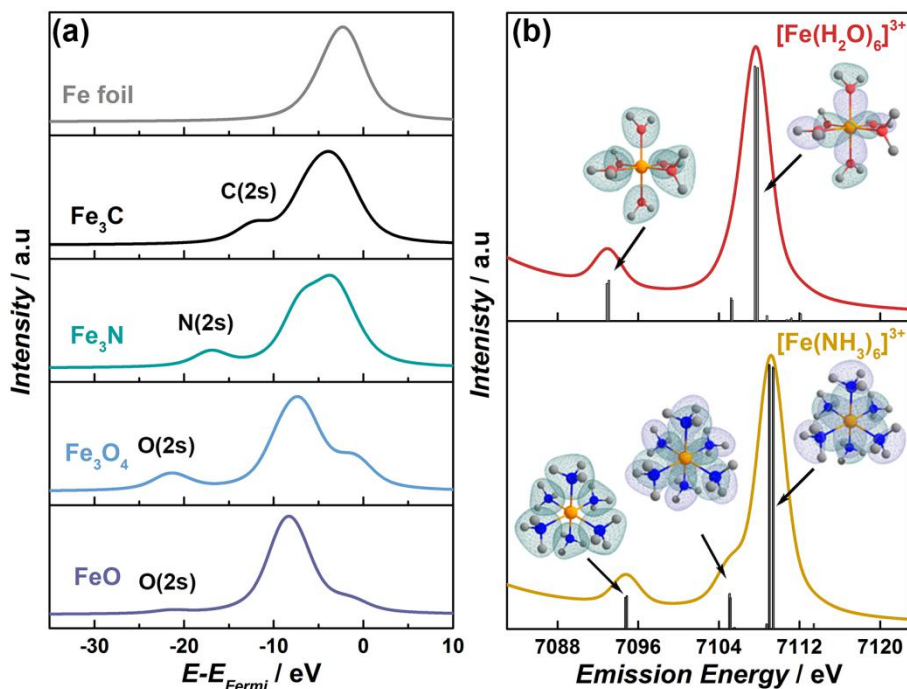


Figure 5.6. Calculated VTC- $K\beta$ spectra for a α -Fe, Fe_3C , Fe_3N , Fe_3O_4 , FeO, $[\text{Fe}(\text{H}_2\text{O})_6]^{3+}$ and $[\text{Fe}(\text{NH}_3)_6]^{3+}$ compounds. Left panel (a): spectra for periodic structures calculated with the FDMNES code with the energy scale referenced against the Fermi level. The ligands states sensitivity of $K\beta''$ is outlined by the ligand orbitals label. Right panel (b): spectra for cluster models calculated with ORCA. A constant shift of +182.5 eV have been applied. Representative alpha molecular orbitals for each peaks are superimposed.

region with no clear peak in the $K\beta''$ region (within the accuracy limits of the background removal). On the other hand, the iron oxides (FeO and Fe_3O_4) and iron carbide (Fe_3C) spectra clearly highlight a $K\beta''$ contribution respectively centered at 7091 and 7099 eV. For the iron foil (α -Fe, *bcc* structure), there is no observable $K\beta''$ contribution, confirming that $K\beta''$ mainly comes from the ligand s states.

The corresponding theoretical calculations performed with the FDMNES code are provided in Figure 5.6a with the extra addition of the Fe_3N

theoretical spectrum that could not be measured experimentally (see the details in the supplementary information). The experimental data are well described by the theory that properly predicts the position of the $K\beta''$ line in respect to the $K\beta_{2,5}$ line position. By selecting the projected density of states theoretical VTC- $K\beta$ spectra of $[\text{Fe}(\text{H}_2\text{O})_6]^{3+}$ and $[\text{Fe}(\text{NH}_3)_6]^{3+}$ are also presented on Figure 5.6b with the visualization of representative alpha molecular orbitals from which the peaks originate. Those cluster calculations were performed with the ORCA program package following the recent and extensive work of DeBeer, Bauer, Glatzel and coworkers [28]. The theoretical spectra for both cations clearly show the presence of both $K\beta_{2,5}$ and $K\beta''$ lines with a significant intensity. Thus, a simple FeL_6 octahedral model with metal-ligand distance of 1.96 Å (calculated from EXAFS data) cannot reproduce the experimental spectrum of mesoNC-Fe, although the experimental XANES spectrum of $[\text{Fe}(\text{H}_2\text{O})_6]^{3+}$ was very similar. Apart from the metal foil which does not show any $K\beta''$ peak, there are no references spectra which are anywhere close to the mesoNC-Fe spectrum.

At this point, further investigations require the understanding of the parameters that determine intensity of transitions in the VTC- $K\beta$ spectrum. With the simplest FeL_6 model, the most intense transitions derived from $\text{H}_2\text{O}/\text{NH}_3$ molecular orbitals belonging to the t_{1u} irreducible representation can be extracted (Figure 5.6b). In octahedral symmetry, the metal np orbitals also transform as t_{1u} and enable the overlap with any ligand-based orbitals with the same symmetry. This is crucial for the prediction of intensities because the latter metal p -contribution in the molecular orbital enables the electric dipole allowed character of the transitions ($\Delta l = \pm 1$) [29]. In general,

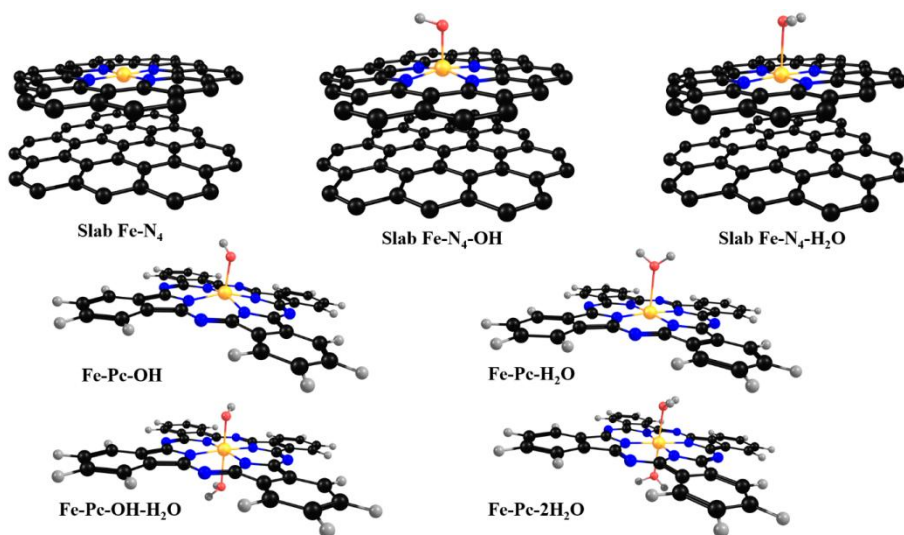


Figure 5.7. DFT-optimized geometry for potential local environments of the iron active site in their most stable multiplicity state.

only ligand orbitals interacting *via* σ -bonding will overlap significantly with the metal p orbitals. A possible explanation of the low $K\beta''$ intensity may involve a conjugated system around the iron center. In that case, VTC- $K\beta$ is expected to highlight mostly the σ -framework. With such coordination, the ligands atomic orbitals contribute significantly through sp^2 hybridization to the π -system decreasing inevitably their participation in the σ -framework. From this idea, we have investigated several conjugated models that we thought to potentially match the experimental XANES together with the VTC- $K\beta$ spectra. At the same time, how the intensity of $K\beta'$ can be impacted by a Fe distorted environment in small iron (III) oxyhydroxide clusters as stated by Genovese *et al.* was not investigated in this study [30], since this structure was reported to produce formic and acetic acid in the liquid phase and none of those products were detected over the whole applied cell potential range from our mesoNC-Fe catalyst.

All geometry optimizations are detailed in the supplementary information while the optimized models can be visualized in Figure 5.7. The first type of model considers periodic slabs based on the nitrogen doped graphene structure with four pyridinic nitrogen coordinating the iron cation (Slab-FeN₄). The top coordination of iron was completed either by a water molecule (Slab-FeN₄-H₂O) or by a hydroxyl group (Slab-FeN₄-OH). The second type of model is based on the FePc complex, with a coordination completed by one hydroxyl (FePc-OH), one water molecule (FePc-H₂O), one hydroxyl plus one water molecule (FePc-OH-H₂O), and two water molecules (FePc-2H₂O). Those structures were inspired by the work of Zitolo, *et al.* who have shown that a porphyrinic geometry could match with the best accuracy the XANES data [9c].

The accuracy of the FDMNES code related to the simulation of Fe *K*-edge absorption spectra was evaluated with reference compounds (Figure S5.8): a reasonable agreement between theory and experiment is obtained with our calculation parameters. The main discrepancies are observed in the pre-edge region especially for Mott insulators such as FeO, α -Fe₂O₃, and Fe₃O₄ for which the energy separation between Fe(3*d*) and Fe(4*p*) metal orbitals is poorly predicted [31]. Then, the XANES spectra of previously optimized models are compared against the HERFD-XANES spectrum of mesoNC-Fe measured at the iron *K* $\beta_{1,3}$ energy (Figure S5.9). The theoretical calculations are used here as a tool to exclude the models producing spectra obviously too far from the experimental results. Ultimately, the Fe-Pc-OH, Fe-Pc-2H₂O and FePc-OH-H₂O structures provide the greatest agreement as shown in Figure 5.8a. The concurrence with the Fe-Pc-OH spectrum is lesser in the main-edge region which suggests that the octahedral symmetry

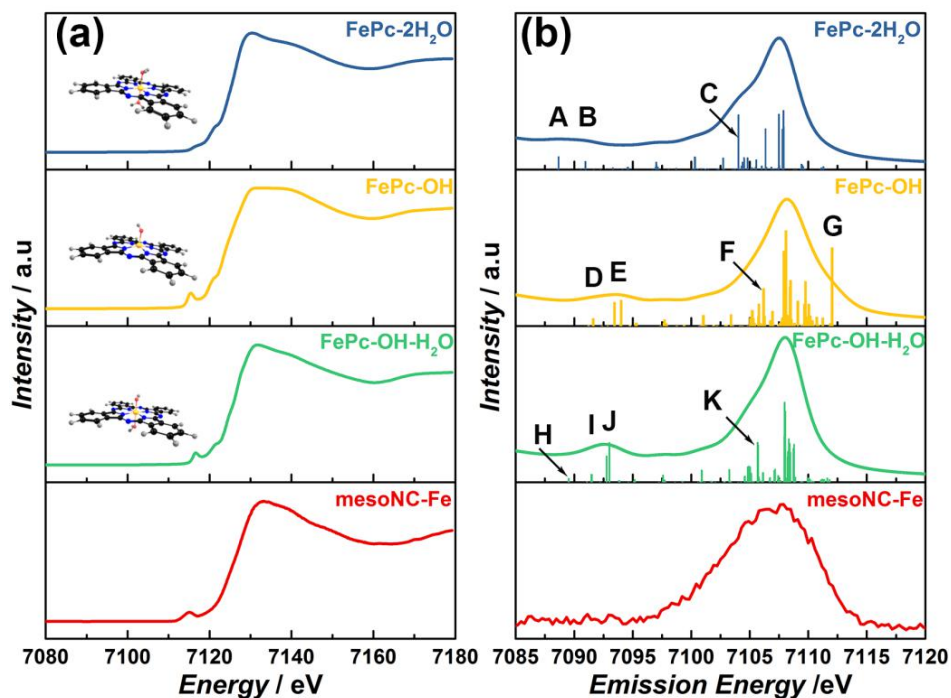


Figure 5.8. Comparison of experiments and theory for HERFD-XANES and VTC- $K\beta$ spectroscopies using FePc-2H₂O, FePc-OH, FePc-OH-H₂O. Left panel (a): XANES spectrum of mesoNC-Fe (2) compared against FDMNES calculations, Right panel (b): VTC- $K\beta$ spectrum of mesoNC-Fe (2) compared against ORCA calculations. A constant shift of +182.5 eV have been applied.

is better suited than a square pyramidal symmetry. Furthermore, the peak in the pre-edge region of the Fe-Pc-2H₂O spectrum has a much lower intensity compared to the experimental data. This is because the octahedral symmetry of Fe-Pc-2H₂O presents only a small axial distortion restricting the $3d-4p$ mixing ($d(\text{Fe-N}) = 1.96 \text{ \AA}$ vs. $d(\text{Fe-O}) = 2.09 \text{ \AA}$). According to XANES spectroscopy, FePc-OH-H₂O would be the best structural model. The VTC-XES experimental spectrum and the ORCA calculations are further considered, as shown in Figure 5.8b. A general observation is that the three structural models lead to VTC- $K\beta$ spectra with a broad $K\beta_{2,5}$ line and a weak

intensity for the crossover peak ($K\beta''$), or almost non-existent for the Fe-Pc-2H₂O model. The calculated spectra are now in much better agreement with the experimental data, especially for the $K\beta_{2,5}$ region. However, the intensity of the $K\beta''$ and the width of the $K\beta_{2,5}$ lines are respectively stronger and sharper than the experiments. This could be due to a difference of energy resolution between calculations and experiment. Besides, the current level of theory does not allow to include the effect of multiplet interactions which may further broaden the predicted $K\beta_{2,5}$ and $K\beta''$ lines.

Figure 5.9 presents the assignment of the transitions labeled by letter in the calculated valence-to-core spectra. The $K\beta_{2,5}$ line arises from electronic transitions from ligands $2p$ into Fe $1s$ orbitals. The most intense peaks are due to transitions from a mixed of Fe-O/N/C $2p$ based molecular orbitals from the phthalocyanine σ -framework. All three models present a shoulder on the lower energy side which is mainly related to O_{H2O} and O_{OH} $2p$ orbitals (C, F, K). The FePc-OH has an additional shoulder on the higher energy side due to a different contribution of O_{OH} $2p$ orbitals (G). The $K\beta''$ feature arises from electronic transitions from O $2s$ and N $2s$ into Fe $1s$ orbitals. The N $2s$ contributions appear at similar energies in all spectra (labeled as B, D, I in Figure 5.8 and 5.9). For FePc-2H₂O, the transitions from O_{H2O} $2s$ (A) orbital are at a lower energy than N₄ $2s$ (B) orbital. Inversely with the FePc-OH model, O_{OH} $2s$ (E) is located at a higher energy than N₄ $2s$ (D). The intermediate model FePc-OH-H₂O has all three transitions appearing consistently in the order O_{H2O} $2s$ (H), N₄ $2s$ (I), and O_{OH} $2s$ (J) from lower to higher energy. Considering the intensities, only the transitions related to hydroxyl groups lead to the appearance of a significant peak. The $K\beta''$ component of the water ligand, has lower intensities due to

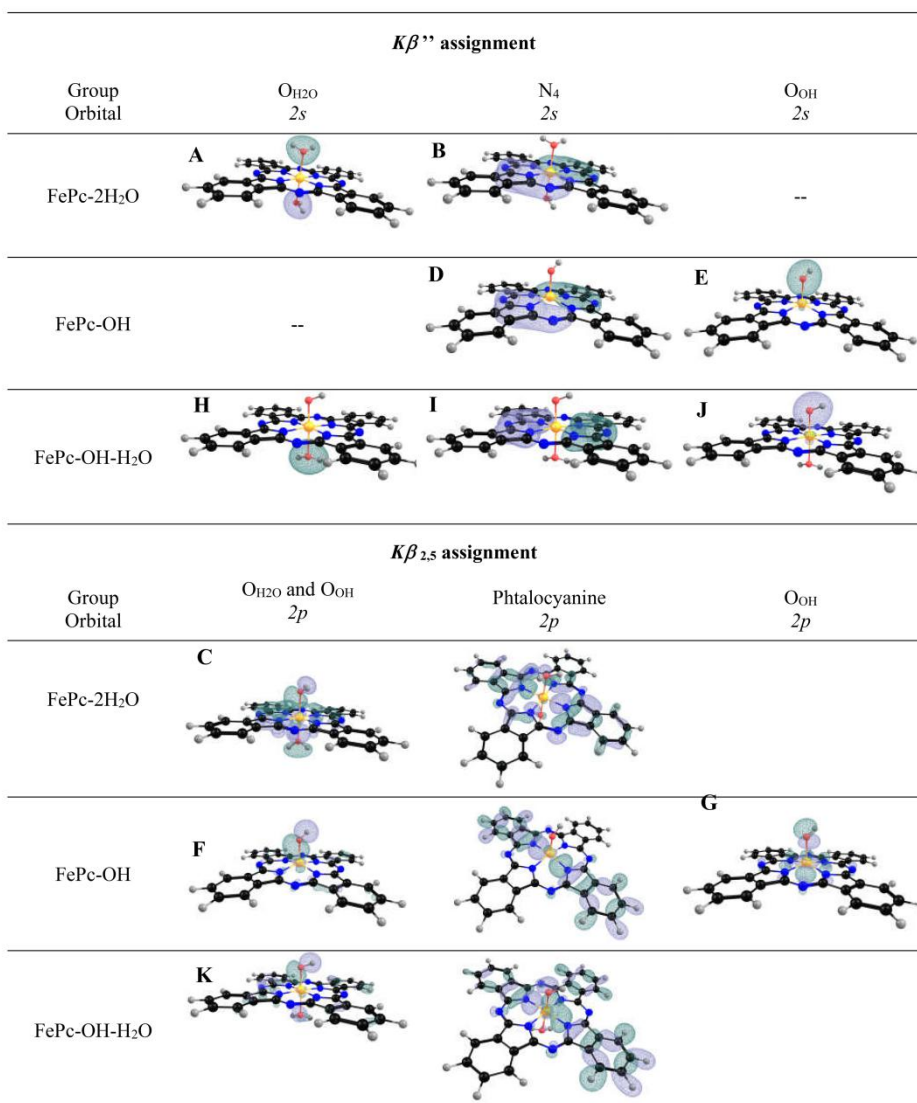


Figure 5.9. Representative donor orbitals corresponding to each of the assign regions of the $K\beta''$ and $K\beta_{2,5}$ peaks.

the lower overlap of the donor with the acceptor orbitals, which is actually related to the distance between donor and acceptor site ($d(\text{Fe}-\text{O}_{\text{OH}}) = 1.8\text{-}1.9 \text{ \AA}$ vs. $d(\text{Fe}-\text{O}_{\text{H}_2\text{O}}) = 2.1\text{-}2.2 \text{ \AA}$). The same argument explains the higher $K\beta''$ intensity for FePc-OH-H₂O compared to FePc-OH due to the shorter Fe-O_{OH}

distance ($\approx 0.1 \text{ \AA}$). Regarding the transitions involving nitrogen $2s$ orbitals, the weak intensity is rather understood by the delocalization of the donor orbital on the phthalocyanine ligand as shown in Figure 5.9 (B, D, I). Thus, a porphyrinic environment completed by the coordination of water and/or hydroxyl group best describes the local environment of these atomically dispersed iron sites. Given the method of preparation, the chemical environment of iron must probably have some variations in terms of number of water/hydroxyl coordinated and iron-oxygen bond length. For this reason, it did not seem pertinent to choose a structural model among FePc-OH, FePc-2H₂O, and FePc-OH-H₂O, but many alternative models could be at least excluded during this study.

5.3.3. Electrochemical reduction of CO₂ over the mesoNC-Fe catalyst

After exploring the chemical environment of iron in mesoNC-Fe by using both experimental spectra and DFT calculations, we further investigate the catalytic performance of mesoNC-Fe in CO₂ electrochemical reduction reaction in this section. The performance of mesoNC-Fe in the electrocatalytic reduction of carbon dioxide was first evaluated by linear sweep voltammetry (LSV) (Figure S5.10a). The current density in the N₂-saturated KHCO₃ solution ($j(N_2)$) is attributed to hydrogen evolution reaction (HER). Apparently, after introducing CO₂ in the KHCO₃ (0.1 M) solution, the current density of $j(CO_2)$ for mesoNC-Fe becomes higher than that of $j(N_2)$. We first investigate the pH effect on the current density when the LSV is performed (Figure S5.11). The value of $j(N_2)$ increases as the pH value of the solution decreases, but is still much lower than the value in the CO₂ saturated KHCO₃ solution. This indicates that in the CO₂-saturated

solutions both the electrochemical reduction of CO₂ and HER contribute to $j(\text{CO}_2)$.

In order to elucidate the role of the nitrogen-doped carbon structure in mesoNC-Fe in CO₂ electroreduction reaction, two reference samples (microNC and mesoNC) were first tested (see Experimental Section for the details). No liquid-phase product was detected after each experiment over the whole applied cell potential range, and CO and H₂ are the only detectable reduction products. The FE_{CO} of microNC displays a volcano-like curve over the whole applied cell potential range with the maximum FE_{CO} of ~33% at V_{RHE} of -0.93 V (Figure 5.10a). Surprisingly, the mesoNC sample with a higher surface area further promotes CO production with the maximum FE_{CO} of ~72% at V_{RHE} of -0.93 V (Figure 5.10a). The electroreduction activity of CO₂ to CO for nitrogen-doped carbon materials has been attributed to the presence of pyridinic- and quaternary-N species, which facilitate the transfer of a proton-electron pair to CO₂ [32]. Moreover, the single Zn sites in the nitrogen-doped carbon matrix (Zn-N_x) was also proved to promote the CO₂ electroreduction performance by facilitating the formation of *COOH [33]. Hence, it cannot be discarded that the remaining Zn also contributes in the electroreduction of CO₂ to CO. The catalytic performance of mesoNC-Fe in electroreduction CO₂ reaction was further studied. As shown in Figure 5.10a, after incorporating these atomically dispersed iron sites in the mesoNC matrix, the maximum FE_{CO} and the corresponding j_{CO} further increase to 85% and -3.7 mA cm⁻², respectively. As mesoNC and mesoNC-Fe show a similar electrochemically active surface area (ECSA) (Figure S5.12d), we demonstrate that these atomically dispersed iron sites in mesoNC-Fe exhibit a higher activity than nitrogen

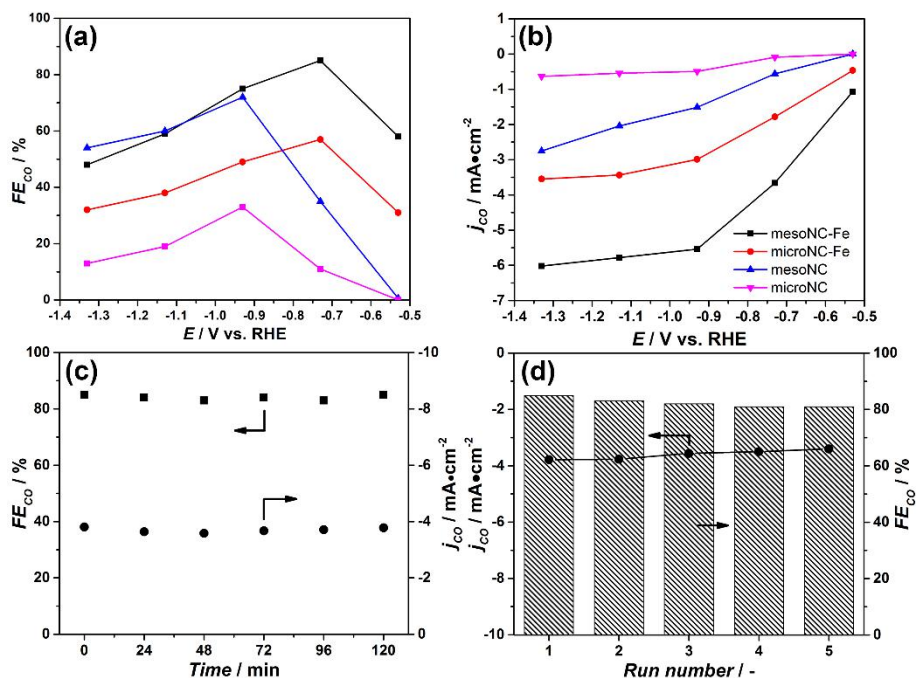


Figure 5.10. FE_{CO} (a) and j_{CO} (b) of mesoNC-Fe (black) microNC-Fe (red) mesoNC (blue) and microNC (pink) in CO₂ reduction to CO; stability (c) and reusability (d) test of mesoNC-Fe in electrocatalytic reduction of CO₂ at -0.73 V vs RHE. Each recycling test lasts 120 min.

dopants. At the same time, the over-potential at the maximum FE_{CO} of mesoNC-Fe also shifts to V_{RHE} of -0.73 V (Figure 5.10a). Previous studies have shown that CO₂ electroreduction to CO in general proceeds through the adsorbed intermediates: *COOH and *CO, where * represents the active site [34]. Hence, the free energy changes (ΔG) during the formation of *COOH and *CO on mesoNC-Fe and mesoNC catalysts are compared by using theoretical calculations with the model built in Section 3.2 (Figure S5.13). Obviously, the atomically dispersed Fe center with hydroxyl ligand (i) decreases the free energy barriers of *COOH formation (Figure S5.13a); and (ii) destabilizes the adsorption of *H, which to some extent enhances

the adsorption of *COOH and *CO (Figure S5.13b), thereby promoting CO₂ electroreduction to CO at lower overpotentials. Moreover, a slope of ~123 mV dec⁻¹ was observed at the low-overpotential region of Tafel curve, indicating that the initial electron transfer to CO₂ to form *COOH intermediates is the rate-determining step (Figure S5.14). We should also acknowledge that the electron transfer, decoupled from proton transfer, can also be operative in this regime.

To highlight the advantages of the SiO₂-protective strategy we utilized, a microNC-Fe sample prepared by direct pyrolysis of ZIF-8-Fe was also tested. As shown in Figure 5.10a and b, microNC-Fe exhibits a lower FE_{CO} and j_{CO} than that of mesoNC-Fe over the whole potential range, with the maximum FE_{CO} of ~57% and the corresponding j_{CO} of -1.9 mA cm⁻² at V_{RHE} of -0.73 V. Interestingly, mesoNC-Fe and microNC-Fe show a good relationship between the double layer capacitance (C_{dl}) (5.88 mF cm⁻² versus 3.05 mF cm⁻²) and j_{CO} (3.7 mA cm⁻² versus 1.9 mA cm⁻²), indicating that the accessible active sites exhibit a similar activity in these two samples (Figure S5.12d). Thus, compared to microNC-Fe, the higher performance of mesoNC-Fe can be explained from the following aspects: (i) the larger surface area enables more atomically dispersed active sites accessible for CO₂ electroreduction; and (ii) the absence of iron nanoparticles to a large extent inhibits the HER reaction. Hence, the synergetic effect of the atomically dispersed active sites in the carbon matrix makes mesoNC-Fe a more efficient catalyst for CO production compared to microNC-Fe. The maximum FE_{CO} and the corresponding j_{CO} of mesoNC-Fe is comparable to those of nitrogen-doped carbon supported iron catalysts reported recently from other groups (Table S5). Finally, the stability and reusability of the mesoNC-Fe catalyst was also investigated, as presented in Figure 5.10c and

d. At the optimal V_{RHE} of -0.73 V, the mesoNC-Fe catalyst exhibits a stable j_{CO} and FE_{CO} during CO_2 electroreduction reaction and can be used at least four times without obvious deactivation, implying the high stability of Fe-N coordination environment in the carbon matrix (Figure S5.16).

5.4. CONCLUSIONS

In this work, a SiO_2 -protective approach was reported to synthesize mesoporous NC with atomically dispersed iron sites (mesoNC-Fe) from a Fe-containing ZIF-8 template. This approach consists of hydrolysis of TMOS in ZIF-8-Fe, high-temperature pyrolysis and SiO_2 removal. We demonstrate that the presence of SiO_2 during pyrolysis is crucial to retain a high surface area in the mesoporous carbon matrix, and to hinder the formation of iron (oxide) nanoparticles. A series of X-ray spectroscopies, including HERFD-XANES, EXAFS and valence-to-core X-ray emission spectroscopies together with theoretical calculations allow us to elucidate the chemical environment of the non-crystalline iron species in mesoNC-Fe: a porphyrinic environment around iron, which is completed by H_2O/OH moieties. The mesoNC-Fe catalyst exhibits much higher FE_{CO} and j_{CO} compared to its counterparts mesoNC and microNC-Fe. This can be explained from two aspects: (i) the iron center coordinating in the porphyrinic environment with OH/H_2O moieties in mesoNC-Fe decreases the free energy barriers of $*COOH$ formation and destabilizes the adsorption of $*H$; (ii) more active sites can be accessible during catalysis because of the higher surface area of the carbon structure in mesoNC-Fe than that in microNC-Fe. Our results also demonstrate that HERFD-XANES and VTC- $K\beta$ spectroscopies combined with theoretical calculation constitute a

powerful tool to explore the coordination environment in atomically dispersed catalysts.

5.5. REFERENCES

1. Costentin, C.; Drouet, S.; Robert, M.; Savéant, J.-M., A Local Proton Source Enhances CO₂ Electroreduction to CO by a Molecular Fe Catalyst. *Science* **2012**, *338* (6103), 90-94.
2. (a) Banerjee, R.; Phan, A.; Wang, B.; Knobler, C.; Furukawa, H.; O'Keeffe, M.; Yaghi, O. M., High-Throughput Synthesis of Zeolitic Imidazolate Frameworks and Application to CO₂ Capture. *Science* **2008**, *319* (5865), 939-943; (b) Schaub, T.; Paciello, R. A., A Process for the Synthesis of Formic Acid by CO₂ Hydrogenation: Thermodynamic Aspects and the Role of CO. *Angewandte Chemie International Edition* **2011**, *50* (32), 7278-7282.
3. (a) Kattel, S.; Ramírez, P. J.; Chen, J. G.; Rodriguez, J. A.; Liu, P., Active sites for CO₂ hydrogenation to methanol on Cu/ZnO catalysts. *Science* **2017**, *355* (6331), 1296-1299; (b) Ulagappan, N.; Frei, H., Mechanistic Study of CO₂ Photoreduction in Ti Silicalite Molecular Sieve by FT-IR Spectroscopy. *The Journal of Physical Chemistry A* **2000**, *104* (33), 7834-7839; (c) Wang, R.; Sun, X.; Ould-Chikh, S.; Osadchii, D.; Bai, F.; Kapteijn, F.; Gascon, J., Metal-Organic-Framework-Mediated Nitrogen-Doped Carbon for CO₂ Electrochemical Reduction. *ACS Applied Materials & Interfaces* **2018**.
4. (a) Zhu, W.; Michalsky, R.; Metin, Ö.; Lv, H.; Guo, S.; Wright, C. J.; Sun, X.; Peterson, A. A.; Sun, S., Monodisperse Au Nanoparticles for Selective Electrocatalytic Reduction of CO₂ to CO. *Journal of the American Chemical Society* **2013**, *135* (45), 16833-16836; (b) Ma, M.; Trzeźniewski, B. J.; Xie, J.; Smith, W. A., Selective and Efficient Reduction of Carbon Dioxide to Carbon Monoxide on Oxide-Derived Nanostructured Silver Electrocatalysts. *Angewandte Chemie International Edition* **2016**, *55* (33), 9748-9752; (c) Ma, M.; Djanashvili, K.; Smith, W. A., Controllable Hydrocarbon Formation from the Electrochemical Reduction of CO₂ over Cu Nanowire Arrays. *Angewandte Chemie* **2016**, *128* (23), 6792-6796.
5. Back, S.; Yeom, M. S.; Jung, Y., Active Sites of Au and Ag Nanoparticle Catalysts for CO₂ Electroreduction to CO. *ACS Catalysis* **2015**, *5* (9), 5089-5096.
6. (a) Sun, X.; Suarez, A. I. O.; Meijerink, M.; van Deelen, T.; Ould-Chikh, S.; Zečević, J.; de Jong, K. P.; Kapteijn, F.; Gascon, J., Manufacture of highly loaded silica-

- supported cobalt Fischer–Tropsch catalysts from a metal organic framework. *Nature Communications* **2017**, *8* (1), 1680; (b) Sun, X.; Sartipi, S.; Kapteijn, F.; Gascon, J., Effect of pretreatment atmosphere on the activity and selectivity of Co/mesoHZSM-5 for Fischer-Tropsch synthesis. *New Journal of Chemistry* **2016**, *40* (5), 4167-4177.
7. (a) Pan, F.; Zhang, H.; Liu, K.; Cullen, D.; More, K.; Wang, M.; Feng, Z.; Wang, G.; Wu, G.; Li, Y., Unveiling Active Sites of CO₂ Reduction on Nitrogen-Coordinated and Atomically Dispersed Iron and Cobalt Catalysts. *ACS Catalysis* **2018**, *8* (4), 3116-3122; (b) Rodenas, T.; Beeg, S.; Spanos, I.; Neugebauer, S.; Girgsdies, F.; Algara-Siller, G.; Schleker, P. P. M.; Jakes, P.; Pfänder, N.; Willinger, M.; Greiner, M.; Prieto, G.; Schlögl, R.; Heumann, S., 2D Metal Organic Framework-Graphitic Carbon Nanocomposites as Precursors for High-Performance O₂-Evolution Electrocatalysts. *Advanced Energy Materials* **2018**, *8* (35), 1802404.
8. Huan, T. N.; Ranjbar, N.; Rousse, G.; Sougrati, M.; Zitolo, A.; Mougel, V.; Jaouen, F.; Fontecave, M., Electrochemical Reduction of CO₂ Catalyzed by Fe-N-C Materials: A Structure–Selectivity Study. *ACS Catalysis* **2017**, *7* (3), 1520-1525.
9. (a) Liu, W.; Zhang, L.; Liu, X.; Liu, X.; Yang, X.; Miao, S.; Wang, W.; Wang, A.; Zhang, T., Discriminating Catalytically Active Fe_Nx Species of Atomically Dispersed Fe–N–C Catalyst for Selective Oxidation of the C–H Bond. *Journal of the American Chemical Society* **2017**, *139* (31), 10790-10798; (b) Fei, H.; Dong, J.; Feng, Y.; Allen, C. S.; Wan, C.; Voloskiy, B.; Li, M.; Zhao, Z.; Wang, Y.; Sun, H.; An, P.; Chen, W.; Guo, Z.; Lee, C.; Chen, D.; Shakir, I.; Liu, M.; Hu, T.; Li, Y.; Kirkland, A. I.; Duan, X.; Huang, Y., General synthesis and definitive structural identification of MN₄C₄ single-atom catalysts with tunable electrocatalytic activities. *Nature Catalysis* **2018**, *1* (1), 63-72; (c) Zitolo, A.; Goellner, V.; Armel, V.; Sougrati, M.-T.; Mineva, T.; Stievano, L.; Fonda, E.; Jaouen, F., Identification of catalytic sites for oxygen reduction in iron- and nitrogen-doped graphene materials. *Nature Materials* **2015**, *14*, 937.
10. (a) Sun, X.; Olivos-Suarez, A. I.; Oar-Arteta, L.; Rozhko, E.; Osadchii, D.; Bavykina, A.; Kapteijn, F.; Gascon, J., Metal–Organic Framework Mediated Cobalt/Nitrogen-Doped Carbon Hybrids as Efficient and Chemoselective Catalysts for the Hydrogenation of Nitroarenes. *ChemCatChem* **2017**, *9* (10), 1854-1862; (b) Sun, X.; Olivos-Suarez, A. I.; Osadchii, D.; Romero, M. J. V.; Kapteijn, F.; Gascon, J., Single

- cobalt sites in mesoporous N-doped carbon matrix for selective catalytic hydrogenation of nitroarenes. *Journal of Catalysis* **2018**, *357*, 20-28.
11. (a) Deng, Y.; Dong, Y.; Wang, G.; Sun, K.; Shi, X.; Zheng, L.; Li, X.; Liao, S., Well-Defined ZIF-Derived Fe–N Codoped Carbon Nanoframes as Efficient Oxygen Reduction Catalysts. *ACS Applied Materials & Interfaces* **2017**, *9* (11), 9699-9709; (b) Chen, Y.-Z.; Wang, C.; Wu, Z.-Y.; Xiong, Y.; Xu, Q.; Yu, S.-H.; Jiang, H.-L., From Bimetallic Metal-Organic Framework to Porous Carbon: High Surface Area and Multicomponent Active Dopants for Excellent Electrocatalysis. *Advanced Materials* **2015**, *27* (34), 5010-5016.
 12. Yin, P.; Yao, T.; Wu, Y.; Zheng, L.; Lin, Y.; Liu, W.; Ju, H.; Zhu, J.; Hong, X.; Deng, Z.; Zhou, G.; Wei, S.; Li, Y., Single Cobalt Atoms with Precise N-Coordination as Superior Oxygen Reduction Reaction Catalysts. *Angewandte Chemie International Edition* **2016**, *55* (36), 10800-10805.
 13. (a) Zhang, L.; Su, Z.; Jiang, F.; Yang, L.; Qian, J.; Zhou, Y.; Li, W.; Hong, M., Highly graphitized nitrogen-doped porous carbon nanopolyhedra derived from ZIF-8 nanocrystals as efficient electrocatalysts for oxygen reduction reactions. *Nanoscale* **2014**, *6* (12), 6590-6602; (b) Torad, N. L.; Hu, M.; Kamachi, Y.; Takai, K.; Imura, M.; Naito, M.; Yamauchi, Y., Facile synthesis of nanoporous carbons with controlled particle sizes by direct carbonization of monodispersed ZIF-8 crystals. *Chemical Communications* **2013**, *49* (25), 2521-2523.
 14. Sastre, F.; Muñoz-Batista, M. J.; Kubacka, A.; Fernández-García, M.; Smith, W. A.; Kapteijn, F.; Makkee, M.; Gascon, J., Efficient Electrochemical Production of Syngas from CO₂ and H₂O by using a Nanostructured Ag/g-C₃N₄ Catalyst. *Chemelectrochem* **2016**, *3* (9), 1497-1502.
 15. Fei, H.; Dong, J.; Arellano-Jiménez, M. J.; Ye, G.; Dong Kim, N.; Samuel, E. L. G.; Peng, Z.; Zhu, Z.; Qin, F.; Bao, J.; Yacaman, M. J.; Ajayan, P. M.; Chen, D.; Tour, J. M., Atomic cobalt on nitrogen-doped graphene for hydrogen generation. *Nature Communications* **2015**, *6*, 8668.
 16. Tang, J.; Salunkhe, R. R.; Liu, J.; Torad, N. L.; Imura, M.; Furukawa, S.; Yamauchi, Y., Thermal Conversion of Core–Shell Metal–Organic Frameworks: A New Method for Selectively Functionalized Nanoporous Hybrid Carbon. *Journal of the American Chemical Society* **2015**, *137* (4), 1572-1580.

17. Wang, S.; Shang, L.; Li, L.; Yu, Y.; Chi, C.; Wang, K.; Zhang, J.; Shi, R.; Shen, H.; Waterhouse, G. I. N.; Liu, S.; Tian, J.; Zhang, T.; Liu, H., Metal–Organic–Framework-Derived Mesoporous Carbon Nanospheres Containing Porphyrin-Like Metal Centers for Conformal Phototherapy. *Advanced Materials* **2016**, *28* (38), 8379-8387.
18. Casanovas, J.; Ricart, J. M.; Rubio, J.; Illas, F.; Jiménez-Mateos, J. M., Origin of the Large N 1s Binding Energy in X-ray Photoelectron Spectra of Calcined Carbonaceous Materials. *Journal of the American Chemical Society* **1996**, *118* (34), 8071-8076.
19. GARCIA, J.; BIANCONI, A.; BENFATTO, M.; NATOLI, C., R., COORDINATION GEOMETRY OF TRANSITION METAL IONS IN DILUTE SOLUTIONS BY XANES. *J. Phys. Colloques* **1986**, *47* (C8), C8-49-C8-54.
20. Ju, W.; Bagger, A.; Hao, G.-P.; Varela, A. S.; Sinev, I.; Bon, V.; Roldan Cuenya, B.; Kaskel, S.; Rossmeisl, J.; Strasser, P., Understanding activity and selectivity of metal-nitrogen-doped carbon catalysts for electrochemical reduction of CO₂. *Nature Communications* **2017**, *8* (1), 944.
21. Kosugi, N.; Yokoyama, T.; Asakura, K.; Kuroda, H., Polarized Cu K-edge XANES of square planar CuCl₄²⁻ ion. Experimental and theoretical evidence for shake-down phenomena. *Chemical Physics* **1984**, *91* (2), 249-256.
22. (a) Wilke, M.; Farges, F. o.; Brown, G. E., Jr.; Petit, P.-E.; Martin, F. o., Oxidation state and coordination of Fe in minerals: An Fe K-XANES spectroscopic study. *American Mineralogist* **2001**, *86* (5-6), 714-730; (b) Westre, T. E.; Kennepohl, P.; DeWitt, J. G.; Hedman, B.; Hodgson, K. O.; Solomon, E. I., A Multiplet Analysis of Fe K-Edge 1s → 3d Pre-Edge Features of Iron Complexes. *Journal of the American Chemical Society* **1997**, *119* (27), 6297-6314.
23. Rehr, J. J.; Albers, R. C., Theoretical approaches to x-ray absorption fine structure. *Reviews of Modern Physics* **2000**, *72* (3), 621-654.
24. (a) Liang, W.; Chen, J.; Liu, Y.; Chen, S., Density-Functional-Theory Calculation Analysis of Active Sites for Four-Electron Reduction of O₂ on Fe/N-Doped Graphene. *ACS Catalysis* **2014**, *4* (11), 4170-4177; (b) Leonard, N.; Ju, W.; Sinev, I.; Steinberg, J.; Luo, F.; Varela, A. S.; Roldan Cuenya, B.; Strasser, P., The chemical identity, state and structure of catalytically active centers during the electrochemical CO₂ reduction on porous Fe–nitrogen–carbon (Fe–N–C) materials. *Chemical Science* **2018**, *9* (22), 5064-5073.

25. Mun, Y.; Kim, M. J.; Park, S.-A.; Lee, E.; Ye, Y.; Lee, S.; Kim, Y.-T.; Kim, S.; Kim, O.-H.; Cho, Y.-H.; Sung, Y.-E.; Lee, J., Soft-template synthesis of mesoporous non-precious metal catalyst with Fe-Nx/C active sites for oxygen reduction reaction in fuel cells. *Applied Catalysis B: Environmental* **2018**, *222*, 191-199.
26. Glatzel, P.; Bergmann, U., High resolution 1s core hole X-ray spectroscopy in 3d transition metal complexes—electronic and structural information. *Coordination Chemistry Reviews* **2005**, *249* (1), 65-95.
27. (a) Bergmann, U.; Horne, C. R.; Collins, T. J.; Workman, J. M.; Cramer, S. P., Chemical dependence of interatomic X-ray transition energies and intensities - a study of Mn K β " and K β 2,5 spectra. *Chemical Physics Letters* **1999**, *302* (1), 119-124; (b) Safonov, V. A.; Vykhodtseva, L. N.; Polukarov, Y. M.; Safonova, O. V.; Smolentsev, G.; Sikora, M.; Eeckhout, S. G.; Glatzel, P., Valence-to-Core X-ray Emission Spectroscopy Identification of Carbide Compounds in Nanocrystalline Cr Coatings Deposited from Cr(III) Electrolytes Containing Organic Substances. *The Journal of Physical Chemistry B* **2006**, *110* (46), 23192-23196; (c) Eeckhout, S. G.; Safonova, O. V.; Smolentsev, G.; Biasioli, M.; Safonov, V. A.; Vykhodtseva, L. N.; Sikora, M.; Glatzel, P., Cr local environment by valence-to-core X-ray emission spectroscopy. *Journal of Analytical Atomic Spectrometry* **2009**, *24* (2), 215-223; (d) Lancaster, K. M.; Roemelt, M.; Ettenhuber, P.; Hu, Y.; Ribbe, M. W.; Neese, F.; Bergmann, U.; DeBeer, S., X-ray Emission Spectroscopy Evidences a Central Carbon in the Nitrogenase Iron-Molybdenum Cofactor. *Science* **2011**, *334* (6058), 974-977.
28. (a) DeBeer George, S.; Neese, F., Calibration of Scalar Relativistic Density Functional Theory for the Calculation of Sulfur K-Edge X-ray Absorption Spectra. *Inorganic Chemistry* **2010**, *49* (4), 1849-1853; (b) Pollock, C. J.; DeBeer, S., Valence-to-Core X-ray Emission Spectroscopy: A Sensitive Probe of the Nature of a Bound Ligand. *Journal of the American Chemical Society* **2011**, *133* (14), 5594-5601; (c) Pollock, C. J.; DeBeer, S., Insights into the Geometric and Electronic Structure of Transition Metal Centers from Valence-to-Core X-ray Emission Spectroscopy. *Accounts of Chemical Research* **2015**, *48* (11), 2967-2975; (d) Bauer, M., HERFD-XAS and valence-to-core-XES: new tools to push the limits in research with hard X-rays? *Physical Chemistry Chemical Physics* **2014**, *16* (27), 13827-13837; (e) Gallo, E.;

- Glatzel, P., Valence to Core X-ray Emission Spectroscopy. *Advanced Materials* **2014**, *26* (46), 7730-7746; (f) Neese, F., The ORCA program system. *Wiley Interdisciplinary Reviews: Computational Molecular Science* **2012**, *2* (1), 73-78.
29. Lee, N.; Petrenko, T.; Bergmann, U.; Neese, F.; DeBeer, S., Probing Valence Orbital Composition with Iron K β X-ray Emission Spectroscopy. *Journal of the American Chemical Society* **2010**, *132* (28), 9715-9727.
30. Genovese, C.; Schuster, M. E.; Gibson, E. K.; Gianolio, D.; Posligua, V.; Grau-Crespo, R.; Cibir, G.; Wells, P. P.; Garai, D.; Solokha, V.; Krick Calderon, S.; Velasco-Velez, J. J.; Ampelli, C.; Perathoner, S.; Held, G.; Centi, G.; Arrigo, R., Operando spectroscopy study of the carbon dioxide electro-reduction by iron species on nitrogen-doped carbon. *Nature Communications* **2018**, *9* (1), 935.
31. Hubbard, J.; Flowers, B. H., Electron correlations in narrow energy bands. *Proceedings of the Royal Society of London. Series A. Mathematical and Physical Sciences* **1963**, *276* (1365), 238-257.
32. Sharma, P. P.; Wu, J.; Yadav, R. M.; Liu, M.; Wright, C. J.; Tiwary, C. S.; Yakobson, B. I.; Lou, J.; Ajayan, P. M.; Zhou, X.-D., Nitrogen-Doped Carbon Nanotube Arrays for High-Efficiency Electrochemical Reduction of CO₂: On the Understanding of Defects, Defect Density, and Selectivity. *Angewandte Chemie International Edition* **2015**, *54* (46), 13701-13705.
33. (a) Yang, F.; Song, P.; Liu, X.; Mei, B.; Xing, W.; Jiang, Z.; Gu, L.; Xu, W., Highly Efficient CO₂ Electroreduction on ZnN₄-based Single-Atom Catalyst. *Angewandte Chemie International Edition* **2018**, *57* (38), 12303-12307; (b) Chen, Z.; Mou, K.; Yao, S.; Liu, L., Zinc-Coordinated Nitrogen-Codoped Graphene as an Efficient Catalyst for Selective Electrochemical Reduction of CO₂ to CO. *ChemSusChem* **2018**, *11* (17), 2944-2952.
34. Tripkovic, V.; Vanin, M.; Karamad, M.; Björketun, M. E.; Jacobsen, K. W.; Thygesen, K. S.; Rossmeisl, J., Electrochemical CO₂ and CO Reduction on Metal-Functionalized Porphyrin-like Graphene. *The Journal of Physical Chemistry C* **2013**, *117* (18), 9187-9195.

5.6. Supporting Information for Chapter 5

5.6.1. Geometry optimization for structural models representing the iron site

Periodic calculations. First-principles calculations were performed for periodic structure with CASTEP code (Cambridge Sequential Total Energy Package, CASTEP Developers' Group, Cambridge (UK) code [1], which employs pseudopotentials to describe electron-ion interactions and represents electronic wave functions using a plane-wave basis set, based on density functional theory (DFT) [2]. The exchange-correlation energy of many-electron systems is described by the generalized gradient approximation (GGA) with the parametrization of Perdew-Wang (PW91) method [3]. An energy cutoff of 517 eV for the plane wave expansion and k-point set 2 X 2 X 1, sampled by Monkhorst-Pack method were used together with a convergence criteria for the total energy of 1×10^{-3} meV/atom level. Calculations were spin polarized and included a Van der Waals dispersion correction [4].

The (200), (120) and (001) vectors of the original hexagonal cell of graphite were selected to build a primitive orthorhombic cell with lattice parameters of $a = 4.940 \text{ \AA}$, $b = 4.278 \text{ \AA}$, $c = 6.800 \text{ \AA}$ [5]. Then, a periodical supercell of 3 x 3 x 1 dimensions containing two graphene single-layers with a 20 \AA vacuum above was built ($a = 12.835 \text{ \AA}$, $b = 14.820 \text{ \AA}$, $c = 23.400 \text{ \AA}$). Two contiguous carbon atoms, part of an arm-chair configuration, were removed and the resultant vacancy was filled by an iron atom coordinated by four pyridinic nitrogen replacing four carbon atoms. This structural model, labeled as Slab Fe-N₄, was fully optimized until all the forces were smaller than 0.03 eV/ \AA . The top coordination of iron was

then completed by a water molecule (Slab Fe-N₄-OH) or a hydroxyl moiety (Slab Fe-N₄-H₂O) and all atomic positions were further optimized with the same calculation parameters.

Cluster calculations. All calculations were performed with the ORCA 4.1.0 electronic structure program package developed by Neese and co-workers [6]. Cartesian coordinates for the iron phthalocyanine complex were obtained from reported crystal structure [7]. Coordinates for hypothetical iron active site were generated by adding reasonable initial coordinates for water molecules and/or hydroxyl moiety to the iron phthalocyanine complex. Geometry optimizations were performed using the B3LYP hybrid functional [8], in combination with the def2-TZVP basis set [9], and the core polarized CP(PPP) basis set for iron atom [10]. A dense grid (ORCA Grid4) was used for the numerical integration of the exchange-correlation potential with a criterion for the total energy convergence tolerance of $5 \cdot 10^{-6}$ E_h. Plots and visualization of the optimized structure was done with CHEMCRAFT software [Chemcraft - graphical software for visualization of quantum chemistry computations. <https://www.chemcraftprog.com>].

5.6.2. X-ray absorption and emission spectroscopies (XAS and XES).

Collection of data. Conventional XANES and EXAFS spectra were measured at the iron *K*-edge (7112 eV), from 150 eV before the edge to 800 eV above the edge, on the Collaborative Research Group beamline FAME (French Absorption beamline in Material and Environmental sciences) at the European Synchrotron Radiation Facility (ESRF), in Grenoble, France. The details of the beamline and its optical devices were described by Proux *et al.* [11]. The presence of the two Rh-coated mirrors ensured the rejection of the harmonics to better than 0.1%, *i.e.*, the intensity of the harmonics was less

than 0.1% of the intensity of the fundamental X-rays. The incident (I_0) and transmitted (I_1) intensities were measured by Si photodiodes collecting the X-rays diffused by Kapton foils placed in the beam. The fluorescence photons were measured by a Canberra™ 30 element solid state detector. The energy was calibrated by measuring the spectrum of a reference metallic foil (first maximum of the derivative set at 7112 eV).

HERFD-XANES spectra at the Fe K -edge were obtained at the European Synchrotron Radiation Facility (Grenoble, France) on the CRG-FAME-UHD beamline (BM16). The ring was operated at 6 GeV with a nominal current of 200 mA in 7/8+1 mode. The beamline was equipped with a liquid-nitrogen-cooled double-crystal Si(220) monochromator surrounded by two Rh-coated mirrors for harmonic rejection. The beam size on the sample was 220x100 μm (HxV, FWHM). The monochromator was energy-calibrated by measuring the iron K absorption edge using a metallic iron foil (7112 eV). The fluorescence emission from the sample was collected by a crystal array spectrometer using five spherically bent Ge(620) crystals with a bending radius of 1000 mm in a Rowland geometry. High-resolution $K\beta_{1,3}$ -detected XANES spectra were recorded using a 2D XPAD detector. The maximum of the $K\beta_{1,3}$ emission was calibrated using a metallic iron foil at 7059 eV. The apparent energy resolution was estimated to be approximately 0.86 eV at the iron $K\beta_{1,3}$ emission.

The X-ray emission spectra, in terms of the main ($K\beta'/K\beta_{1,3}$) emission lines and the satellite ($K\beta''/K\beta_{2,5}$) lines were recorded between 7010-7140 eV while applying an excitation energy of 7145 eV. The energy step size of the main and satellite emission lines was 0.4 and 0.3 eV respectively. The total energy resolution was estimated to be approximately 2.4 eV.

Processing of data. All XAS data were analyzed using the HORAE package, a graphical interface to the AUTOBK and IFEFFIT code [12]. The XANES and EXAFS spectra were obtained after performing standard procedures for pre-edge subtraction, normalization, polynomial removal, and wavevector conversion.

Processing of vtc-XES spectrum. The valence-to-core XES data are extracted from the main $K\beta$ lines via a peak fitting procedure, as employed in previous works [13]. Here, instead of pure Lorentzian functions, asymmetric Pseudo-Voigt functions are employed to account the effects of the experimental broadening introduced by the spectrometer. The peak fitting is performed with the FITYK software [14]. The best results are obtained using four asymmetric Pseudo-Voigt functions (p_0, p_1, p_2, p_3), accounting, respectively for the $K\beta_{1,3}$, $K\beta'_{1,2}$, tail of the $K\alpha$ lines and background offset. An example of peak fittings showing the single components and the residual is given below for Fe_3O_4 (Figure S5.1).

EXAFS curve-fitting. Calibration and data alignment was performed using Athena and obtaining values for reference compounds from Hephaestus [15]. After averaging the spectra of the studied samples were normalized to a total absorption of unity and processed using the Athena data normalization and analysis package. For normalization, the spline r-background parameter was set to 1.0. The background subtraction was carried using a pre-edge range of -120 to -30 eV and a post-edge linear range of 50 to 700 eV. A spline range of $k = 0$ to $k = 13.3 \text{ \AA}^{-1}$ and k -weight of 2 was used to isolate the EXAFS (χ)function. The Fe K-edge EXAFS spectra were Fourier transformed over a k -range of $k = 3$ to $k = 11.4 \text{ \AA}^{-1}$.

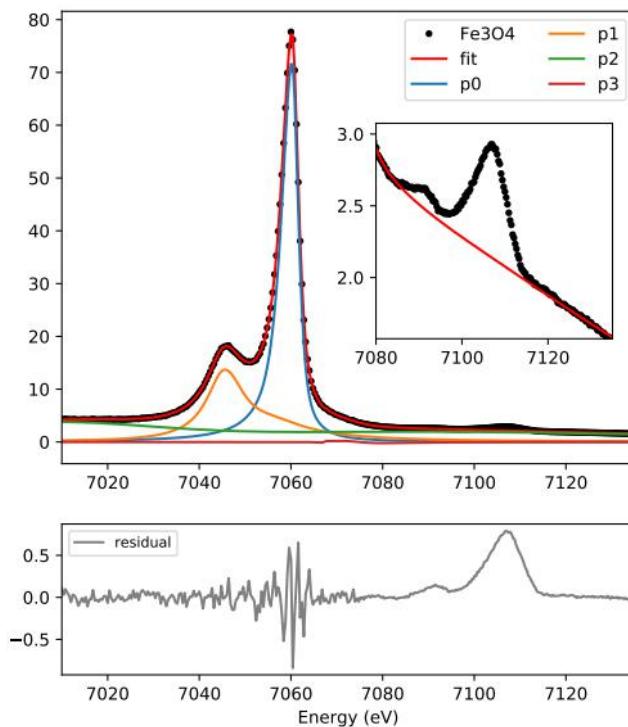


Figure S5.1. Extraction of the $K\beta''$ and $K\beta_{2,5}$ for Fe_3O_4 by peak fitting procedure: (top) single peak components and (bottom) the residual corresponding to the $K\beta_{2,5}$ and $K\beta''$ region.

Fitting of Fe K-edge EXAFS spectra was carried out by Artemis software [15]. The spectra of the different samples were fitted in R -space with a R range of 1 to 4.2 Å, and the fittings were done with a k -weight of 3. The Fourier transform and inverse Fourier transform was carried with a Δk of 1 and ΔR of 0. From the references fits we obtain the amplitude factor (S_0^2) equal to 0.79 ± 0.14 for Fe_2O_3 . In further fittings of the experimental samples $S_0^2 = 0.79$ was used.

Simulation of XANES and VTC- $K\beta$ spectra. Ab initio simulations of the XANES and XES spectra (only for periodic structure) were performed using

the FDMNES package. The FDMNES code features mono-electronic calculations, which are carried out in real space with Hedin-Lundqvist exchange-correlation potential and using clusters built around each non-equivalent absorbing atom. Standard crystal structures (retrieved from the “Inorganic Crystal Structure Database”, FIZ Karlsruhe) are used as inputs. The finite-difference method (FDM) implemented in the FDMNES code was used since the latter is a full potential method that introduces no approximation on the shape of the potential, which is particularly important when dealing with highly distorted structures [16]. The current implementation at KAUST of the recent FDMNES version (30 November 2018) with the MUMPS solver allows FDM calculations with a 7 to 8 Å cluster radius, which were not possible when using the built-in solver because of the required memory footprint and the CPU runtime [17]. Quadrupolar transitions were included in the calculation. To take into account the core-hole lifetime and other multielectronic phenomena occurring in the absorption process, a convolution procedure was applied to all calculated spectra presented in this work. At the Fermi level, the Lorentzian (FWHM) width was set to the apparent broadening of HERFD-XANES and equal to 0.86 eV [18]. At higher photoelectron energies, the plasmon collective interactions increase the Lorentzian width up to 20 eV. For the convolution of XES spectra, the Lorentzian width was set to 2.4 eV.

VTC-XES calculations for cluster models were performed with the ORCA quantum chemistry program [6, 19]. The atomic coordinates were taken from the geometry optimized structures. The calculations parameters below are taken from the numerous studies published by the group of Serena DeBeer [20]. The BP86 functional [21] was utilized in combination with the def2-TZVP basis set [9], and the core polarized CP(PPP) basis set

for iron atom (with a special integration accuracy of 7) [10]. The calculations used a dense integration grid (ORCA Grid4). For of $[\text{Fe}(\text{H}_2\text{O})_6]^{3+}$ and $[\text{Fe}(\text{NH}_3)_6]^{3+}$ cations, the positive charge on the complexes were compensated with the Conductor-like Polarizable Continuum Model (CPCM) parametrized with the dielectric constant of water.

Molecular orbitals were visualized using CHEMCRAFT software. [Chemcraft - graphical software for visualization of quantum chemistry computations. <https://www.chemcraftprog.com>].

5.6.4. Supplementary experimental results

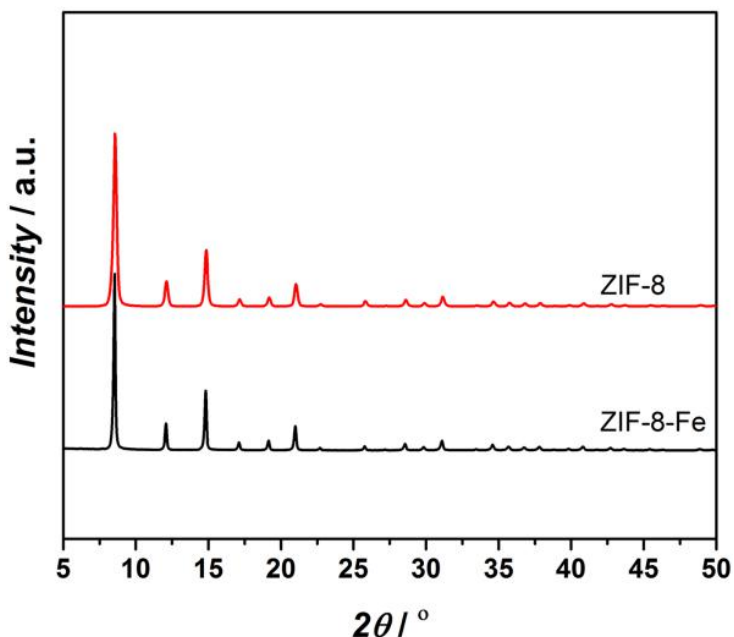


Figure S5.2. (a) X-ray diffraction (XRD) patterns of ZIF-8 and ZIF-8-Fe.

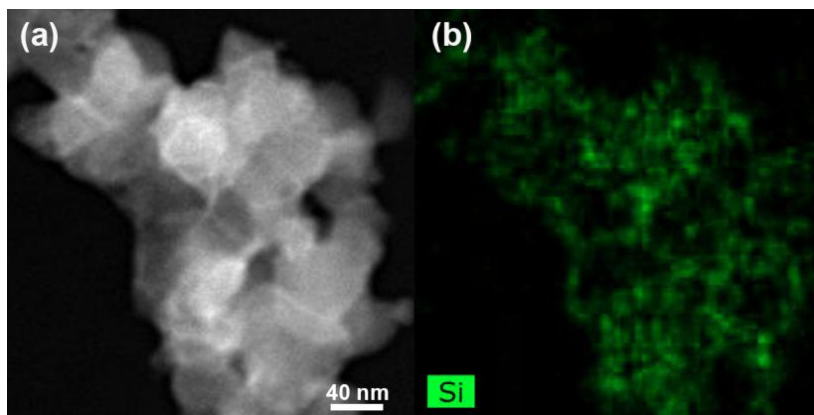


Figure S5.3. Dark field TEM images of ZIF-8-Fe@SiO₂ (a) and Si mapping of ZIF-8-Fe@SiO₂ (b).

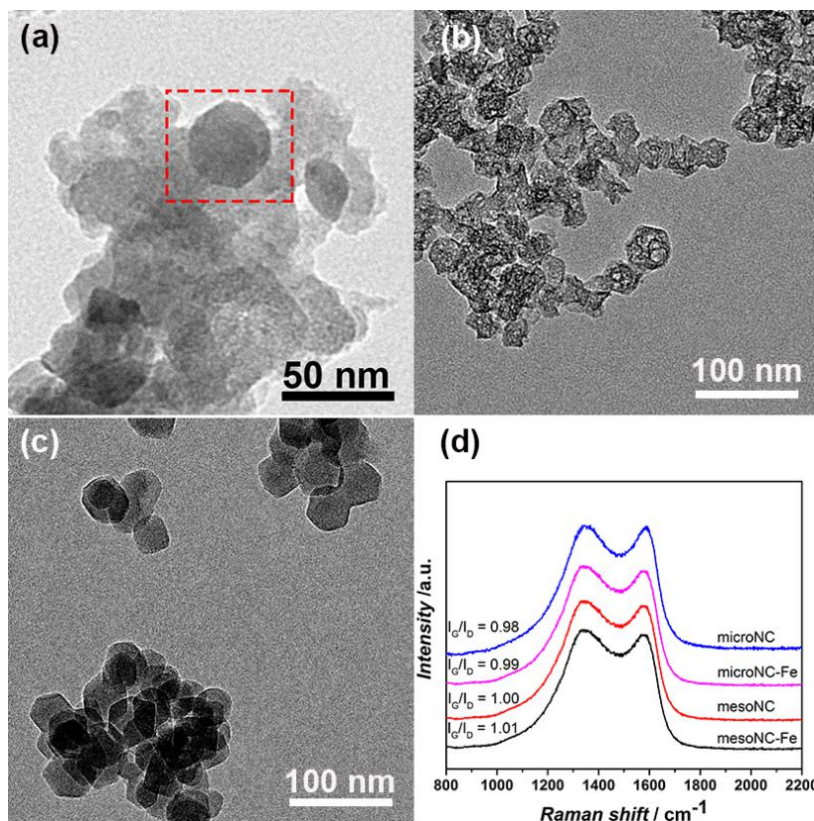


Figure S5.4. Bright TEM images of microNC-Fe (a), mesoNC (b) and microNC (c); Raman spectra of the as-synthesized materials (d).

No zinc (oxide) nanoparticles can be observed in mesoNC and microNC samples.

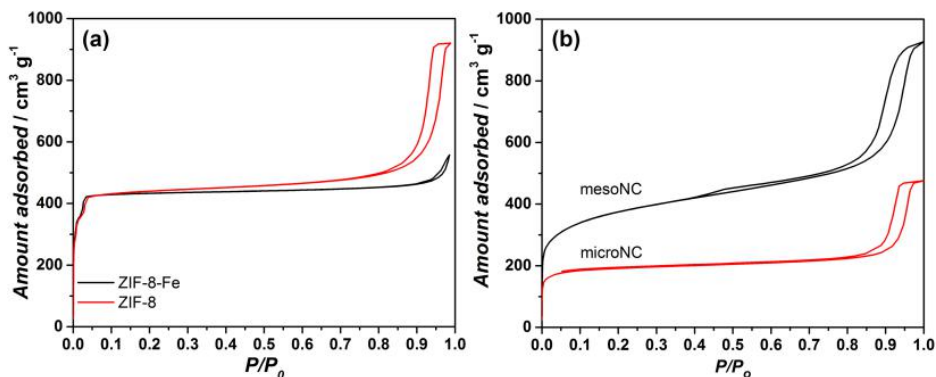


Figure S5.5. N_2 -sorption isotherms at 77 K of the as-synthesized ZIF materials (a) and nitrogen-doped carbon samples (b).

Table S5.1. Texture analysis by N_2 -adsorption-desorption of as-synthesized materials in this work.^a

Samples	$S_{BET} / (m^2/g)$			$V_{pore} / (cm^3/g)$		
	Total	Micro	Meso	Total	Micro	Meso
ZIF-8-Fe	1670	1610	60	0.86	0.64	0.22
ZIF-8	1784	1647	137	1.42	0.62	0.80
mesoNC-Fe	1050	749	301	0.76	0.31	0.45
mesoNC	1347	828	519	1.33	0.35	0.98
microNC-Fe	614	531	83	0.56	0.21	0.35
microNC	732	626	106	0.66	0.25	0.41

a: The given BET areas and pore volumes were calculated per gram of catalyst.

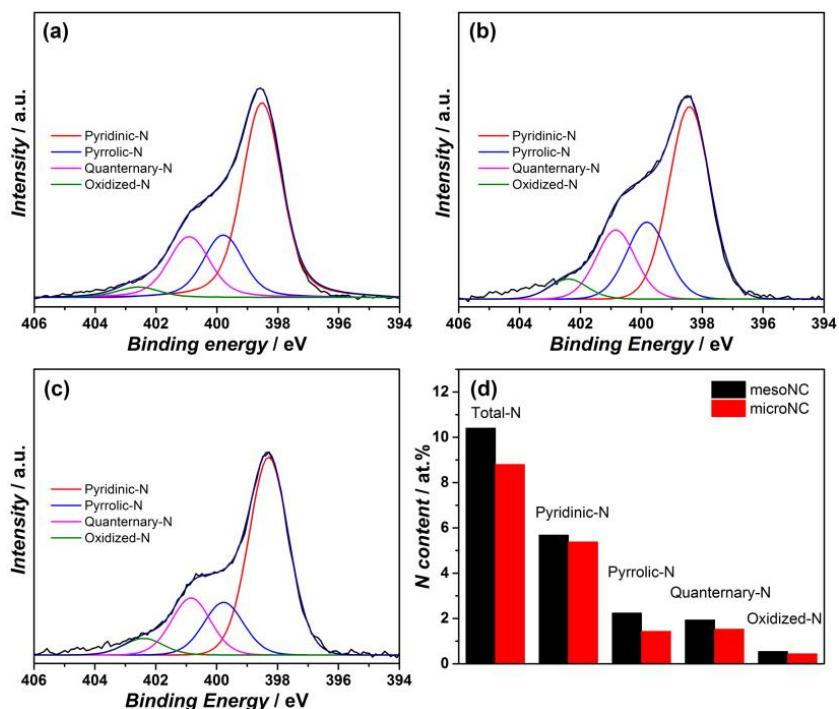


Figure S5.6. N1s XPS regions of microNC-Fe (a), mesoNC (b), and microNC (c) with deconvolution into the N-speciation, and N distribution mesoNC and microNC (d).

Table S5.2. Content of elements (at.%) in NC based samples obtained from XPS survey.

Samples	Content of elements (at.%)				
	C	O	Fe	Zn	Ntotal
mesoNC-Fe	75.1	13.5	0.2	1.2	10.0
mesoNC	76.6	11.6	-	1.4	10.4
microNC-Fe	76.8	12.9	0.2	1.4	8.7
microNC	78.0	11.3	-	1.9	8.8

Table S5.3. Parameters extracted from the fit of EXAFS data for Fe_2O_3 .

Sample	Scattering Paths	N	R [\AA]	σ^2 [\AA^2]	ΔE [eV]	R -factor
Fe_2O_3	Fe-O	3	1.92 ± 0.02	0.003 ± 0.003	-1.1 ± 1.7	0.03
	Fe-O	3	2.09 ± 0.02	0.003 ± 0.003		
	Fe-Fe	1	2.90 ± 0.01	0.004 ± 0.002		
	Fe-Fe	3	2.97 ± 0.02	0.004 ± 0.002		
	Fe-Fe	3	3.39 ± 0.02	0.003 ± 0.002		

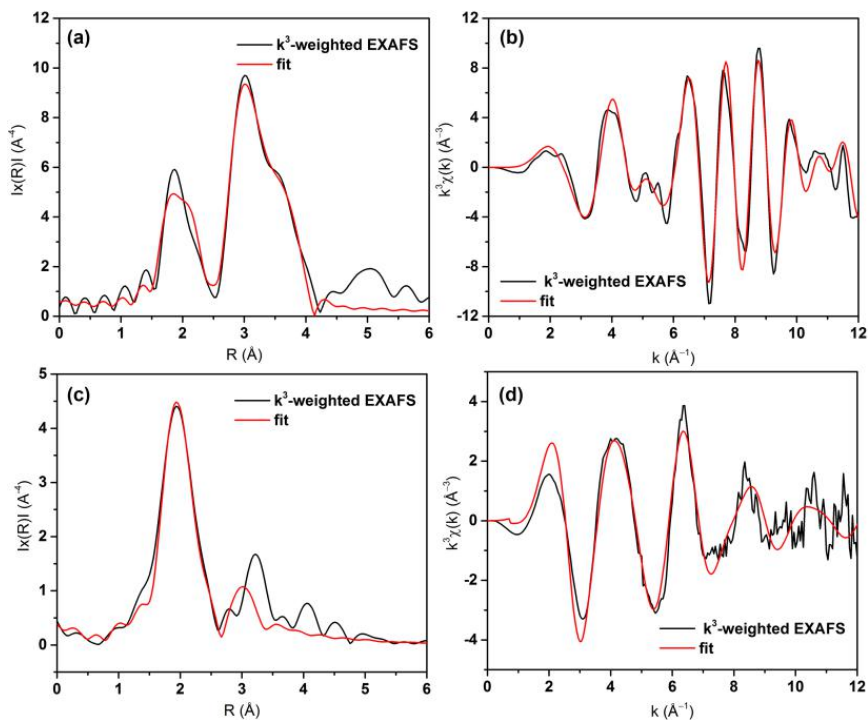
**Figure S5.7.** Fe K-edge EXAFS $k^3\chi(k)$ functions and its Fourier transforms for Fe_2O_3 (a, b) and mesoNC-Fe (c, d).

Table S5.4. Parameters extracted from the fit of EXAFS data for mesoNC-Fe.

Sample	Scattering Paths	Model	N	R [Å]	σ^2 [Å ²]	ΔE [eV]	R -factor
MesoNC-Fe	Fe-O/N	A	5.6 ± 1.2	1.96 ± 0.03	0.005 ± 0.004	2.1 ± 2.3	0.04
	Fe-C		7.2 ± 2.4	2.98 ± 0.04	0.013 ± 0.006		
	Fe-O/N	B	5.7 ± 2.1	1.94 ± 0.05	0.005 ± 0.007	0.4 ± 3.5	0.03
	Fe-C		7.1 ± 4.2	2.97 ± 0.08	0.019 ± 0.015		
	Fe-Fe		2.2 ± 0.8	3.05 ± 0.06	0.022 ± 0.011		

In order to investigate whether iron oxide nanoparticles are present in the sample or not, we have also tried to introduce additional Fe-Fe scattering paths into the fitting (Table S5.4 Model B). However, we could not obtain any satisfactory fits with reasonable parameters in this case (σ^2 for Fe-O/N is not reasonable), as shown in Figure S5.11, which indicates that the presence of bulk iron species in the sample is negligible.

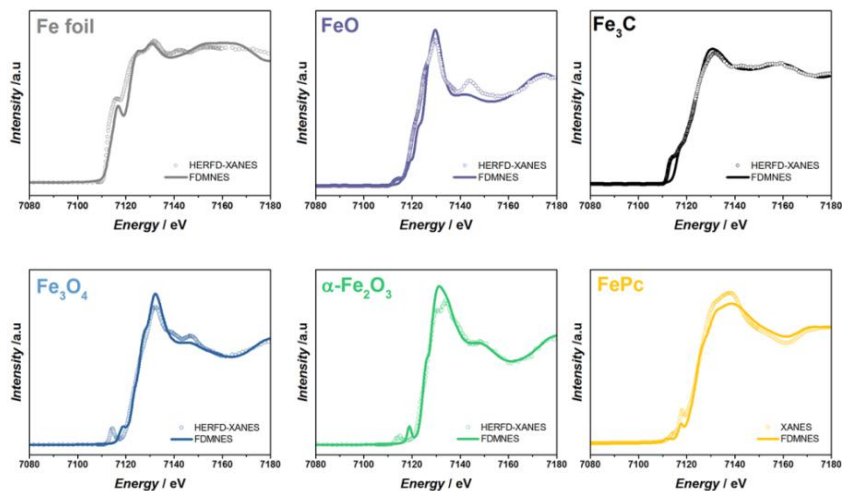


Figure S5.8. Comparison of the experimental and theoretical spectra calculated with the FDMNES code at Fe K-edge for α -Fe, FeO, Fe₃C, Fe₃O₄, α -Fe₂O₃ and iron phtalocyanine (FePc). All experimental data are HERFD-XANES data measured at the iron K $\beta_{1,3}$ emission, except the XANES spectrum of FePc provided by Zitolo, *et al.* [22].

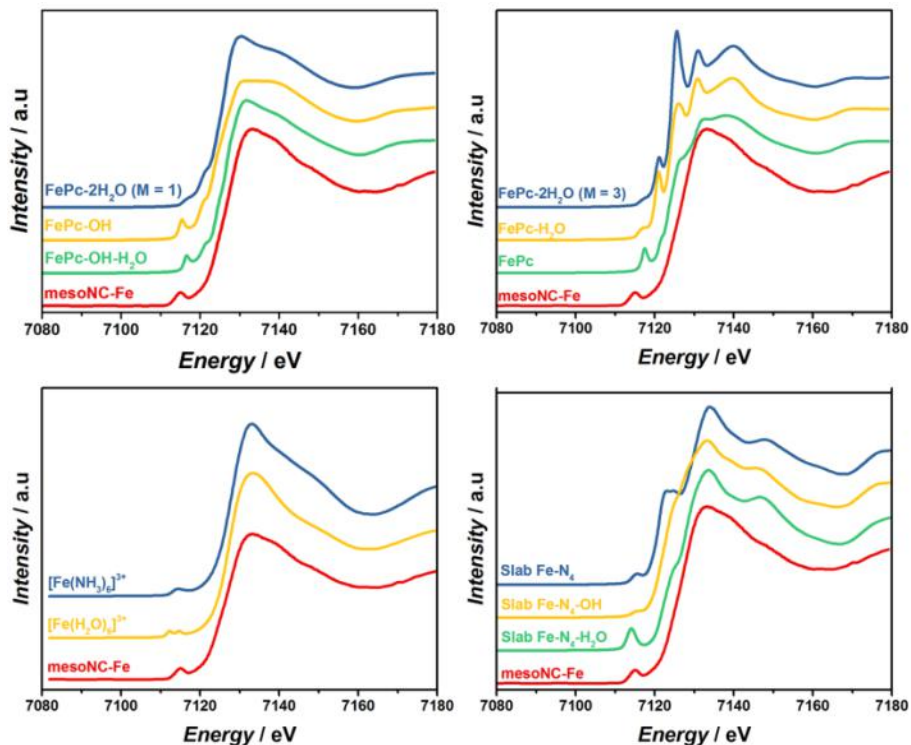


Figure S5.9. Comparison of the mesoNC-Fe HERFD-XANES spectrum with theoretical spectra calculated for various structural models optimized by DFT. (FePc-OH, FePc-H₂O, FePc-2H₂O, FePc-OH-H₂O, iron phtalocyanine (FePc), [Fe(H₂O)₆]³⁺, [Fe(NH₃)₆]³⁺, Slab Fe-N₄, Slab Fe-N₄-OH, Slab Fe-N₄-H₂O, *cf.* Figure 5.4 in main manuscript for the visualisation of the structural models).

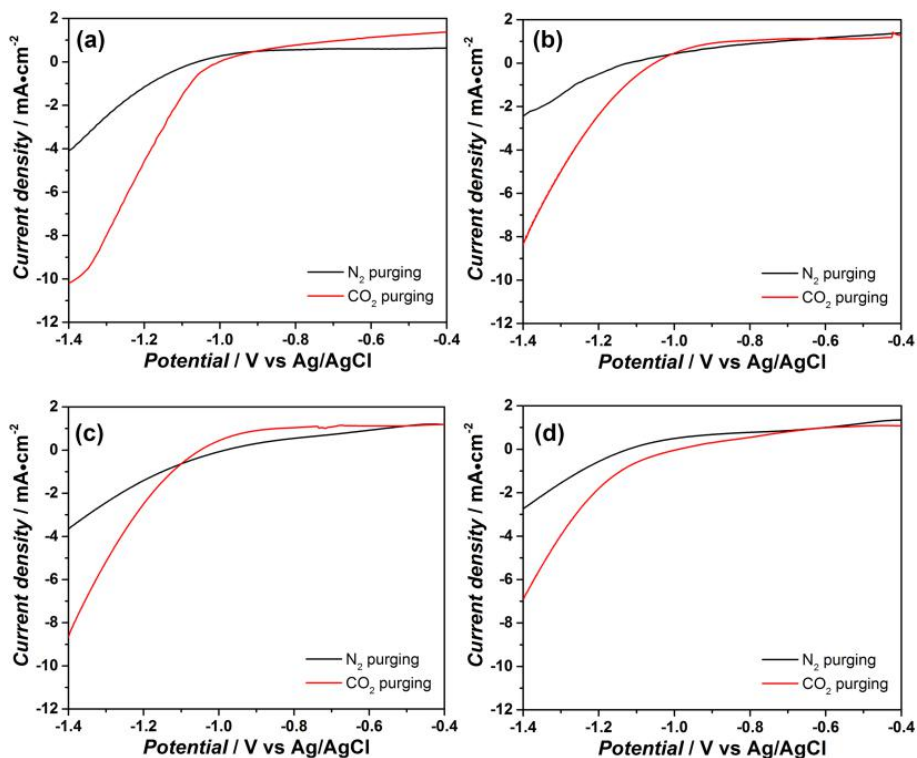


Figure S5.10. Linear Sweep Voltammetry of mesoNC-Fe (a), microNC-Fe (b), mesoNC (c) and microNC (d) when purging N₂ (*black*) and purging CO₂ (*red*).

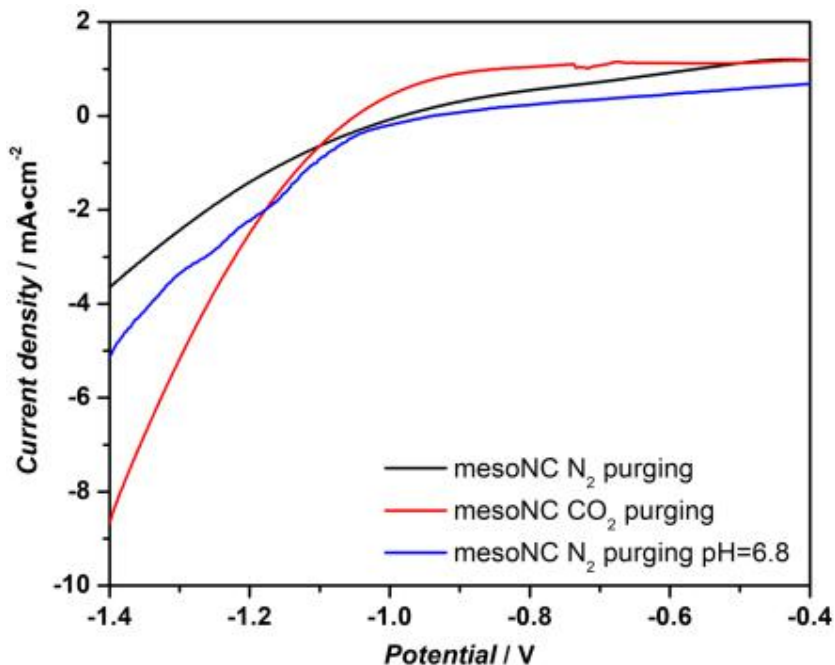


Figure S5.11. Linear Sweep Voltammetry of mesoNC under different pH conditions.

The pH value of 6.8 for mesoNC with N₂ purging was modified by adding drops of 0.05 M H₂SO₄ solution to the KHCO₃ solution.

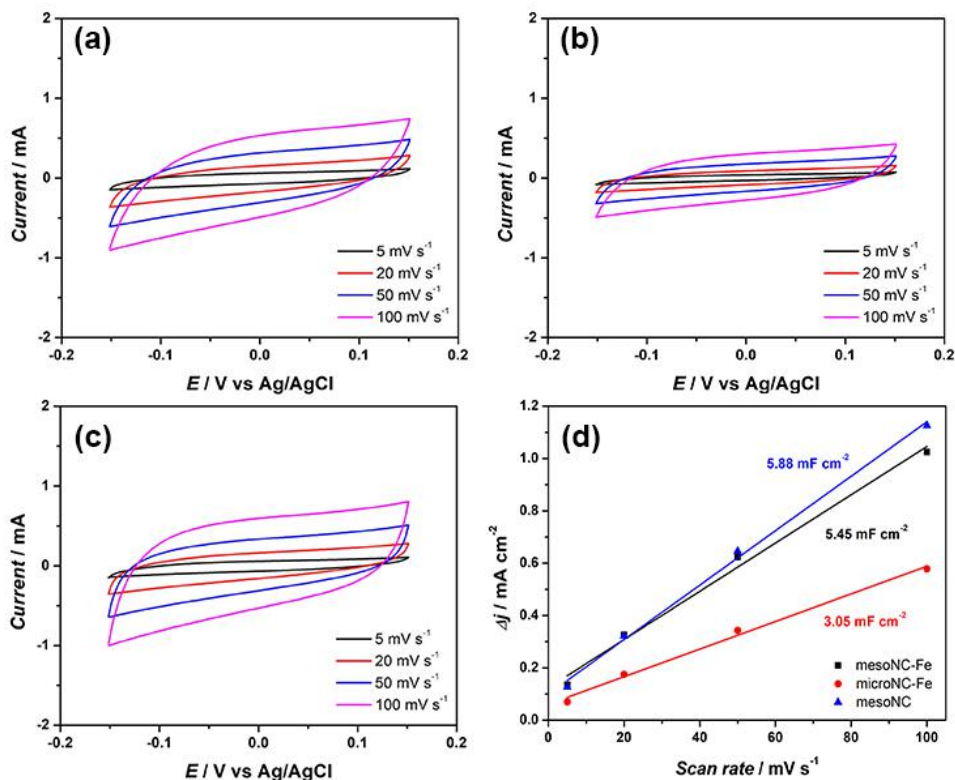


Figure S5.12. Cyclic voltammograms of (a) mesoNC-Fe, (b) microNC-Fe and (c) mesoNC electrodes; and (d) current versus scan rate of each electrode in 0.1 M KHCO_3 aqueous solution of these materials.

Cyclic voltammogram measurements of the as-synthesized samples were conducted from -0.15 V vs Ag/AgCl to 0.15 V vs Ag/AgCl with various scan rates (5, 20, 50, and 100 mV s^{-1}) under CO_2 atmosphere to attain the double layer capacitance (C_{dl}), which was estimated by plotting the Δj ($j_a - j_c$) against the scan rates. The linear slope was equal to twice of the C_{dl} .

The mesoNC and mesoNC-Fe samples show a similar double layer capacitance (C_{dl}) (5.88 mF cm^{-2} versus 5.45 mF cm^{-2}), which indicates a similar electrochemically active surface area (ECSA).

The Gibbs free energies of the reaction intermediates involved in CO₂ reduction to CO and hydrogen evolution reaction over the catalysts of mesoNC and mesoNC-Fe were further calculated by Gaussian 16 software [23]. B3LYP functional [24] and def2-TZVP basis set [25] were used throughout all of the calculations. Van der Waal interaction between catalyst and adsorbates were included by Grimme's dispersion with Becke-Johnson damping [26]. Based on Computational Hydrogen Electrode (CHE) Model [6], the chemical potential of H₂ (g) is equivalent to that of $\mu(\text{H}^+ + \text{e}^-) = 1/2\mu(\text{H}_2)$.

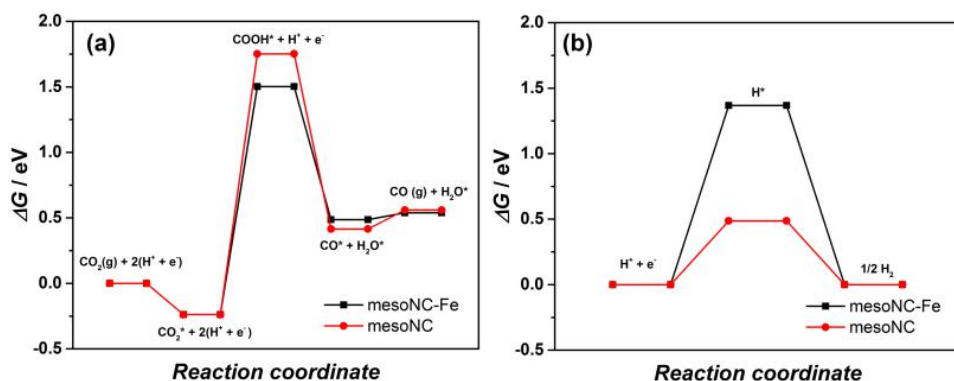


Figure S5.13. Comparison of free energy diagram for CO₂ electroreduction (a) and proton reduction (b) reactions between mesoNC-Fe and mesoNC catalysts. FePc-OH was used as the model for mesoNC-Fe in this calculation.

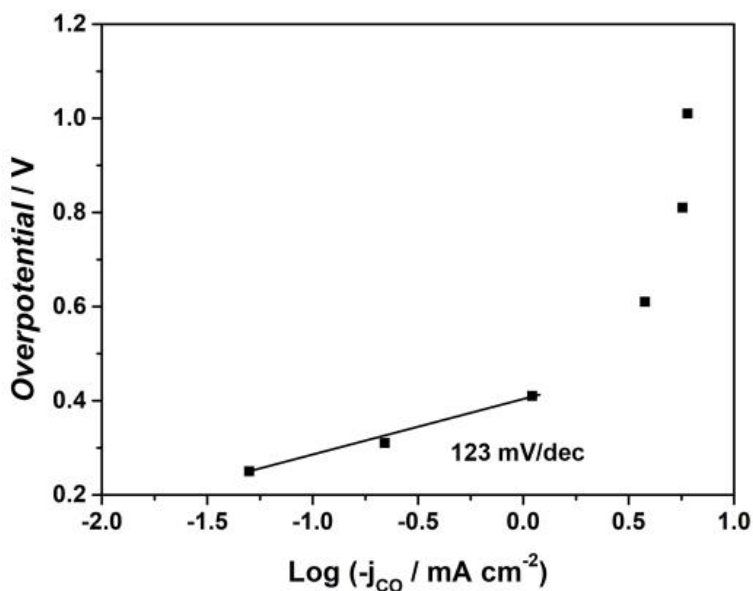


Figure S5.14. Tafel plot for CO formation of mesoNC-Fe.

The Tafel slope region was freshly measured to construct a linear slope, and the linear region is different from the potential range in Figure 5.6.

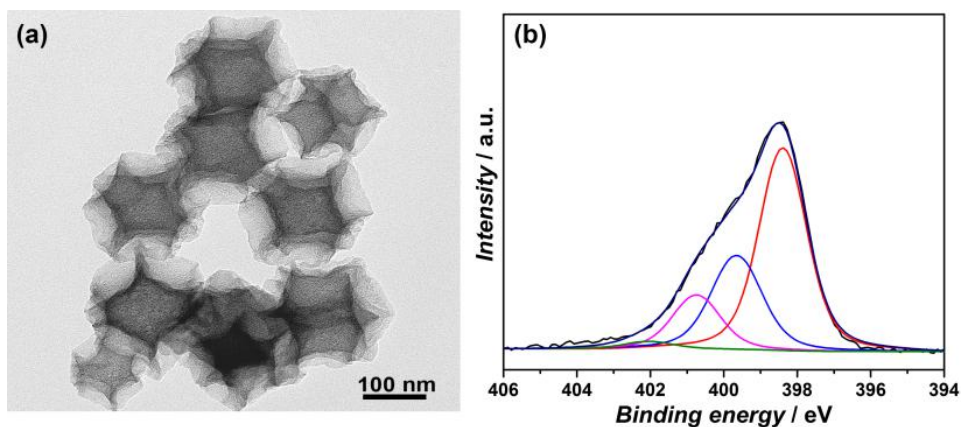


Figure S5.15. TEM image (a) and N1s XPS region (b) of the spent mesoNC-Fe sample after 4 runs.

No iron (oxide) nanoparticles can be observed in the spent mesoNC-Fe catalyst after 4 runs and the N1s XPS region of the spent mesoNC-Fe catalyst is similar as the fresh mesoNC-Fe catalyst, highlighting the high stability of Fe-N coordination environment during CO₂ electroreduction reaction.

Table S5.5. Comparison of the catalytic activity of mesoNC-Fe to recent reported nitrogen-doped carbon supported Fe catalysts for CO₂ electroreduction reaction.

Electro-catalyst	Peak FE_{CO}	Potential of peak FE_{CO} (V vs RHE)	FE_{CO} at -0.73 V vs RHE	Peak j_{CO} (mA cm ²)	Electrolyte	Cathode material	Ref.
MesoNC-Fe	~ 85%	-0.73	~ 85%	-3.7	0.1M KHCO ₃	Carbon cloth	This work
Fe-N-C	~ 80%	-0.5	~ 40%	-2.7	0.1 M KHCO ₃	glassy carbon	[27]
Fe-N-C	~ 65%	-0.55	~ 40%	-2.5	0.1 M KHCO ₃	glassy carbon	[28]
Fe-N-C	~ 80%	-0.60	~ 80%	-2.2	0.5 M NaHCO ₃	carbon paper	[29]
Fe-N-C	~87%	-0.5	~45%	-1.3	0.1 M KHCO ₃	carbon paper	[30]
Fe-N-C	~ 93%	-0.58	~ 85%	-2.8	0.1 M KHCO ₃	carbon paper	[31]
Fe-N-C	~78%	-1.0	~65%	-	0.1 M KHCO ₃	glassy carbon	[32]
FeNx/C	~85%	-0.6	~78%	-	0.1 m Na ₂ SO ₄	carbon paper	[33]
Fe/Fe ₃ C@N CNT	~ 50%	-0.74	~ 50%	-	0.5 M NaHCO ₃	glassy carbon	[34]
NiFe-CNT/CNS	~ 69%	-0.59	~ 60%	-0.8	0.1 M KHCO ₃	carbon paper	[35]
Fe-N-C	~ 85%	-0.55	~ 60%	-3.0	0.1 M KHCO ₃	glassy carbon	[36]
Fe-N/C	~81%	-0.45	~30%	-0.7	0.5 M KHCO ₃	glassy carbon	[37]
Fe-N-C	~93%	-0.43	~60%	-4.2	1 M KHCO ₃	carbon paper	[38]
Fe-N-C	~ 85%	-0.47	~ 60%	-1.5	0.5 M KHCO ₃	glassy carbon	[39]
Fe@NG	~ 85%	-0.68	-	-	0.5 M KHCO ₃	carbon paper	[40]
Fe-N-C	~ 80%	-0.57	~ 20%	-1.0	0.5 M KHCO ₃	glassy carbon	[41]

5.6.5. References for supporting information

1. Segall, M. D.; Lindan, P. J. D.; Probert, M. J.; Pickard, C. J.; Hasnip, P. J.; Clark, S. J.; Payne, M. C., First-principles simulation: ideas, illustrations and the CASTEP code. *Journal of Physics: Condensed Matter* 2002, 14, 2717-2744.
2. (a) Vanderbilt, D., Soft self-consistent pseudopotentials in a generalized eigenvalue formalism. *Physical Review B* 1990, 41 (11), 7892-7895; (b) Hohenberg, P.; Kohn, W., Inhomogeneous Electron Gas. *Physical Review* 1964, 136 (3B), B864-B871.
3. Perdew, J. P.; Wang, Y., Accurate and simple analytic representation of the electron-gas correlation energy. *Physical Review B* 1992, 45 (23), 13244-13249.
4. Ortmann, F.; Bechstedt, F.; Schmidt, W. G., Semiempirical van der Waals correction to the density functional description of solids and molecular structures. *Physical Review B* 2006, 73 (20), 205101.
5. Bernal, J. D.; Bragg, W. L., The structure of graphite. *Proceedings of the Royal Society of London. Series A, Containing Papers of a Mathematical and Physical Character* 1924, 106 (740), 749-773.
6. Neese, F., The ORCA program system. *Wiley Interdisciplinary Reviews: Computational Molecular Science* 2012, 2 (1), 73-78.
7. Kirner, J. F.; Dow, W.; Scheidt, W. R., Molecular stereochemistry of two intermediate-spin complexes. Iron(II) phthalocyanine and manganese(II) phthalocyanine. *Inorganic Chemistry* 1976, 15 (7), 1685-1690.
8. (a) Becke, A. D., Density - functional thermochemistry. III. The role of exact exchange. *The Journal of Chemical Physics* 1993, 98 (7), 5648-5652; (b) Lee, C.; Yang, W.; Parr, R. G., Development of the Colle-Salvetti correlation-energy formula into a functional of the electron density. *Physical Review B* 1988, 37 (2), 785-789; (c) Vosko, S. H.; Wilk, L.; Nusair, M., Accurate spin-dependent electron liquid correlation energies for local spin density calculations: a critical analysis. *Canadian Journal of Physics* 1980, 58 (8), 1200-1211; (d) Stephens, P. J.; Devlin, F. J.; Chabalowski, C. F.; Frisch, M. J., Ab Initio Calculation of Vibrational Absorption and Circular Dichroism Spectra Using Density Functional Force Fields. *The Journal of Physical Chemistry* 1994, 98 (45), 11623-11627.

9. Weigend, F.; Ahlrichs, R., Balanced basis sets of split valence, triple zeta valence and quadruple zeta valence quality for H to Rn: Design and assessment of accuracy. *Physical Chemistry Chemical Physics* 2005, 7 (18), 3297-3305.
10. (a) Neese, F., Prediction and interpretation of the ^{57}Fe isomer shift in Mössbauer spectra by density functional theory. *Inorganica Chimica Acta* 2002, 337, 181-192; (b) Sinnecker, S.; Slep, L. D.; Bill, E.; Neese, F., Performance of Nonrelativistic and Quasi-Relativistic Hybrid DFT for the Prediction of Electric and Magnetic Hyperfine Parameters in ^{57}Fe Mössbauer Spectra. *Inorganic Chemistry* 2005, 44 (7), 2245-2254; (c) Römel, M.; Ye, S.; Neese, F., Calibration of Modern Density Functional Theory Methods for the Prediction of ^{57}Fe Mössbauer Isomer Shifts: Meta-GGA and Double-Hybrid Functionals. *Inorganic Chemistry* 2009, 48 (3), 784-785.
11. (a) Proux, O.; Biquard, X.; Lahera, E.; Menthonnex, J.-J.; Prat, A.; ULRICH, O.; Soldo, Y.; Trévisson, P.; Kapoujyan, G.; Perroux, G.; Taunier, P.; Grand, D.; Jeantet, P.; Deleglise, M.; Roux, J.-P.; Hazemann, J.-L., FAME : A new beamline for X-ray absorption investigations of very-diluted systems of environmental, material and biological interests. *Physica Scripta* 2005; (b) Proux, O.; Nassif, V.; Prat, A.; Ulrich, O.; Lahera, E.; Biquard, X.; Menthonnex, J.-J.; Hazemann, J.-L., Feedback system of a liquid-nitrogen-cooled double-crystal monochromator: design and performances. *Journal of Synchrotron Radiation* 2006, 13 (1), 59-68.
12. Ravel, B.; Newville, M., ATHENA, ARTEMIS, HEPHAESTUS: data analysis for X-ray absorption spectroscopy using IFEFFIT. *Journal of Synchrotron Radiation* 2005, 12 (4), 537-541.
13. Hölzer, G.; Fritsch, M.; Deutsch, M.; Härtwig, J.; Förster, E., $K\alpha_{1,2}$ and $K\beta_{1,3}$ x-ray emission lines of the $3d$ transition metals. *Physical Review A* 1997, 56 (6), 4554-4568.
14. Wojdyr, M., Fityk: a general-purpose peak fitting program. *Journal of Applied Crystallography* 2010, 43 (5 Part 1), 1126-1128.
15. Ravel, B.; Newville, M., ATHENA, ARTEMIS, HEPHAESTUS: data analysis for X-ray absorption spectroscopy using IFEFFIT. *J. Synchrotron Radiat.* 2005, 12 (4), 537-541.
16. Bunău, O.; Joly, Y., Self-consistent aspects of x-ray absorption calculations. *Journal of Physics: Condensed Matter* 2009, 21 (34), 345501.

17. Guda, S. A.; Guda, A. A.; Soldatov, M. A.; Lomachenko, K. A.; Bugaev, A. L.; Lamberti, C.; Gawelda, W.; Bressler, C.; Smolentsev, G.; Soldatov, A. V.; Joly, Y., Optimized Finite Difference Method for the Full-Potential XANES Simulations: Application to Molecular Adsorption Geometries in MOFs and Metal–Ligand Intersystem Crossing Transients. *Journal of Chemical Theory and Computation* 2015, 11 (9), 4512-4521.
18. de Groot, F. M. F.; Krisch, M. H.; Vogel, J., Spectral sharpening of the Pt L edges by high-resolution x-ray emission. *Physical Review B* 2002, 66 (19), 195112.
19. DeBeer George, S.; Neese, F., Calibration of Scalar Relativistic Density Functional Theory for the Calculation of Sulfur K-Edge X-ray Absorption Spectra. *Inorganic Chemistry* 2010, 49 (4), 1849-1853.
20. (a) Pollock, C. J.; DeBeer, S., Valence-to-Core X-ray Emission Spectroscopy: A Sensitive Probe of the Nature of a Bound Ligand. *Journal of the American Chemical Society* 2011, 133 (14), 5594-5601; (b) Lee, N.; Petrenko, T.; Bergmann, U.; Neese, F.; DeBeer, S., Probing Valence Orbital Composition with Iron K β X-ray Emission Spectroscopy. *Journal of the American Chemical Society* 2010, 132 (28), 9715-9727.
21. (a) Becke, A. D., Density-functional exchange-energy approximation with correct asymptotic behavior. *Physical Review A* 1988, 38 (6), 3098-3100; (b) Perdew, J. P., Density-functional approximation for the correlation energy of the inhomogeneous electron gas. *Physical Review B* 1986, 33 (12), 8822-8824.
22. Zitolo, A.; Goellner, V.; Armel, V.; Sougrati, M.-T.; Mineva, T.; Stievano, L.; Fonda, E.; Jaouen, F., Identification of catalytic sites for oxygen reduction in iron- and nitrogen-doped graphene materials. *Nature Materials* 2015, 14, 937.
23. Frisch, M. J.; Trucks, G. W.; Schlegel, H. B.; Scuseria, G. E.; Robb, M. A.; Cheeseman, J. R.; Scalmani, G.; Barone, V.; Petersson, G. A.; Nakatsuji, H.; Li, X.; Caricato, M.; Marenich, A. V.; Bloino, J.; Janesko, B. G.; Gomperts, R.; Mennucci, B.; Hratchian, H. P.; Ortiz, J. V.; Izmaylov, A. F.; Sonnenberg, J. L.; Williams; Ding, F.; Lipparini, F.; Egidi, F.; Goings, J.; Peng, B.; Petrone, A.; Henderson, T.; Ranasinghe, D.; Zakrzewski, V. G.; Gao, J.; Rega, N.; Zheng, G.; Liang, W.; Hada, M.; Ehara, M.; Toyota, K.; Fukuda, R.; Hasegawa, J.; Ishida, M.; Nakajima, T.; Honda, Y.; Kitao, O.; Nakai, H.; Vreven, T.; Throssell, K.; Montgomery Jr., J. A.; Peralta, J. E.; Ogliaro, F.; Bearpark, M. J.; Heyd, J. J.; Brothers, E. N.; Kudin, K. N.; Staroverov, V. N.; Keith, T.

- A.; Kobayashi, R.; Normand, J.; Raghavachari, K.; Rendell, A. P.; Burant, J. C.; Iyengar, S. S.; Tomasi, J.; Cossi, M.; Millam, J. M.; Klene, M.; Adamo, C.; Cammi, R.; Ochterski, J. W.; Martin, R. L.; Morokuma, K.; Farkas, O.; Foresman, J. B.; Fox, D. J. Gaussian 16 Rev. A.03, Wallingford, CT, 2016.
24. Becke, A. D., Density - functional thermochemistry. III. The role of exact exchange. 1993, 98 (7), 5648-5652.
 25. Weigenda, F.; Ahlrichs, R., Balanced basis sets of split valence, triple zeta valence and quadruple zeta valence quality for H to Rn: Design and assessment of accuracy. *Phys. Chem. Chem. Phys.* 2005, 7, 3297-3305
 26. Grimme, S.; Ehrlich, S.; Goerigk, L., Effect of the damping function in dispersion corrected density functional theory. 2011, 32 (7), 1456-1465.
 27. Varela, A. S.; Sahraie, N. R.; Steinberg, J.; Ju, W.; Oh, H. S.; Strasser, P., Metal - Doped Nitrogenated Carbon as an Efficient Catalyst for Direct CO₂ Electroreduction to CO and Hydrocarbons. *Angewandte Chemie International Edition* 2015, 54 (37), 10758-10762.
 28. Ju, W.; Bagger, A.; Hao, G.-P.; Varela, A. S.; Sinev, I.; Bon, V.; Roldan Cuenya, B.; Kaskel, S.; Rossmeisl, J.; Strasser, P., Understanding activity and selectivity of metal-nitrogen-doped carbon catalysts for electrochemical reduction of CO₂. *Nature Communications* 2017, 8 (1), 944.
 29. Huan, T. N.; Ranjbar, N.; Rousse, G.; Sougrati, M.; Zitolo, A.; Mougél, V.; Jaouen, F.; Fontecave, M., Electrochemical Reduction of CO₂ Catalyzed by Fe-N-C Materials: A Structure–Selectivity Study. *ACS Catalysis* 2017, 7 (3), 1520-1525.
 30. Pan, F.; Deng, W.; Justiniano, C.; Li, Y., Identification of champion transition metals centers in metal and nitrogen-codoped carbon catalysts for CO₂ reduction. *Applied Catalysis B: Environmental* 2018, 226, 463-472.
 31. Pan, F.; Zhang, H.; Liu, K.; Cullen, D.; More, K.; Wang, M.; Feng, Z.; Wang, G.; Wu, G.; Li, Y., Unveiling Active Sites of CO₂ Reduction on Nitrogen-Coordinated and Atomically Dispersed Iron and Cobalt Catalysts. *ACS Catalysis* 2018, 8 (4), 3116-3122.
 32. Varela, A. S.; Kroschel, M.; Leonard, N. D.; Ju, W.; Steinberg, J.; Bagger, A.; Rossmeisl, J.; Strasser, P., pH Effects on the Selectivity of the Electrocatalytic CO₂ Reduction on Graphene-Embedded Fe–N–C Motifs: Bridging Concepts between

- Molecular Homogeneous and Solid-State Heterogeneous Catalysis. *ACS Energy Letters* 2018, 3 (4), 812-817.
33. Li, E.; Yang, F.; Wu, Z.; Wang, Y.; Ruan, M.; Song, P.; Xing, W.; Xu, W., A Bifunctional Highly Efficient FeN_x/C Electrocatalyst. *Small* 2018, 14 (8), 1702827.
 34. Jia, J.; Yang, H.; Wang, G.; Huang, P.; Cai, P.; Wen, Z., Fe/Fe₃C Nanoparticles Embedded in Nitrogen-Doped Carbon Nanotubes as Multifunctional Electrocatalysts for Oxygen Catalysis and CO₂ Reduction. *ChemElectroChem* 2018, 5 (3), 471-477.
 35. Pan, F.; Zhao, H.; Deng, W.; Feng, X.; Li, Y., A novel N,Fe-Decorated carbon nanotube/carbon nanosheet architecture for efficient CO₂ reduction. *Electrochimica Acta* 2018, 273, 154-161.
 36. Leonard, N.; Ju, W.; Sinev, I.; Steinberg, J.; Luo, F.; Varela, A. S.; Roldan Cuenya, B.; Strasser, P., The chemical identity, state and structure of catalytically active centers during the electrochemical CO₂ reduction on porous Fe–nitrogen–carbon (Fe–N–C) materials. *Chemical Science* 2018, 9 (22), 5064-5073.
 37. Jung, H.; Lee, S. Y.; Won, D. H.; Kim, K.-J.; Chae, S. Y.; Oh, H.-S.; Min, B. K.; Hwang, Y. J., Understanding Selective Reduction of CO₂ to CO on Modified Carbon Electrocatalysts. *ChemElectroChem* 2018, 5 (12), 1615-1621.
 38. Ye, Y.; Cai, F.; Li, H.; Wu, H.; Wang, G.; Li, Y.; Miao, S.; Xie, S.; Si, R.; Wang, J.; Bao, X., Surface functionalization of ZIF-8 with ammonium ferric citrate toward high exposure of Fe-N active sites for efficient oxygen and carbon dioxide electroreduction. *Nano Energy* 2017, 38, 281-289.
 39. Hu, X.-M.; Hval, H. H.; Bjerglund, E. T.; Dalgaard, K. J.; Madsen, M. R.; Pohl, M.-M.; Welter, E.; Lamagni, P.; Buhl, K. B.; Bremholm, M.; Beller, M.; Pedersen, S. U.; Skrydstrup, T.; Daasbjerg, K., Selective CO₂ Reduction to CO in Water using Earth-Abundant Metal and Nitrogen-Doped Carbon Electrocatalysts. *ACS Catalysis* 2018, 8 (7), 6255-6264.
 40. Bi, W.; Li, X.; You, R.; Chen, M.; Yuan, R.; Huang, W.; Wu, X.; Chu, W.; Wu, C.; Xie, Y., Surface Immobilization of Transition Metal Ions on Nitrogen-Doped Graphene Realizing High-Efficient and Selective CO₂ Reduction. *Advanced Materials* 2018, 30 (18), 1706617.
 41. Shi, J.-J.; Hu, X.-M.; Madsen, M. R.; Lamagni, P.; Bjerglund, E. T.; Pedersen, S. U.; Skrydstrup, T.; Daasbjerg, K., Facile Synthesis of Iron- and Nitrogen-Doped Porous

Carbon for Selective CO₂ Electroreduction. ACS Applied Nano Materials 2018, 1 (7), 3608-3615.

SUMMARY

The electrochemical conversion of CO₂ constitutes an interesting pathway to close the anthropogenic carbon cycles. The ability to reach stable operation in short time makes this method a perfect candidate to buffer the intermittency of renewable power sources, such as solar cells and wind power. As is the case of heterogeneous catalysis, the key to commercialize a process lies in the optimization of the catalytic phase. In this thesis, we take advantage of the unique properties of metal-organic frameworks (MOFs) to synthesize efficient catalysts for electrochemical CO₂ reduction (CO₂ER). Specifically, the two properties we utilize are the atomic dispersion of the elements and the highly designable building blocks (**Chapter 1**).

The research was initiated based on the metal part of MOFs. A coordination polymer was designed through the self-assembly of silver and 2,5-pyridinedicarboxylic acid (**Chapter 2**). Tight control of the Ag content on a conductive carbon support as basis of an electrocatalyst was achieved with the aid of a layer-by-layer growth strategy. During the electro-decomposition of the silver containing coordination polymer, Ag-CP, the organic linkers were leached while the Ag aggregated into particles on the surface of the carbon support. The as-prepared electrode showed an excellent performance in the electrocatalytic CO₂ reduction in the liquid phase with a FE_{CO} of ~90% at 1 V vs. RHE. When this electrode type was applied in a gas diffusion cell, the excellent FE_{CO} was maintained, and the total current density was boosted to as high as 400 mA cm⁻², which highlighted the importance of system integration towards CO₂ER commercialization. Especially, the gas-diffusion electrode demonstrated a

specific mass activity of $\sim 1950 \text{ mA mg}^{-1}_{\text{Ag}}$, one of the highest among the reported electrodes, since the Ag content can be optimized through this MOF-mediated approach.

In **Chapter 3** a bifunctional catalyst based on Ag and Cu was manufactured in order to combine their catalytic properties to a direct conversion process of CO_2 to C_2H_4 via intermediate CO formation. The layer-by-layer growth was combined with spin-coating to ensure a uniform dispersion of Ag on the surface of Cu foil, and control the Ag content. After electro-decomposition Ag particles were produced, resulting in a composite electrode of Ag particles on Cu foil. The Ag-Cu composite showed a favourable selectivity toward C_2H_4 , with a $FE_{\text{C}_2\text{H}_4}$ as high as 43%, while suppressing H_2 and CH_4 formation. Indeed, the CO production scaled with Ag content, confirming the hypothesis to consider Ag as an independent functionality for CO production in this system, and then transfer of CO to the Cu surface for further reduction to C_2H_4 in a sequential catalytic process.

Carbon-based electrocatalysts, especially with nitrogen doping, emerged as novel catalysts in electrochemical CO_2 reduction, and the carbon-rich organic linkers and the atomic dispersion of the N-element in their structure make MOFs an attractive precursor. ZIF-8 was chosen as the sacrificial template for the synthesis of N-doped carbon electrocatalysts (**Chapter 4**). After pyrolysis, most of the reduced Zn was evaporated because of its low boiling point, leaving a N-doped carbon matrix. The ZIF-8 derived N-doped carbon electrocatalyst exhibited a nice FE_{CO} of $\sim 80\%$ in the liquid phase CO_2 reduction, but with a fairly low current density of $\sim 1.1 \text{ mA cm}^{-2}$ at -1.13 V vs. RHE . The electrochemical CO_2 reduction performance was shown to be dependent on the carbon texture and the functionality of the N-

species. Especially pyridinic-N and quaternary-N species in the carbon structure were favourable, whose formation increased with increasing pyrolysis temperature. A well-developed porosity promoted the activity by improving the accessibility of the active sites.

Following this lead, after doping the ZIF-8 with a small amount of Fe a mesoporous structure could be realized with single site iron in the carbon-based catalysts through a silica template-assisted strategy (**Chapter 5**). The silica template created more porosity and stabilized single Fe-sites. The porous structure exposed more active sites and improved accessibility, significantly enhancing the current densities to $\sim 10 \text{ mA cm}^{-2}$ at -1.13 V vs. RHE , while the single Fe-sites facilitated CO formation, demonstrating a peak FE_{CO} of $\sim 85\%$ and a lowered overpotential for CO production by about 200 mV. To prove their existence and elucidate the detailed coordination environment of single Fe-sites, several synchrotron techniques were utilized, including HERFD-XANES, EXAFS and valence-to-core X-ray emission spectroscopies. Combined with theoretical calculations, the chemical environment of the single Fe-sites was determined to be a porphyrinic environment completed by $\text{H}_2\text{O}/\text{OH}$ moieties.

To sum up, in this thesis it is demonstrated that the MOF-mediated synthesis (MOFMS) approach has great potential in the catalyst engineering for electrochemical CO_2 reduction. At the same time, it is fair to admit that the catalyst engineering should be combined with system integration, as shown increasingly in literature. Long term catalyst performance testing under high current conditions is, however, required to be more meaningful for evaluation towards commercialization. As for the MOF-mediated synthesis, there should be more synthesis routes developed than the current pyrolysis and electro-decomposition of MOFs. The highly designable MOF-

building blocks render the MOF-mediated strategy promising potential to be expanded to a toolbox, in which all catalysts can be synthesized with tunable content and structure, while the atomic dispersion of elements in the MOF structure already guarantees the uniform distribution of catalytic phases. All in all, it is felt that the MOF-mediated synthesis approach can play an important role in the catalyst engineering for electrochemical CO₂ reduction.

SAMENVATTING

De elektrochemische omzetting van CO_2 is een interessante manier om de antropogene koolstofcyclus te sluiten. De mogelijkheid om in korte tijd een stabiele procesoperatie te bereiken, maakt deze techniek bij uitstek geschikt om het wisselende energieaanbod van hernieuwbare energiebronnen, zoals zonnecellen en windenergie, op te vangen. Zoals het geval is bij heterogene katalyse, ligt de sleutel tot het commercialiseren van een proces in de optimalisatie van de katalytische fase. In dit proefschrift maken we gebruik van de unieke eigenschappen van 'metal-organic frameworks' (MOF's) om efficiënte katalysatoren te synthetiseren voor de elektrochemische CO_2 -reductie (CO_2ER). De twee specifieke eigenschappen die we vooral gebruiken zijn de atomaire dispersie van de elementen en de zeer goed te ontwerpen bouwstenen (**Hoofdstuk 1**).

Het metaal element in de MOF vormde de basis van het onderzoek. Een coördinatiepolymeer werd ontwikkeld door zelfassemblage van zilver en 2,5-pyridinedicarbonzuur (**Hoofdstuk 2**). Het Ag-gehalte op een geleidende koolstofdrager als basis van een elektrokatalysator kon nauwkeurig worden ingesteld met behulp van een laag-voor-laag ('layer-by-layer', LBL)groeistrategie. Tijdens de elektro-ontleding van het zilver bevattende coördinatiepolymeer, Ag-CP, werden de organische linkers uitgelooft terwijl het Ag aggregaarde tot deeltjes op het oppervlak van de koolstofdrager. De alzo bereide elektrode leverde uitstekende prestaties in de elektrokatalytische vloeistoffase CO_2 -reductie met een FE_{CO} van $\sim 90\%$ bij 1 V vs. RHE. Deze uitstekende FE_{CO} bleef behouden bij toepassing van dit elektrodetype in een gasdiffusiecel, waarbij de totale stroomdichtheid kon worden verhoogd tot 400 mA cm^{-2} , wat het belang van verdere

systeemintegratie voor CO₂ER-commercialisering benadrukte. In het bijzonder vertoonde de gasdiffusie-elektrode een specifieke massa-activiteit van $\sim 1950 \text{ mA mg}^{-1}_{\text{Ag}}$, één van de hoogste onder de gerapporteerde elektroden, omdat het Ag-gehalte kan worden geoptimaliseerd via deze 'MOF-mediated' syntheseaanpak.

In **Hoofdstuk 3** werd een bifunctionele katalysator op basis van Ag en Cu vervaardigd om hun katalytische eigenschappen te combineren tot een direct conversieproces van CO₂ naar C₂H₄ via intermediaire CO-vorming. De laag-voor-laag groei werd gecombineerd met spincoating om een uniforme verdeling van Ag over het oppervlak van Cu-folie te verkrijgen en het Ag-gehalte goed in te kunnen stellen. Na elektro-ontleding werden Ag-deeltjes gevormd, resulterend in een samengestelde elektrode van Ag-deeltjes op Cu-folie. Deze Ag-Cu-composiet vertoonde een gunstige selectiviteit voor C₂H₄, met een $FE_{\text{C}_2\text{H}_4}$ zo hoog als 43%, terwijl de vorming van H₂ en CH₄ onderdrukt werd. De CO-productie schaaft inderdaad met het Ag-gehalte, wat de hypothese bevestigt om Ag als een onafhankelijke functionaliteit voor CO-productie in dit systeem te beschouwen, waarna CO op het Cu-oppervlak een verdere reductie ondergaat tot C₂H₄ in een sequentieel katalytisch proces.

Elektrokatalysatoren op koolstofbasis met stikstofdoping, zijn boven komen drijven als nieuwe katalysatoren bij elektrochemische CO₂-reductie. De koolstofrijke organische linkers en de atomaire dispersie van het N-element in hun structuur maken MOF's tot een aantrekkelijke uitgangsstof voor de synthese van zulke katalysatoren. ZIF-8 werd gekozen als op te offeren uitgangsstructuur voor de synthese van N-gedoteerde koolstofelektrokatalysatoren (**Hoofdstuk 4**). Na pyrolyse was het grootste

deel van het gereduceerde Zn verdampt vanwege het lage kookpunt, waardoor een N-gedoteerde koolstofmatrix achterbleef. De van ZIF-8 afgeleide N-gedoteerde koolstofelektrokatalysator vertoonde een mooie FE_{CO} van $\sim 80\%$ in de vloeistoffase CO_2 -reductie, maar met een vrij lage stroomdichtheid van $\sim 1,1 \text{ mA cm}^{-2}$ bij $1,13 \text{ V vs. RHE}$. De elektrochemische CO_2 -reductieprestaties bleken afhankelijk te zijn van de koolstofstructuur en de functionaliteit van de N-species. Vooral pyridine N- en quaternaire N-species in de koolstofstructuur bleken gunstig, waarvan de vorming toenam met toenemende pyrolysetemperatuur. Een goed ontwikkelde porositeit bevorderde daarnaast de activiteit door verbetering van de toegankelijkheid van de actieve sites.

Op basis van deze werkwijze kon na het doteren van de ZIF-8 met een kleine hoeveelheid Fe en toepassing van silica-templates mesoporeuze koolstof katalysatoren gemaakt worden met single-site ijzer (**Hoofdstuk 5**). De silica-template induceerde meer porositeit en stabiliseerde de atomair gedispergeerde Fe-sites. Door de poreuze structuur waren meer actieve plaatsen geëxposeerd en hun toegankelijkheid verbeterd, waardoor de stroomdichtheden aanzienlijk werden verhoogd tot $\sim 10 \text{ mA cm}^{-2}$ bij $-1,13 \text{ V vs. RHE}$, terwijl de single Fe-sites CO-vorming mogelijk maakten, met een piek- FE_{CO} van $\sim 85\%$, en de overpotentiaal voor CO-productie verlaagd werd met ongeveer 200 mV . Om het bestaan van afzonderlijke Fe-sites

te bewijzen en hun coördinatieomgeving in detail op te helderen, werden verschillende synchrotrontechnieken gebruikt, waaronder HERFD-XANES, EXAFS en valence-to-core röntgenemissie-spectroscopieën. Gecombineerd met theoretische berekeningen werd geconcludeerd dat de de single Fe-sites een porfyrische omgeving hadden, gecomplementeerd met H_2O/OH -species.

Samenvattend wordt in dit proefschrift aangetoond dat de MOF-mediated synthesis (MOFMS) een groot potentieel heeft in de engineering van katalysatoren voor elektrochemische CO₂-reductie. Tegelijkertijd moet daarbij worden aangetekend dat deze katalysatortechnologie moet worden gecombineerd met systeemintegratie, zoals steeds vaker in de literatuur wordt aangegeven. Het bepalen van de katalysatorprestaties in duurproeven onder omstandigheden van hoge stroomdichtheid is echter vereist om een zinvolle evaluatie voor commercialisering te kunnen maken. Wat betreft de MOF mediated synthesis, zouden er meer routes moeten worden ontwikkeld dan de huidige pyrolyse en elektro-decompositie van MOF's. Door de zeer goed te ontwerpen MOF-bouwstenen heeft de MOFMS strategie veel potentie om een stuk gereedschap te worden, waarmee alle katalysatoren kunnen worden gesynthetiseerd met goed gedefinieerde samenstelling en structuur, waarbij de atomaire dispersie van elementen in de MOF-structuur al een uniforme verdeling garandeert van katalytische fasen. Al met al wordt aangenomen dat de MOF-mediated synthesebenadering een belangrijke rol kan spelen in de engineering van katalysatoren voor elektrochemische CO₂-reductie.

ACKNOWLEDGEMENTS

I come to the stage of finishing my PhD study, and I would like to thank a few people for their support during my PhD.

First of all, **Freek** and **Jorge**, thank you so much for your supportive manner of promotion. I decided not mention your title Prof., because Jorge told me during my first week at TUD that “no professor stuff here”. I always admire your engineering wisdom, Freek. Discussions with you could inspire solutions for problems I had. Your “curious about everything” attitude toward science helped me find my passion. Great thanks also for you, Jorge. I have to admit that I spent quite some time getting used to your Spanish accent. But I did get your point when you told me “Shit happens, no worries” after I reported to you the experiment failure in Leiden during my first year. That motto led through a lot of frustrations over experiments afterwards.

Of course, I relied on technical help to run my experiments. I would like to thank you all, **Bart**, **Harry**, **Willy**, **Liliana**, **Ben**, **Duco**, and **Ruben**, for your technical support. Bart, your help with the electrocatalysis and photocatalysis setups is invaluable. Harry, thanks for your help with large activation setup in the old building. Willy, thank you for the BET measurements and analysis. Liliana, thanks for your help with UPLC and GC. Ben, your training with XRD was priceless. Duco, thanks for helping me with SEM. Ruben, without your help with spin-coating Chapter 3 would have been impossible.

Collaboration advances science. I would like to extend my gratitude to all of my collaborators, specially **Xiaohui**, **Dima**, **Samy**, **Henrik**, **Wilson**, **Alla**, **Alexey**, and **Guanna**. Xiaohui, thanks for sharing your fabulous ideas

of using MOF-derived carbon electrocatalysts. Dima, your help with XPS helped me to elucidate species of my samples. Samy, thank you for the nice TEM images. Henrik, it was a great experience to collaborate with you, from which I learned a lot. Wilson, thanks for your contribution to my PhD works. Thank you, Alla and Alexey, for solving the crystal structure of the “unknown MOF of Riming”. And Guanna, your help with DFT calculation helped us to explain mechanistic details, and I am glad to hear that you are interested in joining electrocatalysis community in the future, and I am looking forward to future collaborations.

It's my great honour to work in Catalysis Engineering section. Thank you, **Els**, for your help with paper works, and **Caroline** for sending packages. Thanks for your help, Maxim and Francesc, to kick me off in my first year. **Eduardo**, you always create a joyful environment around you. **Nastya** and **Irina**, thanks for your help with my visit to KAUST. **Monique** and **Michiel**, thanks for evaluating my SAS sheets and approving them. I would also like to thank my outstanding colleagues, **Rob**, **Adrian**, **Davide**, **Han**, **Srinidhi**, **Constantino**, **Robert**, **Sorin**, **Nat**, **Donato**, **Ina**, **Agi**, **Elena**, **Stefano**, and **Anahid**, for all kinds of discussions and companion. My gratitude also goes to my Chinese colleagues in ChemE department. **Xinlei** and **Xuerui**, you organized so many amazing events, I enjoyed them a lot. **Meixia**, best wishes to you and your growing family. **Guotai**, thanks for organizing badminton events. Zilong, it's always fun to talk to you. **Fan**, **Chuncheng**, and **Wenjun**, good luck to your PhD life ahead.

Friends helped me through ups and downs. **Ding** and **Hao**, thanks for being my roommates. Especially Hao, I will always remember the cooking time we shared. Thank you, **Yi**, **Lixue**, **Kai**, and **Kaikai**, for inviting me to

all the parties and board games. My football mates, **Liangyuan** and **Bowen**, thanks to you, too. Surely, I would not forget Suancaiyou (酸菜鱼) group, **Chao**, **Ailian**, **Xixia**, **Xinyu**, **Jiawen**, **Bingming**, **Zhizhong**, **Zhaojing**, **Qingya**. I got to know you guys, since the first day of my college life, and after eleven years, we are still in touch. It was you guys who helped me and encouraged me to rise against the difficulties. Great thanks to you. Thanks also go to **Xiaodi**, **Junxiao**, **Ke**, **Xueyi**, it always makes me feel less stressful to talk or travel with you.

Most importantly, thank you, **Dad** and **Mom**, for your unconditional support. I know that you are always curious about the progress of my PhD study, but you never asked, being afraid that it would put me under pressure. Now I can proudly tell you that I have finished my PhD, and thanks for your endless love.

Finally, I would like to thank **Yitong**, my girlfriend. Your appearance in my third year was prompt. You comforted me when I was in stress. Your smile led me out of a mess. We might be kept apart in distance, but I can feel you are close. Special thanks for your patience, hopefully we shall reunite in months, all the waitings have their ends, and our story just begins.

At the end of PhD study, I have to say that doing a PhD is not an easy job. However, the great support I got from you made it less tough. Sincere gratitude goes to all of you.

LIST OF ACADEMIC CONTRIBUTIONS

Publications:

- **Riming Wang**, Henrik Haspel, Alexey Pustovarenko, Alla Dikhtiarenko, Artem Russkikh, Genrikh Shterk, Dmitrii Osadchii, Samy Ould-Chikh, Ming Ma, Wilson A. Smith, Kazuhiro Takanabe, Freek Kapteijn, Jorge Gascon, Maximizing Ag Utilization in High-Rate CO₂ Electrochemical Reduction with a Coordination Polymer-Mediated Gas Diffusion Electrode. *ACS Energy Lett.* 2019, 4, 8, 2024-2031.
 - **Riming Wang**, Freek Kapteijn, Jorge Gascon, Engineering Metal–Organic Frameworks for the Electrochemical Reduction of CO₂: A Minireview. *Chem. Asian J.*, 2019, 14, 3452-3461.
 - **Riming Wang**, Xiaohui Sun, Samy Ould-Chikh, Dmitrii Osadchii, Fan Bai, Freek Kapteijn, Jorge Gascon, Metal-Organic-Framework-Mediated Nitrogen-Doped Carbon for CO₂ Electrochemical Reduction, *ACS Appl. Mater. Interfaces*, 2018, 10, 17, 14751-14758.
 - Xiaohui Sun, **Riming Wang**, Samy Ould-Chikh, Dmitrii Osadchii, Guanna Li, Antonio Aguilar, Jean-louis Hazemann, Freek Kapteijn, and Jorge Gascon, Structure-Activity Relationships in Metal Organic Framework Derived Mesoporous Nitrogen-doped Carbon Containing Atomically Dispersed Iron Sites for CO₂ Electrochemical Reduction, *Journal of Catalysis*, 2019, 378, 320-330.
 - **R. Wang**, F. Kapteijn, J. Gascon, Metal-organic Framework Mediated Ag-Cu Composite for Enhanced Production of Ethylene in Electrochemical CO₂ Reduction, *in preparation*.
-

Presentations:

- ***Riming Wang, F. Kapteijn, J. Gascon***, MOF-mediated catalyst engineering for electrochemical CO₂ reduction, 1st GRMH-GDL Symposium of Young Researcher in Chemistry, Guangzhou, China, July, **2019. (Oral)**
- ***Riming Wang, F. Kapteijn, J. Gascon***, Maximizing Ag utilization in CO₂ electrochemical reduction: a MOF-mediated approach, 20th Netherlands Catalysis and Chemistry Conference, Noordwijkerhout, the Netherlands, March, **2019. (Oral)**
- ***Riming Wang, F. Kapteijn, J. Gascon***, Maximizing Ag utilization in CO₂ electrochemical reduction: a MOF-mediated approach, 69th Annual Meeting of International Society of Electrochemistry, Bologna, Italy, September, **2018. (Poster)**

ABOUT THE AUTHOR

Riming Wang was born on 28th September, 1989 in Qingdao, China. He received his bachelor degree in 2012 from the School of Materials Science and Engineering at Shandong University, China. He continued his master study at the same university under the supervision of Prof. dr. Longwei Yin. He obtained his MSc degree in 2015.



From September 2015 on, he moved to Netherlands and started his PhD project under the supervision of Prof. dr. Freek Kapteijn and Prof. dr. Jorge Gascon at the Catalysis Engineering group of Department of Chemical Engineering, Delft University of Technology. His PhD project focused on the application of metal-organic framework mediated synthesis for electrochemical CO₂ reduction.